Experimental and numerical analysis of nonlinear properties of rail fastening systems

Yan Liu

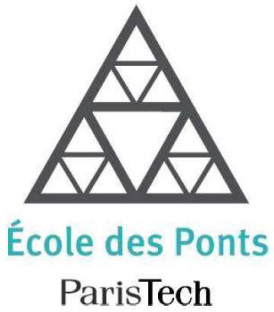

THESE

Pour obtenir le grade de

Docteur de l'Université Paris-Est

Discipline: Mécanique

Présentée par

Yan LIU

Experimental and numerical analysis of nonlinear properties of rail fastening systems

Soutenance le : 20/03/2015

JURY

Prof. Tianxing WU	Rapporteur	Shanghai Jiaotong University
Prof. Qiang GUO	Rapporteur	Shanghai University
Prof. Denis Duhamel	Examinateur	Ecole des Ponts ParisTech
Prof. Rongying SHEN	Examinateur	Shanghai Jiaotong University
Prof. Songliang LIAN	Examinateur	Tongji University
SN ENGR Xun PENG	Examinateur	Jiangyin Haida Co., Ltd
Prof. Honoré YIN	Directeur de thèse	Ecole des Ponts ParisTech
Prof. Yanyun LUO	Co-Directeur de thèse	Tongji University

Résumé

Le besoin en isolation vibratoire des voies ferrées conduit de plus en plus souvent au recours à des systèmes d'attache de rail souples avec des designs sophistiqués. Par contre, les produits deviennent diversifiés mais leur conception se fait de manière empirique dans la pratique. Dans ce travail de thèse, deux systèmes d'attache de rail sont étudiés expérimentalement et numériquement: un système qui travaille principalement en cisaillement et l'autre en compression. Des essais quasi-statiques et dynamiques sont menés puis les résultats sont analysés à l'aide de différents modèles mécaniques. En plus, une série de tests sur les élastomères utilisés dans les deux systèmes sont réalisés. Ces tests permettent de choisir des modèles hyperélastiques et viscoélastique appropriés, et de déterminer les paramètres de propriétés mécaniques des élastomères dans ces modèles par des simulations Abaqus. En utilisant également Abaqus, des analyses par élément fini des deux systèmes d'attache sont effectués et les résultats sont comparés aux ceux des essais. Des non-linéarités d'origine matérielle et géométrique sont ainsi analysées et expliquées. Enfin, des études de sensibilité des paramètres sont effectuées, suivies d'études d'optimisation structurale. Cet étude devrait être utile pour une meilleure compréhension du comportement mécanique des systèmes d'attache de rail sous chargement statique et dynamique, et au final pour une meilleure pratique dans la conception et l'optimisation des produits.

Mots clés: systèmes d'attache de rail, expérience et modèle de mathématique, FEA, sensibilité des paramètres, optimisation structurale

Abstract

Higher demand on vibration isolation of track structure in modern railway track leads to a trend of lower stiffness of rail fastening systems, places an increasing need for better design approach as well. However the current development status of rail fastening industry is dramatically diversified but mainly empirical. In this work, a shear type and a bonded compressed type of rail fastening systems are investigated experimentally and numerically. Quasi-static and dynamic experiments are carried out and the results are analysed with different mechanical models. Besides, a series of fundamental rubber material tests is performed to accurately describe the rubber material used in the two fastening systems. The most appropriate hyperelastic and hysteresis models are chosen with the help of simulations by Abaqus. Also by using Abaqus, finite element analyses are conducted for the two fastening systems and the numerical results are compared with those of experiments. Material and geometrical nonlinear features observed in the measured displacement-force curves are analysed and explained. Finally, parameter sensitivity of the two fastening specimens is studied, followed by an optimization process to meet practical optimization objectives. The present work is believed to be helpful for understanding the mechanical behaviour of rail fastening systems, while enlightening the engineering practice, and eventually improving product designing and optimizing measures.

Key words: Rail fastening systems, nonlinear properties, numerical modelling, FEA, parameter sensitivity analysing, structural optimization

TABLE OF CONTENTS

ABSTRACT

Since the beginning of railways industry, principle of ballasted track structure has not changed substantially. Important developments since II World War includes introduction of continuous welded rail (CWR), use of concrete sleepers, heavier rail-profiles, innovative elastic fastenings, mechanization of maintenance, and introduction of advanced measuring equipment and maintenance management systems. However, slab track structure was introduced due to its low maintenance, high availability, low structure height and relatively low structure weight. As a consequence, the introduction of continuous welded rail (CWR) track and concrete sleepers, especially in case of slab track gives rise to more and more urgent need for fastenings with great flexibility. As heavy freight axle loads increases and high-speed railway development, in addition to the increased service demands, the improved performance of high elastic rail fastening system is becoming increasingly necessary. However the current development status of rail fastening industry is dramatically diversified but mainly empirical. Except a few leading companies in the worldwide, such as Pandrol of UK, Vossloh of Germany, Delokor in Australia and so on, nearly most products especially in the developing countries are imported or imitative. Though rail fastening systems play a more and more important role in present railway track structures in nowadays, hundreds of products were newly introduced with only a few simple specifications and nearly no thorough theoretical analysis can be found and documented studying on the rail fastening systems. Furthermore, there is even no a generally accepted standard for rail fastening products' designing and selecting. This work aims at enhancing understanding of two typical kinds of fastening systems and to provide a few reasonable product optimization objects and measures.

Initially, a set of quasi-static and dynamic experiments of the two rail fastening specimens was carried out. This serves two purposes. Firstly, quasi-static and dynamic mechanical behaviour, such as nonlinear elasticity at large deformation, hysteresis loss during dynamic loading and pre-load dependent, frequency as well as amplitude dependent properties, can be observed and compared to other vibration isolation system; secondly, the measured results will be used for fitting the numerical model parameters proposed later on.

Additionally, three mathematical models are presented and discussed. Since it is extremely difficult to implement a model considering all applications with wide range of working conditions in the mean while considering all complex mechanical properties, the three models were used respectively emphasizing on different characteristics. The models presented herein benefits in enhancing understanding and predicting the mechanical properties and how they are influenced by certain working conditions, also providing theoretical basis for product design, optimization and production. In addition to the models, which concentrate on the general mechanical properties, finite element analysis is also employed in analysing the detailed performance of the rubber components in the two fastening specimens.

A family of fundamental rubber material experiments is therefore followed. Uniaxial tension, uniaxial compression and planar tension measurements are carried out to describe the hyperelasticity of the present rubber; a set of dynamic experiments (DMA) are presented in order to decide the viscoelasticity of the rubber material Different hyperelastic and viscoelastic models are compared according to the measured data and, at last, the most suitable model is selected. Model parameters are determined by using the measured results.

Furthermore, each nonlinear feature existing in the working curves of the two fastening specimens are explained. By using the selected material models and parameters the two fastening systems are modelled in Abaqus. Quasi-static experiment and the dynamic measurement under different loading conditions are simulated. Simulated results are compared to the measured results, and all the nonlinear features observed in the working curves, such as geometric nonlinearity, material nonlinearity, boundary nonlinearity as well as nonlinear dynamic properties, are analysed in this virtual environment. The different nonlinear properties of the shear type and compressed type rail fastening systems are also proposed and interpreted.

At last, parameter sensitivity analysing of the present shear type and the compressed type rail fastening systems are introduced, followed by an optimization process to meet different demands. Nonlinear properties discussed above are taken good use or avoided during the optimization. Optimization objectives include isolation efficiency, displacement response, vertical and lateral stiffness match, free surface rationalization and material cost, etc.

An important term “shear-compression ratio” is firstly proposed in present research in order to meet the expecting vibration isolation capability and the vertical-and-lateral stiffness ratio with the lowest cost.

The presented work is thus believed to be helpful for understanding the mechanical behaviour of rail fastening systems in detail, while enlightening the theoretical basis of the its engineering practice, and eventually improve product designing and optimizing measures more than imitation and empirical method.

ACKNOWLEDGMENTS

The work forming this thesis was carried out between September 2011 and March 2015 in École Nationale des Ponts et Chaussées in France and Tongji University in China. Special gratitude is given to China Scholarship Council, Graduated School of Tongji University and École des Ponts ParisTech for their gratefully acknowledged financial support.

To the great numbers of people who have helped me during the time period I would like to express my sincere gratitude. Firstly, I'm very thankful to my dear professor Honoré YIN. It is his excellent guidance and supervision from time to time helping me making the progress of this work. Special gratitude is given to Prof. Tianxing WU and Prof. Qiang GUO for reviewing my thesis. A lot of thanks are given to them as well as Prof. Rongying SHEN, Songliang LIAN and Xun PENG for their time and valuable comments. Sincere gratitude is given to Prof. Denis Duhamel for accepting invitation and traveling so far distance from Paris for attending my defence. I am also grateful to the colleagues, faculty and staff at Laboratoire NAVIER of École des Ponts ParisTech for their friendly help. Furthermore, the group of friends in Paris made my life studying abroad colourful and full of happiness.

Additionally, I also would like to give my deep gratitude to my Chinese supervisor, professor LUO Yanyun. Thanks very much for his contribution to my thesis, and permanent support, encourage and trust. Thank my dear brothers and sisters in the research group of Tongji University, and my dear friends giving me consistent care and support. Special gratitude is given to Haida Rubber and Plastic LTD.in Jiangyin, China, to Prof. WEI Yintao of Tsinghua University in Beijing, to Prof. XING Yufeng of Beihang University in Beijing, to Prof. YANG Deqing of Shanghai Jiaotong University.

To my parents, elder brother and my dear,

that I’m so thankful and proud to have.

LIST OF ILLUSTRATIONS

FIGURES **PAGE**

CHAPTER 1 Research background

CHAPTER 2 Experiment of rail fastening systems

CHAPTER 3 Modelling of the rail fastening systems

CHAPTER 4 Fundamental rubber material tests and simulation

CHAPTER 5 Finite element modelling and experiment-simulation comparison

CHAPTER 6 Parameter sensitivity analysing and structural optimization

LIST OF TABLES

TABLES **PAGE**

Chapter 1 Research background

1.1 Track structure

1.1.1 Ballasted track structure

Ballasted track structure which is also called “classical track” or “conventional track” consists basically of a flat framework made up of rails and sleepers supported on ballast [1]. Since the beginning of the railways, principle of the ballasted track structure has not changed substantially. Important developments since II World War includes introduction of continuous welded rail, use of concrete sleepers, heavier rail-profiles, innovative elastic fastenings, mechanization of maintenance, and introduction of advanced measuring equipment and maintenance management systems. As a result, the traditional ballasted track structure still can satisfy the demands in nowadays, as demonstrated by the TGV in France. France is the country mostly admires the ballasted superstructure in the new era of railway system all over the world due to their advanced maintenance instruments. The main advantages of ballasted track are, for examples: proven technology, relatively low construction costs, simple replacement of track components, relatively simple correction of track geometry, i.e. maintenance, small adjustments of track curves possible, good drainage properties, good elasticity and good damping of noise and vibrations. Generally in a ballasted track structure, ballast bed rests on a sub-ballast layer which forms the transition layer to the formation. The rails and sleepers are then connected by fastenings. These components and other structures such as switches and crossings are all considered as part of the track. Since the ballast bed consists of a layer of loose, coarse grained material which, as a result of the internal friction between the grains, can absorb considerable compressive stress, but no tensile stress. The bearing strength of the ballast bed in the vertical direction is considerable, but in the lateral and longitudinal direction it is clearly reduced. In addition, the thickness of the ballast bed should be such that the subgrade is loaded as uniformly as possible. The optimum thickness is usually 25-30 cm measured from the lower side of the sleeper.

1.1.1.1 Concrete sleepers

In ballasted track the rails rest on sleepers and together form the built-up portion of the superstructure. Timber and concrete and to a limited extent steel sleepers are used. In general, the general functions and requirements of sleepers are: to provide support and fixing possibilities for the rail foot and fastenings, to sustain rail forces and transfer them uniformly, to preserve track gauge and rail inclination, to provide adequate electrical insulation and to be resistant to mechanical influences and weathering over a long time period, etc.

Due to the scarcity of wood, the introduction of CWR track and the improvements in concrete technology and pre-stressing techniques, concrete sleepers became significantly developed and used in the newly constructed ballasted track structures. Generally speaking, concrete sleepers have such advantages as heavy weight which is useful in connection with stability of CWR track, long service life and can be replaced easily, as well as relatively simple to manufacture. Moreover, climatic influences have little effect on the concrete sleepers which also significantly enhances its service life compared with the timber sleepers.

However, concrete sleepers still have such many drawbacks as being less elastic than wood, susceptible to corrugations and poor quality welds, even risk of damage from impacts. In addition, dynamic loads and ballast stresses could even be as much as 25% higher. At this situation, elastic properties of whole track structure needs to be supplemented by such measures like continuous ballast bed and sleepers and the innovative fastening systems, especially on non-moveable bridges and viaducts. In order to improve the structural behaviour of ballasted track with concrete sleepers, other developments are also discussed in section 1.1.1.2 and 1.1.1.3.

1.1.1.2 Ballast mats and soffit pad

Installing resilient mats between the bottom of the ballast and the subgrade surface (normally tunnel floor and bridge deck) has been employed as an elasticity-improved method for ballasted track. No matter which type of ballast mats such as profiled mats, granular mats and foam mats, the top layer consists of a hard protection layer preventing ballast grans to penetrate into the mat surface. Generally speaking, the mat's thickness is approximately 3cm in total. The rubber layer produces damping by changing the motion of the ballast; while it is

not as a result of significant energy absorption within the layer itself. In other words, the object of inserting the rubber layer is to introduce resilience and hence generate a mass-spring effect carrying away energy. Brief, the softer the mats are the larger and faster the vibrations are attenuated.

Another way to attenuate track vibrations is to use a sleeper soffit pad which is similar as the ballast mats, while the soffit pads are placed between the sleeper and the ballast. The composite pad comprises 22mm of rubber bonded cork normally, also with a hard facing to prevent damage by ballast particles.

1.1.1.3 Innovative fastening system

The term "fastening system" was considered as an integration including all components together forming the structural connection between rail and sleeps. There are a great variety of fastening systems worldwide and they are introduced in order to keep up with the changes in requirements and options; the choice of fastening also greatly depends on the properties of sleepers. Generally speaking, the rail fastening systems have such functions and requirements as: to "absorb" the rail force elastically and transfer them to the sleeper, to damp vibrations and impacts cause and to provide electrical insulation between the rails and sleepers especially in the case of concrete sleepers. In the long history of ballasted structure with concrete sleepers, a lot of innovative fastening systems have been introduced to meet the new requirement such as anti-vibration requirement on bridge or in tunnels, track geometry accurate keeping for high speed railway and so on. Examples of the first group of innovative fastening systems include those with resilient baseplate and/or resilient rail pad.

Though the rail can be fastened to the sleepers with or without the use of steel baseplates which provides sloping upper surfaces and upright ribs between which the rail can be well locked, the baseplate has the following advantages: vertical load can be distributed over much larger area of the sleeper and this may lengthen the sleeper's service life; horizontal load can be absorbed much better due to friction effect and also because it is distributed over all the fastening anchored in the sleeper; baseplates are also excellent for sustaining larger lateral forces if large cant deficiencies are provided; they also have a higher bending stiffness and grooves in the ribs can also provide good fastening locations of the rail;

baseplates also gives extra weight to the sleepers, etc. Noteworthy that this kind of rail fastening systems with a resilient pad underlying baseplate (sometimes there are more than one layer of the baseplate and baseplate pad) are not only used in the ballasted track structures but also can be seen in slab track. Similar, the function of rail pads is to transfer the rail load to the sleeper while filtering out the high frequency force components. Modern rail pads vary considerably in material properties (rubber or foam structured) and in appearance such as with grooved surfaces or studded surface. Traditionally, the rail pads are relatively stiff in order to effectively reduce sleeper strains arising from the high frequency wheel-rail load; while softer rail pads are used in a lot of new railway lines with stiffness of about 70-90kN/mm, especially if combined with concrete sleepers.

Given the advantages of resilient baseplate and rail pads, the drawbacks of this type of rail fastening systems on the other hand are relatively high price because a typically classic in-direct fastening system consists of a baseplate fixed to the sleeper using coach screws and clip bolts, rigid sleeper clips, spring washers and nuts to rails. The clip bolt is inserted into the holes in the plate. Besides the expensive cost, the elasticity of the baseplate type rail fastening systems are also not enough, sometimes, to meet the resilience requirements since the fastening derives its vertical elasticity only from the two or more layer of resilient pads in compression.

In a word, with ballasted track vibrations may be reduced by increasing the ballast depth, installing resilient mats between the bottom of the ballast and structure surface, inserting sleeper soffit pads with the pads between sleepers and ballast, or introducing innovative fastening systems with resilient baseplate pad and rail pad and some other highly elastic fastening systems according to special anti-vibration requirements. Studies show that a reduction of 6 dB at frequencies below 10 Hz by increasing the ballast depth from 30 to 75 cm, however this is definitely not an attractive solution because of the costs, the weight and the extra height. This is why the resilient mats, sleeper pads as well as a great varies of innovative fastening systems are more and more dominated in the newly constructed ballasted rail way lines.

1.1.2 Slab track

Though most of the current track structures are still of traditional ballasted type, amplifications tend more and more towards non-ballasted track (slab track) whose major advantages are low maintenance, high availability, low structure height and relatively low structure weight. Of the most important, slab track is very competitive from the cost point of view since maintenance for ballasted track structures is much more intensive. According to research literatures, night time possessions often last no longer than 5 hours or even less on European networks, whose intensive traffic becomes more and more difficult to carry out the maintenance and renewal work. In a word, one of the severe problems of ballasted track is the high cycle costing besides investment costs; another prominent problem is the slow deterioration of the ballast material since ballast loose grain wandering and breaking up may cause increasing geometrical unevenness and ballast bed clogging may cause drainage problems. However, slab track can provide much higher lateral and longitudinal stability and deviation of the track is less likely to happen. The condition of the track geometry is therefore good enough and also will improve passenger comfort and decreases considerably the amount of maintenance. Specifically, in comparison to ballasted track structure slab track is to a large extent maintenance free since for which tamping and ballast cleaning as well as track lining is nearly unnecessary (amounting to 20% to 30% of the maintenance costs of ballasted track); as a result, slab track system has nearly the maximum availability and there is hardly any hindrance to residents; service life of the slab track is also largely increased; the excess of superelevation and cant deficiency at special cases, such as the mixed use of freight and passenger trains, does not cause altering of the track position; adjustment up to 26mm in vertical direction and 5mm in horizontal positions are also possible to counteract small deformations. Besides, relatively reduced height and weight, track accessibility to the road vehicles and bicycles, preventing the release of dust from the ballast bed into the environment and so on are all incidental advantages of slab track systems.

Slab track is well acceptable either in high-speed railway lines or metro networks also civil structures like bridges and tunnels currently. There is a large variety of existing superstructure designs of slab track system [2-4] which can be generally derived into three main types except the continuous rail support applied primarily for tramway, sleepers or blocks embedded in concrete or top of asphalt-concrete roadbed, prefabricated concreted slabs,

concrete slabs and sleepers with high elastic fastening systems. Brief description of each kind will be discussed in the following sections.

1.1.2.1 Sleepers or blocks embedded in concrete

Concrete sleepers embedded in concrete bed are most commonly used in Germany for newly constructed high speed railway lines, such as the famous Rheda system since 1970 [3-7] and Zublin system since 1974 [3-4,8]. Other examples of concrete sleepers embedded in slab bed are low vibration track (LVT) and the Stedef system [9]. This type of embedded elastic blocks has proved to be one of the perfect solutions for all types of slab track systems, irrespective if that is a high-speed line where accurate track geometry is required, or within the city centre in the metro system where vibration attenuation is of primary importance. It is therefore not surprising that three of the four longest tunnels in the world are included in over 100km of the LVT system installed. The LVT system consists of a concrete block, a resilient pad and a rubber boot surrounded by unreinforced concrete. Except a piece of rail pad nearly no extra demands are required on the rail fixation system.

1.1.2.2 Prefabricated slabs

Prefabricated slabs have already applied in a lot of different places all over the world which considerably contributes to track structure qualities. Moreover, the high level of mechanization, labour-saving construction and a lot of other advantages make it very competitive in slab track structure. The most well-known example of the prefabricated slabs is the one used in Shinkansen-lines of Japan, whose working principle is also used in IPA-system in Italy. The prefabricated slab used firstly on the high speed railway line between Osaka and Okayama on the Sanyo Shinkansen, Japan, consists of a layer of cement asphalt on the structural surface such as a viaduct or other rugged bed, cylindrical stoppers to prevent lateral and longitudinal movement, and a reinforced concrete slab on above the cement mortar layer. In total, one slab weighs about five tons.

Another kind of famous slab track system is referred to as “floating slab track” consisting of a pre-cast reinforced concrete slab on the resilient bearings made of rubber material or steel springs, in order to form a large isolated mass and therefore low natural frequency mass spring system. It thus can provide large reduction of force transmissibility and

vibration isolation efficiency for metro systems. Examples include the short pre-cast slab with double sleepers applied in Toronto, the Eisenmann track applied in Munich and Frankfurt as well as New York subway, etc.

1.1.2.3 Elastic fastening systems

There are dramatically lots of elastic rail fastening systems in modern slab track structures after innovative fastening systems with resilient baseplate and rail pad have been introduced to ballasted track. Germany, England, Australia, Japan and China are all highly advanced countries in the fastening systems industry. Generally speaking, fastening systems are designed and selected due to a lot of reasons, for instance the demand of anti-vibration grade, requests for integrity and maintenance, restricts of accessing in the railway line, compatibility with existing lines in a renewed project, terrain limitation, and so on.

Elastic fastening systems contains three different types in general, the unbounded elastomer pad under rail and/or a flat baseplate as discussed in section 1.1.1.3, bounded assembly with flat top and bottom plates as well as other non-baseplate elastic fastening systems. Fig. 1:1 (a) shows a typical unbounded compressed type rail fastening system designed and produced by company Tiflex of UK. It was enlightened by the fastening systems used in ballasted track and was developed initially for the first group of non-ballasted track construction, which took place in Netherlands and Spain. The objective was to provide approaching resilience in non-ballasted track construction as ballasted track structure and to reduce the ground borne vibration with two layers of flat rubber pads, i.e. rail pad and baseplate pad. A great deal of analogical rail fastenings from different countries can be recited, see Fig. 1:1 (b-e). Though introduce different clamping, fixing, insulate components according to different engineering requirements and sometime few more layers of resilient pad are introduced in order to apply more elasticity, they keep the basic resilience principle with vertically deformed elastic rubber pad and as a result they are called compressed-type fastening systems.

Pandrol VANGUARD is neither a bonded nor an unbounded compressive fastening system, but a typical shear type fastening systems which cushions vertical force from passing trains by rubber component in shear deformation mode, see Fig. 2:2. Pandrol VANGUARD,

with a nominal static stiffness value as low as 5kN/mm, has a remarkable vibration isolation performance without significant dynamic gauge widening under traffic. The significant reduction of vibration and secondary noise makes it ideal for applications in the most sensitive areas to the environmental concerns. Since been demonstrated to be practical and effective all over the world such as London, South korea, China, Singapore since 2002. Shear type rail fastening systems represented by Pandrol VANGUARD have been recognized as a highly innovative solution for rail fixings particularly in challenging circumstances, achieving significant rail noise suppression, and in the same time, with less construction cost in comparison with in-situ resilient concrete slab and floating slab track systems.

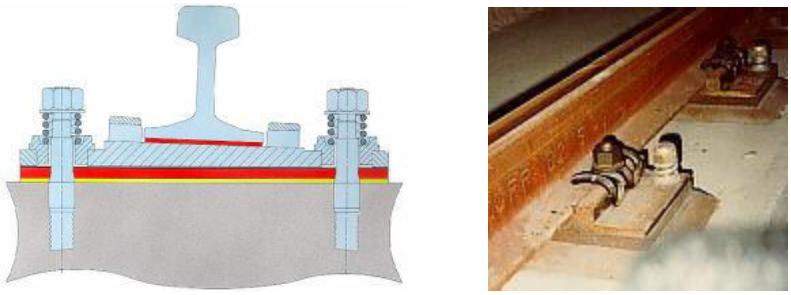

(a) Fastening system with resilient pads from Tiflex of UK (rail pad and baseplate pad)

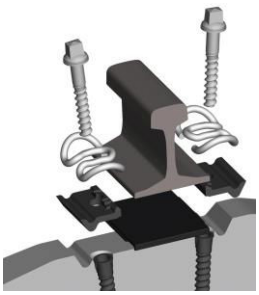

(b) Vossloh W14 from Germany

(c) Pandrol VIPA from UK

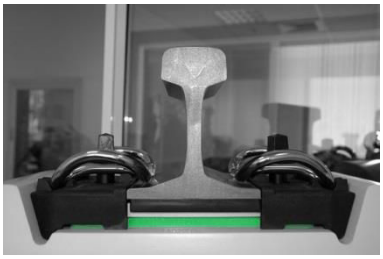

(d) Getzner from Australia

(e) Tie captive system from Amsted RPS of America

Fig. 1:1 Un-bonded compressed type rail fastening systems

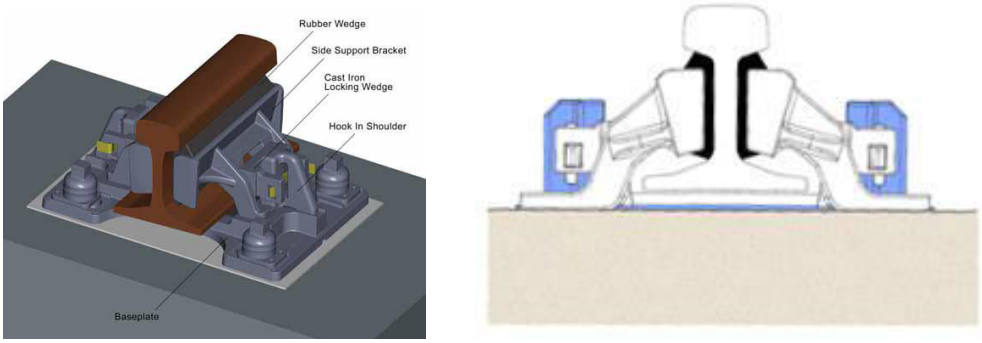

Fig. 1:2 VANGUARD from Pandrol of UK

The very high elasticity of PANDROL VANGUARD is due mainly to the low shear modulus of rubber material compared of compressive modulus and the dual stiffness capability designed for sake of safety also takes the advantage of compressive property of rubber material. In fact, shear type rail fastening system with high resilience and sometimes with a double stiffness definition can be traced back to early 60th in the 19 century when Cologne Egg was newly designed and manufactured by Clouth Gummiwerke AG company [10]. Cologne Egg is the first fastening system making full use of the advantages of shear elasticity of rubber material. The novel design was rapidly approved to be of excellent quality in high vibration attenuating occasions. In 1983, the Washington Metropolitan Area Transit Authority's (WMATA) Metrorail systems had been seeking an alternative of floating slab track structure for mitigating underground noise and vibration and conducted an in-service testing program of Cologne Egg fastening systems [11]. Testing results indicated that with the egg-shaped rail fastener WMATA can not only find an alternative method for mitigating underground vibrations but also save 3.5 million dollars in the new construction by replacing the floating slabs with the egg-shaped fasteners. Subsequently, the fastening system called ATP egg was procured from Advanced Track Products, Inc. (ATP) of Stanton, New Jersey. The shape of ATP egg was portion of the design that was adopted from original Cologne egg. Delokor egg also originates from Cologne egg [12] which is produced by a world leader company (Delokor Rail) dedicating to supplying technical advices and track related products in Australia and overseas of more than 20 years. Delokor egg can also ensure optimum vibration and structure-borne noise reduction in six degrees of movement and achieve a high degree of noise attenuation. An optimized innovation of Delokor egg is that it provides a dual stiffness at the bottom rubber elliptical ring as shown in Fig. 1:3. Specifically, Delokor egg

consists of a top plate, a bottom frame plate and a rubber component; all of the three parts are vulcanized directly. From Fig. 1:3 (c), the rubber ring with inclined angle mainly deformed in

(a) Top view (b) Exploded view (c) Side view

Fig. 1:3 Delokor egg rail fastening system

shear as loaded vertically. Yet, when vertical displacement is beyond a limit the bottom surface of rubber component reaches the under-surface of iron frame and the overload component begins to deform in compression. This dual stiffness design similar as PANDROL VANGUARD makes use of shear characteristics of rubber material and compressive properties as well.

In addition to the two different kinds of rail fastening systems, i.e. un-bonded compressed and shear type, there is another which is referred to as the bonded compressed type rail fastener. At the early time, bonded compressed type fasteners were designed in order to eliminate the need for steel springs for preventing fatigue failure of anchor bolts. Delkor ALT 1 shown in Fig. 1:4 is a good example of the bounded compressed fastening systems. [13] In fact, it's also originated and transformed from the product Alternative 1 designed by company Clouth in the year 1978.

Though being a compressed type of rail fastening system [12], Delokor ALT 1 has generally the same design concept with egg-shape fastener, consisting of a top and a baseplate and a rubber component inside of them. The underside of this rubber component is specially profiled and designed to allow movement of the top plate holding the rail. The outer frame of the ALT 1 is totally encompassed the rubber component and the top plate, making the unit totally fail-safe. This ALT 1 rail fastener also ensures the necessary resilience in all six degrees of movement, subsequently reduces the dynamic stress on the anchoring elements and the base structure. From Fig. 1:4 (c) we can see that, the main body of the rubber component

is designed with studded surface and it would help to provide much better compressive elasticity and lower vertical stiffness.

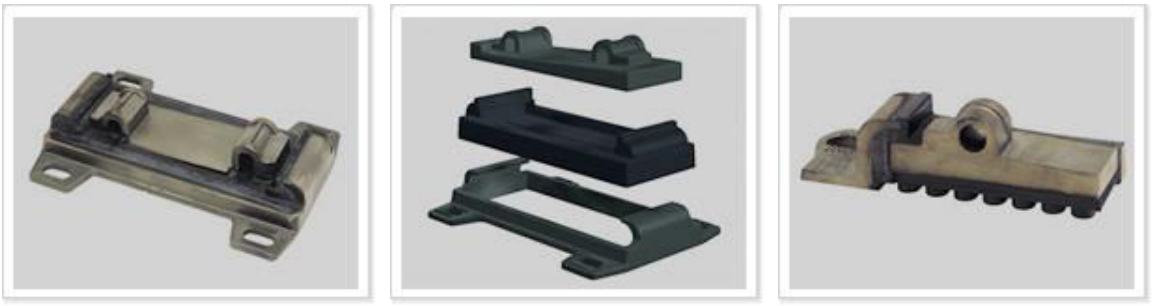

(a) Top view (b) Exploded view (c) Side view

Fig. 1:4 Delokor ALT 1 rail fastening system

1.1.2.4 Brief conclusion

Generally speaking, using slab track, i.e. ballastless track, especially in tunnels and bridges in urban railway transit systems, has been finding increasing support mainly due to the much less expensive maintenance cost and more reliable stability. However, certain precautions should be taken such as the superstructure discussed above in the cases traditional ballast bed is substituted by a rigid concrete slab; at the mean while the old fiber sleepers are also taken the place by concrete sleepers. Otherwise, vibration force transmissibility will be increased considerably. Specifically, slab track systems are normally designed to offer equivalent vibration attenuation capability by interposition of resilient layers with the rigid track structures. Either sleepers or blocks embedded in concrete, prefabricated slabs or floating slab track, they are all in fact mass-spring systems.

The concept of inserting a resilient layer is put forward at first for the innovative fastening systems when concrete sleeper was newly introduced into ballasted track structure as discussed in section 1.1.1.1 and 1.1.1.2. However, in comparison, slab track systems, which employs the principle of resiliently mounted blocks and sleepers such as LVT-system, gives much better anti-vibration efficiency by virtue of increased mass. Extending further the principle of increasing the resiliently supported mass, thereby reducing system nature frequency and therefore enhancing vibration isolation effectiveness, slab tracks including a large precast concrete slab such as floating slab track came into wide service all over the world. However, due to the expensive cost of prefabricated slab track, highly elastic rail

fastening systems become the alternate at large anti-vibration requirement cases. The highly elastic fastening systems are very competitive compared to other measure due not only to its high anti-vibration effectiveness, but also to the relatively reasonable price and other advantages such as easy replaceability, flexible adjustment, etc.

1.2 Basic concept of vibration isolation

Generally speaking, vibration isolation is concerned with reducing the force magnitude transmitted through a peace of resilient component from the force input terminal to the supporting foundation as shown the single degree system, see Fig.1:5.

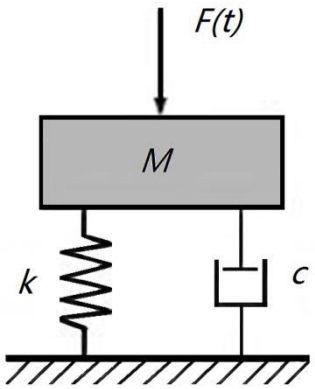

Fig. 1:5 Single degree vibration isolation sketch map

As is shown in Fig.1:5, the spring stiffness k and the linear damping coefficient c represent equivalent parameters of the resilient layer, m represents the mass of the component supported above the resilient pad and subjected to input stimulate loadings, x is the displacement response of the mounted mass, $F_0 sin(\omega t)$ represents the input cyclic force with the $maximum\ F_0$ and angle frequency ω. By the single degree freedom system shown in Fig.1:5, the equation of motion is

$$m\ddot{x} + c\dot{x} + kx = F_0 sin(\omega t), \tag{1:1}$$

where the dot denotes to time derivative. The differential equations of the motion in terms of the damping factor and the un-damped natural frequency of the system are

$$\ddot{x} + \eta\omega_n\dot{x} + {\omega_n}^2 x = F_0 sin(\omega t)/m, \tag{1:2}$$

where $\eta\omega_n = c/m$, η is the damping factor of rubber material and $\omega_n = \sqrt{k/m}$ is the undamped natural frequency of the one degree system. The force transfer function of the vibration isolation system is therefore derived as

$$TR = \frac{F_T}{F_0} = \frac{\sqrt{1+(\eta r)^2}}{\sqrt{(1-r^2)^2+(\eta r)^2}}, \tag{1:3}$$

where $r = \omega/\omega_n$ called frequency ratio and $F_T = \sqrt{(kx)^2 + (c\dot{x})^2}$. The dimensionless amplitude ratio $TR = F_T/F_0$ is referred to as force transmissibility and this force transmissibility in Equation 1.3 is normally used to evaluate the vibration isolation efficiency of a rubber elastomer. Fig. 1:6 shows the dependence of the force transmissibility TR on excitation frequency ratio r for various values of the damping factor η. It is clearly can be seen from Fig. 1:6 that only if the frequency ratio is greater than $\sqrt{2}$ can transmitted force F_T be smaller than the input force amplitude F_0. For the frequency ratio less than $\sqrt{2}$, the transmitted force F_T is amplified from F_0. And in the isolation frequency range, the smaller the value of the damping ratio, the smaller the value of force transmissibility and the better the isolation is.

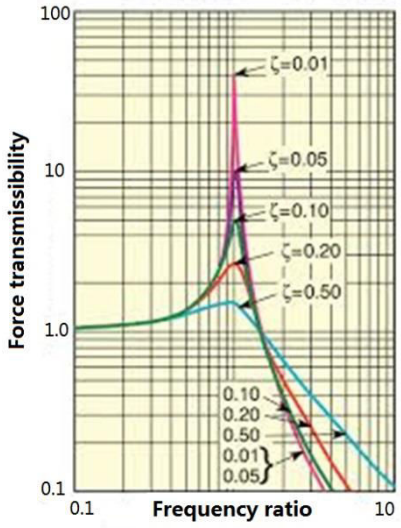

Fig. 1:6 Force transmissibility

Rail fastening systems are typical vibration isolation systems with the rubber component inside which can be described by the elastic and viscous elements; the section of the railway mass is considered as the mounted mass, and the sleeper or concrete slab is

supposed to be the boundary. Obviously, lower stiffness of the rail fastening system gives rise to lower nature frequency and smaller force transmissibility. The performance of vibration isolation systems is often evaluated by the transmissibility, which measures the reduction of transmitted force. In order to achieve high isolation efficiency, force transmitted to the foundation needs to be less than the excitation force as much as possible which entails an excitation frequency greater than $\sqrt{2}$ times the natural frequency of the system. As a result, efficient vibration isolation can be obtained from a system with lower natural frequency.

1.3 Research situation of rail fastening systems

1.3.1 Current situation of product development

The introduction of CWR track as well as the use of concrete sleepers and non-ballast track gave rise to the need for fastenings with greater elasticity [1]. As a result, hundreds of elastic rail fastening systems, with their own advantages and drawbacks, were designed and introduced into newly constructed as well as re-constructed railway lines in the world wide. The leading fastening system companies include Vossloh of Germany, Pandrol of UK, Delkor located in Australia, Amsted RPS of USA, and so on. However, though wrong usage of the rail fastening system either for high speed railway or for light ways or others may give rise to expensive consequences and create serious problems such as slowing down or shutting down the production process, excessive and irregular wear of the rail, damage of the mechanical components, damage of the supporting base, shortening the service life of track components, and so on, there is still no yet a general accepted design and selection criterion dedicated to rail fastening systems to the authors' knowledge which is similar as the performance evaluation testing standard. Since the dominant design method for rail fastening systems still remains primarily empirical and imitative from developing countries such as China where the railway networks are dramatically constructed, the general and superficial common consensus, such as keeping the track geometry accurate should be the primary position for high speed railway lines while anti-vibration should be the chief task for urban railway lines especially in the sensitive region like schools, libraries, business buildings and closely resident places, is far from enough. Current research aims at enhancing understanding of the mechanical behaviour of fastening systems mainly applied to urban railway networks, concentrates mainly on their resilient property under guidance of basic theories of viscoelastic mechanics,

rubber engineering behaviours and vibration isolation mechanism. It's believed to be beneficial for cost reduction due to elasticity overdesign and as the theoretical guidance for the performance and service life optimization of two rail fastening systems.

1.3.2 Theoretical study situation

1.3.2.1 Numerical analysis of rubber material and elastomers

The wide use of rubber components (elastomers) in engineering applications should be back to good digest of rubber material properties first. A lot of information of mechanical behaviour of rubber material can be gained from the literature such as [14-23].

The accuracy of a rubber material model, i.e. a viscoelastic model, depends firstly on the ground state elastic strain-stress relations, i.e. hyperelasticity, and then on the evolution constitutive law of the internal variable. [24] Hyperelastic model provides a general capability for modelling rubber-like materials that exhibit highly anisotropic and nonlinear elastic behaviour, which are valid for large elastic strains. For purely elastic finite-strain calculations hyperelastic models are almost the only choice to give realistic predictions of actual material behaviour at large elastic strain (generally larger than 5% in applications). All hyperelastic models are based on the assumption of isotropic behaviour so that strain energy potential can be formulated to define the strain energy stored in the material per unit of reference volume as a function of the strain at that point. There are a great number of strain energy potentials to model approximately incompressible isotropic elastomers. Examples are Mooney Rivlin (first order polynomial model), higher order reduced polynomial model, neo Hookean, Yeoh, Arruda Boyce, Van der Waals, Ogden models, etc. The reduced polynomial and Mooney Rivlin models are viewed as particular cases of the polynomial model; the Yeoh and neo Hookean potentials, in turn, are viewed as special cases of the reduced polynomial model. Therefore, these models are collectively referred to as polynomial models. In general, the strain energy potential forms are written as separable functions of a deviatoric component and a volumetric component, while the deviatoric part of the strain energy function and the volumetric property can also be omitted and assessed by a Poisson's ratio.

Since hyperelastic models are based on the definition of strain energy potential, [25] as for an isotropic and incompressible material the function can be expressed either in term of

the strain invariants which are functions of the stretch ratios or directly in terms of the stretch ratios themselves. The stretch ratio is defined as the deformed gauge length divided by the initial gauge length by using the nominal engineering strain. Specific hyperelastic models defined by using corresponding strain energy functions will be further discussed in Chapter 4.

Besides hyperelasticity, viscous component of viscoelasticity is also crucial to accurately modelling of rubber materials [26]. In linear viscoelastic theory, it is important to take time as a physical parameter and the detailed comparison between pure elastic solids and viscoelastic solids were presented in [27]. Rubber material shows the phenomena of creep and stress relaxation indicating its dependence on time. Measurements also provide further evidence of this time dependence and also imply a memory effect of rubber material which manifests that stress response at time t depends on the preceding strain history or that the strain at time t depends on the preceding stress history. As a result, constitutive assumption for the stress at time t in terms of the strain history up to time t can be denoted by a function which is generally referred to as response function. Similarly, there can also be the dual constitutive assumption for the strain in terms of stress history. In another word, for every statement of stress in terms of strain history, there is a dual statement of strain in terms of history. A central issue in the modelling of viscoelastic material is the determination of the mathematical form of the response function. In the meanwhile, the essence of the linear viscoelasticity consists of two parts: scaling and superposition. In other terms, the assumption of linearity of response states that if a strain history is scaled by a constant λ, then the corresponding stress is also scaled by λ and if two strain histories are superposed, the corresponding stresses are also superposed. A very useful corollary of the linearity of viscoelasticity is that there is no interaction between the stress responses to separate strain histories. It however should be noted that this linearity of viscoelasticity on the basis of scaling and superposition does not refer to the shape of any strain-stress curve. It refers to a method of constructing the stress response to a composite strain history by scaling and superposing the stress responses to the component strain histories.

Generally there are two standard approaches that have been used to develop constitutive equations of linear viscoelasticity of rubber materials: mechanical analogy and the Boltzmann superposition principle [28]. By using mechanical analogy, linear viscoelastic behaviour is normally conceived as a linear combination of a spring and a dashpot and

correspondingly we can obtain an elastic modulus with units N/m^2 and a viscosity value with units $N \cdot s/m^2$. The mechanical analogues method results in a linear differential equation with constant coefficients relating stress and its rates of different orders. Some of the coefficients are only related to the elastic modulus while some others indicating the viscosity are usually determined from the physical experiments. Three basic models that are typically used to model the linear viscoelasticity of rubber material are the Maxwell model, the Kelvin-Voigt model and the standard linear solid model. However, they only differ from each other in the arrangement of the springs and dashpots. The Maxwell model is represented by a viscous damper connected in series with a purely elastic spring. Since the spring and the dashpot are subjected to the same stress, this model is also known as iso-stress model. Though the Maxwell model can accurately predict the stress decaying exponentially with time, a serious limitation of this model is its inability to correctly represent the creep response of rubber-like material increasing without an up bound. The Kelvin-Voigt model has a Newtonian damper in paralleled with a Hookean elastic spring. Since the two elements are kept in the same strain, this model is also known as iso-strain model. The total stress is derived from the sum of the stress in both of the two branches. Kelvin-Voigt model is extremely accurate in modelling creep in many materials however there is a fatal limitation in its ability to describe the stress relaxation in numerous strained viscoelastic materials. The standard linear solid model which is also referred to as the three-element model is a combination of the Maxwell model and a Hookean spring in parallel. Besides the mechanical analogy measures, a more general approach widely used to model the linear viscoelastic material is the Boltzmann superposition model. The relaxation modulus function of this Boltzmann superposition model consists of an instantaneous relaxation modulus and a gradual relaxation modulus function. It, in fact, can be reduced to the Maxwell mode, if and only if the stress relaxation modulus satisfies specific conditions [29]. Other special cases of Boltzmann model include a generalization of the single spring-dashpot paradigm to one pure elastic spring with multiple spring-dashpot system in parallel which is referred to as generalized Maxwell model or generalized standard linear model or Wiechert model [28-30].

However, linear viscoelastic models are apparently not accurate on every occasion. For example, nonlinear viscoelastic behaviour is often exhibited when the elastomer deformation is large or sometimes the material changes its properties under deformations.

Nonlinear viscoelastic theory has been attracting the attention of a large number of researchers over the past century [31-38]. Normally two types of constitutive models can be read from the literatures, one of which is based on the phenomenological mechanical behaviour. In other words, the form of the constitutive model is not based on the explanation of how the properties arise from microscopic structures [32, 39-41]. The other type of nonlinear viscoelastic model entails formulations based on the molecular mechanisms. Doi and Edwads presented a reputation model for concentrated solutions and polymer melts based on an assumption that an entangled polymer molecule, the chain, slides through a "tube". The polymer chain is free to diffuse along the tube axis but cannot move perpendicularly to the tube as other molecules restrict such movement [31]. In [42], the presented Curtiss-Bird model is similar to the Doi-Edwards model but is based on a systematic kinetic development and does not use the phenomenological constraints of a chin in a tube. It was approved that Curtiss-Bird model is more accurate than Doi-Edwards model in predicting the nonlinear behaviour. Furthermore, a thorough review of the molecular types of models, relations between the nonlinear viscoelastic models and molecular structures are given in [43].

Besides the hyperelastic model, linear and nonlinear viscoelastic models, there is also a great deal of research literatures describing the response and developing constitutive models for rubber materials under dynamic loadings. This is due to the significant use of rubber material in engineering practice such as tires, engine mounts, dampen in structures and bridges are all subjected to dynamic load. [21] Industrially-used elastomers make rubber material modelling much more complicated since the filler particles like carbon black change the microstructure of the material in many aspects, some of which are positive such as higher stiffness, damping and crack resistance, better adhesion while others are negative such as the pronounced viscoelastic nonlinearity under cyclic loadings. [44] The most conventional approach in characterizing the dynamic material properties of rubber material is to define the dynamic modulus and damping factor of the rubber in frequency domain in terms of a storage modulus and a loss modulus. Dynamic properties of rubber material differ from the quasi-static properties in terms of a hysteresis loop, the larger stiffness value as well as the frequency and dynamic amplitude dependent dynamic stiffness and damping factor in terms of the varied storage modulus and the loss modulus. This content will be further discussed in Chapter 2.

Dynamic material analysis test (DMA) is the most common means to measure the frequency dependent properties of rubber material specimens. [5R] Frequency dependency of rubber material means the changing storage and loss modulus along with stimulating dynamic frequency [45-46]. In an attempt to fit the frequency dependent DMA (dynamic material analysis) result, the generalized Maxwell models or Prony series discussed above were often used [47]. Haupt and Lion [48] presented a model with much fewer material constants in comparison with Prony series of high orders to describe the frequency dependency by DMA test by introducing a fractional derivative calculus to describe frequency dependent relaxation function. There are a great number of other constitutive models addressing the steady-state rate-dependent behaviour of rubber material subjected to cyclic loadings. The advantages of Bergstrom-Boyce model or briefly referred to as BB model [49, 50] compared to the traditional viscoelastic models such as Prony series is its capability of indicating the frequency dependent hysteresis loss. However, it was found that BB model doesn't demonstrate the hysteresis property increasing with enlarged strain rate at relatively higher range. A more recent viscoelastic constitutive model by Tomita et al. [51] addresses the dependence of the hysteresis losses on the strain rate during cyclic loading. In contrast to the micro-mechanistic approach, rate-dependent constitutive models have also been derived on the basis of continuum thermodynamics [52-56], by using which the Helmholz free energy is split into equilibrium and non-equilibrium components, which give the equilibrium stress and viscosity-controlled overstress, respectively. It is worthwhile to note that BB model will be further discussed since it is used in the FEA part of current research in Chapter 4-7; this is becasue BB model is embedded in Abaqus and also because the main working frequency range of rail fastening system is relatively low which is within the BB model's applicability. The evolution law proposed in BB model is a more general representation of the viscoelastic model of Reese and Govindjee [57]. By ignoring the volumetric viscosity term in the finite viscoelasticity model and extending the materially linear evolution of Reese and Govindjee, BB model was obtained. It was already demonstrated that the algorithmic implementation of the model can be done similarly to the algorithm proposed by Simo and Miehe [58] and by Simo [59]. Integration of the evolution law is carried out by an exponential mapping algorithm [60, 61] and such approach has been used to finite viscoelasticity by Rsses and Govindjee [57].

The case of the frequency dependence with stiffening modulus and the increasing hysteresis losses with frequency was modelled in many ways as discussed above. In the case of the amplitude dependence, a reversible softening with increasing strain amplitude can be found in great deal numbers of literatures such as [62, 63]. The reversible breakdown and re-aggregation of filler clusters in the elastomer matrix play a decisive role for the amplitude dependence which is known more famous as Payne effect [64]. Payne effect was firstly systematically investigated by Payne in the early 1960s when the Payne-effect was only addressed originally as the amplitude dependence of the storage and loss modulus at a constant frequency [65]. Later on, Payne effect was investigated and reclassified in a broader framework by Wrana et al., Heinrich et al., Robertson et al., P. Hofer et al., etc. Based on dynamic mechanical measurements, there are some widely used models presented by Kraus [65] which is based on microstructural destruction and reorganization rates of the filler network, by Ulmer which is derived from Kraus model for a better flexibility and adaptability to experimental data, by Huber et al., by Rabkin and Bruger and by Lion et al., and so on. Different concepts to model the Payne-effect can be also found in [29, 34, 39, 66-67]. Another well-known stress-softening phenomenon is known as Mullins effect. It's different from the Payne effect because this softening phenomenon is irreversible at room temperature and occurs in both filled and unfilled rubber materials [68-70]. [65] Further insight into experimental results and modelling approaches of Mullins effect can be referred to the references by Mullins, Miehe, Lion, Qi and Boyce, Govindjee and Simo, Ihlemann and so on.

1.3.2.2 Numerical modelling of elastomers

Modelling of rubber components can be done from different ways, one common approach is to use continuum mechanics and formulate constitutive laws of rubber material. Nevertheless, such an approach often deals with static, large strains and finite element models [71]. If any, dynamic models of rubber material are still mostly based on linear viscoelastic theory [72] and thus the nonlinear behaviour of filled rubber components in engineering practice cannot be captured. EICKHOFF and BERG [73-75] outline that the models of rubber components should be more global, concentrating more on force-displacement relations rather than on stress-strain relations compared to rubber material constitutive models. In fact, we should well generalize that material as well as component properties should be related in that a rubber component exhibits the same basic characteristics concerning stiffness and loss angle

as the material does in terms of shear modulus magnitude and loss factor [76]. Only exceptions to this rule are e.g. when the geometry of the component introduces additional nonlinearities, such as a progressive stiffness or when the evaluated frequency range is extended, resulting in component internal forces which influence its dynamic properties.

Stiffness and damping property of rubber component depend not only on additives in the material but also on geometry, pre-compression, frequency and amplitude of the motion; the complicated geometries of engineering component and pre-compression may introduce nonlinearity. As a result, modelling of rubber component normally cannot take all the experimental phenomena into consideration. The simplest model of a rubber isolator accounting for both elastic and viscous effects is the Kelvin-Voigt model derived from rubber material constitutive model where a linear elastic frequency independent stiffness is coupled in parallel with a viscous dashpot and damping force is proportional to a first order time derivative of the displacement. However, it overestimates rubber high frequency losses due to the viscous dashpot. Replacing the dashpot with a Maxwell element and forming a three-parameter Maxwell model or the standard linear solid can provide better high frequency description of stiffness but still in a poor loss factor description. Furthermore, the standard linear solid can be expanded to Wiechert model, obtaining improved broad band frequency description [77-81], which nevertheless inevitably increases the number of parameters to clearly describe elastomer dynamic behaviour and brings about computational cumber. The efficient alternative in reducing the required number of model parameters while still obtaining a good description of viscoelastic materials' or components' frequency dependence is incorporating constitutive relations including fractional calculus [82], referring to the thorough review given by Rossikhin and Shimizu [83-84]. Koeller [85] discusses spring-ports, which replace ordinary dashpots in viscoelastic models. Replacing the Kelvin-Voigt's dash-pot by a spring-pot results in a fractional Kelvin-Voigt [86, 87]. The fractional standard linear solid is used in references [82, 86, 88-90] and by Kari [91] applying the model to fit rubber dynamic material property of a wider frequency range subsequently calculating isolator behaviour. Time-domain solutions of the fractional derivatives models are investigated by references [92-99].

Since rubber component also displays strong preload and amplitude dependent properties, vibration isolators are inherently nonlinear [100-101]. They respectively rate to the

finite deformation induced nonlinearity and the Payne effect of rubber material. The latter not only influences on dynamic stiffness but also on damping. An estimable progress in nonlinear dynamic vibration isolator modelling is noticeable in a lot of references [102-110]. In particular, force response of cyclic input displacement is modelled as a combination of a nonlinear elastic and a liner viscous damping force [102, 105-106, 110], a linear elastic and a nonlinear viscous damping force [109], or a nonlinear elastic and a nonlinear viscous damping force [103-104, 107-108], where the dynamic amplitude dependent force, i.e. nonlinear amplitude dependency, is expressed by a Coulomb friction model in [109]. All of these started to provide a deep insight into various nonlinear isolator phenomena, constructively applicable in any vibration isolation optimization process. Reference [111] elaborate on another model that includes friction components in series with an elastic spring which is later used as the three-parameter Maxwell model [112]. Another way of considering the friction dependent damping force is by replacing the viscous component in a standard linear solid by a friction component [113]. The same author of reference [111] also present results for the rate independent friction component when implemented in a finite element analysis [114]. Kaliske [115] describes a friction model based on numerous Coulumb dampers in series with elastic springs. It is expanded by Bruni et al. [115], Austrell et al. [104] and Brackbill et al. [116] to include frequency dependence, giving good representation of measured properties. Dynamic amplitude dependence is modelled by Mallik et al. [117] through separating a nonlinear elastic force and a nonlinear damping force, needing a total of eight parameters. Another model also taking into account the amplitude and frequency dependence is presented by Barber [118] which however needs extensive measurements to properly adjust the numerous model parameters. References [76, 10-11, 100], and [14, 75, 119] by Berg give a very widely used rate independent frictional component showing a smooth behaviour using only two parameters and very good description of the measured amplitude dependent characteristics.

Though nearly all rubber elastomer models are simplified description since it is extremely difficult to implement a model considering all applications with wide range of working conditions in the mean while considering about computational effort, it is still important to enhance understanding of the mechanical properties and how the component properties are influenced by certain working conditions by modelling rubber component combined with experiment process. The simplified models can be used in complete system

investigations and as a means of finding simpler model parameters for predicting mechanical properties of isolation systems. As rail fastening systems is ultimately used as vibration isolation system for dynamic improvement, there is a great need to understand and properly predict their behaviour by means of experiments combined with mechanical modelling, see Chapter 3 for further information.

1.3.2.3 Numerical analysis of track components

Generally speaking, track structure consists of rails, sleepers, rail pads or/and fastening systems, ballast bed with sub-ballast structures and subgrade or a concrete slab instead. Nearly all the other track components have been intensively studied by great deal of research papers except rail fastening systems, though it plays an increasingly important role in the newly constructed track structures with concrete sleepers or direct concrete slab bed. If any, nearly all the literatures include a rail fastening system briefly as a linear pure elastic spring or that in parallel with a dashpot which conflict with its real complicated mechanical behaviour, such as the nonlinear elasticity at large deformation, close frequency dependency, nonlinear amplitude dependency, etc. In addition to the great deal of researches on the integrated track structure, further insight into the mechanical behaviour of each track component has also been went further and finite element methods were often used [120]. In [121] Frohling proposed a mathematical model to predict the track deterioration originated from dynamic wheel rail loading and track stiffness irregularity. Gonzalez-Niciez et al. presented and compared a single-crosstie and a multiple-crosstie model in order to look into the cracking causes, where the important elasticity of rail fastening system however was ignored [122]. There are in fact a lot of references studying on the mechanical properties of concrete sleepers while rail fastening systems are not mentioned at all or largely simplified. Finite element analysing was carried out by Rezatie et al. in [123] to capture the longitudinal crack mechanisms in concrete crossties and dynamic responses of concrete crossties were also studied by Kaewunruen, et al. in [124]. Two finite element models were used to simulate the behaviour of concrete crosstie subjected to vertical wheel load by Yu et al. in [125] and [126], one of which ignores the interaction between concrete and strand while the other takes it into account. Dahlverg et al. [127] investigated the effects of different support conditions on the rail track system by proposing a finite element model, in which rail fastening systems were taken only as a pure elastic spring. The limitation of ignoring the rail mechanical behaviour of rail fastening

systems, which in fact may lead to inaccurate knowledge of the whole track structure performance, was realized by Zhe Chen et al. In [120, 122], behaviour of the pre-stressed concrete sleepers and their dependence on special parameters are studied, where rail fastening systems are considered as one of the influence parameters being studied, such as support conditions, wheel load position and so on. However, the rail fastening system included in this study is a rather easy type with only a layer of rubber pad which cannot represent the general properties of the modern fastening systems, especially those used in metro systems with high elasticity. Though very few studies on behaviour of the integrated fastening systems were found up to today, researches on the fastening clip component such as [120, 122, 124] and on rail pad [121, 123] start to provide detailed insight into the important properties of rail fastening systems.

1.4 Scope of the present research

The outline of current research is as follows. Chapter 2 presents the quasi-static and dynamic experiments of two different types of rail fastening specimens, one of which is a shear-type fastening system while the other is a compressed-type fastening system. This serves two purposes. Firstly, quasi-static and dynamic mechanical behaviour, such as nonlinear elasticity at large deformation, hysteresis loss during dynamic loading and pre-load dependent, frequency as well as amplitude dependent properties, can be observed and compared to those of other common vibration isolation systems discussed in Chapter 1; secondly, the measured results will be used in Chapter 3 for fitting the numerical model parameters.

Three different models introduced in other vibration isolation systems were used and compared in Chapter 3 according to the observed mechanical behaviour through experiment data. Since it is extremely difficult to implement a model considering all applications with wide range of working conditions in the mean while considering all complex mechanical properties, the three models were used respectively emphasizing on different characteristics. The models presented herein benefits in enhancing understanding and predicting the mechanical properties and how they are influenced by certain working conditions, also providing theoretical basis for product design, optimization and production.

In addition to the models, which are used to describe and predict the general mechanical properties, finite element analysis is also important to be employed in analysing the detailed performance of the rubber components in the two fastening specimens. A family of fundamental rubber material experiments is therefore depicted in Chapter 4. Uniaxial tension, uniaxial compression and planar tension measurements are carried out to describe the hyperelasticity of the present rubber; a set of dynamic experiments (DMA) are presented in order to decide the viscoelasticity of the rubber. Different hyperelastic and viscoelastic models are compared according to the measured data and, at last, the most suitable model is selected. Model parameters are determined by using the measured results.

In Chapter 5, displacement-force relationships of the two rail fastening specimens are studied and compared with each other. Firstly, by using the selected material models and parameters the two fastening systems are modelled in Abaqus. And then each quasi-static experiment and the dynamic measurement under different loading conditions are simulated. Simulated results will be compared with the measured results to ensure the fitted models and simulation process. At last, all the nonlinear features observed in the working curves, such as geometric nonlinearity, material nonlinearity, boundary nonlinearity as well as nonlinear dynamic properties, will be analysed and explained in this virtual environment. The different nonlinear properties of the shear type and compressed type rail fastening systems are also proposed and explained.

In Chapter 6, parameter sensitivity analysing of the present shear type and the compressed type rail fastening systems are introduced, which are followed by an optimized process from different ways. Nonlinear properties discussed above are taken good use or avoided during the optimization. Optimization objectives are put forward such as isolation efficiency, displacement response, vertical and lateral stiffness match, free surface rationalization and material cost. An important term “shear-compression ratio” is firstly proposed in present research in order to meet the expecting vibration isolation capability and the vertical-lateral-stiffness ratio with the lowest optimization cost.

Chapter 2 Experiment of rail fastening systems

In this Chapter, a shear type and a compressed type rail fastening systems are used to carry out a family of quasi-static and dynamic experiment. The quasi-static experiment aims at observing the nonlinear features especially at large deformation. Dynamic experiments are used to exhibit the frequency-and-amplitude dependent properties of rail fastening system. Experiment results will be compared with the mechanical behaviour of other type vibration isolation systems. Testing data will also be used to fit the mechanical model parameters in Chapter 3.

2.1 Introduction

The introduction of continuous welded rail (CWR) track, especially in the case of slab track gives rise to more and more urgent need for fastenings with great flexibility. As heavy freight axle loads increases and high-speed railway development, in addition to the increased service demands, the improved performance high elastic rail fastening system is becoming increasingly necessary. Flexible feature is one of the most important parameter of rail fastening systems, which should be tested in laboratory before and after designing process [128-129]. The presented measurements in this chapter aims not only at experimentally determining the quasi-static nonlinear elasticity of the two given rail fastening specimens, but also at observing their amplitude-dependent and frequency-dependent dynamic properties. The two specimens were produced only for research under the reference to the products from company Clouth Gummiwerke of Germany originated as early as 1979. They are selected to be fully studied because of their muchly universal and worldwide use until today; and they are also compared with each other for their different deformation state. One specimen is a compressed type elastic fastening with a piece of rectangle rubber pad vulcanized to a top and a bottom base frame, while the other is a highly resilient rail fastener providing elasticity mainly by shear deformation with an elliptical rubber ring vulcanized to a top and a bottom base plate. It should be noted that the preload dependent nonlinearities shown in the experiment results may be due to either the intrinsic rubber material properties or to their geometrical designing.

2.2 Test apparatus and specimens

2.2.1 Test apparatus

The static and the dynamic experiments were carried out with a SDS-200 electro-hydraulic servo testing machine. Testing schemes are shown in Fig. 2:1. The core brain of this testing instrument is the FlexTestSE integrated control system designed by company MTS, consisting of a digital controller and computer analysing system. It incorporates data acquisition, signal processing, displaying, printing parts. The testing process can be controlled by displacement or force. It can apply a disturbance frequency range of 0.001Hz to 200 Hz; actuator is capable of applying the force up to ±200kN (+/ tension, -/ compression) and the stroke of piston can be ±75 mm; force and displacement measurement accuracy are respectively ±1% of the reading load and ±1% of the reading displacement; examples of the wave shapes are sinusoidal wave, square wave, triangular wave, drab wave and different inputting waves. The testing instrument complies with EN ISO 9513:2002 and EN 13146 series; it is therefore qualified to be used to test the quasi-static and dynamic mechanical behaviour of the two given rail fastening specimens.

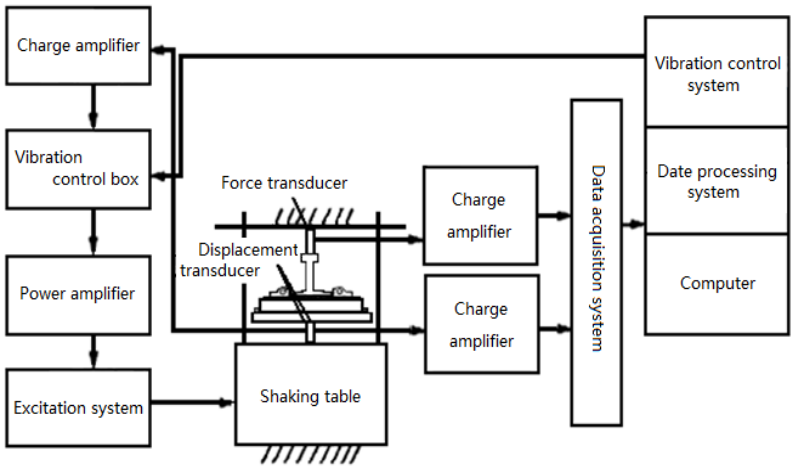

Fig. 2:1 Test schemes

2.2.2 Specimens

There are dramatically different types of rail fastening systems in modern railway structures. Generally speaking, they are designed to be various due to many reasons, such as the demand of vibration isolation efficiency, requests for integrity and maintenance, restricts

of accessing in the railway line, compatibility with the existing lines in a renewing project, terrain limitation, etc. The two fastening systems are selected and studied because of their muchly universal and worldwide use and different deformation state, one of which is a compressed type fastener while the other is shear type fastening system.

2.2.2.1 The compressed type fastening systems

Specimen I is a bonded compressed rail fastening system (Fig.2:2(a)) with a resilient rubber boot vulcanized directly to the top and thee bottom iron frames. As can be seen from Fig. 2:2(b-d), the blue grid represents the rubber component and the black diagonal lines indicate the steel plates. Detailed dimensions of its rubber component, a cubic rubber boot, and the key parameters are listed in Table 2:1. The main part of the rubber component is a

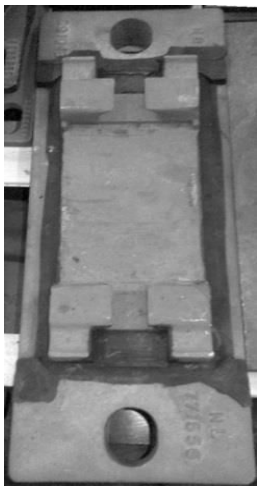

(a) Specimen I

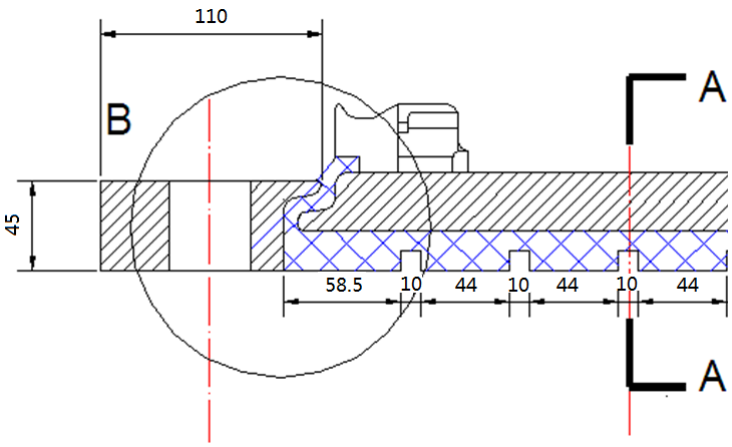

(b) Longitudinal profile

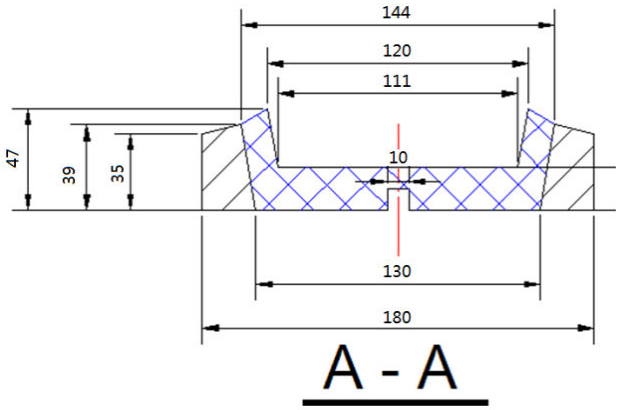

(c) Cross-section profile

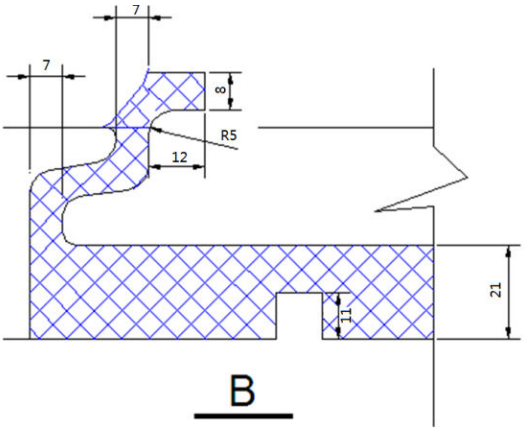

(d) Detailed dimension of the rubber component

Fig. 2:2 The compressed type fastening system (Specimen I)

21mm-height cubic rubber pad with five 10mm-width and 11mm-height slots at the bottom surface in order to apply better elasticity. In addition, there is a strip-shape "sensitive area" on both sides of the rubber component specified in Fig. 2:2(d), which are designed to integrate all the three parts. Since this area has a very small dimension which may lead to large deformations and may also result in local high stress, it is considered as sensitive. It should be noted that both specimens are produced with the same material prescription and the shore's hardness of the rubber is given by manufacturer as 65 degree. Producer also delivers the nominal vertical stiffness (static) of specimen I, 40kN/mm, and the ratio of the dynamic versus static stiffness equals 1.1.

2.2.2.2 The shear type fastening system

Specimen II is an egg-shape shear type fastening system consisting of a top, a bottom frame plate and a rubber elliptical ring as shown in Fig. 2:3(a). Geometric properties of its rubber component are also specified in Table 2:1 and in Fig. 2:3(b). Though the used rubber material is the same as specimen I, it has a much lower nominal vertical stiffness, 10kN/mm, in compared with the compressed type fastener. Ratio of its dynamic and static stiffness is also 1.1.

Specimens	Specimen I	Specimen II
Type	Compressed type	Shear type
Shape of the rubber component	Cubic	Elliptical ring
Material prescription	1701A	1701A
Shore's hardness	65 degree	65 degree
Nominal static stiffness	40kN/mm	10kN/mm
Ratio of dynamic and static stiffness	1.1	1.1
Size	Height	Height: 50mm
	21mm	Outside long axis: 205mm
	Width	Outside short axis: 124mm
	180mm	Inside long axis: 186mm
	Length	Inside short axis: 105mm
	320mm	Tangent inclined angle: 110^{o}

Table 2:1 Rubber component dimensions of the two specimens

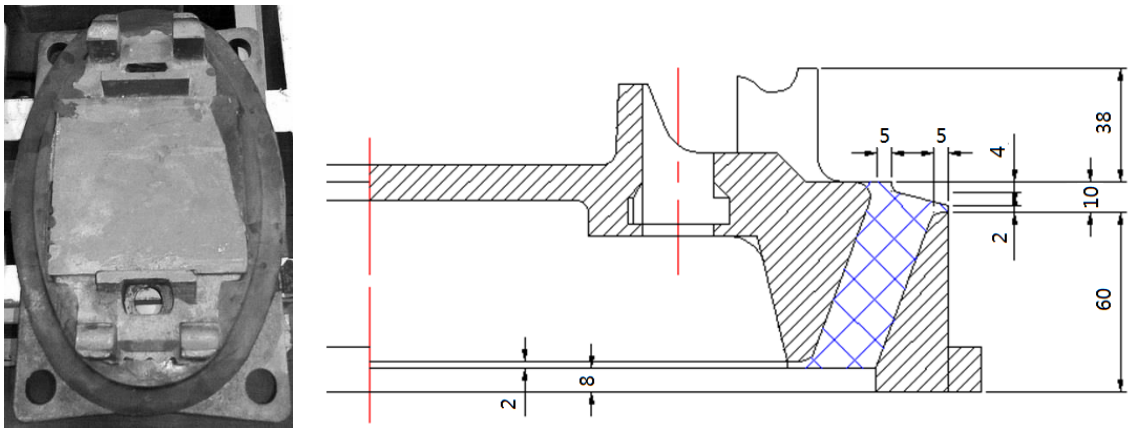

(a) specimen II (b) Longitudinal profile (a quarter of the model)

Fig.2:3 The shear type fastening system (Specimen II)

2.3 Test operating conditions

2.3.1 Quasi-static loading

The total vertical wheel-rail load is made up of two components in general: static force and dynamic force. The former equals half the static axle load; the dynamic forces arise from sprung mass ranging at 0 to 20 Hz, un-sprung mass at 20 to 125 Hz, and corrugations, welds as well as wheel flats from 0 to approximately 2000 Hz. It thus can be seen that rail fastening systems, unlike most other rubber elastomer applications, work under a pre-compression state superimposed with dynamic forces. Besides, though the clamping force and track mass are comparatively much smaller than the axle load, they contribute to the static force as well.

It's rather easy to calculate a statically loaded system by using the beam theory. As can be seen from the 2D beam in Fig. 2:4, the track is considered as a beam which is supported by spring systems representing sleepers and fasteners, where l is the displacement between two adjacent nodes, L is the wheel base and F represents half of the axle load. The fastening systems are considered directly as pure springs because the loading condition herein is static. We correspondingly use a 3D track system consisting of a slab bed, fastening systems and a section of rail tracks modelled in FEA software to calculate the maximum static loading amplitude due to the axel load, see Fig. 2:5 (a). Taking specimen I for example: as the wheel load values 23 tones and the displacement between two nodes and the wheel base value respectively 625mm and 2200mm, the maximum static load subjected to the track can be

obtained. From Fig. 2:5 (b) we can see that, the maximum vertical static force locates at the nodal position. Moreover, it was found that the longer the rail track is used the larger value of the maximum static force we obtain. This instability, however, becomes stable as the section of the rail track is longer than 12m. As a result, the length of the rail track is taken as 15m. It should be noted that normally the lighter axial load of a railway car is mainly for urban railway transit while the larger axial load is for high-speed railway or normal passenger train, and urban railway track systems demand smaller stiffness value of rail fastening systems. Since the nominal stiffness of the present two rail fastening systems are respectively 10kN/mm and 40kN/mm, different axle load should be adopted to calculate the nodal force: 160kN for the shear type specimen while 230kN for the compressed specimen. As a consequence, the maximum vertical static force is obtained to be 40.94kN for specimen I and 22.4kN for specimen II as depicted in Table 2:2.

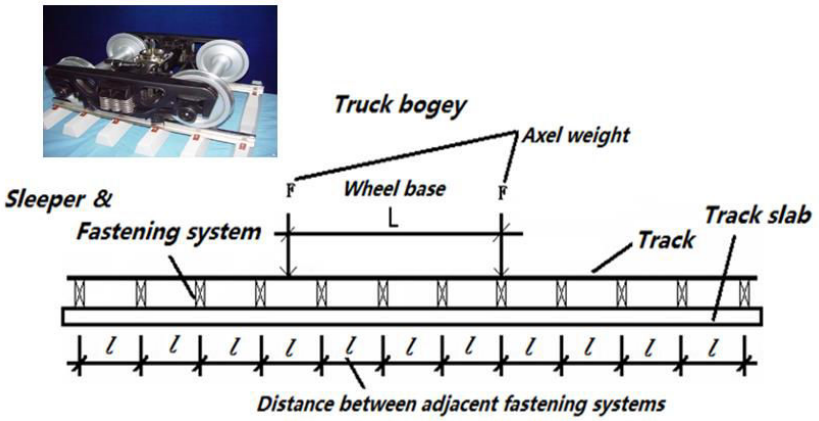

Fig.2:4 Sketch map of track structure under static loading

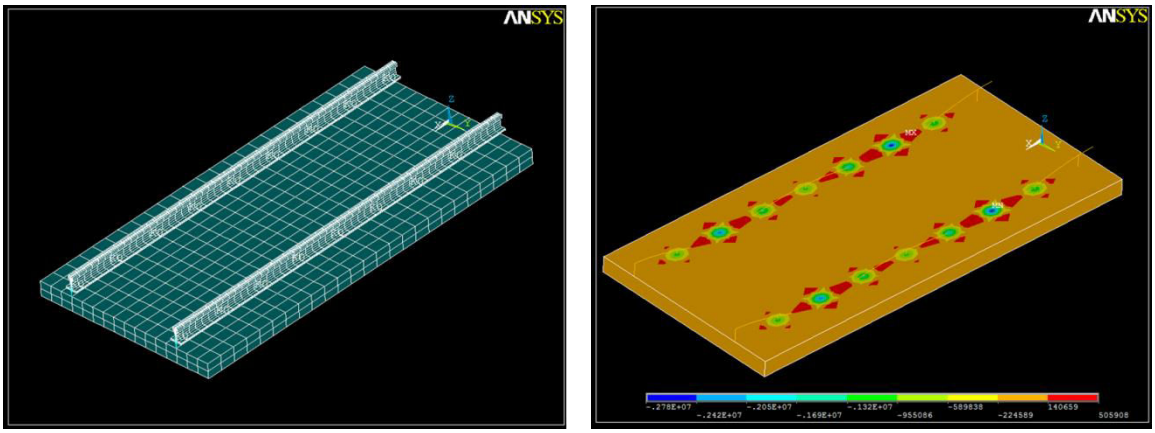

(a) FEA 3D model (b) Calculation results

Fig. 2:5 Determination of the maximum static force on the track nodes

Specimen	Nominal stiffness (kN/mm)	Axle load (kN)	5m	7m	9m	12m	15m
I	40	230	-39.519	-40.738	-40.910	-40.940	-40.941
II	10	160	-17.462	-21.167	-22.366	-22.401	-22.408

Table 2:2 The maximum vertical static force obtained with different rail length

It is common practice to take the dynamic effects of wheel-rail contact by a speed coefficient or dynamic amplification factor (DAF) when a statically loaded track system is under study. The effect of running speed on dynamic force is in fact highly complex because of the uncertain interaction between vehicle wheels and track. Several formulas have been proposed aiming at assessing the dynamic effect however they are only rough approximation because the geometric quality of the track, the mechanical characteristics of the track and the trucks are not sufficiently taken into account. Among the theoretical calculations, one formula developed by Eisenmann is accepted and well used by European railway companies. The Eisenmann scheme is dependent on the train speed v, track quality factor φ, and a multiplication factor of standard deviation t, which depends on the confidence interval. It reads as

$$\mathrm{DAF} = 1 + \mathrm{t}\varphi, \qquad \text{if } v < 60 km/h$$

$$\mathrm{DAF} = 1 + \mathrm{t}\varphi(1 + (v - 60)/140), \quad \text{if } 60\ km/h \leq v\ \leq 200\ km/h. \tag{2:1}$$

Since railway track is closely related to safely operation and to the reliability of the traffic, unfavorable conditions are often considered when $\varphi = 0.3$ and $\mathrm{t} = 3$, although the probability of such condition is only 0.3% (see Table 2:3).

Probability	*t*	Application	Track condition	*φ*
68.3%	1	Contact stress, subgrade	Very good	0.1
95.4%	2	Lateral load, ballast bed	Good	0.2
99.7%	3	Rail stresses, fastenings, supports	Bad	0.3

Table 2:3 The chosen factor depending on confidence interval and track condition factor

Fig. 2:6 gives the graphical presentation of the Eisenmann scheme showing the variable values of DAF ranging from 1.1 to 2.8 as train speed is lower than 200 km/h. To give an idea, supposing train speed is 70km/h, a DAF value equalled to 2 can be read from Fig.2:6 as $\varphi = 0.3$ and $\mathrm{t} = 3$. At this situation, the total vertical loading value is obtained as

$40.94\text{kN} \times 2 = 81.88\text{kN}$; in addition, in order to take the clamping force into account, the final maximum loading value of quasi-static experiment for specimen I is taken as 100kN. In the same way, 70kN should have been determined as the maximum loading value for specimen II. However, since there is an obvious nonlinearity as specimen II is loaded up to about 70kN, it's extended to 120kN until the nonlinear property exhibits completely.

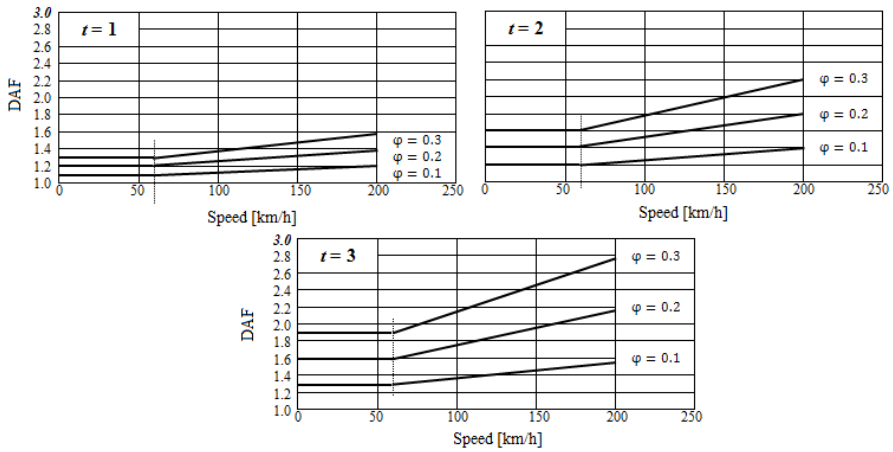

Fig. 2:6 DAF values as a function of the train speed at different track qualities and probabilities

To underline, though the loading limit value in experiments for determining static stiffness of rail fastening assemblies is no larger than 80kN according to European standards, 100kN for specimen I and 120kN for specimen II are used in present research for enhancing the understanding of the large deformed properties of rubber component in the two rail fastening systems [128-130].

Specimens were kept in room temperature at around 23 degree for two days prior to starting the test. Specimen I was loaded at a speed of 50kN/min until 100kN; the same loading speed is conducted to specimen II. As the maximum loading value is reached, unloading process is followed until zero. Fig. 2:7 depicts the testing site and instruments. The loading-unloading process was repeated two times in order to exclude the Mullins effect before the real test, and the vertical displacement of the shaking table and the loading value on the rail head are recorded with the force transducers at the third cycle. Specimens were subsequently removed from the testing machine. Letting them sit for half an hour on the testing site can help to recover the deformation. The whole testing process needs to be repeated for three times and the measured data will be compared. If any two of them differ

from each other by 10%, the fourth time test needs to be complemented. The quasi-static testing results for both of the specimens will be shown and discussed in the following part. Nonlinear properties shown in the measured working curves will also be studied.

(a) The compressed type fastening system

(b) The shear type fastening system

Fig. 2:7 Testing site and instruments

2.3.2 Dynamic loading

Railway systems have increasingly received complaints from people living alongside lines and above underground lines. The disturbance is generally caused by either the direct emission of noise or by vibration from the railway, and sometimes noise in buildings is produced by the walls vibrating which is referred to as re-radiated noise. As Table 2:4 depicts, vibrations and structure-born noise mainly occur at low to middle frequency range (<100Hz) due to vehicle kinematic modes, truck precession wave, short waves and long waves of wheel-rail interaction, i.e. railway track irregularities. At higher frequency, from 100Hz to 2000Hz, vibrations attenuate rapidly; however short waves, wheel corrugations, rail roughness, track condition, curving, rail wear, hunting and so on, radiate the energy directly as noise, i.e. air-born noise. Roughly speaking, vibrations and structure-born noise occur normally in the frequency range of 0 to100 Hz and noise between 30 – 2000 Hz. However, though the disturbance frequency range is so large, truck precession wave frequency is believed to be the main disturbance for rail fastening systems. The main frequency range, 2Hz to 10 Hz, can be obtained either from a simple formula $f = \frac{v}{L}$, where v is the travel speed and L is the wheel-base bogie, or a filed test (Fig. 2:8). Supposing the train speed is 20km/h to 80km/h and the wheel base is 2.2m, frequency range can be determined as 2Hz to 10 Hz. The higher the train speed, the larger the frequency range we get. Fig. 2:8 shows a wild test to

measure the vertical force and displacement of the rail. From testing results in frequency range we can also know that the main frequency range for a node is below 10Hz.

Disturbance	Vibration source	Frequency range
Vibration	(a) Vehicle kinematic modes; (b) Truck precession wave; (c) Wheel-rail interaction (long wave);	0.75Hz- 5Hz 2Hz-10Hz 0Hz-50Hz
Re-radiated noise	(d) Wheel-rail interaction (short wave); (e) Wheel corrugations, rail roughness, track condition, curving, rail wear, hunting, etc.	30Hz-100Hz
Air-born noise	(d) (e)	100Hz-2000Hz

Table 2:4 Disturbances of track structure

(a) The field test site

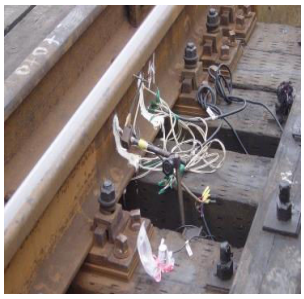

(b) Testing for the main frequency at node

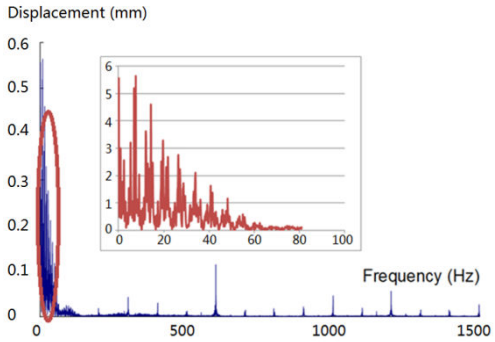

(c) Testing results

Fig. 2:8 Field test to determine the main frequency for rail fastening system

As a result, dynamic force ranging from 2Hz to 10Hz is applied to the compressed type fastening system (specimen I) with the preload, 20kN. The dynamic displacement amplitudes are from 0.4mm to 1.0mm for specimen I. All the input data for dynamic experiments are listed in Table 2:5. In order to study and compare the preload dependent, frequency dependent as well as dynamic amplitude dependent properties of rail fastening systems, preload for applying a pre-compression, frequency range and dynamic amplitude values all all expanded to a wider range for specimen II because its lower nominal stiffness allows larger vertical displacement.

Conditions	The compression type system (Specimen I)	The shear type system (Specimen II)
Nominal stiffness (*kN/mm*)	40	10
Preload (*kN*)	20	15, 20, 25, 30
Frequency (*Hz*)	2 - 10	2 - 18
Amplitude (*mm*)	[0.4: 0.1: 1.0]	[0.4: 0.1: 1.5]

Table 2:5 Dynamic experiment conditions

2.4 Testing results and analysing

2.4.1 Quasi-static test

Fig. 2:9 shows the measured displacement-force relations of the compressed type (a) and the shear type (b) rail fastening systems. Vertical axis is the force input read by the transducer while the horizontal axis is the displacement response of the shaking table. Obviously unloading process follows a different way from the loading procedure for both specimens, giving rise to a hysteresis loop although the loading speed is very slow. At the end of unloading procedure, zero force does not give a full deformation recovery which means that displacement response lags behind the input force. This is due to the intrinsic viscosity of rubber material. In addition, the quasi-static stiffness of the two specimens is found to be severely dependent on the curve shape and the deformation range selection. For specimen I, secant stiffness calculated from zero to the maximum displacement is 37kN/mm which is very close to the nominal stiffness, 40kN/mm; however this value increases to be nearly 50kN/mm if the softening segment at the very beginning of the loading line is excluded. For specimen II, in another hand, the stiffness starting from zero point to 6mm is approaching the nominal stiffness 10kN/mm; but it will be strongly enlarged if the following nonlinear segment is included in.

There are different nonlinearities shown in these two working curves in Fig. 2:9 due to either the material properties or their geometries. Someone looks remarkable while someone even can be neglected. Detailed analysis on these nonlinear properties will be fully discussed in Chapter 5.

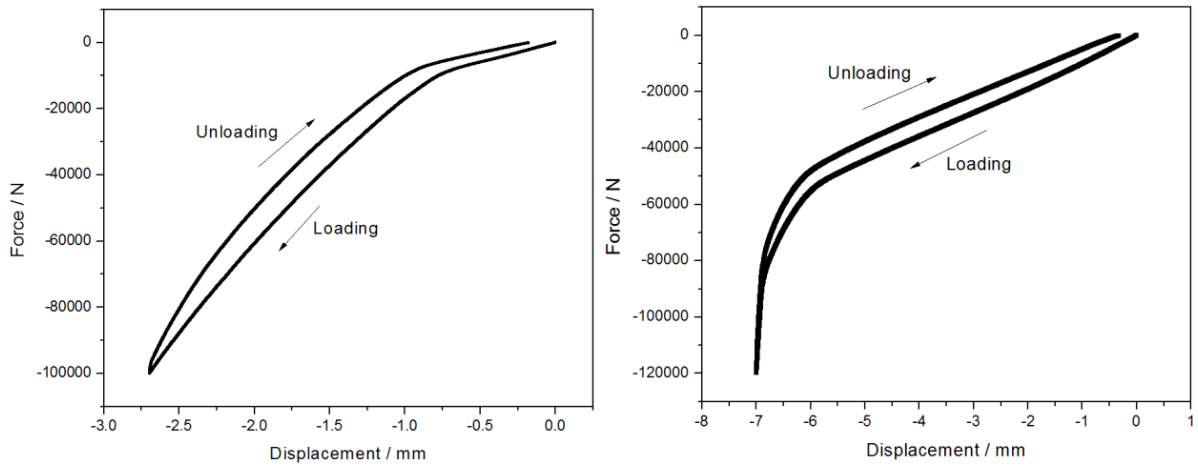

(a) Compressed type (Specimen I) (b) Shear type (Specimen II)

Fig. 2:9 Quasi-static working curves

2.4.2 Dynamic test

If an input cyclic displacement is varying as a sinusoidal function in time, i.e. $x = x_0 + Xsin(2\pi ft)$, f is frequency, X is the dynamic amplitude and x_0 is the pre-compression, see Fig. 2:10. The force response of a linear viscoelastic system is also sinusoidal in time, but it will lag the displacement by a phase angle δ as $F = F_0 + Asin(2\pi ft - \delta)$, where F_0 is the preload needs to obtain the pre-comression, A is the force response amplitude. The phase angle is related to the time lag Δt between the sinusoids by $\delta = \frac{2\pi(\Delta t)}{T}, T = 1/f$. If we remove the intermediate component time t, input displacement and output force compose a hysteresis loop.

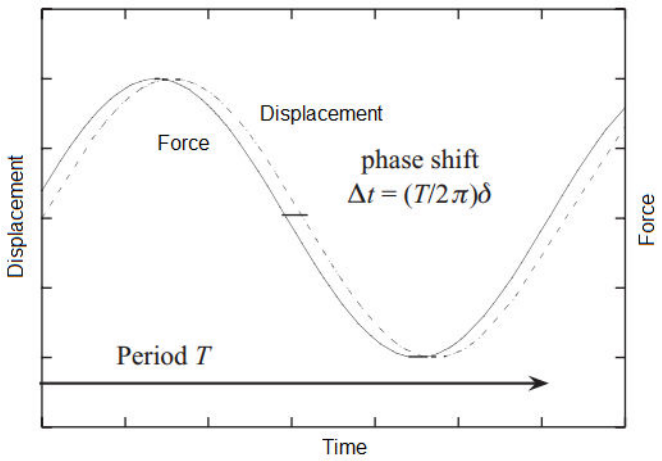

Fig. 2:10 Time-displacement and time-force relationship

According to international standards [130], a maximum loading value F_{max} needs to be determined before the test and the minimum loading value F_{min} is supposed to be about 5 ± 1kN in order to test the dynamic stiffness of a rail fastening assembly. Taking the working conditions of 20kN preload, 4Hz frequency for example in the present experiment, F_{max} is selected to be about 35kN. In order to study the amplitude influence on the dynamic mechanical behaviour of the fastening systems, measurement is controlled by displacement, as a result both F_{max} and F_{min} are not exactly same as the testing standards. The cyclic displacement disturbance of 4 ± 1Hz is applied for 1000 cycles, and during the last 100 cycles testing data are recorded. The measured displacement-force curve of both compressed type and the shear type specimens are shown in Fig. 2:11. The dynamic stiffness can be obtained from the hysteresis loops as disturbance frequency is 4Hz, preload value is 20kN and the displacement amplitude is 0.4mm for specimen I and 1.5mm for specimen II. For the compressed type fastening system, the tested dynamic stiffness is 42.706kN/mm and the ratio of dynamic versus static stiffness is thus 1.067 which is approaching to the value given by manufacturer; for specimen II, these two values are respectively 10.692kN/mm and 1.069 which also agrees with the nominal value 1.1.

Obvious different shape of the hysteresis loops can also be seen in Fig. 2:11, where specimen I shows a crescent-shaped loop while specimen II exhibits an elliptical loop. Generally speaking, this is believed to be due to the preload (or pre-compression) dependent property of a rubber component. This nonlinear property will be further studied in Chapter 5.

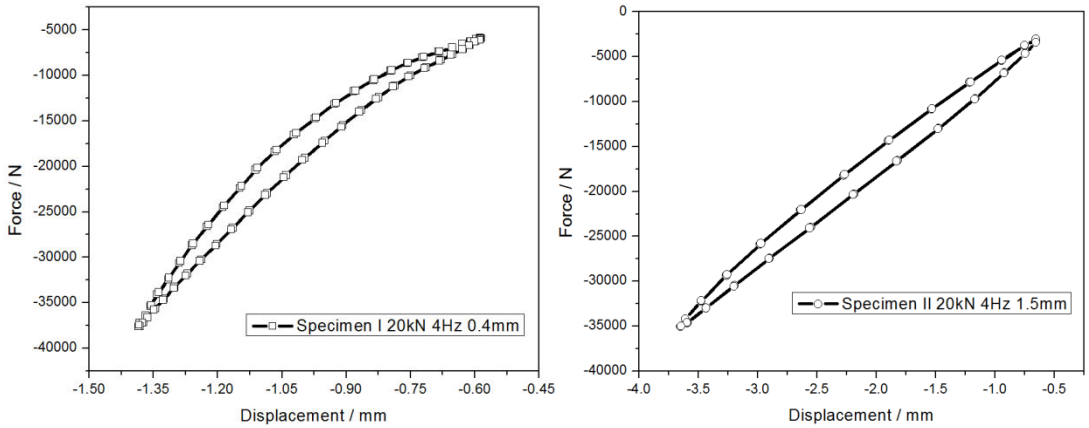

(a) The compressed type (b) The shear type

Fig. 2:11 Dynamic testing results

With the hysteresis loop of single working condition as shown in Fig.2:11, it's hard to distinguish nonlinear viscoelastic properties. However, studying on the time-displacement and time-force response relations can help to tell the nonlinearities. Taking the loading case of preload 20kN, frequency 2Hz and amplitude 0.6mm of specimen I for example, whose input displacement can be simulated as a sinusoidal function

$$x = x_0 + Xsin\big(2\pi f(t+\delta_0)\big) = -1.0028 + 0.6037sin(2\pi \times 2 \times (t+0.8133)) \quad (2:2a)$$

and a comparison of time-displacement relationships for the measurement and calculation as Eq. 1:2a is shown in Fig. 2:12 (a). However, this single frequency harmonic displacement excitation results not only in a force response of the fundamental frequency [76], but also in other physical overtones. Specifically, what is shown in Fig. 2:12 (b) in red line is the simulated force response with only the fundamental frequency 2Hz, and the simulation function can be described as

$$F = F_0 + Asin\big(2\pi f(t+\delta)\big) = -21038 + 22174sin(2\pi \times 2 \times (t+1)). \quad (2:2b)$$

Visible difference can be seen between measurement and the fitting result in Fig. 2:12 (b). The green line, however, meets the test result much better with a second overtone (4π) reads:

$$\begin{aligned} F &= F_0 + Asin\big(2\pi f(t+\delta_1)\big) + Bsin\big(2\pi f(t+\delta_2)\big) \\ &= -21030 + 22158\,sin\big(2\pi \times 2 \times (t+1)\big) + 4342sin(4\pi \times 2 \times (t)) \end{aligned} \quad (2:2c)$$

This frequency split indicates that the rubber used in current research is not a typically linear viscoelastic material, whose response is not simply same as the input function. [131-132] Tariq et al. and Onogi quantify the degree of viscoelastic nonlinearity by evaluating such overtones.

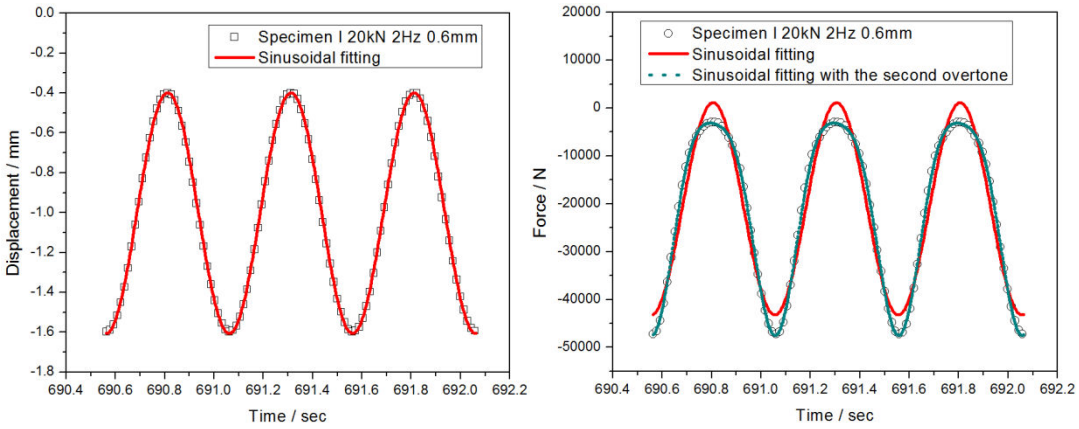

(a) Time-displacement (b) Time-force response

Fig. 2:12 Measured and simulated time-displacement and time-force curves

2.4.2.1 Dynamic amplitude dependence

The rubber material used for producing rail fastening system is normally filled rubber in order to reinforce its tensile and shear strength. As discussed above, the filled rubber has two well-known amplitude effects, the Mullin's effect and the Payne effect. When the material specimens or a rubber component is subjected to a cyclic forced deformation, the first few oscillations result in reducing peak value of the force response [133-135]. The Mullin's effect is eliminated in the present quasi-static and dynamic experiments by loading the specimens a few cycles, so that the molecular networks can rearrange prior to the real measurement. Payne effect is in general explained as a decreased modulus with increasing dynamic amplitude. Filled rubber exhibits more pronounced Payne effect compared to nature rubber. Payne effect is believed to be the consequence of the molecule interaction breaking as motion increases at the relatively small deformation range; but the breakings can almost fully recover back within each cycle [136]. An intact filler structure displays a larger modulus magnitude for small motions; as the amplitude increases the filler structure breaks resulting in a decreased modulus. This breaking of the microscopic structures is always described as a frictional behaviour which leads to an increased energy loss. As the amplitude increases further, the frictional behaviour is released resulting in a decreased energy dissipation mechanism and a lower loss factor value, and the gradually reduced modulus magnitude is applied by the remaining polymer chains and rubber-filler hydrodynamic effect. A thorough discussion is given in [137] on the examples of a strong amplitude dependence of the shear modulus and loss factor of the rubber material with various filler concentrations. It's also well

documented by Mattias Sjoberg and Dean et al. [138], Jurado et al. [139], Sommer and Meyer [140], Wang [141], and Medalia [136]. Similar amplitude dependent behaviour of rubber components as the Payne effect of rubber material are presented in [76, 10-11, 100, 142]. Rubber component in the rail fastening systems are nearly the most important resilient element and obvious displacement amplitude dependence also shows in the dynamic testing results of the two specimens.

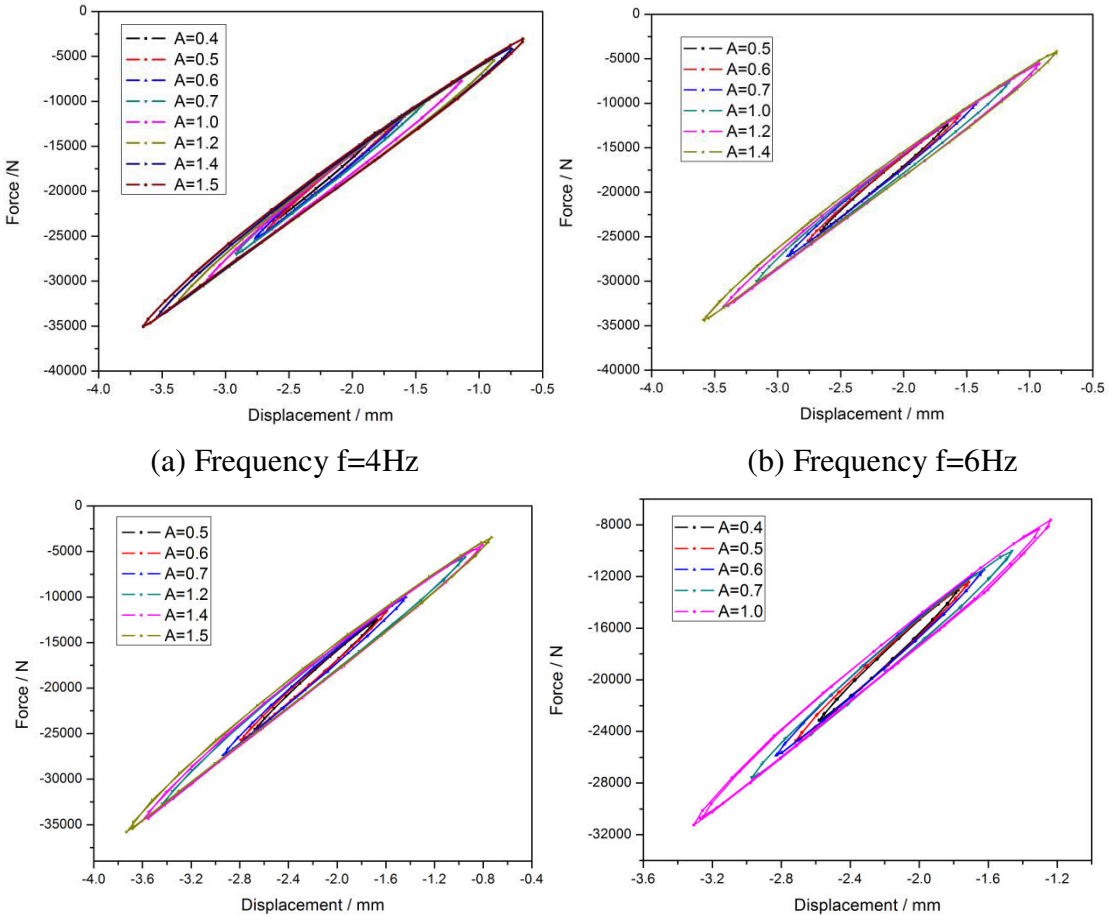

(a) Frequency f=4Hz (b) Frequency f=6Hz

(c) Frequency f=8Hz (d) Frequency f=18Hz

Fig. 2:13 Dynamic amplitude dependent hysteresis loops

Taking specimen II for example, Fig. 2:13 demonstrates the displacement-force relations at different frequency and amplitude, i.e. the frequency and amplitude dependent hysteresis loops [143]. The preloading value is 20kN. We can see from Fig. 2:13 that for all the instanced frequency case the secant dynamic stiffness increases as the stimulating amplitude decreases and the secant stiffness is defined by an oblique from the beginning to the end of the loops. In addition, we can also see that the enclosed area of the loops increases

with the enlarged amplitude. For example in Fig. 2:13 (a) the hysteresis loop of 0.4mm is approaching to an inclined straight line; on the contrary, the area increases with the enlarged displacement amplitude. However it should be noted that the increasement of the loop area is mainly influenced by the enlarged disturbance amplitude. Although, according to viscoelastic theory, the damping property of the fastening specimens is also varied with the varied amplitude, it cannot be clearly distinguished from the Fig. 2:13. In order to make it clear, the calculated dynamic stiffness of three cases 2^1Hz, 2^2Hz and 2^3Hz for instance are shown in Fig. 2:14 (a), the increased area of the hysteresis loops indicating the energy loss per cycle is drawn with amplitude in Fig. 2:14 (b) and the damping measure calculated by the measured energy loss according to

$$loss\ angle = artan(\frac{measured\ energy\ loss}{\pi \times (measured\ static\ stiffness) \times (displacement\ amplitude)^2}) \qquad (2:3)$$

is depicted in Fig. 2:14 (c). Compared to Fig. 2:13, Fig. 2:14 (a) and (b) show the same influence by disturbance amplitude on the dynamic mechanical properties, where the increased amplitude results in the decreased secant stiffness and the hysteresis loss increases with amplitude at all frequencies. However, Fig.2:18 (c) illustrates that the amplitude dependent loss angle obtained by Eq.1:3 increases first following the amplitude and then decreases. A peak value can be observed in all three presented cases in coincidence with the occasion of rubber material. As discussed above, the decreased dynamic stiffness is due to the filler structure breakings and the increasing loss angle at small amplitude is because of the accompanying frictional effect, while the decrement of the loss angle as the amplitude increases further is due to the released friction effects at larger motions. Specimen I shows the similar amplitude dependent properties as specimen II, the experiment results of specimen I is omitted herein for brief.

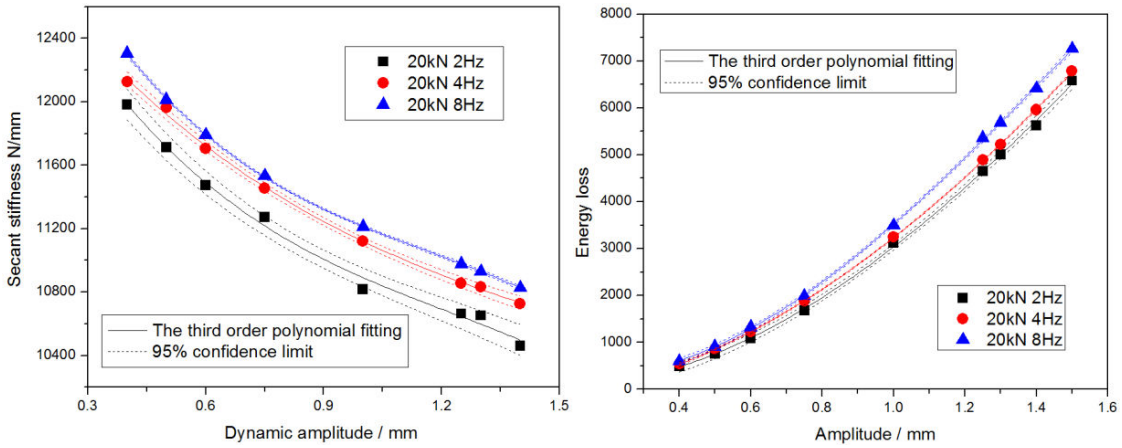

(a) Amplitude dependent secant stiffness (b) Amplitude dependent energy loss

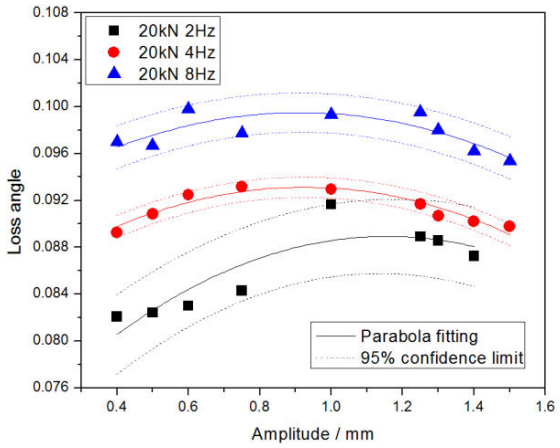

(c) Amplitude dependent loss angle

Fig. 2:14 Dynamic amplitude dependent stiffness and damping properties

2.4.2.2 Frequency dependence

Rubber material additionally exhibits strong frequency dependent properties displaying glassy region, transition process and rubber region. Theoretically, material modulus magnitude increases with frequency throughout all the three steps, and the increasement is moderate in the glassy and rubber region but is severe in the transition region. In another hand, the loss factor increases with frequency in the rubber region, and decreases in glass region after reaching a pick value in the transition step. It is in fact impossible to measure the dynamic characteristic of a rubber material at such wide frequency range; it is possible, however, to obtain the properties by using the knowledge of temperature-frequency shifts as discussed in Chapter 3

The dynamic stiffness, hysteresis loss and the loss angle of the two fastening specimens were tested and outlined under the influence of stimulating frequency. Taking specimen II for example, Fig. 2:15 shows this frequency dependence at several amplitude cases. It is clearly can be seen that the stiffness, the hysteresis loss as well as the loss angle all increases with frequency. However, since the interested frequencies locate in a relatively low and narrow range (below 20Hz) the influence on the frequency on the dynamic stiffness and hysteresis loop therefore is very limited. Theoretically, obviously nonlinear frequency dependence can be observed only when the stimulating frequency is as high as 2000Hz (or by controlling with temperature). Specimen I also shows the similar frequency dependent properties which is omitted herein for brief.

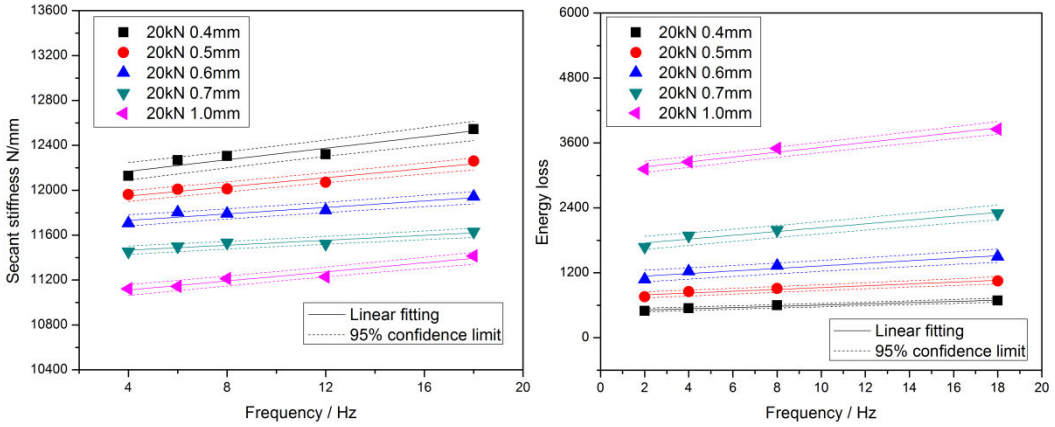

(a) Frequency dependent secant stiffness (b) Frequency dependent energy loss

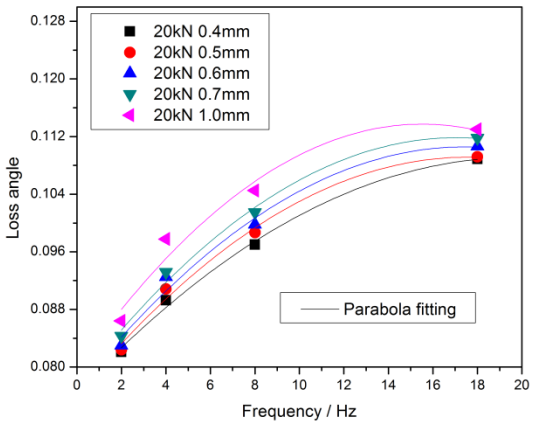

(c) Frequency dependent loss angle

Fig. 2:15 Frequency dependent stiffness and damping properties

2.4.2.3 Preload influence

Rail fastening systems exhibit nonlinear properties for small to intermediate amplitudes due to material behaviour where small cyclic deformation results in increased stiffness compared to that of larger cyclic deformation. This nonlinearity referred to as the Payne effect for material, was already discussed in section 2.4.2.1. In addition to this, rail fastening systems also show another nonlinear property at relatively large strain. As a rubber component, this nonlinearity can be due to either the intrinsic rubber material or the component geometry. A sketch of how dynamic displacement-force relations are influenced by the preload (pre-compression) is depicted in Fig. 2:16. Normally, if the dynamic hysteresis loop locates in the small deformation region the shape of the enclosed displacement-force curve doesn't change; however if the dynamic hysteresis loop locates in the relatively large deformation domain the shape of the dynamic hysteresis loop is varied due to the nonlinear features of the quasi-static loading curve. Since the nonlinearity of rubber components may due to the intrinsic material properties or to the geometries and structures, the preload dependence on the dynamic properties may also arise in the small deformation part. As shown in Fig. 2.16(a) for specimen I, the shape of the dynamic hysteresis loop is changed by the nonlinear feature of the quasi-static loading curve although in the very small deformation range. In another hand as shown in Fig. 2.16(b), although there are four different preloading values, 15kN, 20kN, 25kN and 30kN, and the dynamic curves locate in different parts, they are nearly not influenced.

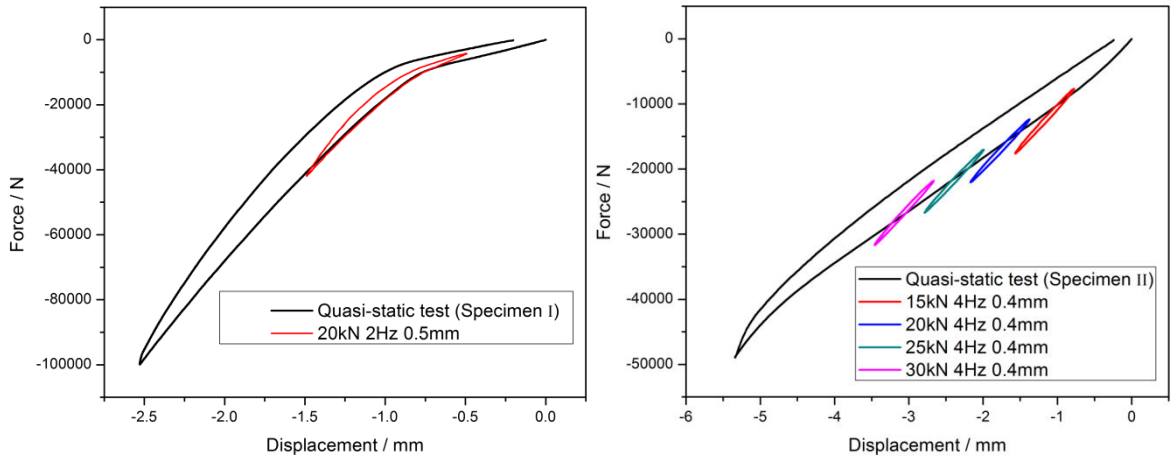

(a) The compressed type fastening system (b) The shear type fastening system

Fig. 2:16 Nonlinear displacement-force curve under the influence of preload

In fact, if we put the preload influenced dynamic stiffness of specimen II as shown in Fig. 2.17, it's not hard to find Z-axis (dynamic stiffness) changing with X-axis (preload) following the quasi-static loading curve. In addition, Z-axis (dynamic stiffness) also varies with Y-axis (dynamic amplitude) severely where the increasing dynamic stiffness increases with the dynamic stiffness. Apparently, dynamic amplitudes have stronger influences on stiffness in YZ axis than that of preload in X-Z axis.

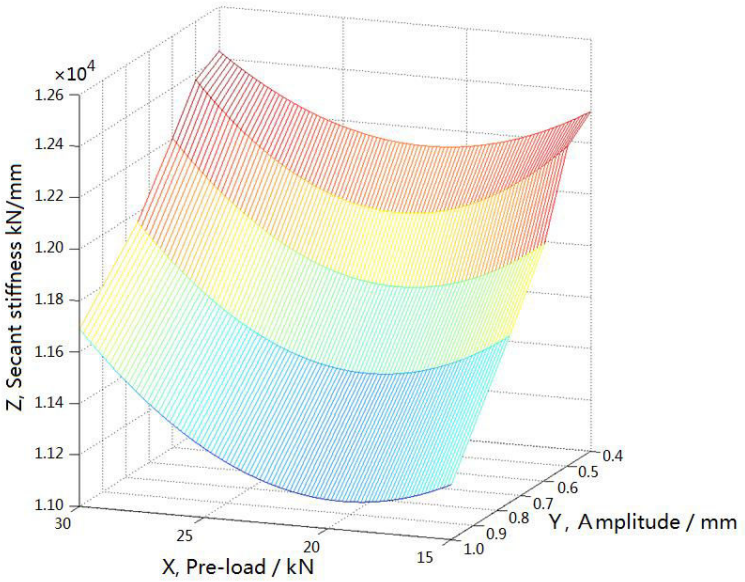

Fig. 2:17 Preload-and-amplitude dependent properties

2.5 Summary

In this chapter, quasi-static and dynamic experiments of two different kinds of rail fastening systems were conducted. Specimen I is a compressed type fastener and specimen II is shear type. The quasi-static measurement doesn't aim at determining their static stiffness, but mainly at discovering their nonlinear elastic properties. The nonlinearity shown in the two working curves will be further studied and explained in Chapter 5. Through dynamic experiments, both compressed and shear type specimens exhibit motion amplitude dependent and frequency dependent properties. Preload dependency was also observed by superimposing oscillations to the quasi-static loading curves. Generally speaking, rubber components show the same basic characteristics concerning stiffness and loss angle as the rubber material does in terms of modulus magnitude and loss factor. As for both the two rail fastening systems, decreased secant dynamic stiffness and increased energy loss during a

oscillating cycle, as well as a peak value of the loss angle were observed, which coincides with the Payne effect of rubber material very well. Frequency dependency was linearized because the loading frequency range is only below 20Hz and it is so far away from the nonlinear frequency dependent area. Preload influence is supposed to be due to either the finite strain characteristic of rubber material or the geometries and boundary conditions of the specimens. All these nonlinearities will be further explained and simulated by using FEA in Chapter 5.

Chapter 3 Modelling of the rail fastening systems

In this Chapter, three different models will be introduced to depict the mechanical properties observed in the experimental results. Since it is extremely difficult to implement a model considering all applications with wide range of working conditions in the mean while considering all complex mechanical properties, the three models emphasize on different characteristics. The mechanical modelling in this Chapter benefits in further understanding and predicting the mechanical properties of rail fastening systems, also can provide theoretical basis for product design, optimization even production process.

3.1 Introduction

Is was found in Chapter 2 that the force response to the harmonic displacement excitation, superimposed on a long term static displacement of the rail fastening systems consists of stiffness and damping properties, which respectively concern the elastic force and damping force. The dynamic properties, i.e. dynamic stiffness characteristics and the hysteresis energy loss are strongly dependent on static preload, dynamic amplitude as well as frequency [144, 145].

Nearly all rubber isolator models are simplified description since it is extremely difficult to implement a model considering all applications with wide range of working conditions in the mean while considering computational effort. However it is still important to model the rubber isolation systems in order to enhance understanding of the mechanical properties and how the component properties are influenced by specified working conditions. As rail fastening systems is ultimately a vibration isolation system for dynamic improvement, there is a great need to understand and properly predict their behaviour by means of combined experiments and mechanical modelling.

The study on the rubber components should be back to good digest of rubber material properties. A lot of information of mechanical behaviour of rubber material can be gained from the literature such as [15-23]. Among the different methods in modelling rubber components in the engineering practice, one common approach is to use continuum mechanics and formulate constitutive laws originated rubber material [71-72]. EICKHOFF

and BERG [73-75] outline that rubber component models should be more global, and should concentrate on the force-displacement relations rather than stress-strain relations. However, generalizes that material as well as component properties should be related in that a rubber component exhibits the same basic characteristics concerning stiffness and loss angle as the material does in terms of shear modulus magnitude and loss factor [76]. Only exceptions to this rule are e.g. when the geometry of the component introduces additional nonlinearities, such as a progressive stiffness or when the evaluated frequency range is extended, resulting in component internal forces which influence its dynamic properties.

It is well accepted that dynamic properties of rubber isolator, i.e. stiffness and damping, depend not only on the material prescription but also on geometry, pre-compression, frequency and amplitude of the motion. However, rubber component modelling normally doesn't take all these experimental phenomena into consideration in one single formula. The simplest model of a rubber isolator accounting for both elastic and viscous effects is the Kelvin-Voigt model where a linear elastic frequency independent stiffness is coupled in parallel with a viscous dashpot and damping force is proportional to a first order time derivative of the displacement [30], however, it overestimates hysteresis loss at high frequencies and impulsive load due to the viscous dashpot. Replacing the dashpot with a Maxwell element, forming the three-parameter Maxwell model or the standard linear solid, normally results in better high frequency description of stiffness but still poor at predicting the damping properties. The standard linear solid can be expanded through incorporating the generalized Maxwell model, known as Wiechert model or generalized Maxwell model. It can obtain improved broad band frequency description [77-81], nevertheless inevitably increases the number of parameters to clearly describe elastomer dynamic behaviour and brings about computational cumber. At this situation, an efficient alternative in reducing the required number of model parameters while still obtaining a good description of viscoelastic materials' or components' frequency dependence is incorporating a fractional calculus [82]. Thorough review of using the fractional derivatives in dynamic modelling of viscoelasticity is given by Rossikhin and Shimizu [83-84]. Koeller [85] discussed the spring-ports taking the places of the ordinary dashpots in viscoelastic models. Replacing the Kelvin-Voigt's dash-pot by a spring-pot results in a fractional Kelvin-Voigt [86-87]. Replacing the dashpot of the standard linear solid model results in a fractional standard linear solid [82, 86, 88-90]. [91] Kari

applied the fractional model to fit rubber material and component measurement data of a wider frequency range. Time-domain solutions of the fractional derivatives models are investigated by references [92-99].

Since generally displaying a strong preload and amplitude dependent properties, vibration isolators are inherently nonlinear [101]. This nonlinearity means either taking into account nonlinear behaviour due to the statically deformation or the dynamic amplitude dependence, i.e. Payne effect for rubber material. The dynamic amplitude dependence does not only influences dynamic stiffness but also damping properties. These nonlinearities clearly reveal that prevailing linear models for rubber component are inadequate. An estimable progress in rubber component nonlinear models is noticeable in a lot of references [102-110]. In particular, force response of cyclic input displacement is modelled as a combination of a nonlinear elastic and a liner viscous damping force [102, 105-106, 110], a linear elastic and a nonlinear viscous damping force [135], a nonlinear elastic and a nonlinear viscous damping force [103-104, 107-108] with the nonlinear amplitude dependence expressed by a Coulomb friction model [109]. All of these studies start to provide a deep insight into various nonlinear phenomena, which is constructive and applicable in optimization process of vibration isolation systems. One way of considering the rate independent damping force (i.e. friction dependent damping force) is by replacing the viscous component in a standard linear solid by a friction component [113]. References [111, 115] elaborate on another model that includes friction components in series, which is later used to combine with a three-parameter Maxwell model [114]. It is expanded by Bruni et al. [115], Austrell et al. [104] and Brackbill et al. [116] to include frequency dependence, giving a good representation of measured properties. Dynamic amplitude dependence is modelled by Mallik et al. [117] through separating a nonlinear elastic force and a nonlinear damping force with eight parameters in total. Another model also taking into account the amplitude and frequency dependence is presented by Barber [118] which however needs even more measurements to properly adjust the numerous model parameters. References [76, 10-11, 100] and [14, 75, 119] by Berg presented a widely used rate independent frictional component showing a smooth behaviour with only two parameters and this model give a very good description of the measured amplitude dependent characteristics.

Three different models will be introduced in this Chapter. They are in accordance with the observed experiment result in Chapter 2. Since it is extremely difficult to implement a model considering all applications with wide range working conditions, the three models emphasize on different characteristics.

3.2 Presented model I

Although several attempts to describe the vibration behaviour of rubber component have been successful, most proposed models relate only to particular applications with specific working conditions. In general, the restoring force of rubber components subjected to harmonic excitation consists of two parts: the damping force and the elastic force. That is, the total restoring force $F_{restoring}$ can be obtained from the direct summation of the two parts as:

$$F_{restoring} = F_k + F_c, \tag{3:1}$$

where F_c is the damping force with energy loss, and F_k is the elastic force without energy loss. The first model is based on the superposition theory illustrated in Fig. 3:1. A horizontal ellipse is used to indicate the damping characteristics of rubber component. The elastic force is supposed to be a polynomial function of displacement which will account for the nonlinear stiffness properties, especially for the compressed type fastening system. Thus the force-displacement hysteresis loop is accordingly decomposed into two parts, i.e. Fig. 3:1 (a) and (b), where A is the stimulating displacement amplitude and x_0 is the initial displacement given by the preload.

It can be seen from Fig. 3:1 that both the damping force-displacement loop and the elastic force-displacement curve are in a nonlinear shape. The former is due to the intrinsic viscous property of rubber material (hysteresis), while the later can be due either to geometric property or to the hyperelasticity of rubber material. In Fig. 3:1 (a) it should be noted that there is an initial displacement x_0, that is the equilibrium position of the x-coordinate is non-zero. The area of this closed ellipse is equal to that of the hysteresis loop in Fig. 3:1 (c), both of which represent the energy lost during a loading cycle. To describe the frequency and amplitude dependent stiffness characteristics (Fig. 3:1(b)), parameters of the dynamic

stiffness are evaluated to be varied with different working conditions; however the damping property is assumed to be frequency independent in this model.

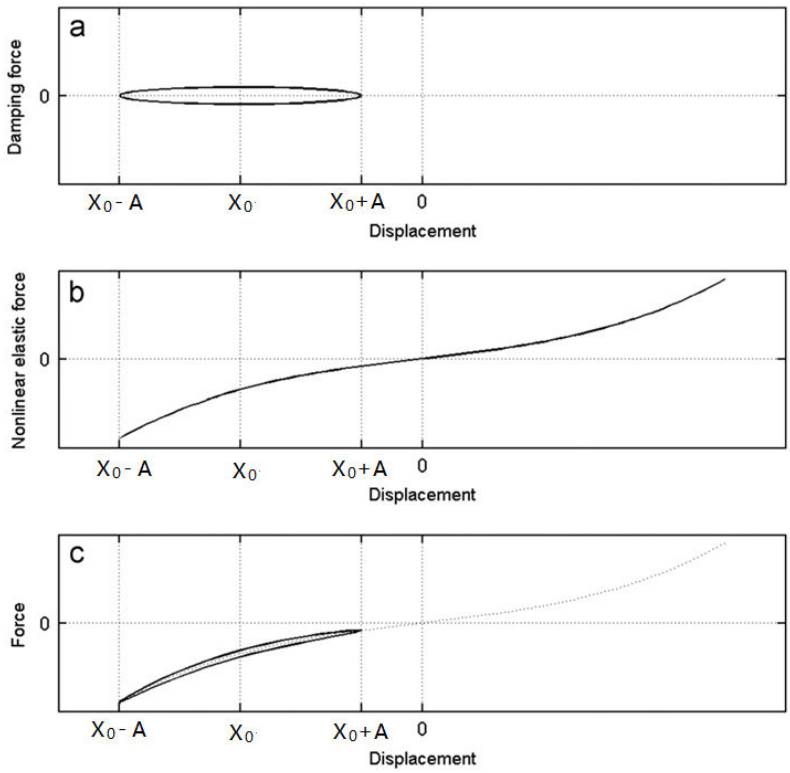

Fig. 3:1 Decomposition diagram of the hysteresis loop of rubber component in rail fastening: (a) decomposed damping force (b) decomposed elastic force and (c) hysteresis loop

3.2.1 Modelling

3.2.1.1 Damping force

Supposing we have an input disturbance displacement

$$x = x_0 + Asin(\omega t) \tag{3:2}$$

and the force response

$$F = F_0 + F_A sin(\omega t - \emptyset). \tag{3:3}$$

Hysteresis, in general, refers to a lag between cause and effect presented by the loss angle $\emptyset$ in Equation 3:3. The loss angle $\emptyset$ is often used to describe the damping properties of rubber material. Besides, other damping parameters are such as the damping ratio, $tan\emptyset = K''/K'$,

where K' and K'' respectively define the relation between displacement input and force response in the same and the different phase, or the damping measure (or damping capacity) defined as $D = K''/\sqrt{K'^2 + K''^2} = (1 + tan^{-2}\emptyset)^{-1/2}$.

As depicted in Fig. 3:1 (a), damping force corresponding to the input displacement is horizontal ellipse-like shape. To interpret the displacement-force relation, the dimension of this enclosed curve is explained. Intercept of X axis is the displacement amplitude A while intercept of the force axis denoted as b is assumed to be $b = A \cdot K''$. As a result, the area of the hysteresis loop $S = \pi Ab = \pi A^2 K''$ is only varied by the dynamic amplitude A because the damping property which can be described by the loss stiffness K'' is supposed not influenced by A. As a consequence, the energy loss during a loading cycle is obtained as $E(A) = S = \pi A^2 K''$.

Therefore the expression of the ellipse is

$$\frac{(x-x_0)^2}{A^2} + \frac{{F_c}^2(A)}{b^2(A)} = 1, \tag{3:4}$$

where x is displacement (mm); x_0 is initial displacement (mm); A is dynamic amplitude; b is an undetermined coefficient indicating the interpret of the vertical axis in Fig. 3:1 (a); F_c is the amplitude dependent damping force. The undetermined coefficient b can be obtained from the measured elliptical area S as:

$$b(A) = \frac{S}{\pi A} = \frac{E(A)}{\pi A}. \tag{3:5}$$

Substituting Eq. (3:5) into Eq. (3:4), the nonlinear damping force F_c is given by:

$$F_c(x, x_0, A) = \pm b(A)\sqrt{1 - \frac{(x-x_0)^2}{A^2}} = \pm \frac{E(A)}{\pi A}\sqrt{1 - \frac{(x-x_0)^2}{A^2}} \tag{3:6}$$

3.2.1.2 Nonlinear elastic restoring force

The nonlinear elastic force-displacement curve is assumed to be a polynomial function according to the observed test curve, and the terms will be determined according to accuracy

requirements. The nonlinear elastic force F_k is therefore a functions of x, ω and A. It can be described by

$$F_k(x, A, \omega) = \sum_{i=1}^{\frac{n+1}{2}} K_{2i-1}(A, \omega)x^{2i-1} = K_1(A, \omega)x + K_3(A, \omega)x^3 + K_5(A, \omega)x^5 \ldots \ldots, \quad (3:7)$$

where the polynomial coefficients of each order are defined as the dynamic stiffness $K_{i(i=1,3,5,\ldots)}$.

3.2.1.3 Total restoring force

The total restoring fore of the rail fastening system exposed to harmonic excitations thus can be written as the sum of the damping force and nonlinear elastic force based on the superposition principle given by:

$$F_{restoring}(x, x_0, A, \omega) = \sum_{i=1}^{\frac{n+1}{2}} K_{2i-1}(A, \omega)x^{2i-1} \pm \frac{E(A)}{\pi A}\sqrt{1 - \frac{(x-x_0)^2}{A^2}}. \quad (3:8)$$

3.2.2 Determination of model parameters

3.2.2.1 Evaluation of dynamic stiffness

The model parameters were evaluated by using the measured data of specimen I (the compressed type rail fastening system for instance) by the least squares method. Coefficients representing the dynamic stiffness and the damping properties were obtained from all excitation cases by using MATLAB. Calculation results with polynomial terms $n = 3$ and $n = 5$ are respectively compared to the measured result in paper [145]. It was found that the fifth-order dynamic stiffness has much lower value than the first and third order dynamic stiffness. And the required accuracy can be met by the first and the third order dynamic stiffness.

3.2.2.2 Frequency and amplitude dependence

From the simulation result we know that the first order dynamic stiffness K_1 decreases slightly with increasing frequency, whereas the third order stiffness K_3 increases with the

frequency. K_1 also decreases with increasing displacement amplitude, whereas K_3 increases with displacement amplitude at first and then decreases after reaching a peak value.

If the first order dynamic stiffness is written as a function of displacement amplitude in the form of

$$K_1(A,\omega) = a_0(\omega) + a_1(\omega)\cdot A + a_2(\omega)\cdot A^2, \tag{3:9}$$

the parameters of K_1 are closely associated with frequency which can be written as

$$(a_0\ a_1\ \ a_2) = (1\ \ \omega\ \ \omega^2\ \ \omega^3)\cdot b_{K_1}, \tag{3:10}$$

where b_{K_1} is simulated as

$$b_{K_1} = \begin{pmatrix} 3.77 & -1.75 & -2.93 \\ 0.61 & -3.56 & -3.59 \\ -0.11 & 0.56 & -0.54 \\ 0.01 & -0.03 & 0.03 \end{pmatrix}. \tag{3:11}$$

Substituting Eq. (3:10) into Eq. (3:9), the first order dynamic stiffness is obtained as

$$K_1(A,\omega) = (1\ \ \omega\ \ \omega^2\ \ \omega^3)\cdot b_{K_1}\cdot(1\ \ A\ \ A^2)^T. \tag{3:12}$$

Similarly, the third order dynamic stiffness is given by

$$K_3(A,\omega) = (1\ \ \omega\ \ \omega^2\ \ \omega^3)\cdot b_{K_3}\cdot(1\ \ A\ \ A^2)^T, \tag{3:13}$$

where

$$b_{K_3} = \begin{pmatrix} 2.11 & 11.28 & -11.43 \\ -0.08 & 0.87 & -1.03 \\ 0.02 & -0.15 & 0.07 \\ 0 & 0.01 & -0.01 \end{pmatrix}. \tag{3:14}$$

In terms of Eq. (3:8), the restoring force of the rubber component in the compressed type fastening system exposed to harmonic excitations therefore becomes

$$F_{restoring}(x,x_0,A,\omega) = \Omega\cdot b_{K_1}\cdot \Lambda^T\cdot x + \Omega\cdot b_{K_3}\cdot \Lambda^T\cdot x^3 \pm \frac{E}{\pi A}\sqrt{1-\frac{(x-x_0)^2}{A^2}} \tag{3:15}$$

where $\Omega = (1 \ \omega \ \omega^2 \ \omega^3)$, $\Lambda = (1 \ A \ A^2)$.

3.2.2.3 Results and discussion

The hysteresis loop of the specimen I at sinusoidal displacement excitation of frequency 6 Hz and displacement amplitude 0.5mm is taken for example and shown in Fig. 3:2. The simulated results are depicted by stars and the measured values are shown in dots. The good agreement between simulated and measurement demonstrates that the proposed nonlinear model is capable of simulating the hysteresis loop for the given working conditions of the fastening specimen. In addition, Fig. 3:3 shows the relations between dynamic stiffness, excitation frequency and displacement amplitude in the form of three-dimensional surfaces comparing Eq. (3:12) and Eq. (3:13). As can be seen in figures, both K_1 and K_3 depend less on frequency than amplitude. Increased amplitude greatly decreases first order stiffness in Fig. 3:3(a), whereas increasing the frequency slightly reduces the dynamic stiffness. Variation of frequency from 2Hz to 10Hz results in a slight increasement of the third order dynamic stiffness (Fig. 3:3 (b)); however, increasing amplitude enlarges the third order dynamic stiffness at the small deformation range and it is followed by a rapid decrease process as amplitude increases further.

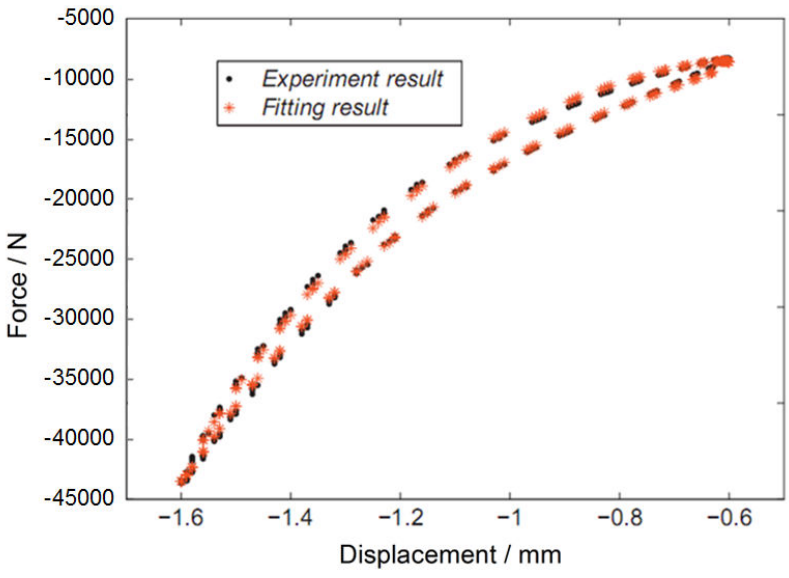

Fig. 3:2 Measured and calculated hysteresis loop of the compressed type fastening system when f=6 Hz and A=0.5mm

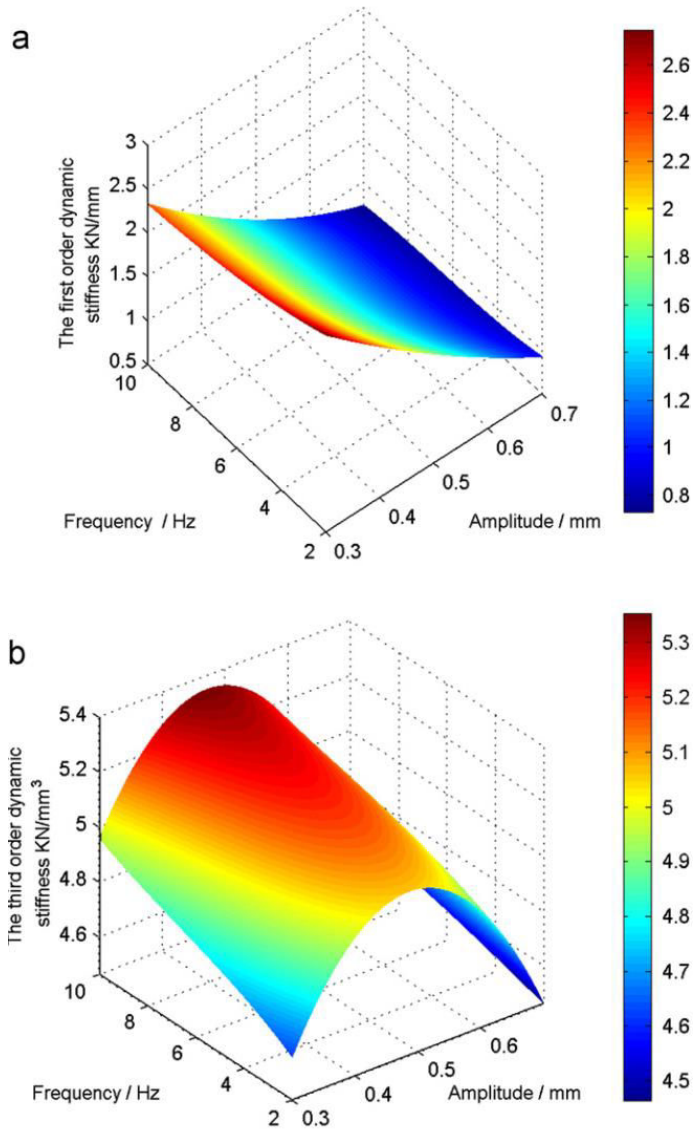

Fig. 3:3 Amplitude and frequency dependent dynamic stiffness (a) the first order dynamic stiffness (b) the third order dynamic stiffness

The model of the compressed type fastening system subjected to harmonic excitations proposed above decomposes the total restoring force into elastic force and damping force. The elastic force term accurately indicates the geometry induced nonlinearity or/and material hyperelasticity; it also characterizes the frequency and amplitude dependent stiffness property through K_1 and K_3. However, the evaluated $K_1(A,\omega)$ and $K_3(A,\omega)$ are limited within the measured cases. Though the model can meet the measured result rather well, it cannot be used to predict the working conditions beyond the testing cases; in addition, the current model cannot describe the frequency and dynamic amplitude dependent damping coefficients and the damping force is also frequency independent. In order to take the frequency and dynamic

amplitude dependent damping properties into consideration, a second model was presented on the basis of the superposition principle.

3.3 Presented model II

In the model I proposed in section 3.2, the damping property, expressed by loss angle $\emptyset$, or damping ratio $tan\emptyset = K''/K'$, or the imaginary stiffness K'' or the damping capacity defined as $D = K''/\sqrt{K'^2 + K''^2}$, was considered as frequency-independent. As a result, the damping force and the area of the dynamic loops are only related to dynamic amplitude. In fact, the damping property is closely related to the disturbance frequency and the frequency dependent damping factor of rubber materials also increases the damping force and the area of the hysteresis loops as shown in Fig. 3:4. Higher frequency gives rise to an increased damping factor, and correspondingly leads to a more and more full-rounded ellipse from the slender ones. However, supposing it also can be decomposed into the elastic force and the damping force part in the Fig. 3:4, the nonlinear curve in Fig. 3:1 (b) should now be replaced by a straight line for describing the linear elasticity.

Therefore, on the basis of superposition principle, the total restoring force of the rail fastening systems for the second model still consists the two parts F_k and F_c, i.e. $F_{restoring} = F_k + F_c$. Elastic stiffness K_{Ela} derived from the elastic force F_k is dependent on the pre-compression x_0 due to a preload as well as the dynamic amplitude A; and the damping force is dependent on the frequency. As a result, F_k and F_c together give a amplitude and frequency dependent dynamic stiffness $K_{Dyn}(x, x_0, A, \omega)$ as well as a frequency dependent damping capacity $D(\omega)$.

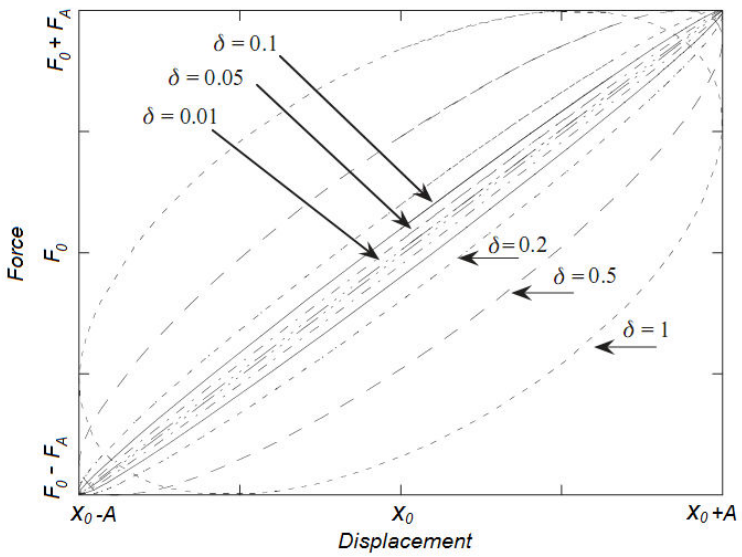

Fig. 3:4 Displacement versus responding force for a linearly viscoelastic rubber material with different damping factors

3.3.1 Modelling

3.3.1.1 Damping force

The fractional operator has performed indeed a simplified description of the frequency dependent viscoelastic behaviour of rubber elastomers. Among the abundant literature on this subject, we can refer to the precursory works [146-150] and some meaningful applications conducted on polymers [151-153]. A more complete review can be found in [154] by Metzler and Nonnenmacher.

Fractional calculus was found appropriate with a more correct description for material damping over an increased frequency. The most common definition of the fractional derivative is by using of the Reimann-Liouville integral [154]

$$cD_t^{\alpha}x(t) = \frac{d^N}{dt^N}\left[\frac{1}{\Gamma(N-\alpha)}\int_c^t \frac{x(\tau)}{(t-\tau)^{\alpha-N+1}}d\tau\right], \tag{3:16}$$

where $\alpha + 1 \geq N \geq \alpha \geq 0$, $N \in N$, $N = \{1,2,3,\ldots\}$; α is the arbitrary order of the derivative; the Γ denotes the gamma-function and $\Gamma(n) = \int t^{n-1}e^{-t}dt, n > 0$. Normally the lower integration limit c is zero.

Modelling of viscoelastic behaviour normally results in $0 \leq \alpha < 1$, which enables Eq. (3:16) to be rewritten in a simpler form

$$D^{\alpha}x(t) = \frac{1}{\Gamma(1-\alpha)}\frac{d}{dt}\int_0^t \frac{x(\tau)}{(t-\tau)^{\alpha}}d\tau, \qquad 0 < \alpha < 1. \tag{3:17}$$

Furthermore, Eq. (3:17) can be transformed as a discrete expression according to Grunwald theory, which presented the determination of fractional derivation as

$$D^{\alpha}x(t) = \lim_{n\to\infty} \frac{(t/n)^{-\alpha}}{\Gamma(-\alpha)} \sum_{j=0}^{n-1} \frac{\Gamma(j-\alpha)}{\Gamma(j+1)} f\left(\mathrm{t} - \frac{jt}{n}\right) \approx \frac{(t/n)^{-\alpha}}{\Gamma(-\alpha)} \sum_{j=0}^{n-1} \frac{\Gamma(j-\alpha)}{\Gamma(j+1)} x(n-j),$$

$$0 \leq \alpha < 1. \tag{3:18}$$

The new viscous component in current model is known as spring-pot and the constitutive equation of the damping force is given by

$$F_c = bD^{\alpha}x(t), \qquad 0 < \alpha < 1 \tag{3:19}$$

where $D^{\alpha}x(t)$ is the fractional time derivative of $x(t)$ of α order as defined above and b is the fractional damping parameter.

Fourier transforming Eq. (3:19) while using the property of transforming fractional time derivatives by means of the principle root as discussed by [155-156] results in

$$D^{\alpha}x(\omega) = (i\omega)^{\alpha}x(\omega), \tag{3:20}$$

where $(\mathrm{i}\omega)^{\alpha}$ is evaluated to be

$$(i\omega)^{\alpha} = \omega^{\alpha}e^{i\pi\alpha/2+n2\pi\alpha}. \tag{3:21}$$

Selecting $n = 0$ for the principal root gives

$$(i\omega)^{\alpha} = \omega^{\alpha}e^{i\pi/2\alpha} = \omega^{\alpha}(cos\,\alpha\pi/2 + isin\,\alpha\pi/2). \tag{3:22}$$

It is clearly can be seen from Eq. (3:22) that

- the sine equals 0 and the cosine equals 1 as $\alpha = 0$. The imaginary term in Eq. (3:22) disappears leaving a pure elastic component. This thus equals the ordinary spring;
- the sine equals 1 and the cosine equals 0 as $\alpha = 1$. Only an imaginary term is present in Eq. (3:22) making Eq. (3:19) dependent solely on the first derivative of motion, $x(\dot{t})$. This equals the ordinary dashpot;
- both the sine and the cosine of Eq. (3:22) are present as $0 < \alpha < 1$. This means that $(i\omega)^{\alpha}$ includes a real and an imaginary part, both being frequency dependent. This property of exhibiting elastic and viscous behaviour is the reason for the component's name, spring-pot.

As can be seen from Fig. 3:5 there are only two parameters to be simulated, α $(0 < \alpha < 1)$ and b, for the frequency dependent spring-pot combined with a frequency-independent elastic force model.

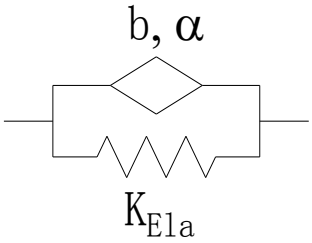

Fig. 3:5 Mechanical analogy of the spring-pot combined with an elastic spring

The complex dynamic stiffness of this model therefore can be written as

$$\widehat{K}_{Dyn}(\omega) = K_{Ela} + \widehat{K}_{Rel} = K_{Ela} + b(i\omega)^{\alpha}, \tag{3:23}$$

where the symbol on top of K_{Dyn} means transforming it from time domain to frequency domain by Fourier transformation, K_{Ela} and K_{Rel} are respectively the frequency-independent long-term elastic stiffness and the relaxation stiffness which is closely related to disturbance frequency. Different from the first model, the constant K_{Ela} results in a frequency-independent elastic force F_k while $b(i\omega)^{\alpha}$ gives rise to a frequency-dependent damping force F_c. Furthermore, current model is not only able to describe the frequency-dependent dynamic stiffness property due to the relaxation stiffness term but also can indicate the frequency-dependent damping parameters.

3.3.1.2 Nonlinear elastic force

The nonlinear elastic force-displacement curve is also assumed to be a polynomial functions in this model according to the observed test curve of specimen I as

$$F_k(x) = K_0 + K_1 x + K_2 x^2, \tag{3:24}$$

where$K_{i,i=0,1,2}$ are the static stiffness of different order. It should be noted that an equal elastic stiffness K_{Ela} is relative to the pre-compression x_0 and the amplitude A by

$$K_{Ela}(x_0,\ A) = \frac{F_k(x_0+A)-F_k(x_0-A)}{2A}. \tag{3:25}$$

Given a preload F_0 and the corresponding pre-compression x_0, the secant elastic stiffness K_{Ela} at x_0 can be decided. It should be taken special attention to that K_{Ela} is not influenced by frequency and the frequency dependence on dynamic stiffness K_{Dyn} is only originated from the K_{Rel} component in Eq. (3:23), and the damping force part is not a closed curve horizontally as shown in Fig. 3:1 (a) but one with specific inclination.

3.3.1.3 Nonlinear restoring force

The total restoring fore of a rail fastening system exposed to harmonic excitations is therefore the sum of the nonlinear elastic force and the frequency-dependent damping force based on the superposition principle given by:

$$F_{restoring}(x,\omega) = F_k(x) + F_c(x,\omega) = K_0 + K_1 x + K_2 x^2 + bD^{\alpha}x(t). \tag{3:26}$$

3.3.2 Determination of model parameters

3.3.2.1 Evaluation of elastic restoring force

The model parameters as shown in Fig. 3:5 need to be fit and the frequency-independent elastic stiffness K_{Ela} will be firstly identified. The elastic force F_k is evaluated by using the measured quasi-static experiment result of specimen I. As can be seen in Fig. 3:6 the loading curve presented with black solid line has lower secant stiffness than that of all the other three dynamic loops. In addition, from the three dynamic curves we can also find that

dynamic stiffness increases with the frequency. That is, $K_{Ela}(-1.0mm, 0.5mm) < K_{Dyn}(f = 2Hz) < K_{Dyn}(f = 8Hz) < K_{Dyn}(f = 18Hz)$. The quasi-static loading curve is defined by the parameters listed in Table 3:1 and the comparison between the measured and the calculated loading curves is shown in Fig. 3:6 with black solid line and red dot respectively. Good agreement can be observed from the figure. By introducing the evaluated parameters in Table 3:1 into Eq. (3:24), the equivalent elastic stiffness within the given displacement range $(x_0 - A, x_0 + A) = (-1.5, -0.5)$ can now be decided by using Eq. (3:25). The equivalent elastic stiffness K_{Ela} is decided under a given special pre-deformation x_0 and amplitude A. On the basis, the frequency dependent relaxation stiffness K_{Rel} with the two model parameters b and α can be decided.

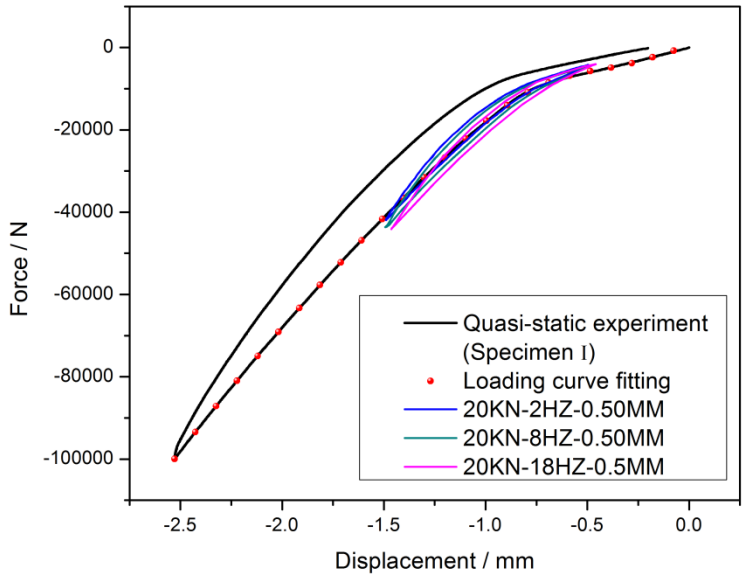

Fig. 3:6 Quasi-static measured curve superimposed with frequency dependent hysteresis loops of the compressed type fastening system

Stiffness of each order (N/mm)	K_0	K_1	K_2
Evaluated parameters	2443.5	10156.7	-12300.4

Table 3:1 The evaluated parameters of Eq. 3:24

Spring-pot (N/mm)	$K_{Ela}(x_0, A)$	$b(N \cdot s^{\alpha}/mm)$	α
Evaluation	34952.1	870.71	0.35

where $x_0 \approx -1.0$mm and A = 0.5mm

Table 3:2 The evaluated parameters of spring-pot according to Eq. 3:19

3.3.2.2 Evaluation of dynamic stiffness and frequency dependence

The evaluated parameters b and α in damping force part can now be optimized to fit the measurement of dynamic stiffness and damping. Error between the measured dynamic stiffness, $\widehat{K}_m(\omega)$, and simulated complex stiffness, $\widehat{K}_s(\omega)$, can be written as

$$e^2 = \sum_n (\widehat{K}_m(\omega) - \widehat{K}_s(\omega))(\widehat{K^*}_m(\omega) - \widehat{K^*}_s(\omega)), \quad (3:27)$$

where $*$ denotes the complex conjugate. When the error is minimized a best fit of the simulated complex dynamic stiffness to the measurement is obtained. The process of the minimization is performed by using Matlab.

The simulated frequency influenced dynamic stiffness is compared to the measured results in Fig. 3:7. Good agreement can be observed between the black square and the red solid circle, and both of them show an ascending trend influenced by the increasing frequency. To confirm the evaluated parameters listed in both Table 3:1 and Table 3:2, the measured and calculated damping defined are also compared in Fig. 3:7. From the figure, calculated damping can be found well meeting the measured damping capacity. However, the damping influenced by stimulating frequency appears to be a constant value, because present frequency range is still relatively rather narrow to show obvious frequency dependent damping features.

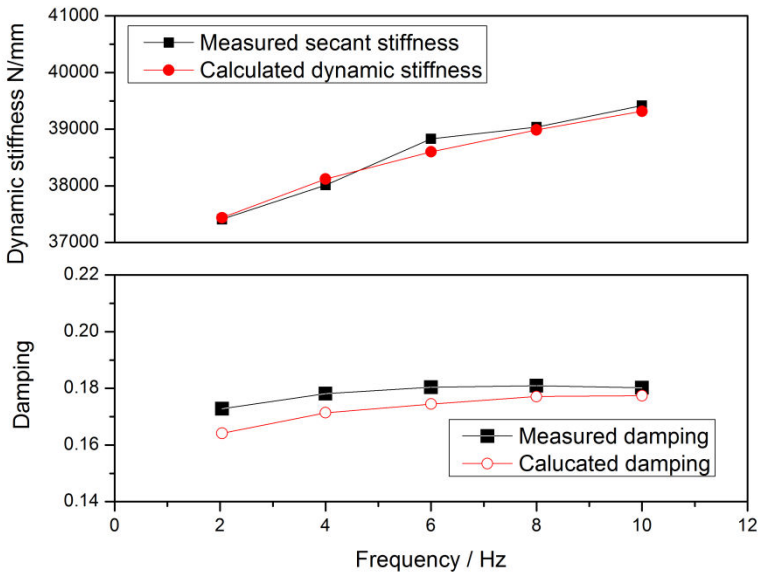

Fig. 3:7 Comparison between the measured and calculated dynamic stiffness and damping for the testing condition of $F_0 = -20kN$ and $A = 0.5mm$

3.3.2.3 Evaluation of the hysteresis loop

By now, both elastic force and the damping force have been identified and the total restoring force can be written with the fitted parameters as

$$F_{restoring}(x,\omega) = F_k(x) + F_c(x,\omega) = K_0 + K_1 x + K_2 x^2 + bD^{\alpha}x(t) \quad = 2443.5 + 10156.7x - 12300.4x^2 + 870.31D^{0.35}x(t) \tag{3:28}$$

Taking the loading case $x_0 = -1.0mm$, $A = 0.3mm$ and $\omega = 2\pi \cdot 4Hz$ for example, the calculated and measured hysteresis loops are compared in Fig. 3:8. The red dot indicating the simulating results and the black solid line are in good agreement which means the validity of the presented model. All the other working conditions show good fitting results compared with measurement as well and they are not depicted again for brief.

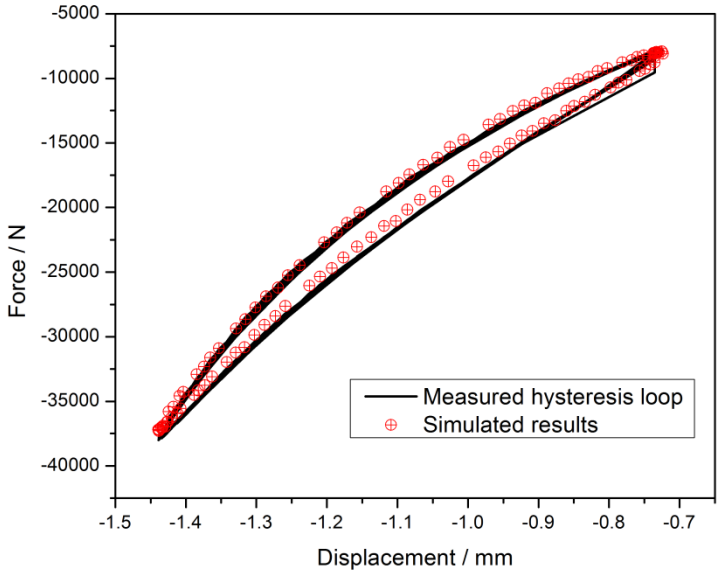

Fig. 3:8 Compared hysteresis loop of measurement and calculation as $f_0 = -20\text{kN}$, $A = 0.3\text{mm}$ and $\omega = 2\pi \cdot 4\text{Hz}$

3.3.2.4 Results and discussion

The advantage of current model developed in this section is taking the frequency dependency into consideration of the dynamic properties of rail fastening systems. Different from the one presented in section 3.2 where the loss factor is kept in constant, frequency dependent damping feature parameters is included in the present model. The fractional derivative viscous component, which is used herein, was proved to be appropriate to correctly describe the frequency dependent dynamic properties. And the only two model parameters b and α makes the relevant experiment easier. From Fig. 3:8 the good agreement between the measurement and the calculation indicates the accuracy of the model and the evaluated model parameters. Also the correct frequency dependency on the dynamic stiffness can be observed from Fig. 3:7 where increasing frequency gives rise to an increment of dynamic stiffness value.

However, there are still a few defects in current model:

- it is clearly can be seen from Fig. 3:7 that the damping almost keeps unchanged as frequency increases and the interested frequencies locate, in fact, at a low and narrow scope. It indicates that the fractional derivative model is not necessary whose advantage is instantiated in high frequency range in fact. On the country, it brings a drawback due to the

introducing the fractional calculus -- difficulties in solving equations of motion in the time domain.

- the predicted damping are still independent of the dynamic amplitude that doesn't satisfy the measured results. In fact, the testing results shows stronger influence of the dynamic amplitude than the stimulating frequency

3.4 Presented model III

The proposed model in this section is represented by superposition of a purely elastic spring, a viscous component as well as a frictional component. Different from the decomposing principle of the other two models, the three components of present model decomposes the total restoring force into three parts and represents respectively the displacement-force relations of the frequency-and-amplitude independent elasticity, frequency dependent viscosity and amplitude dependent friction. With clear physical meanings, the parameters of each force component are not influenced by others; the amplitude dependence is independent on the frequency dependent properties and vice versa.

3.4.1 Modelling

3.4.1.1 Amplitude dependent damping force

Most models of rubber isolations used to predict stiffness and damping properties are independent of the applied displacement amplitude. According to the definition of Boltzmann superposition principle, these models are linear models [157]. However, the rubber material used for the fastening specimens in current research is filled rubber, and the fillers such as carbon black may introduce additional bonds. These bonds exhibit a frictional behaviour as discussed in reference [10]. In fact, it is also the frictional effect that brings the overtones on the basis of the fundamental frequency of the harmonic excitation. Influences of the frictional effect in the time-force scale might be seen very small, but they strongly influence the measured hysteresis loops of different dynamic amplitude.

Friction effect can be modelled using a stick-slip component of Coulomb type as shown in Fig.3:9 (a). Normally the fractional component is coupled in parallel with an elastic component with frequency-and-amplitude-independent stiffness, K_{Ela} . As the model is

subjected to an input deformation the responding force is developed and participated by the elastic spring with stiffness K_{Ela} and the frictional component with the frictional stiffness K_{Fri}, see Fig. 3:9 (b). The total stiffness is equalled to $K = K_{Ela} + K_{Fri}$. When the force distributed in the K_{Fri} bunch exceeds a certain maximum value F_{fmax} the frictional component begins to slide. Sliding between the frictional pads repeals the force generation in the frictional component and results in a smaller stiffness. The stiffness value at this moment is only from the purely elastic spring, i.e. $K = K_{Ela}$. Though being rather coarse, this stick-slip frictional model has the essential behaviour of hysteresis loops of amplitude dependence.

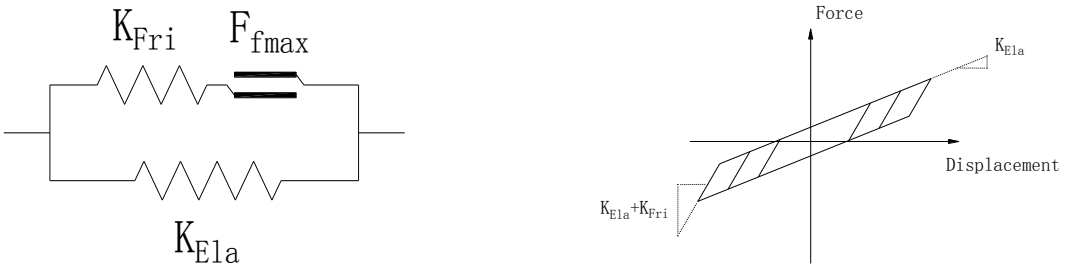

(a) Stick-slip friction model (b) Hysteresis loops for various amplitudes

Fig.3:9 Mechanical analogy of stick-slip friction model and the calculated hysteresis loops

Alternative is a smoother frictional component whose mechanical analogy is shown in Fig. 3:10 (a). It is combined with a frequency independent elastic spring. At this time, the frictional force F_f, i.e. the amplitude dependent damping force, in the present model depends not only on the displacement x but also on a reference state point (x_s, F_{fs}), see Fig. 3:10 (b). There are two model parameters F_{fmax} and $x_{(F_{fmax}/2)}$ introduced to the smooth frictional model; F_{fmax} is the maximum friction force; $x_{(F_{fmax}/2)}$, as it looks like, is the displacement needed to reach half of the maximum friction force. This displacement describes how fast the maximum friction force is reached. In other words, a smaller value of $x_{(F_{fmax}/2)}$ gives a steep force increase and high frictional stiffness, K_{Fri}.

Specifically, the friction force F_f in the model depending on how displacement is related to the reference displacement x_s is defined as

$$F_f = F_{fs} \qquad \text{for } x = x_s \tag{3:29a}$$

$$F_f = F_{fs} + \frac{x-x_s}{x_2(1-\alpha)+(x-x_s)}(F_{fmax} - F_{fs}) \qquad \text{for } x > x_s \tag{3:29b}$$

$$F_f = F_{fs} + \frac{x-x_s}{x_2(1+\alpha)+(x-x_s)}(F_{fmax} + F_{fs}) \qquad \text{for } x < x_s \tag{3:29c}$$

where $\alpha = F_{fs}/F_{fmax}$ is an quantity ranging from -1 to 1.

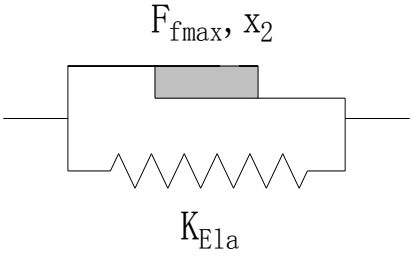

(a) Mechanical analogy of smooth friction model

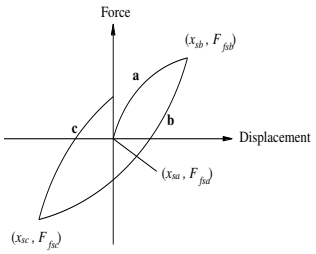

(b) Hysteresis loop of various amplitudes

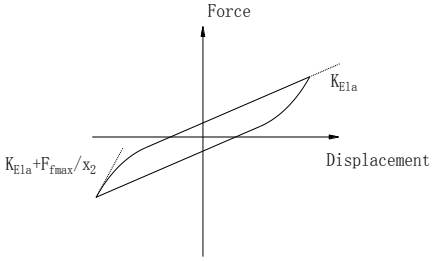

(c) Typical displacement-force curve with large amplitude displacement

Fig.3:10 Mechanical analogy of smooth friction model and the calculated hysteresis loops

Specifically, in order to clearly illustrate the behaviour of present frictional model, the response to the harmonic displacement excitation with no pre-deformation is explained, i.e. $x_0 = 0$. In Fig. 3:10 (b), if he first branch has the reference state $(x_{sa}, F_{fsa}) = (0, 0)$ the Eq. (3:29b) for increasing x becomes

$$F_f = \frac{x}{x_2+x} F_{fmax}, \tag{3:29d}$$

from where we can see that $F_f = F_{fmax}/2$ for $x = x_2$ and that $F_f = F_{fmax}x_0/(x_0 + x_2)$ for $x = x_0$. As the x_0 becomes larger, the friction force F_f will approach to the maximum force F_{fmax}. As the displacement is decreases and enters the second branch the reference state turns to be $(x_{sb}, F_{fsb}) = (x_0, F_{fmax}x_0/(x_0 + x_2))$ and it should be introduced in Eq. (3:29c). Similarly, the third branch takes over from the reference state (x_{sc}, F_{fsc}) which in turn should

be introduced in Eq. (3:29b) again. It also can be seen from Fig. 3:10 that steady state is finally reached after several cycles with steady force-displacement loop.

From Eq. (3:29) the response force amplitude F_{f0} at steady state and the energy loss per cycle, E_f, can be obtained by

$$F_{f0} = \frac{F_{fmax}}{2x_2}[\sqrt{{x_2}^2 + {x_0}^2 + 6x_0x_2} - x_2 - \mathrm{x_0}], \tag{3:30a}$$

and

$$E_f = 2F_{fmax}[2x_0 - x_2(1+\alpha_0)^2 \ln\frac{\mathrm{x_2}(1+\alpha_0)+2\mathrm{x_0}}{\mathrm{x_2}(1+\alpha_0)}] \tag{3:30b}$$

respectively, where $\alpha_0 = F_{f0}/F_{fmax}$. F_{f0} and E_f both are functions of the displacement amplitude x_0 and the two parameters x_2 and F_{fmax}.

As a result, amplitude dependent frictional stiffness K_{Fri} and damping D_{Fri} become

$$K_{Fri} = \frac{F_{f0}}{x_0} = \frac{F_{fmax}}{2x_2x_0}[\sqrt{{x_2}^2 + {x_0}^2 + 6x_0x_2} - x_2 - x_0], \tag{3:31a}$$

and

$$D_{Fri} = \frac{E_f}{F_{f0}\cdot x_0} = \frac{2}{\alpha_0 x_0}[2x_0 - x_2(1+\alpha_0)^2 ln\frac{x_2(1+\alpha_0)+2x_0}{x_2(1+\alpha_0)}]. \tag{3:31b}$$

The frictional stiffness K_{Fri} approaches F_{fmax}/x_2 as x_0 goes to zero; it becomes zero as x_0 tends to infinity. Damping D_{Fri} goes to zero as x_0 approaches to zero; on the other hand, it is also found to reach the value 4 as x_0 goes to infinity, at which time the hysteresis loop approaches a rectangle with intercepts of x_0 and F_{f0}. It should be taken special attention that the tangent stiffness of the friction force versus displacement curve equals $K_{Ela} + F_{fmax}/x_2$ at each start of every branch, see Fig. 3:10 (c); as displacement keeps increasing, stiffness approaches the linear pure elastic stiffness K_{Ela}. Experimental results of specimen II is used herein for instance whose elastic stiffness is almost linear compared to specimen I. The restoring force model presented, of course, is also able to be applied to specimen I; however the simulation results are omitted for brief.

3.4.1.2 Frequency dependent damping force

Instead of the spring-pot component used for describing the frequency dependent damping force in section 3.3, an easier Maxwell model is adopted as the viscous component for current model. The fractional derivative model might be found more appropriate with accurate description for material damping properties in much larger frequency range, however as mentioned above the damping barely vary with frequency for the presented two fastening specimens. At this situation, the drawback of the fractional calculus, the fractional derivative component can be modified by replacing the spring-pot with the Maxwell model, see Fig. 3:11.

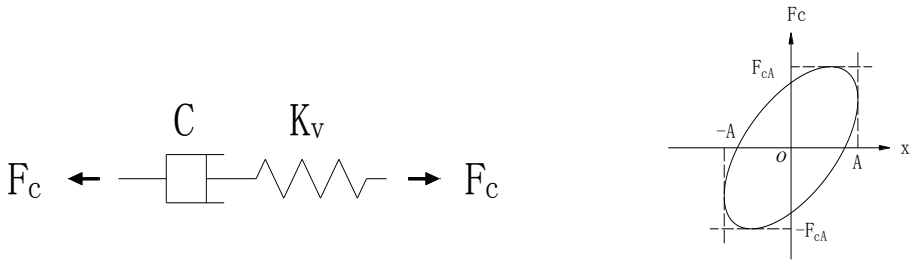

(a) Mechanical analogy (b) Viscous force versus displacement

Fig.3:11 Mechanical analogy of linear viscous damper and the calculated hysteresis loop

Increasing stiffness and hysteresis loops with increasing frequency can also be described at low frequency range by introducing such a viscous component. As is shown in the figure, the viscous force is represented by a linear damper with a damping coefficient C, in series with a linear spring with stiffness K_v. F_{cA} is the force amplitude related to displacement amplitude A. For a harmonic excitation this model gives an elliptic displacement-force relation at steady state. When the excitation frequency goes to zero to the loop as descried in Fig. 3:11 (b) will approach a horizontal line. Thus the viscous force contribution approaches zero. It can be shown that the force amplitude F_{cA} in Fig. 3:11 (b) and the energy loss per cycle, E_c, respectively equal

$$F_{cA} = \frac{\omega C}{\sqrt{1+(\omega C/K_v)^2}} A, \tag{3:32a}$$

and

$$E_c = \frac{\pi\omega C}{1+(\omega C/K_v)^2} A^2. \tag{3:32b}$$

The loss energy has a maximum of $0.5\pi K_v A^2$ at the characteristic frequency $\omega = K_v/C$. Therefore, the stiffness and damping can be given by

$$K_c = \frac{F_{cA}}{A} = \frac{\omega C}{\sqrt{1+(\omega C/K_v)^2}}, \tag{3:33a}$$

and

$$D_c = \frac{E_c}{F_{cA} \cdot A} = \frac{\pi}{\sqrt{1+(\omega C/K_v)^2}}. \tag{3:33b}$$

The stiffness K_c becomes zero for $\omega = 0$ and approaches K_v as the excitation frequency increases. The damping D_c goes to its maximum value, π, as $\omega = 0$, while for large disturbance frequencies the damping D_c tends to zero.

3.4.1.3 The total restoring force

As for the current model presented in current section, the shear type fatening system is taken for example. A pure elastic spring is used to produce the frequency and amplitude independent elastic force. Due to the visually linear elasticity of the shear type specimen, only a pure elastic stiffness $K_{Ela}$is used for describing the elastic restoring force.

The total restoring force therefore takes into account both frequency and amplitude influences through a Maxwell model and the smooth friction model coupled in parallel with the elastic spring. When exposed to an input harmonic disturbance, amplitude dependent damping force can be described by Eq. (3:29), the frequency dependent part can be described by Eq. (3:32) and the pure elastic force with the elastic stiffness K_{Ela} is used to give the uncoupled elastic force contributions as

$$F_{Restoring} = F_f(x, A) + F_c(x, \omega) + F_e(x). \tag{3:34}$$

3.4.2 Determination of model parameters

3.4.2.1 Evaluation of the elastic force and frictional damping force

Recognizing amplitude dependence is independent of the frequency and vice versa enables the corresponding parameters to be evaluated separately. The frequency independent friction parameters F_{fmax} and x_2 and the pure elastic stiffness K_{Ela}, can be determined by the measured data at low frequency and large dynamic amplitude. The low frequency guarantees almost all viscous effects are eliminated; the large dynamic amplitude assures that all friction is developed in the loop. By using the measured results of 1.5mm and 0.5Hz, following values were obtained and presented in Table 3:3 for the shear type fastening system (Specimen II).

Parameters	Elastic stiffness	The maximum friction force	Friction displacement	Viscous damping	Viscous stiffness
Notations	K_{Ela}	F_{fmax}	x_2	C	K_v
Units	kN/mm	kN	mm	$kN \cdot s/mm$	kN/mm
Evaluation	8.1	7.0	1.1	0.017	1.0

Table 3:3 Evaluated parameters with the testing results of A=1.5mm and f=0.5Hz

The resulting parameters in Table 3:3 are used to simulate the hysteresis loop of 1.5mm and 0.5Hz and comparison between measured and simulated results are shown in Fig. 3:12, from where we can see that they agree with each other rather well. Furthermore, Fig. 3:13 shows the dynamic stiffness and damping for the specimen at five different dynamic amplitude under the same low frequency, 0.5Hz. Apparently, the model accurately describes the amplitude dependent properties even if only one amplitude measurement, i.e. 1.5mm, was used to extract the parameters, where the dynamic stiffness decreases with amplitude while damping increases with amplitude.

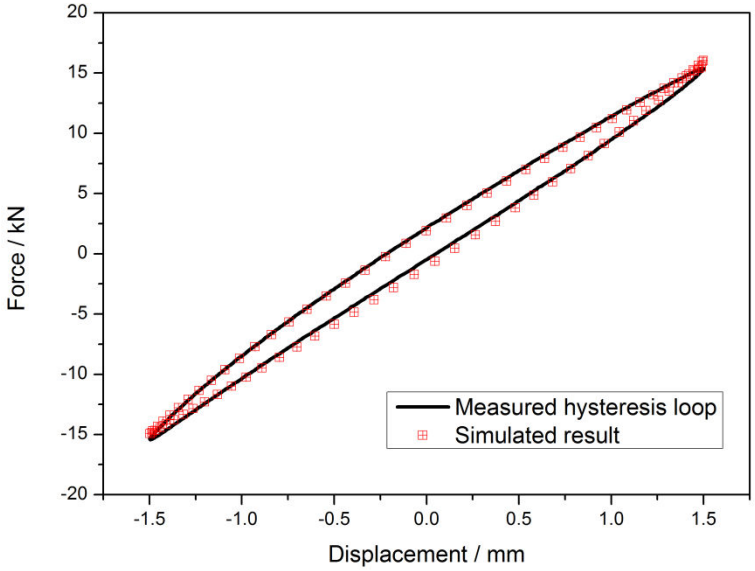

Fig. 3:12 Comparison between measured and simulated hysteresis loop of the working condition A=1.5mm and f=0.5Hz

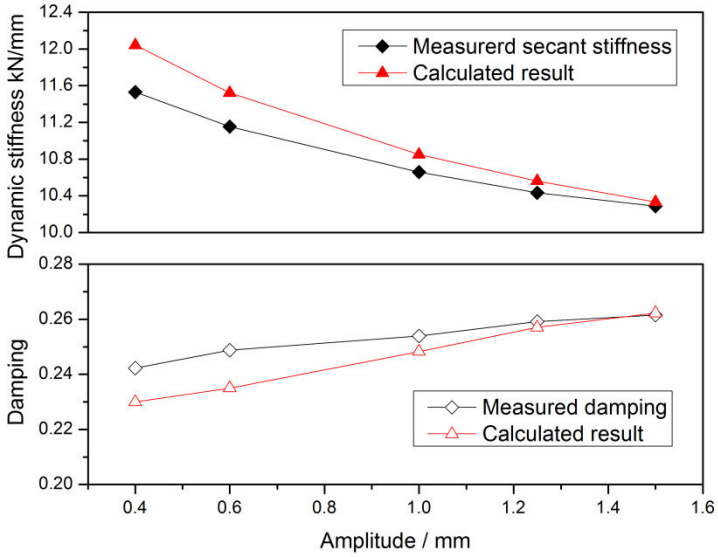

Fig. 3:13 Amplitude dependence of stiffness and damping for the shear type fastening system

3.4.2.2 Evaluation of frequency dependent damping force

The parameters of the liner viscous component, C and K_v, which determines the frequency dependent damping force, can now be optimized to fit the measured stiffness K_c and damping D_c at a constant dynamic amplitude but different stimulating frequency testing cases. The evaluated C and K_v are also presented in Table 3:3.

3.4.2.3 Results and discussion

Including the viscous component with the two optimized two parameters into the total responding force, Fig. 3:14 shows the compared calculation and measurement of dynamic stiffness and damping for different disturbance frequencies. The integrated model accurately describes the frequency dependent properties: both dynamic stiffness and damping increase with frequency at the range of [2Hz, 18Hz].

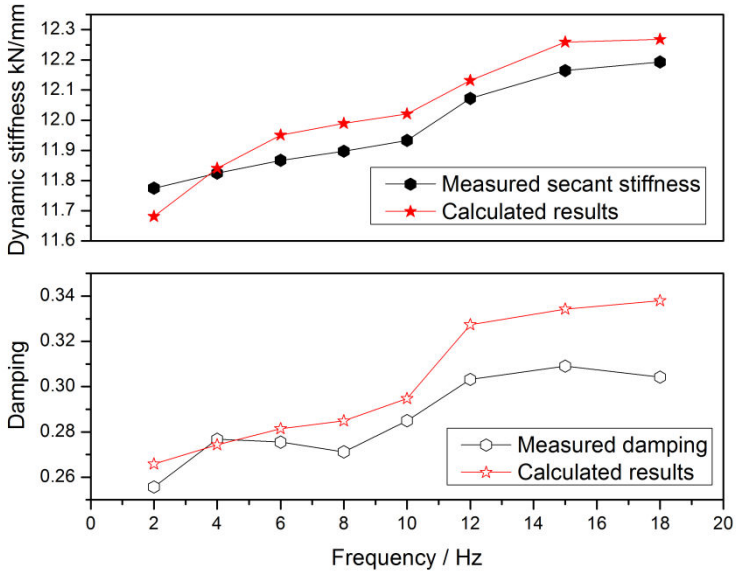

Fig. 3:14 Frequency dependent stiffness and damping of the shear type fastening system

By using the evaluated model, simulated and measured displacement-force loops of other testing cases, such as $f = 2Hz$, $A = 0.4mm$ and $A = 1.4mm$ are shown and compared in Fig. 3:15 (a) and (b). Good agreement between simulation and measurement can be observed, which indicates the accuracy of the evaluated parameters. The secant stiffness of the hysteresis loop for $A = 0.4mm$ in Fig. 3:15 (a) is found relatively larger than that for $A = 1.4mm$ in Fig. 3:15(b). and the energy loss per-cycle for occasion $A = 1.4mm$ is larger than that of $A = 0.4mm$. In addition, the condition as displacement amplitude $A = 0.4mm$ and the frequency $f = 2Hz$ is again used to be compared with the measurement case as frequency equals $15Hz$, see Fig. 3:15 (c). We cannot distinguish the frequency dependent properties between Fig. 3:15 (a) and (c) from the figures, but a gradual influencing trend on the dynamic stiffness and damping features were already shown Fig. 3:14 with the frequency

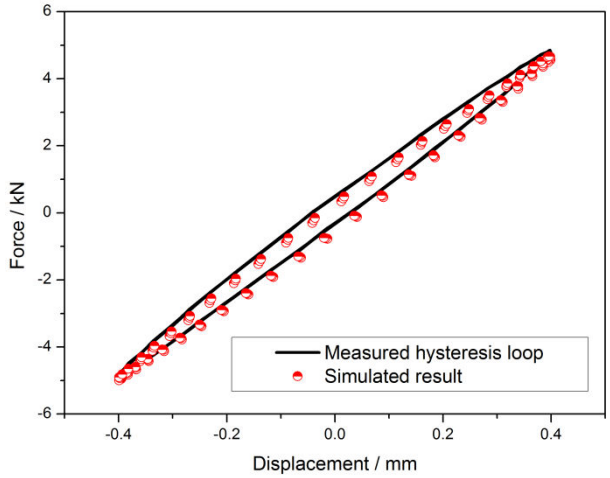

(a) f=2Hz A=0.4mm

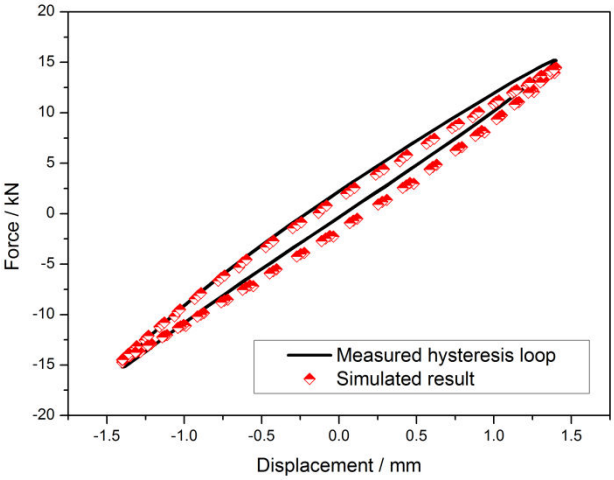

(b) f=2Hz A=1.4mm

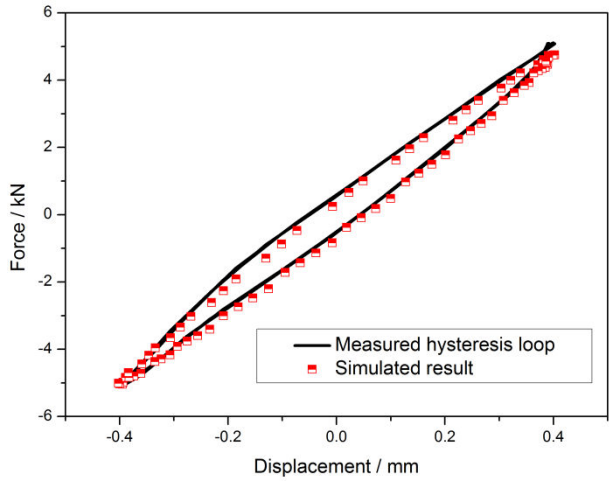

(c) f=15Hz A=0.4mm

Fig. 3:15 Compared measured and calculated hysteresis loops by using the integrated model at different working conditions

as x-axis. The hysteresis energy loss shown in Fig. 3:15 (a) and (c) also do not show too much difference. Similar comparison results for all other amplitudes are omitted for brief.

Special attention should be taken to that the hysteresis loop as $f = 15Hz$ in Fig. 3:15 (c) was supposed to be more like ellipse compared with $f = 2Hz$ in Fig. 3:15 (a) indicating the viscous effects coming into play. However, the relatively higher frequency (15Hz) nearly has the same sharp corners obtained for the loops as low frequency (2Hz). It confirms that rail fastening system works at a low-frequency stage where frequency dependency is in fact not as distinct as is supposed to be, especially comparing with amplitude dependent properties.

3.5 Summary

In Chapter 3, the nonlinear, dynamic response of rail fastening systems exposed to sinusoidal displacement stimulating is analysed by three different models. The total restoring force related to the harmonic disturbances consists of an elastic force and a damping force emphasized by the first model. The preload, frequency as well as amplitude dependent stiffness properties are described by using a first order and a third order stiffness. However, the first model is only valid within the maximum testing frequency and dynamic amplitude which doesn't have a wide generalizability; in addition, the influence of the frequency on the damping force part is also omitted.

In order to take into account the frequency dependent properties on the damping force, a fractional derivative model is introduced. Fractional derivative viscoelastic model is able to describe material damping and stiffness accurately even in an extended frequency range. Furthermore, the only two model parameters b and α needed to be fit simplifies the experiment process. However, such defects in the second model still exist as, (1) due to the very low and narrow frequency range for the two fastening systems in current research, frequency dependency especially on the damping properties is rather limited. As a consequence, a simpler viscous model can be used to replace the fractional derivative model; and (2) on the basis of linear viscoelasticity, the predicted damping force is still independent of the dynamic amplitude.

Eventually, the third model is represented by combining a purely elastic spring, a viscous component and a frictional component. Different from the decomposing principle as the first two models, these three components decomposes the total restoring force into the frequency-and-amplitude independent elastic force part, the frequency dependent viscous damping force part and the amplitude dependent frictional damping force part. With clear physical meanings, the parameters of each component are also not influenced by others. This model was found to be successful to represent the measured results of the two fastening systems.

Though the models proposed in present chapter are believed to enlighten the understanding of mechanical behaviour of rail fastenings as a vibration isolation system, the following finite element analysing process will promote the understanding to the details such as geometric properties and will also help in design and structural optimization process.

Chapter 4 Fundamental rubber material tests and simulation

In this Chapter, a family of fundamental rubber material experiments is performed in order to accurately model the rubber material made up of the two fastening specimens during the finite element analysing procedure in Chapter 5. Uniaxial tension, uniaxial compression and planar tension measurements are carried out to describe the hyperelasticity of the present rubber; a set of frequency scanning test if presented in order to decide the viscous property of the rubber. Different hyperelastic and viscoelastic models are used to fit the testing results in Abaqus and they are compared with each other. Eventually, the most suitable model is selected.

4.1 Introduction

The analysis of mechanical behaviour of elastomers requires knowledge of the viscoelastic properties of rubber material at large strain. Experiments used for analysing the material properties of elastomers are often misunderstood. The tests for determining the rubber material properties are different from those commonly performed on elastomer in laboratories. These fundamental tests are normally used to define and satisfy mathematically material models existing in the commercial software such as Abaqus.

Normally six different types of experiments are used for defining a hyperelastic material, namely uniaxial tension, uniaxial compression, equal-biaxial, planar tension (or pure shear), simple shear, and volumetric tests. In general, a combination of uniaxial tension and simple shear is required at the very least and the volumetric data must be included for elastomers undergoing large compressed deformations. For rail fastening systems, free surface of rubber component is specifically designed for large deformation; in addition, the deformation of the rubber component in rail fastening systems is in the form of combined compression, tension as well as shear normally. Therefore, a combination of uniaxial tension test, uniaxial compression test and planar tension test at a very low deforming rate is performed in this chapter to define the hyperelasticity of rubber material. Hyperelasticity is only concerned with the current state, and is independent of its deformation history undergone

[158]. Hence the uniaxial tension test, uniaxial compression and planar tension tests only define the nonlinear elasticity which is fully reversible, and cannot include the nonreversible viscous properties of rubber material.

Rubber material also exhibits time-dependent behaviour and the mechanical behaviour depends on both motions and time. When given a loading-unloading process, it eventually returns to the original and un-deformed state, i.e. elasticity. When subjected to a constant stress, it creeps; when given a prescribed and constant strain, the stress decreases with time named relaxation; and hysteresis refers to the different stress-strain trace of unloading process as it is subjected to the cyclic loading. Collectively, these features are called viscoelasticity.

In Abaqus time-dependent constitutive relations is always represented in terms of Prony series [159]. A stress relaxation test is enough to provide sufficient data to define the Prony series parameters [160]. Though Prony series can predict the frequency dependent loading curves accurately, it does a poor job in capturing a hysteresis loop due to its linear attribute. Another embedded viscoelastic model in Abaqus named Bergstrom-Boyce hysteresis model (BB model for simplicity) will be used eventually. The whole set of fundamental rubber material experiments includes uniaxial tension test, uniaxial compression test, planar tension test and frequency sweep test.

4.2 Test details and results

4.2.1 Specimens preparation and test apparatus

The rubber material used in the two fastening systems has a shore hardness of 65 degree. Test specimens used to run the fundamental material tests use the same compound.

4.2.1.1 Uniaxial Tension Test

The specimen preparation and test procedure of uniaxial tension test follows BS ISO 37 [161]. However non-dumbbells specimens are used because the aim of current test is not to determine the tensile strength. Hence five thin rectangular strips were cut from a 2mm ± 0.2mm-thick vulcanized rubber sheet for uniaxial tension test in order to give a small uncertainty. The overall length and width of rubber strips are 150mm ± 0.2 mm and 10mm ±

0.2mm respectively while the test length of 50mm± 0.2 mm was marked with two cross lines, see Fig. 4:1 (a). Much longer overall length is used to ensure that enough end tabs come into contact with the machine grips and to guarantee the middle part the specimens in a pure state of extension. Specimens are conditioned at a room temperature forty-eight hours before the test. The thickness and height at the centre and at each end of the test length were measured with a vernier caliper. Mean value of the five measurements is used in calculating the area of the cross-section. If any of the five measurements differs from the mean value by more than 2%, another specimen needs to be complimented. The test apparatus, a Zwich/Roell Z020 universial testing machine shown in Fig. 4:1 (b), complies with the requirements of ISO 5890. It has an accuracy of force measurement complying with class 2, an accuracy of extensometer complying with class D. It's also capable of operating at large range of traverse rate. Specimens were conditioned in the testing room forty-eight hours before the test carried out.

(a) Specimens

(b) Apparatus

(c) Testing procedure

Fig. 4:1 Uniaxial tension test

4.2.1.2 Uniaxial Compression Test

Unlike other materials such as metal, rubber material behave rather differently in compression than in tension or shear. When rubber elastomers are under study, it's desirable to fit experimental data of rubber material in multiple states of strain so that the material model can be used effectively in predicting complex strain states that occurs in real working condition of rubber component. [162]

Generally, equal biaxial tension test is desirable for analysis of compressed type of rubber component [163]. However, the advantage of performing the uniaxial compression test instead is that the testing equipment is much easier than the equal biaxial tension as shown in

Fig. 4.2. In fact, the uniaxial compression test is equivalent to the equal-biaxial extension test as long as a ‘‘pure’’ compression strain state can be achieved in the centre part. The strain and stress of these two deformation mode can be converted directly to each other as follows:

$$\sigma_c = \sigma_b(1 + \varepsilon_b)^3 \tag{4:1a}$$

$$\varepsilon_c = \frac{1}{(1+\varepsilon_b)^2} - 1\ , \tag{4:1b}$$

where σ_c and ε_c are nominal compression stress and nominal compressioin strain, and σ_b and ε_b are nominal extension stress and nominal extension strain respectively. It should be noted that as we say experimental data represent ‘‘pure’’ strain state, it means that experiment should be performed in a state of only one strain state existing without other disturbance. As a result, uniaxial compression experiment needs to be free of shear or tensile strains. To achieve this as much as possible, the specimen needs to be compressed between two rigid platens without friction effects on the surfaces of platens and the specimens.

Specimen preparation and test procedure of uniaxial compression test follows BS ISO 7743 [164]. In order to obtain a pure compression strain sate, two polytetrafluoroethylene (PTFE) blocks of regular shape are used instead of flat metal plates for two reasons. Very small density of PTFE ensures near-zero pre-compression on the rubber specimens before expected deformation is applied; of more importance, both surfaces of the PTFE blocks are highly polished before applying lubricant to eliminate friction effect as good as possible. Test pieces are rubber cylinders of diameter 29mm ± 0.5mm and height 12mm ± 0.5mm shown in Fig. 4:3 (a). Five pieces of specimens were tested as well. It’s essential to make the testing specimens with flat and paralleled surfaces, therefore the height of the five specimens are measured accurately with difference less than 0.2%. Specimens are also conditioned at a room temperature forty-eight hours before the test carried out. The test apparatus complies with the relevant requirements of ISO 4648. The testing set with two PTFE blocks are shown in Fig. 4:3 (b) and (c).

Fig. 4:2 Equal-biaxial tension test

(a) Specimens

(b) Apparatus

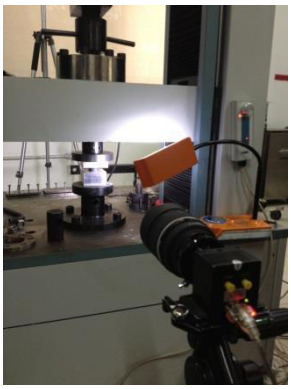

(c) Testing procedure

Fig. 4:3 Uniaxial compression test

4.2.1.3 Planar Tension Test

Planar tension test of rubber material has not been specified in any of the international standards but only in some referenced literatures [165-177]. As the references put it, if the deformation of the testing component includes shear mode a planar tension experiment is expected [166], which is also known as the pure shear test or constrained tension test. The term ‘‘constrained tension’’ means that the specimen of planar tension test is normally a thin rectangular sheet as well and it is gripped or bonded along its long edges to prevent lateral contraction, in direction 2 as shown in Fig. 4:4 (a) when it is loaded along the short edge direction, direction 1. The sheet is freely contract in its thickness dimension, direction 3. In order to achieve sufficient constraint and homogeneity, the length of the specimen needs to be much larger than its width; that is, very good lateral constants and all thinning occur in the direction 3, see Fig. 4:4 (b). It might appear at first glance to be nothing more than a very

wide uniaxial tensile test, however a state of "pure planar shear" exists in the sheet specimen shown in Fig. 4:4 (b) due to the nearly incompressible property of rubber material [165].

The test is very sensitive to the width to length ratio. Neglecting the edge effects results in a perfectly lateral constraint so that all specimen thinning occurs in the thickness direction and puts the central part of the specimen into a pure shear condition [177]. In Fig. 4:4 (b), as axial deformation is applied it maintains parallel plans that experiences lateral relative displacement. The difference between a pure shear test and a simple shear test can be seen from Fig. 4:4 (c) that there is no rigid body rotation for the former.

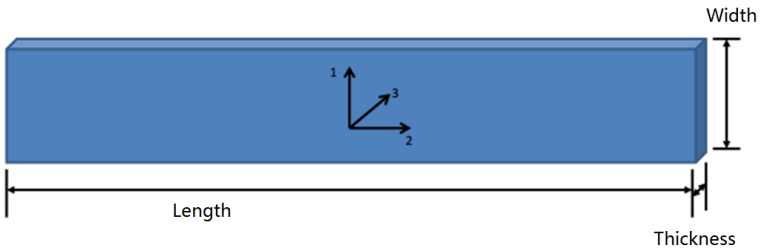

(a) Constrained tension test specimen dimensions

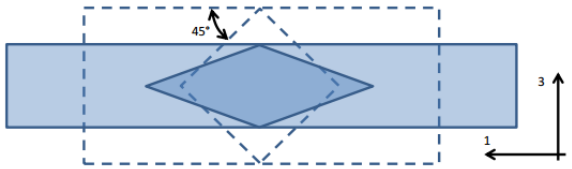

(b) Pure shear existing in the constrained tension test specimen

(c) Simple shear

Fig. 4:4 Planar tension test equals to pure shear test by uniaxial constrained tension [166]

Fig. 4:5 (a) shows that 120mm ± 0.5mm length specimens are prepared with grip separations about 12mm ± 0.2 mm, which are marked by silver ink along the grip edges and the grips are 140mm length; the grips are about 10mm out of the end each side over the entire 120mm specimen width. To make sure the specimens are securely held in the grips four pairs of additional clamping bolts are fastened along the length of the grips. Same as the first two tests, five specimens were used to achieve a low uncertainty. The thickness, which is supposed to be 2mm ± 0.2mm, was measured and compared to obtain a mean value.

Specimens were laid out at a room temperature forty-eight hours before the test. Test instrument is a modified universal mechanical testing machine so as to install the two extra steel apparatus holding clamping bolts, shown in Fig. 4:5 (a).

(a) Specimens

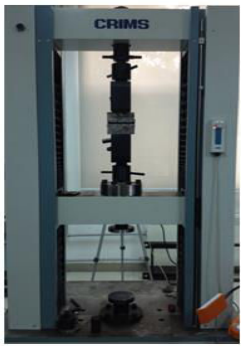

(b) Apparatus

(c) Testing procedure

Fig. 4:5 Planar tension test

4.2.1.4 Dynamic Mechanical Analysing (DMA)

Every material has the tendency to flow which is measured as viscosity, i.e. [178] "everything flows if you wait long enough". Material viscosity property can be observed in many different forms [22] such as: if the stress is held constant, the strain increases with time (creep); if the strain is held constant, the stress decreases with time (relaxation); the effective stiffness depends on the loading rate; if cyclic loading is applied, hysteresis loop occurs, leading to a dissipation of mechanical energy; rebound of an object is less than 100 percent, etc.

The dynamic mechanical analysing (DMA) under frequency sweep mode is used in current research to captures the "flow" characteristics. DMA can be simply described as applying an oscillating force (of forced deformation) with different frequencies to a sample and analysing the relations between the input fore and the response. We can obtain the damping and stiffness information directly from the DMA test and the properties are often explained as the ability to lose energy and the ability to recover from deformation. The normal forced oscillation test is normally conducted at a fixed temperature, fixed dynamic amplitude and constant frequency, however, through the DMA test we can obtain material modulus as a function of frequency by sweeping frequency from 0.01Hz to 100 Hz for example all at once. Compared with the traditional approach, we don't have to restart the

experiment every time when a new frequency is set up. We can also use DMA to rapidly map the modulus as a function of frequency. As we say the modulus is a function of frequency, it actually indicates that the modulus measured in DMA test is the dynamic modulus, which is also known as the complex modulus consisting of an elastic modulus and an imaginary modulus.

As the viscosity behaviour is not sensitive to the deformation mode, only uniaxial tensile test is performed for DMA test. Tensile specimens are cut from the same 2mm ± 0.2mm-thick rubber sheet as uniaxial tension test. The width and the testing length of the specimens are approximately 5mm ± 0.2mm and 20mm ± 0.5mm. Since one sweep procedure at a constant dynamic amplitude value would take hours and certain amount of dry ice for controlling the testing temperature in order to expand the frequency range through time-temperature equivalence principle, only two DMA specimens are prepared and their geometries are carefully measured and recorded before the test. The effect of the temperature will also be discussed further in the coming sections.

4.2.2 Testing procedure and results

4.2.2.1 Uniaxial Tension

In order to achieve a pure extension state, the testing length of the tensile specimen is much longer than its width or thickness. Since the experiment is not intended to fail the specimen, there is no need to use a dumbbell shaped specimen which is commonly used in a strength test. Five specimens are tested to meet the consistency. All the five samples were stretched by a universal testing machine Zwich/Roell Z020 at a room temperature of about 23 degree. After inserting each testing piece into the machine, the end tabs need to be gripped symmetrically so that the tension is distributed uniformly over the cross-section.

All the specimens are initially preconditioned to the maximum strain of 200% at a rate of 50mm/min for three times in order to exclude the Mullins effect. Testing data of the fourth cycle are recorded. Input displacement and the force response are related as shown in Fig. 4:6. A non-contacting video extensometer is used to capturing the deformation of the specimen. Since the clamps create an indeterminate state in the region near the clamps and therefore the deformation must be measured away from the clamp where a pure tension state is occurring.

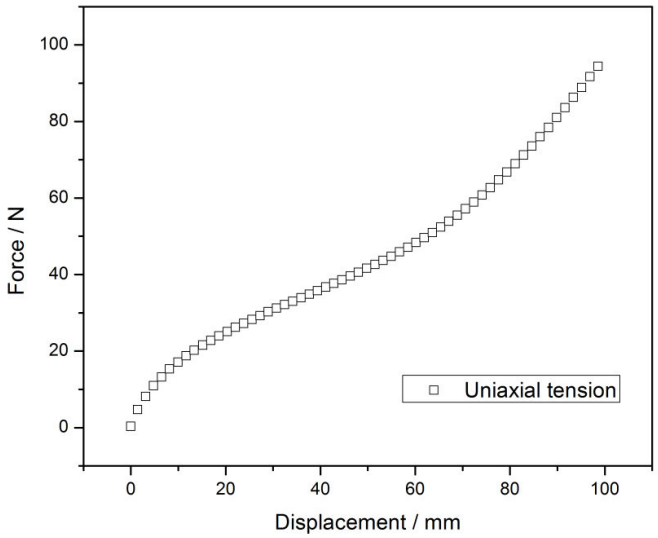

Fig. 4:6 Uniaxial tension test results

4.2.2.2 Uniaxial Compression

In the uniaxial compression test, even very small friction between the cylinder specimen and the rigid blocks may cause substantial shear strain. That may lead to non-uniform and inaccurate testing results. Sometimes this shear strain might even exceed the compression strain. As a consequence, methylsilicone oil was applied to both surface of the specimen and the two polytetrafluoroethylene blocks in order to exclude the friction that may happen. Loading speed of the uniaxial compression test is 5mm/min and the specimens are forced until an engineering strain of 50% is reached. Similarly, the precondition process is repeated for three times and the testing data are recorded starting from the fourth loading process. Testing results are shown in Fig. 4:7. Furthermore, the video extensometer can be seen from Fig. 4:3 (c), and the little silver dots evenly spread on the specimen surfaces are used to be traced by the video. During data analysing procedure, the small dots at the centre of the specimens will be selected and analysed in order to obtain the compressive strain.

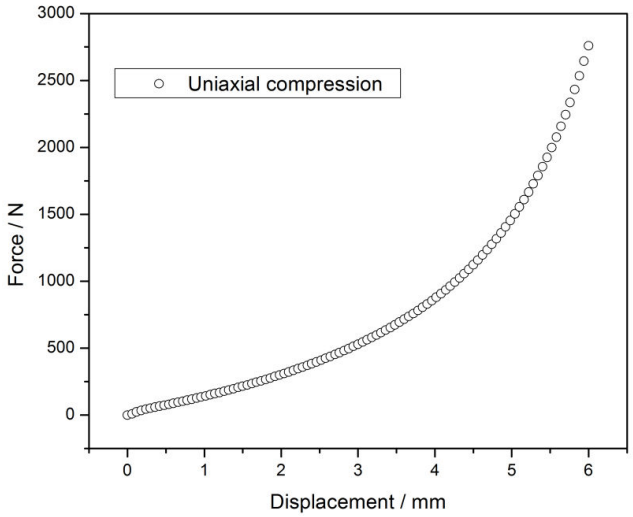

Fig. 4:7 Uniaxial compression test results

4.2.2.3 Planar Tension

The planar tension test doesn't have to be included normally. However, the deformation mode of the rubber component in rail fastening systems is relatively complex with combined extension, compression and shear, so planar tension test is carried out. The most significant aspect of the planar tension specimen is that it is at least ten times shorter in the direction of stretching than the width to create a perfectly constrained state in the lateral direction so that specimen thinning occurs in the thickness direction. As the same, only the centre region of the dots marked on the surfaces are traced for capturing the deformation. Specimens are loaded at a speed of 15mm/min to the maximum strain value of 100%. The measured displacement-force curve is shown in Fig.4:8. However, the unusual decreasing tendency marked in red is due to the rubber specimen slipping from the grips. Indeed, wide grips with sharp edges can fix the test specimens very tight and they can also extend the planar tension strain range [167]. However, they are easy to give unexpected specimen failures during the loading process. As a result, rubber specimens were bonded directly to the grips and the clamping bolts are used only for tightening in the present experiment, which leads to its slipping from grips beyond a certain loading value.

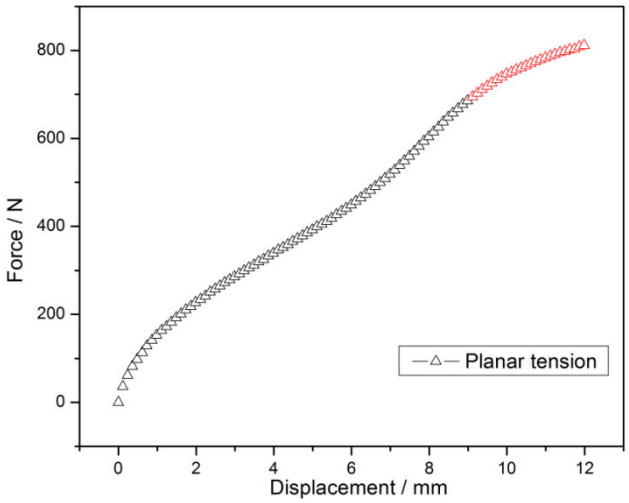

Fig. 4:8 Planar tension test results

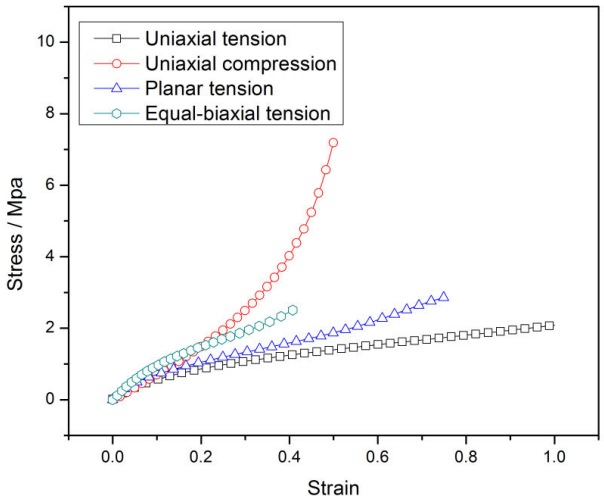

Fig. 4:9 Strain-stress relationships of uniaxial tension test, uniaxial compression test, planar tension test as well as the equal-biaxial tension transformed by using Eq. 4:1

In Fig. 4:9, the final strain-stress relations are obtained, and the equal-biaxial tension test data is also converted by using Equation 4:1 and depicted in the figure. The differences in the strain-stress behaviour are due to the different lateral stress presented in specimens. Firstly, in the uniaxial tensile test the long edge of specimens are unconfined and the specimen can contract laterally when axial stress is applied. This allows high axial strains to be produced. Secondly, by contrast, in the planar tension test, specimens are sufficiently wide and very well constrained along the long edge, and the material at the centre of the specimen is unable to contract laterally. As a consequence, the axial stress required to produce a particular axial strain is considerably larger than that needed in a tensile test. Larger lateral stresses are found in the equivalent equal-biaxial extension test shown in green hexagon in

Fig. 4:9, in which specimens are supposed to be drawn simultaneously in both axial and lateral directions. As a result, the axial stress required to draw the material to a particular axial strain in the equal-biaxial tension test is considerably larger than that required in either the tensile and planar tests.

4.2.2.4 Time-temperature Equivalence

As mentioned above, the major difference between frequency sweep test and traditional dynamic test is that the former can collect frequency-dependent data at a fixed temperature and dynamic amplitude while scanning across the frequency range of interest. However, it should be noted that [179] when a frequency range is being scanned, the testing machine occasionally find conditions where the system begins to resonate. These frequencies are either the natural frequency of the sample-instrument system or one of its harmonics. Under such experiment conditions the desired information of the sample-instrument system may be obscured. But we can solve the problem by redesigning the sample dimensions or geometries to increase or decrease the resonance frequency of the system. However changing specimen dimensions still have a limit and, often, data outside of the available range are required. At this situation, the time-temperature superposition proposed by Ferry [180] as a method of reduced variables based on time-temperature equivalence theory [178] can be used to meet the requirement.

Rubber materials become softer and more fluid as it is heated and they go through transition from glassy state to fluid state, which increases the available space for molecular motions. Over long enough time periods, or small enough frequencies, at a constant temperature, similar changes occur. This relationship is referred to as time-temperature equivalence that can also be often stated as “low temperature is equivalent to short times or high frequency”.

A lot of materials exhibit this special mechanical behaviour, and they are normally classified as the thermo-rheologically simple material (TRS). As shown in Fig. 4:10, if a characteristic curve of the material modulus at temperature T_1 translates along the logarithmic time axis, the modulus curve at temperature T_2 or T_3 can be obtained correspondingly, and we now have

$$E(T,t) = E(T_{ref}, t/\alpha_T) \tag{4:2a}$$

$$E(T,\omega) = E\left(T_{ref}, \omega\alpha_T\right), \tag{4:2b}$$

where E is modulus, T_{ref} is the reference temperature of the main curve, t is a time parameter, ω is a frequency parameter and $log\alpha_T$ is the shift factor at each temperature used to measure the transverse distance for developing a main curve. Normally shift factor $log\,\alpha_T$ in terms of temperature can be described by different types of shift functions, such as the well-known Williams-Landel-Ferry shift (WLF by Williams et, al., 1955) given by

$$log\alpha_T = -\frac{C_1(T-T_{ref})}{C_2} + (T - T_{ref}), \tag{4:2c}$$

where T is the temperature in degrees Kelvin, and $C_1$and $C_2$are material constants. Another well-known shift function named "BKZ-shift" is devoted by Bernstein, Kearsley, and Zapa, 1963.

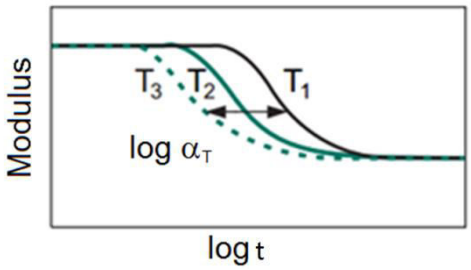

Fig. 4:10 Thermo-rheologically simple behaviour of rubber-like materials

After shifting the frequency sweep curves at each temperature following the fitted shifting factor by using testing data, the resultant master curve can cover a range much wider than that of the original data.

4.2.2.5 Frequency sweep test

In the frequency sweep test of present chapter, the frequency range is from 0.01Hz to 100Hz and temperature is from -30 ℃ to 50 ℃ with a step of 10℃. Specimens were under oscillation under pre-deformation of 0.4% and dynamic amplitude of 0.1%. The tested frequency-dependent storage modulus and loss modulus at each temperature are shown in Fig. 4:11. According to the time-temperature superposition discussed above, all curves shift in a

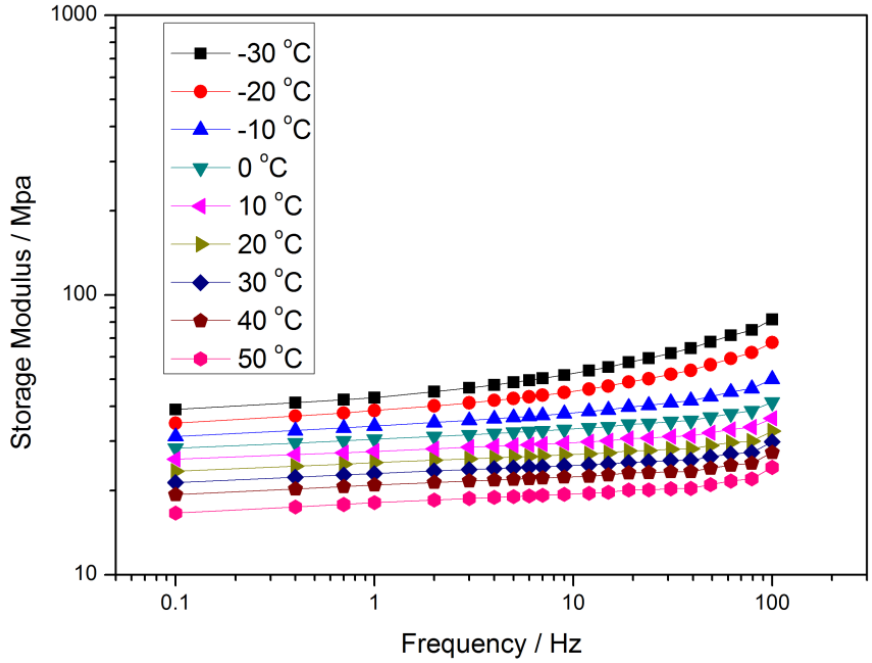

(a) Frequency-dependent storage modulus

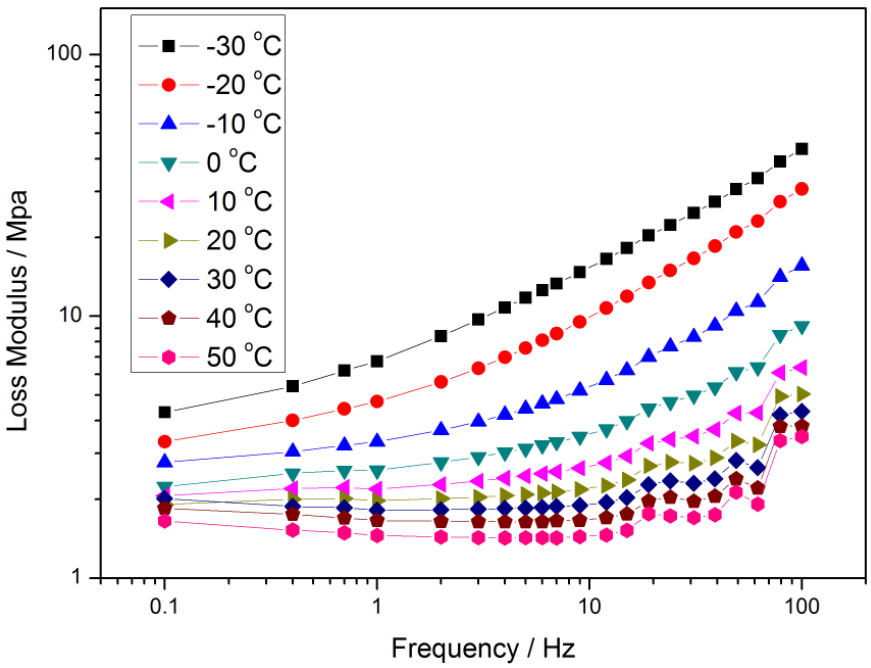

(b) Frequency-dependent loss modulus

Fig. 4:11 Frequency sweep testing results at different temperature

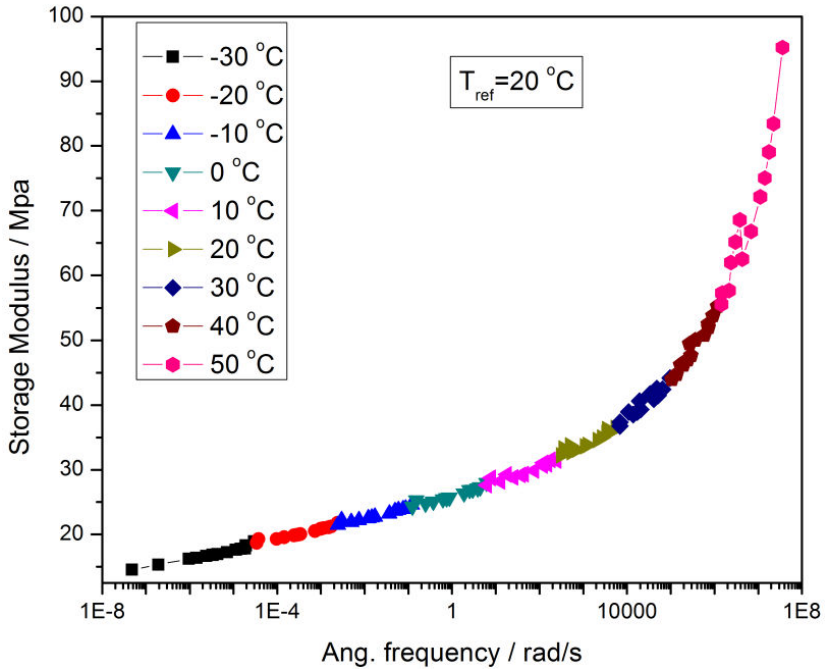

(a) Storage modulus and

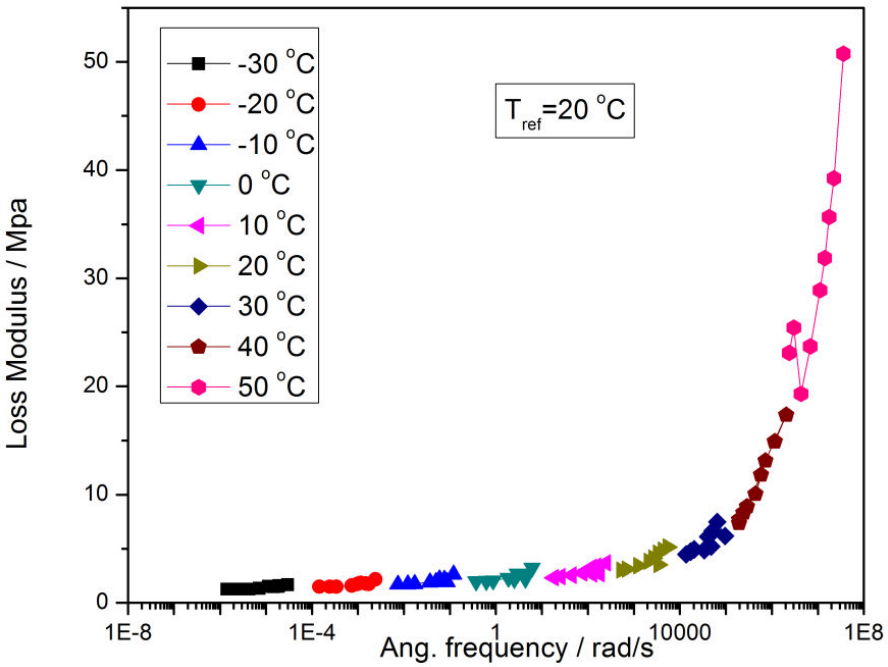

(b) Loss modulus

Fig. 4:12 Main curve at the referent temperature of 20℃

logarithm coordinate except that under the reference temperature, 20℃. Main curve of the storage modulus as shown in Fig. 12(a) and the corresponding shift factor of each temperature are indicated in Fig. 4:13. With the same shift factor, loss factor is also shifted to obtain a main curve at reference temperature 20 ℃ in Fig. 12 (b). The modulus and damping properties under a full influence of frequency are now obtained, and they are going to be used to identify the viscosity of rubber material presented in this study.

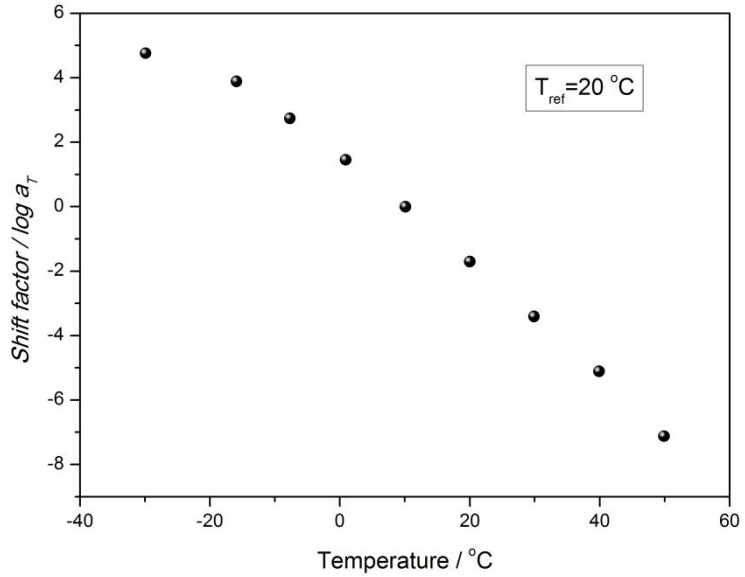

Fig. 4:13 Relationship between shift factor and the corresponding temperature

4.3 Hyperelastic models and simulation

4.3.1 Hyperelastic constitutive models

Hyperelastic models are capable of modelling the rubber-like materials that exhibit nonlinear elastic behaviour. They can give realistic predictions of actual material behaviour at large strains (generally larger than 5%). The hyperplastic constitutive models of rubber material are widely used in finite-strain calculations [181]. All hyperelastic models are based on the assumption of isotropic behaviour so that strain energy potential, W_ε, can be formulated to define strain energy stored in the material per unit of reference volume as a function of the strain. There are a large number of strain energy potentials to model approximately incompressible isotropic elastomers. Some of them are embedded in Abaqus, e.g. Mooney Rivlin (first order polynomial model), higher order or reduced polynomial models, neo Hookean, Yeoh, Arruda Boyce, Van der Waals, Ogden models, etc. The reduced

polynomial and Mooney Rivlin models are viewed as particular cases of the polynomial model; the Yeoh and neo Hookean potentials, in turn, are viewed as special cases of the reduced polynomial model. Therefore, they are collectively referred to as polynomial models. In general, the strain energy potential forms are written as separable functions of a deviatoric component and a volumetric component, and the so-called hyperelastic models herein only describe the deviatoric part of the strain energy function and the volumetric property is assessed by a Poisson's ratio.

As mentioned above, hyperelastic models are based on the definition of strain energy function, W_ε. For an isotropic and incompressible material W_ε can be expressed either in terms of the strain invariants I_i which are functions of the stretch ratios or directly in terms of the stretch ratios themselves λ_i, i.e.

$$W = W(I_1, I_2, I_3) \text{ or } W = W(\lambda_1, \lambda_2, \lambda_3), \tag{4:3}$$

$$I_1 = {\lambda_1}^2 + {\lambda_2}^2 + {\lambda_3}^2,$$

$$I_2 = {\lambda_1}^2{\lambda_2}^2 + {\lambda_2}^2{\lambda_3}^2 + {\lambda_3}^2{\lambda_1}^2,$$

$$I_3 = {\lambda_1}^2{\lambda_2}^2{\lambda_3}^2. \tag{4:4}$$

where the stretch ratio λ_i is defined as the deformed gauge length L divided by the initial gauge length L_0, namely, $\lambda = L/L_0 = 1 + (L - L_0)/L_0 = 1 + \varepsilon$, where ε is the nominal engineering strain. In addition, for an incompressible (or nearly incompressible) material $I_3 = {\lambda_1}^2{\lambda_2}^2{\lambda_3}^2 = 1$, *i.e.* $\lambda_3 = (\lambda_1\,\lambda_2)^{-1}$.

The principal Cauchy stresses are given by

$$\sigma_i = \lambda_i \frac{\partial W}{\partial \lambda_i}, \tag{4:5}$$

where only the deviatoric part of stress is shown. For impressible materials, eliminate λ_3 from Equations 4:4 and $\lambda_3 = (\lambda_1\,\lambda_2)^{-1}$ *s*o that W becomes a function of λ_1 and λ_2 only, $W = W(\lambda_1, \lambda_2)$.

Introducing Equation 4:5, it derives from Equation 4:4 that

$$\sigma_1 - \sigma_3 = \lambda_1 \frac{\partial W}{\partial \lambda_1}\,, \sigma_2 - \sigma_3 = \lambda_2 \frac{\partial W}{\partial \lambda_2}. \tag{4:6}$$

In uniaxial tension (and uniaxial compression) test, $\lambda_2 = \lambda_3$ and we have

$$\lambda_1 = \lambda;\ \lambda_2 = \ \lambda_3 = \lambda^{-1/2}. \tag{4:7}$$

Correspondingly, we can define a strain energy function depending only on the one remaining independent stretch λ in the loading direction. In this case $\sigma_2 = \sigma_3 = 0$ and the Cauchy stress associated with λ is

$$\sigma = \ \lambda \frac{\partial W}{\partial \lambda}. \tag{4:8}$$

For the equivalent equal-biaxial extension where $\sigma_3 = 0$ and $\lambda_1 = \lambda_2 = \lambda,\ \lambda_3 = \lambda^{-2}$ where λ is in the loading direction, Equation 4:6 reduces to

$$\sigma_1 = \sigma_2 = \lambda \frac{\partial W}{\partial \lambda}\,. \tag{4:9}$$

In the case of planar tension, $\lambda_1 = \lambda,\ \lambda_2 = 1, \lambda_3 = \lambda^{-1}$ and λ_2 occurs in the thinning direction and $\lambda_1 = \lambda$ in the loading direction, so we have the similar Cauchy stress.

The Ogden model is the type of strain energy potential with principle stretch ratio with the independent variable, which can be represented as follows

$$W = \sum_{i=1}^{N} \frac{2\mu_i}{{\alpha^2}_i} ({\lambda_1}^{\alpha_i} + {\lambda_2}^{\alpha_i} + {\lambda_3}^{\alpha_i} - 3). \tag{4:10}$$

where μ_i and α_i are the material parameters. The initial shear modulus G_0 is given by $G_0 = \sum_{i=1}^{N} \mu_i$.

As mentioned above, strain energy potential can also be defined in terms of three strain invariants I_i that are in their turn functions of principal stretches. The Mooney-Rivlin model (the first order polynomial model) is represented by the equation

$$W = C_{10}(I_1 - 3) + C_{01}(I_2 - 3), \tag{4:11}$$

where C_{10} and C_{01} are material parameters. Extending Equation 4:11 to the second order terms we have

$$W = C_{10}(I_1 - 3) + C_{01}(I_2 - 3) + C_{20}(I_1 - 3)^2 + C_{11}(I_1 - 3)(I_2 - 3) + C_{02}(I_2 - 3)^2, \tag{4:12}$$

where C_{10}, C_{01}, C_{20}, C_{11} and C_{02} are material parameters. The second order polynomial model introduces the dependence of strain energy potential on three more material parameters and is often useful to describe stress response at large stretch. Higher order polynomial model can be obtained by adding more terms to Equation 4:11 but usually they do not produce appreciable improvement. Material parameters are often determined by using the measured data, which are related to the initial shear modulus G_0 by $2\sum_{i,j} C_{ij} = G_0$.

The form of the reduced polynomial strain energy potential is

$$W = \sum_{i=1}^{N} C_{i0}(I_1 - 3)^i, \tag{4:13}$$

where N is the order, C_{i0} are material parameters. The initial shear modulus G_0 is given by $G_0 = 2C_{10}$. Thereupon, Neo-Hookean form (the first order reduced polynomial model) and Yeoh form (the third order reduced polynomial model) can be respectively represented as

$$W = C_{10}(I_1 - 3), \tag{4:14}$$

and

$$W = C_{10}(I_1 - 3) + C_{20}(I_1 - 3)^2 + C_{30}(I_1 - 3)^3. \tag{4:15}$$

In addition to all the above phenomenological models, micro-mechanically based hyperelastic models are also discussed by a lot of references. Arruda-Boyce is one of the micro-mechanical models that reads

$$W = \mu\left[\frac{1}{2}(I_1 - 3) + \frac{1}{20\lambda_m{}^2}\left(I_1{}^2 - 9\right) + \frac{11}{1050\lambda_m{}^4}\left(I_1{}^3 - 27\right) + \frac{19}{7000\lambda_m{}^6}\left(I_1{}^4 - 81\right) + \frac{519}{673750\lambda_m{}^8}\left(I_1{}^5 - 243\right)\right], \quad (4:16)$$

where μ and λ_m are the material parameters. The initial shear modulus G_0 is related by $G_0 = \mu(1 + \frac{3}{5\lambda_m{}^2} + \frac{99}{175\lambda_m{}^4} + \frac{513}{875\lambda_m{}^6} + \frac{42039}{673750\lambda_m{}^8})$.

In addition, the form of the Van der Waals strain energy potential is

$$W = \mu\left\{-\left(\lambda_m{}^2 - 3\right)[\ln(1-\eta) + \eta] - \frac{2}{3}a\left(\frac{I-3}{2}\right)^{\frac{3}{2}}\right\}, \quad (4:17a)$$

where

$$I = (1-\beta)I_1 + \beta I_2 \text{ and } \eta = \sqrt{\frac{I-3}{\lambda_m{}^2 - 3}}. \quad (4:17b)$$

Here, μ is the initial shear modulus, i.e. $G_0 = \mu$; λ_m is the locking stretch; a is the global interaction parameter; β is an invariant mixture parameter.

4.3.2 Simulation results and discussion

In order to fit the hyperelastic constitutive models the uniaxial tension, uniaxial compression as well as planar tension tests are all performed at a very low speed. Strain rate is about 0.6% per second. Abaqus allows users to input one of, two of, or three of the uniaxial tension, equal-biaxial extension and planar tension tests to evaluate the parameters, and the root mean square errors (RMS) between measured and calculated data by using each model can be obtained. RMS values of all the fitted models are summarized in Table 4:1. A comparison of the fitting result by inputting only uniaxial tension test data (Test 1), both uniaxial tension and the equivalent equal-biaxial extension data (Test 1 and 2), and all the three test data (Test 1, 2 and 3), are also shown in Fig. 4:14. It's clear can be seen that the parameter estimated results by using only uniaxial tension test data gives a more accurate fitting result for uniaxial tension testing result (see Fig. 4:14 (a)), but it does a poor job for the other two tests. Models with the parameters from such fitting procedure are not suitable for complex deformation mode. Taking the Ogden model of the third order for example: when

only the uniaxial test data are used to define the material, it gives a very good result with a RMS value of only 0.008 for uniaxial tension test Fig. 4:14 (a), however when the parameters are used to predict the equal-biaxial extension and planar tension measured data it gives a unacceptable solution with a RMS error of up to 1.891E6 and 3.644E4 respectively as shown in Fig. 4:14 (b) and Fig. 4:14 (c). And the mean RMS value considering all the three tests is up to 6.425E5 as shown in Fig. 4:14 (d). Oppositely, we can also see from Table 4:1 and Fig. 4:14 that, when data from multiple experimental tests are used nearly all the hyperelastic models are more accurate in fitting the experimental results and it keep the mean RMS error below 0.295.

Test data used for simulation	RMS of each test and the mean value of all	MOONEY RIVLIN	POLY N2	NEO HOOKE	YEOH	ARRUDA BOYCE	VAN DER WAALS	OGDEN N1	OGDEN N3
Test 1	Test 1	0.055	0.005	0.170	0.075	0.170	0.049	0.042	0.008
	Test 2	0.963	29.747	0.491	0.552	0.491	0.555	3.603	1.89E6
	Test 3	0.276	8.425	0.334	0.442	0.334	0.436	1.172	3.64E4
	General	0.431	12.73	0.332	0.356	0.332	0.347	1.605	6.45E5
Test 1 & 2	Test 1	0.084	0.038	0.257	0.113	0.257	0.036	0.070	0.048
	Test 2	0.111	0.028	0.406	0.468	0.406	0.018	0.097	0.138
	Test 3	0.176	0.693	0.239	0.359	0.239	0.234	0.202	0.246
	General 4	0.124	0.253	0.301	0.313	0.301	0.096	0.123	0.144
Test 1 & 2 & 3	Test 1	0.095	0.075	0.322	0.157	0.322	0.050	0.073	0.051
	Test 2	0.147	0.108	0.352	0.420	0.352	0.082	0.110	0.124
	Test 3	0.147	0.124	0.184	0.308	0.184	0.196	0.196	0.218
	General 4	0.130	0.102	0.286	0.295	0.286	0.109	0.126	0.131

Test 1: Uniaxial tension test; Test 2: Equal-biaxial extension test; Test 3: Planar tension test

Table 4:1 The RMS values for all the fitted models

Among the models listed in Table 4:1 the second order polynomial model, the Van der Waals model and the first order Ogden model give the most accurate result by using the multiple test data, who gives a mean RMS value of 0.102, 0.109 and 0.126 respectively. The initial shear modulus corresponding to each model was calculated, and the evaluated parameters are reported in Table 4:2. Fitting results compared to the measurement are shown in Fig. 4:15. Though the three models have the similar fitting results with close RMS error, the Van der Waals model not only can meet the tested curve well but also can predict the upward tendency at the end of each curve. Therefore, Van der Waals model is selected to be used for describing the hyperelasticity of the present material eventually.

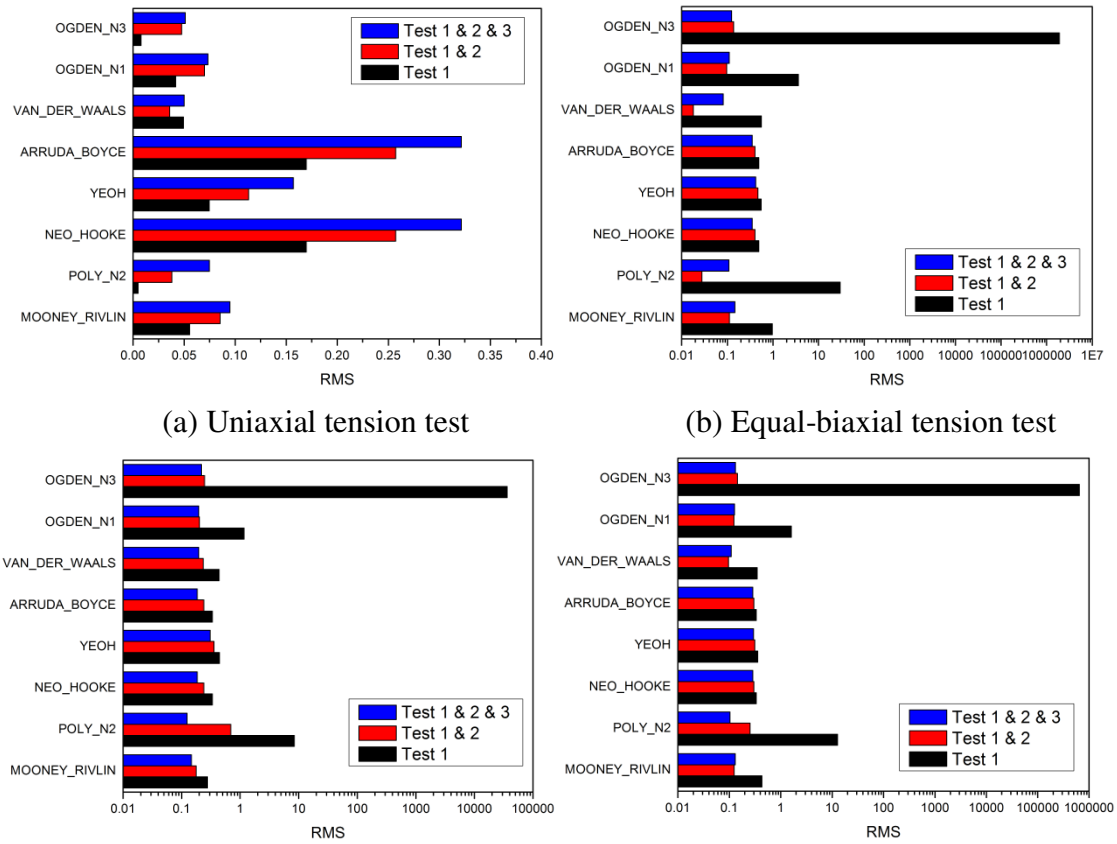

(a) Uniaxial tension test (b) Equal-biaxial tension test

(c) Planar tension test (d) The RMS value considering all three tests

Fig. 4:14 Fitting results of the quasi-static testing data

Model	Parameters						Equal initial shear modulus (Mpa)
Poly_N2	C_{10}	C_{01}	C_{11}	C_{20}	C_{02}	ν	G_0
	0.472	**0.354**	**0.229**	**-0.113**	**-0.119**	**0.495**	**1.646**
Van der Waals	*mu*	*lambda*	*A*	*Beta*	*ν*		G_0
	2.255	3.158	1.353	0.413	0.495		2.255
Ogden_N1	*mu*		*lambda*		*ν*		G_0
	1.797		0.283		0.495		1.797

Table 4:2 Evaluated hyperelastic model parameters

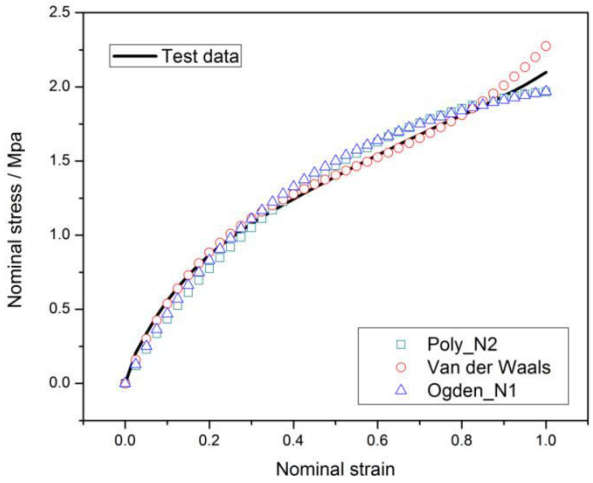

(a) Uniaxial tension

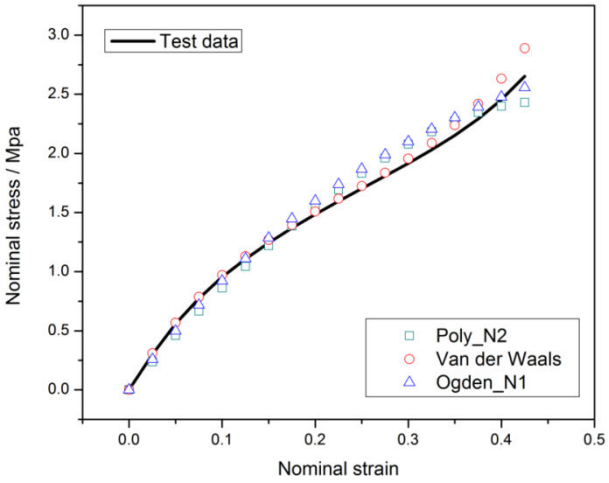

(b) Equivalent equal-biaxial tension

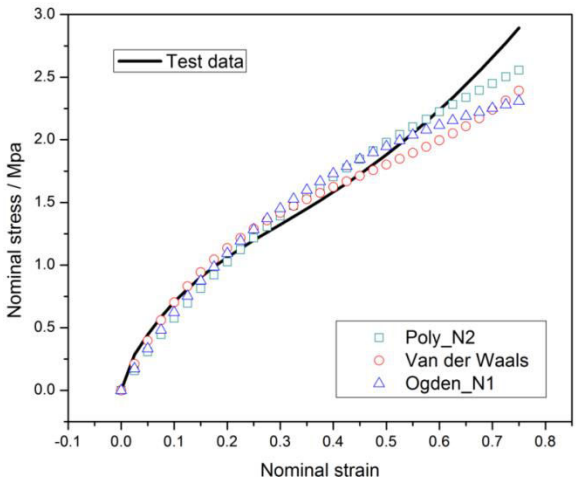

(c) Planar tension data

Fig. 4:15 The measured strain-stress curves compared with the fitting results by using three selected models

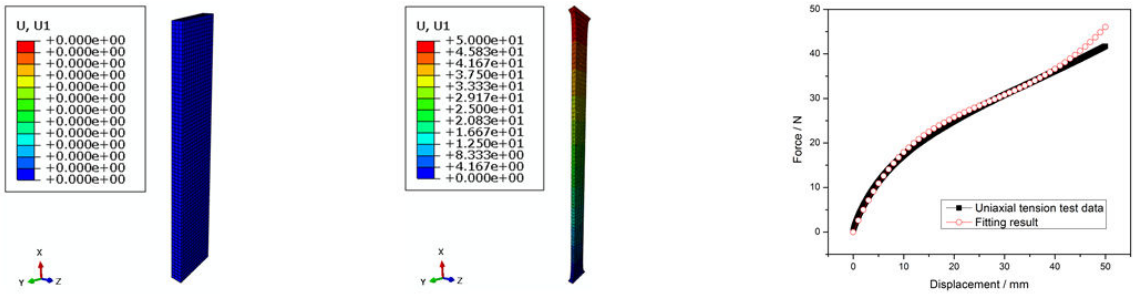

(a) Uniaxial tension test

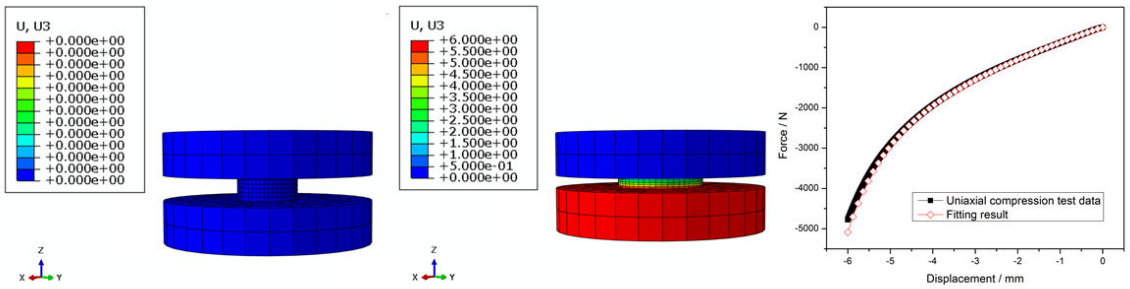

(b) Uniaxial compression test

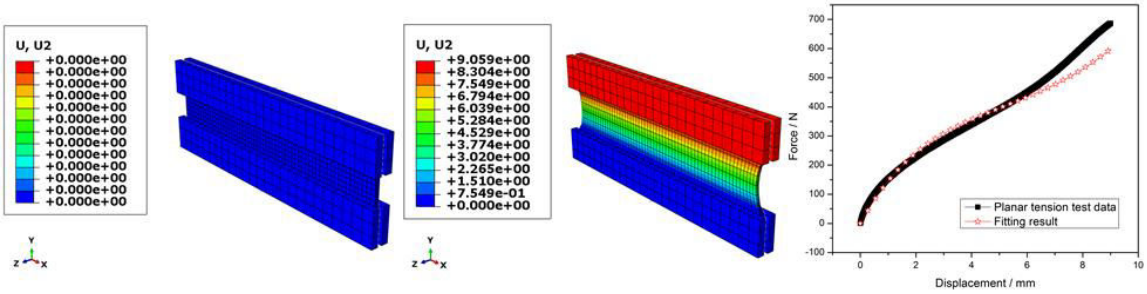

(c) Planar tension test

Fig. 4:16 Simulation procedure and results

The evaluated Van der Waals model is now applied to simulate the material fundamental test. As can be seen from Fig. 4:16, all the rubber component were modelled using C3D8R element, and the two PTFE blocks in uniaxial compression test as well as the four grips in planar tension test were modelled by R3D4 due to their relatively high rigidity. Input signals and loading speed are applied according to the real testing procedure. Both the original state and the deformed condition of the specimens are shown in the figure; the predicting results compared with the experimental data are also plotted. In all the three displacement-force curves, simulation results give a reasonable description and the good agreement confirms the accuracy of the model and the parameters.

It should be noted that a frictional coefficient of 1e-10 was applied to the surfaces between PTFE blocks and the rubber specimen during uniaxial compression test simulation. Good agreement between measurement and prediction indicates that the frictional effect is almost eliminated in the real testing procedure. In order to clearly reveal this friction behaviour, different frictional coefficients were used to reproduce the compression procedure. The deformation mode for the coefficient va1e 1-10 and 5e-1 are respectively shown in Fig. 4:17 (a) and (b); the compared displacement-force curves of several conditions are plotted in Fig. 4:17 (c). A large frictional coefficient gives rise to an obvious bulge (Fig. 4:17 (b)); it also leads to uneven compression with high shear strain value. Sometime the accompanying shear strain is even larger than the compressive strain. Inflated rubber component brings a nonlinear effect on the displacement-force relationship as shown in Fig. 17 (c) especially when the coefficient is larger than 0.1. We should pay special attention to that even with a very small frictional coefficient (1e-10), the nonlinear features still shows especially compared with other deformation mode. That's to say the nonlinearity is not only from the frictional behaviour but also from other factors. This nonlinearity will be analysed in the next chapter.

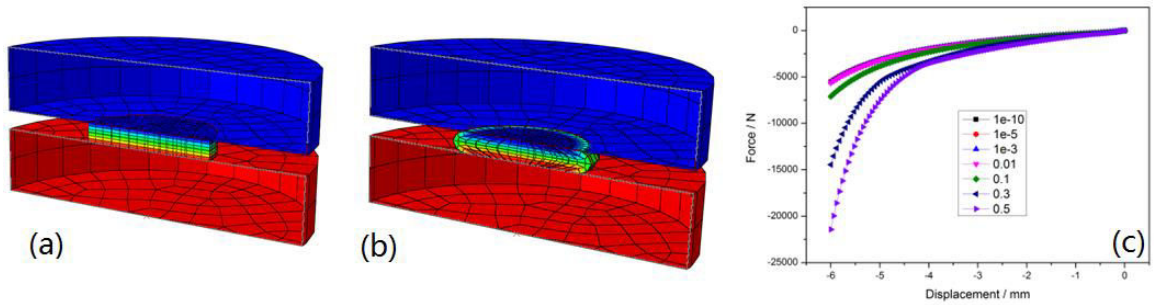

Fig. 4:17 Predicting results influenced by the frictional coefficient (a) Coefficient equals 1e-10 (b) Coefficient equals 0.5 (c) Simulation results

4.4 Viscoelastic model simulation and analysing

4.4.1 Prony series

On the basis of linear viscoelastic theory, Prony series is often used to describe a stress relaxation testing data of rubber material. The initial stress is due to the elastic response of the material deformation while the stress relaxes over time due to the flow effects of the material. Normally, the Prony series for a shear relaxation test can be written as

$$E(t) = E_\infty + \sum_{i=1}^{N} E_i \exp(-t/\tau_i) \tag{4:18a}$$

where E_∞ is the long term modulus once the material is totally relaxed, τ_i are the relaxation times. The higher the values of τ_i are, the longer it takes for the stress to relax. Experimental data are used to fit the model parameters E_∞, E_i and τ_i. An alternative form of Equation 4:18a is

$$E(t) = E_0 - \sum_{i=1}^{N} E_i [1 - exp\left(-\frac{t}{\tau_i}\right)], \tag{4:18b}$$

where

$$E(t=0) = E_0 = E_\infty + \sum_{i=1}^{N} E_i. \tag{4:19}$$

This form of Prony series is convenient when the elastic shear modulus E_0 is obtained from the data independent from the relaxation data. The normalized shear stress relaxation modulus is often represented in terms

$$e(t) = 1 - \sum_{i=1}^{N} e_i [1 - exp\left(-\frac{t}{\tau_i}\right)], \tag{4:20}$$

where $e(t) = E(t)/E_0$ and $e_i = E_i/E_0$ and E_0, e_i, τ_i are material parameters.

The DMA test results are a set of frequency influenced storage modulus $E'(\omega)$ and loss modulus $E''(\omega)$. Prony series therefore can be determined from the following implicit equations

$$E'(\omega) = E_0[1 - \sum_{i=1}^{N} e_i] + E_0 \sum_{i=1}^{N} \frac{e_i {\tau_i}^2 \omega^2}{1 + {\tau_i}^2 \omega^2}, \tag{4:21a}$$

$$E''(\omega) = E_0 \sum_{i=1}^{N} \frac{e_i \tau_i \omega}{1 + {\tau_i}^2 \omega^2}. \tag{4:21b}$$

In this case we are interested in the reverse relationship, that is, as storage modulus $E'(\omega)$ and loss modulus $E''(\omega)$ are obtained from the experiment how we can determine the material parameters. Supposing $N = 3$ the storage modulus or the loss modulus can now be calculated by using Equation 4:21. In order to make the residual between the calculated dynamic data and the experimental data below a limit, the values of (E_0 e_i τ_i) are optimized through iterative analysis. Eventually, the evaluated parameters are depicted in Table 4.3 and the good

agreement between the fitting curve and the measured curve as shown in Fig. 4:18 confirm the accuracy of the parameters. In order to make it clear, only a section of the frequency testing data is displayed in the figure.

i	e_i	τ_i
1	9.49e-2	0.0118
2	1.02e-1	0.2912
3	9.01e-2	12.2656

Table 4:3 Evaluated Prony series ($E_0 = 31.75$)

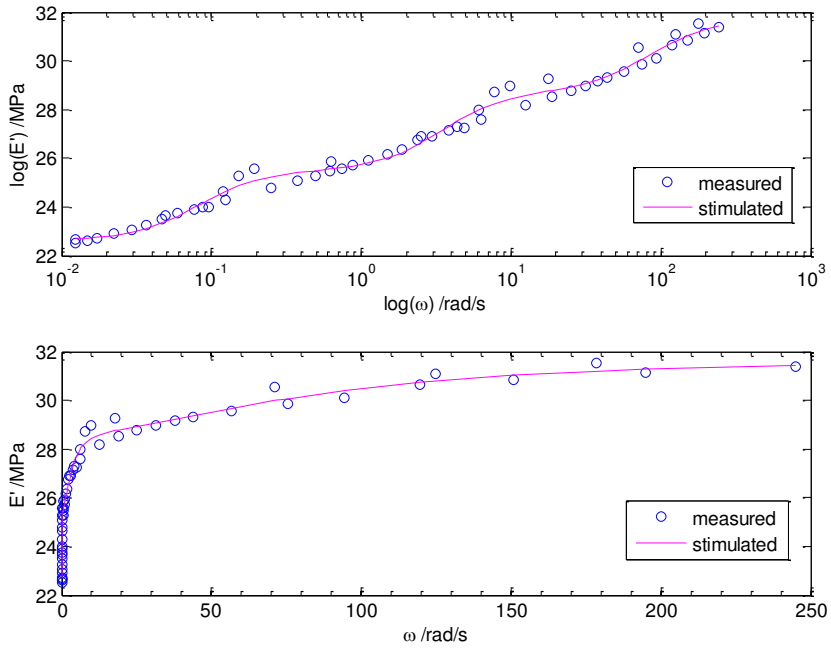

Fig. 4:18 Compared frequency dependent storage modulus by using Prony series and the measurement in both (a) log axis and (b) linear axis

4.4.2 Bergstrom-Boyce model

Though Prony series is good at representing the frequency dependent modulus, it does a poor job in fitting a hysteresis loop. As a result, another viscoelastic model named Bergstrom-Boyce model is included in current research. The Rheological representation of BB model is shown in Fig. 4:19. It is used to describe strain-rate dependence of elastomers by decomposing the mechanical response into that of an equilibrium network (A) corresponding to the state that is approached in long-time stress relaxation tests and that of a time-dependent network (B) that captures the rate-dependent deviation from the equilibrium state. The total

stress is assumed to be the sum of the stresses in these two networks. BB model is established completely by:

- a hyperelastic material model (Van der Waals for present research) to characterize the elastic response of network A;
- a stress scaling factor, S, that defines the ratio of the stress carried by network B to the stress carried by network A under instantaneous loading; i.e., identical elastic stretching in both networks;
- a positive exponent, m, generally greater than 1, characterizing the effective stress dependence of the effective creep strain rate in network B;
- an exponent, C, restricted to lie in [-1, 0], characterizing the creep strain dependence of the effective creep strain rate in network B;
- a nonnegative constant, A, in the expression for the effective creep strain rate – this constant also maintains dimensional consistency in the equation;
- a constant, E, in the expression for the effective creep strain rate. The effective creep strain rate in network B is given by the expression

$$\dot{\varepsilon_B} = A[\lambda_B - 1 + E]^c {\sigma_B}^m . \tag{4:22}$$

where $\dot{\varepsilon_B}$ is the effective creep strain rate in network B, $\lambda_B - 1$ is the nominal creep strain in network B, and σ_B is the effective stress in network B, and S, A, C, m are material parameters.

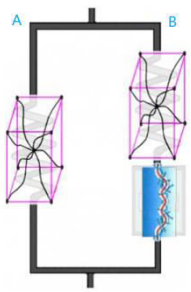

Fig. 4:19 Rheological representation of Bergstrom-Boyce model [182]

Since the evaluated Prony series is proved to be able to fit the frequency dependent properties, a set of virtual fundamental experiment at a higher loading speed is carried out in

Abaqus in order to include in the flow effect of rubber material. Subsequently, BB model embedded in Abaqus is used to fit the virtually measured loading curves. The BB model parameters are listed in Table 4:4 and the family of virtual experiment curves are shown in Fig. 4:20, where the simulation results (read solid circle) have a good agreement with the virtual experiment data (black solid squares).

BB model parameters	***S***	***A***	***m***	***C***
Evaluations	1.6	0.7312	3.5	-1

Table 4:4 Evaluated BB model parameters

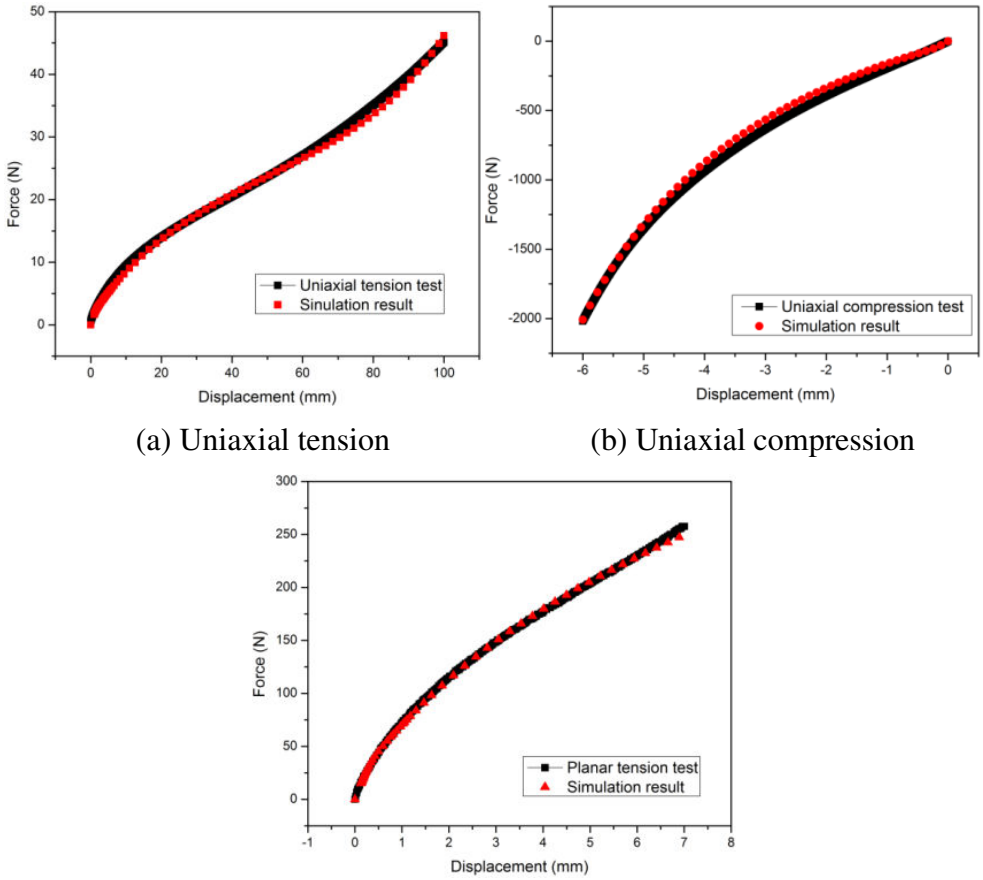

(a) Uniaxial tension (b) Uniaxial compression

(c) Planar tension

Fig. 4:20 Simulation results by using BB model in comparison with the virtual measured data

4.5 Summary

In the present chapter, a set of fundamental material tests including the uniaxial tension, uniaxial compression, planar tension and the DMA tests were performed. The first

three were used to describe the nonlinear elasticity of rubber material at large strain, i.e. hyperelasticity. This property is rate in-dependent, as a result the experiments are carried out at a very slow loading speed. Most of the typical hyperelastic models existing in Abaqus were fitted by using the measured data. They are compared with each other and Van der Waals model is finally selected due to its best fitting results. As for the viscoelastic property, DMA test results can be fitted by both Prony series and Bergstrom-Boyce model existing in Abaqus. Though a three order Prony series can meet the frequency dependent stiffness quite well, it is widely accepted that the Prony series is poor at predicting the hysteresis loop when a rubber component is subjected to a cyclic loading. The Bergstrom-Boyce model is therefore selected for depicting the hysteresis property of rubber material.

Chapter 5 Finite element modelling and experiment-simulation comparison

In this Chapter, the evaluated hyperelastic and hysteresis models obtained in Chapter 4 will be used to simulate the quasi-static and dynamic experiments of the two rail fastening specimens by using Abaqus. Simulation results will be compared with the experiment data. After that, all the observed nonlinear features including the boundary nonlinearity, geometric nonlinearity as well as material nonlinearity will be studied. During the analysis, a set of quasi-static experiments is complemented in order to confirm the boundary nonlinearity.

5.1 Introduction

Normally, to determine the quasi-static vertical stiffness of a rail fastening system, specimen should be loaded by a vertical force of 80±1kN with a loading speed 50±5kN/min as shown in Fig. 5:1 according to authoritative references [183]. Repeat the loading-unloading cycles five times to exclude the Mullins effect of rubber material and during the sixth cycle the testing results are recorded. Finally, the vertical secant stiffness is determined as the slope factor of the load interval between 5kN and 80kN and the corresponding displacement.

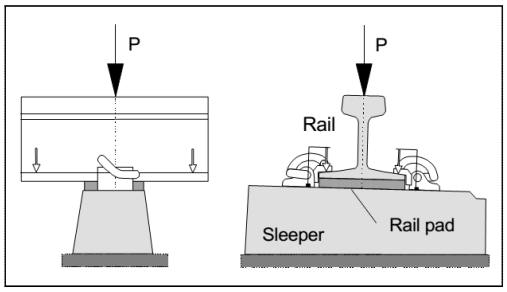

Fig. 5:1 General view of vertical stiffness measurement [183]

During the quasi-static experiment in current research, clips were not assembled onto to specimens, but the applied vertical force was extended to include the clamping force, approximately 10kN for each clip. According to the test result, if secant vertical stiffness of the compressed type fastening (specimen I) is determined by using loading force between 5kN and 100kN and their corresponding vertical displacement interval, the calculated

stiffness is approaching to 50kN/mm which is much larger than then then stated stiffness given by manufacturer. Similarly, when the loading interval between 5kN and 100kN is used for determining vertical stiffness of specimen II the calculated vertical stiffness is two times larger than the stated stiffness value. It indicates that the suggestive load interval for calculating vertical stiffness of rail fastening systems is not adaptive for all situations and products. The nonlinear properties shown in quasi-static working curves due to several reasons, may give rise to a wrong evaluation of their resilient characteristics. Hence, nonlinearities of rail fastening systems should be well analysed so as to accurately define the vertical stiffness value in a reasonable loading/deformation range.

It also should be noted that in order to accurately define a vertical stiffness, a reasonable maximum loading value is very important value. The bearing force on the rail nodes can give a suggestive value. Even for the same railway line, the same axel load of the rail car, the maximum bearing force on the railway nodes may be different. As depicted in Fig. 5:2, lower vertical stiffness of a rail fastening system takes more rail nodes participating into the rail deformation; while larger stiffness of a rail fastening system makes less rail nodes share the axel load. Accordingly, it is very important to evaluate the bearing force according to the given axel load before determining an appropriate loading interval for calculating the stiffness value.

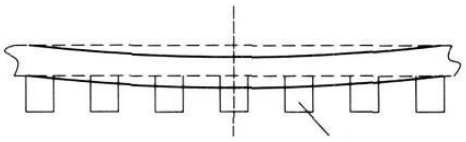

(a) Smaller fastening stiffness

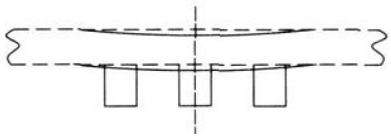

(b) Larger fastening stiffness

Fig. 5:2 Different mode of rail nodes participating in deformation

In fact, the loading interval for determining static stiffness of rail fastening systems has already been drawn attention by manufacturers. As the Table 5:1 listed, different fastening systems have different evaluation range. Generally speaking, the larger the stated stiffness is the wider the loading range is used; while only for Pandrol VIPA-SP, 5kN-80kN is

used in accordance with the standards. It can be seen that accurately giving a loading interval is very important for defining the vertical stiffness, especially for the products are designed with nonlinear properties or inevitable with a few nonlinear features. Adequate study on the nonlinearity of quasi-static displacement-force relations is also directly related to product designing and optimizing. Some of the nonlinear properties should be avoided during optimization while some others can be taken full advantages.

Type of rail fastening systems (Manufacture)	Stated vertical stiffness (kN/mm)	Load interval (kN)
SFC (Pandrol)	40	1-51
DFF MC (VOSSLOH)	30	18-51.2
VIPA-SP (Pandrol)	20	5-80
VANGUARD (Pandrol)	5	5-30

Table 5:1 Stated stiffness and the corresponding loading intervals

5.2 Boundary nonlinearity

As is known, assumptions for the linear viscoelasticity and linear elasticity involve such measures as small strain, small displacements/rotation, small changes in temperature, and so on [184]. Linear approximations are often used because it takes smaller computational cost and the solutions can be superposed on each other. However, in the common practice linear analysis is not always adequate; nonlinear analysis for largely deformed component, for example, is often necessary.

Though all engineering projects are inherently nonlinear to a certain extent, doing a nonlinear analysis or a simple linearization depends on the analysing objective and the acceptable amounts of difference between them [185]. Such a cost-benefit analysis is usually necessary before embarking on a nonlinear problem. In current research, in order to well understand on the mechanical behaviour of the two present fastening specimens, to make them optimized on the basis of full understanding, nonlinear analysis shown in the two measured working curves are going to be studied. Generally speaking, nonlinear properties of rubber components include boundary nonlinearities, geometric nonlinearities, and material nonlinearities. The boundary nonlinearity is also specified as contact nonlinearity sometimes.

5.2.1 Supplementary test

5.2.1.1 The compressed type specimen

The obvious nonlinearity at the very beginning of the loading curve for the compressed type fastening system (specimen I) marked with a circle in Fig. 5:3 (a) is believed to be due to nonlinear contact, which is also putted as boundary nonlinearity in a few references. When the softening segment of the loading line is excluded, the secant stiffness of specimen I is 135% larger than its stated vertical stiffness. Therefore, it's meaningful to carry out research on this boundary nonlinearity.

We can see from Fig. 2:2 that the rubber component of specimen I is directly vulcanized to a top plate inside and a bottom plate outside on the two sides; its bottom surface is a free surface which is supposed to be in the same level as the bottom surface of the iron framework. However, all rubber component show shrink phenomenon to some extent after chemical processing [186]. The amount of shrinkage depends on different factors, such as the material compound and the mixing method. Supposing that the free under-surface of the rubber boot shrinks inward approximately 0.7mm, it would give rise to a discrepancy between the bottom surface of the rubber component and that of the iron bottom plate. This discrepancy gives rise to the contact nonlinearity as shown in Fig. 5:3(a).

The assumption was verified by a set of supplementary test shown in Fig. 5:4 (b), compared with the original experiments in Fig. 5:4 (a). A piece of steel plate is laid on the shaking table and below the fastening specimen. The dimension of the steel plate is smaller than the free under-surface of the rubber boot. Thus, discrepancy on the surrounded edge of rubber boot does not influence on the displacement-force relations. It is found the nonlinearity is no longer in existence in the supplementary testing result, referring to Fig. 5:3 (b). Since the steel plate changes the system stiffness significantly and detailed numerical relationship makes no sense in compared with the working curve in Fig. 5:3 (a), they are not specified.

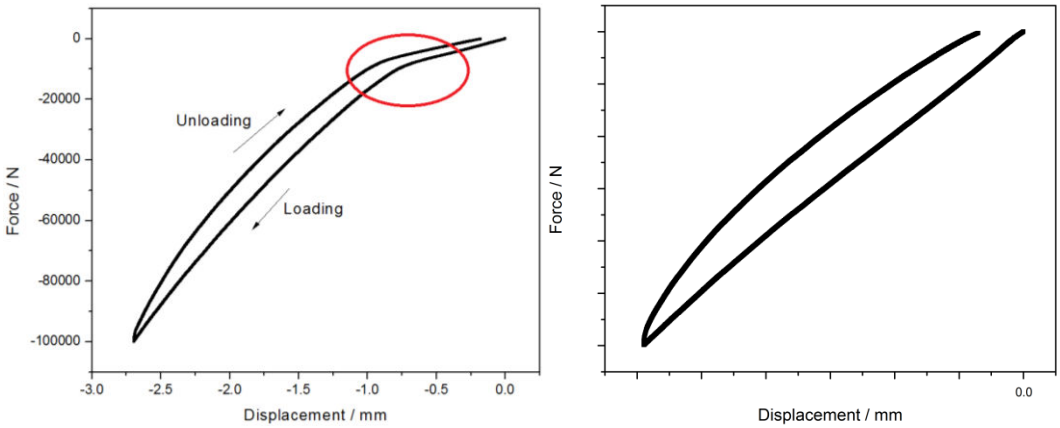

(a) Quasi-static test (b) Supplementary test

Fig. 5:3 Testing result of the compressed type fastening system

(a) Quasi-static test (b) Supplementary test

Fig. 5:4 Test scheme of the compressed type fastening system

5.2.1.2 The shear type specimen

Another distinct nonlinear feature can be observed in the working curve of the shear type fastening system (specimen II), which is also believed to be boundary nonlinearity, see Fig. 5:5 (a). It appears when the displacement of the shaking table is larger than about 6mm. As the displacement is smaller than 6mm, quasi-static load is input from 0kN to 60kN; after that, however, another 60kN leads to only 1mm. That is, the boundary nonlinearity gives rise to an increased vertical stiffness by 600%.

The substructure of specimen II is shown in Fig. 5:5(b), where the rubber elliptical ring (the black component) is bonded with top plate inside and bottom plate outside. An elevation difference is in existence between the undersurface of rubber component and with the bottom plate, which is more conscious in the longitudinal profile diagram (Fig. 2:3). As displacement increases, the bottom surface of the rubber component bulges downwards. Gradually, this free surface starts to reach the shaking table. As the displacement increase furthermore, area of the free surface decreases while the contacting area between rubber

component and the shaking table keeps increasing. The contact and the following compression process of the rubber elliptical ring results in a very steep increasement of vertical stiffness.

In order to verify this assumption, supplementary test was also carried out for specimen II. A thin file of oil was applied onto the subsurface of the rubber ring. Contact was observed by the oil stains on the shaking table as can be seen in Fig. 5:5 (c).

For specimen II elastic shear is the main deformation mode before the displacement reaches 6mm. However, when the boundary condition of the rubber component is varied, i.e. contact occurs, the main deformation is changed to be compression in the bottom local part. According to the detailed geometries of specimen II, compression arises on local part of the rubber component with a very small dimension where the height is only 2mm. This is also believed to be the main reason for the sharp increasement of vertical stiffness.

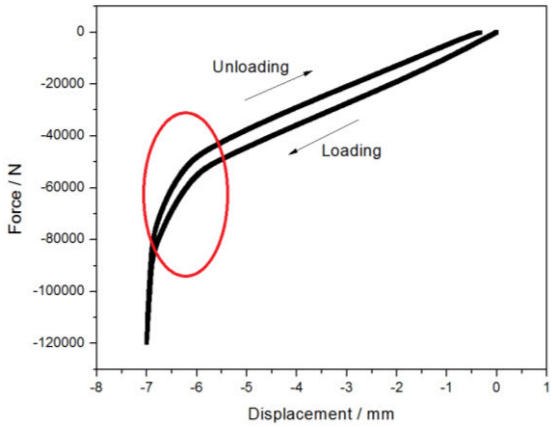

(a) Boundary nonlinearity of the shear type fastening system

(b) Substructure of specimen II

(c) Supplementary test

Fig. 5:5 Test scheme and results of the shear type fastening system

5.2.2 FE simulation and analysis

This section will show the possibility to use FE approach in product designing or product optimization [187]. In the rail fastening system industry, market requires the manufacturers to efficiently reduce the time spend and the high cost due to bunches of experiments and structural optimization process. FE analysis, however, can provide an important virtual producing and testing platform [188].

5.2.2.1 FE modelling

Simulation of the quasi-static experiment is a dynamic analysing process in fact. Generally, a static analysis is sufficient if the interest is to investigate the long-term response, and the inertia effects can be neglected. However, though loading speed of the quasi-static experiment is quite slow, response still has time-dependent features due to the viscous property of rubber material.

During the geometric modelling, each fastening specimen consists of five principal parts in general (Fig. 5:6): a section of railway track, a rubber component tied to the top and the bottom steel plates, and a bottom rigid part simulating the shaking table. The bolts and the withholding components are omitted. A few detailed geometries are simplified; but some other part deserved to be the sensitive area are not reduced although they have very small geometries.

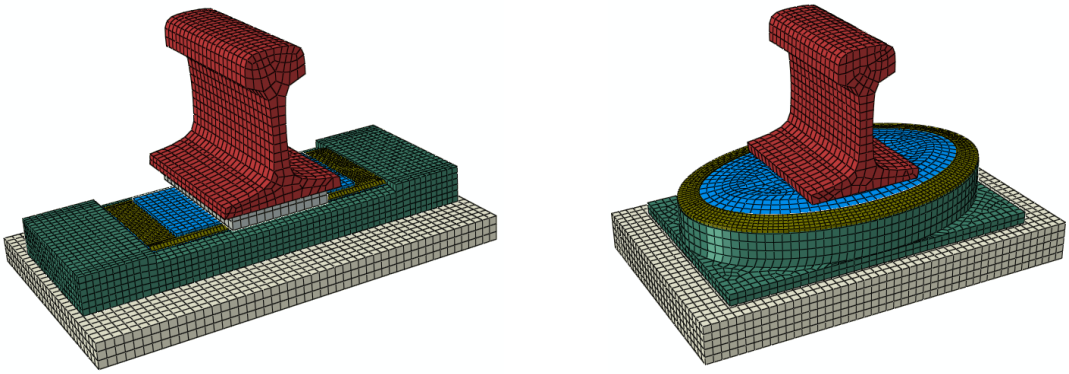

(a) The compressed type specimen (specimen I) (b) The shear type specimen (specimen II)

Fig. 5:6 Assembly modelling of the rail fastening specimens in Abaqus

The rail is fixed in all directions on the top, fastening system is under imposed deformation upwards by the shaking table. The analysis is force controlled; 100kN and 120kN are the maximum load value for the compressed type and the shear type fastening system respectively. In addition, all the possible contacts between different parts were considered: rubber and the two iron frameworks are tied together between the vulcanized surfaces; the interaction property between rail and the top plate and that between the bottom rigid component and the bottom plate is defined as “hard” contact in the normal direction without penetration. In the tangential direction, a frictional coefficient of 0.5 is given; since rubber components of the two specimens also contact with the shaking table, similar contact property except a frictional coefficient of 0.3 is specified. The contact process, i.e. the boundary nonlinearity proved by supplementary tests, is going to be reproduced in the virtual environment visually.

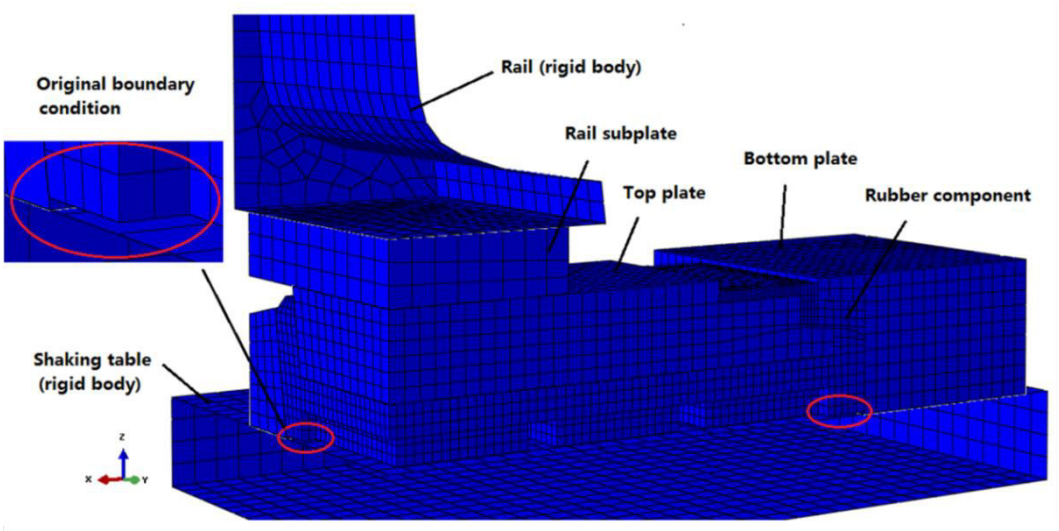

(a) The original boundary condition

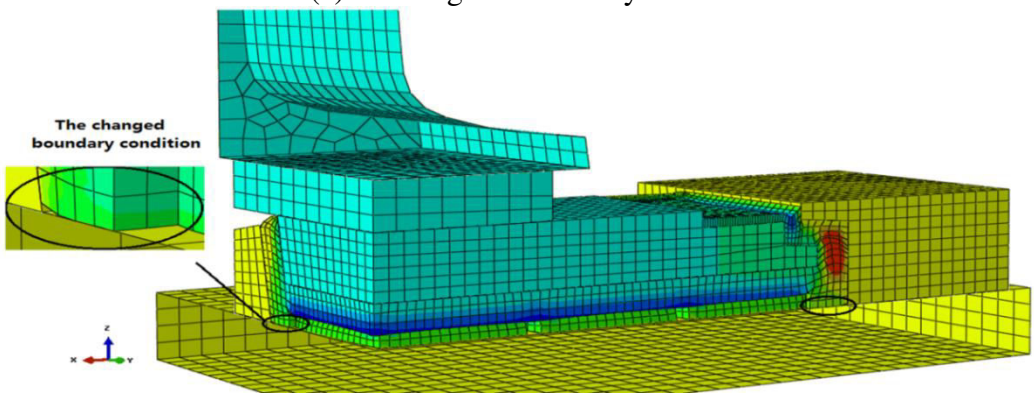

(b) The changed boundary condition

Fig. 5:7 Simulation of the compressed type specimen (a quarter of the model)

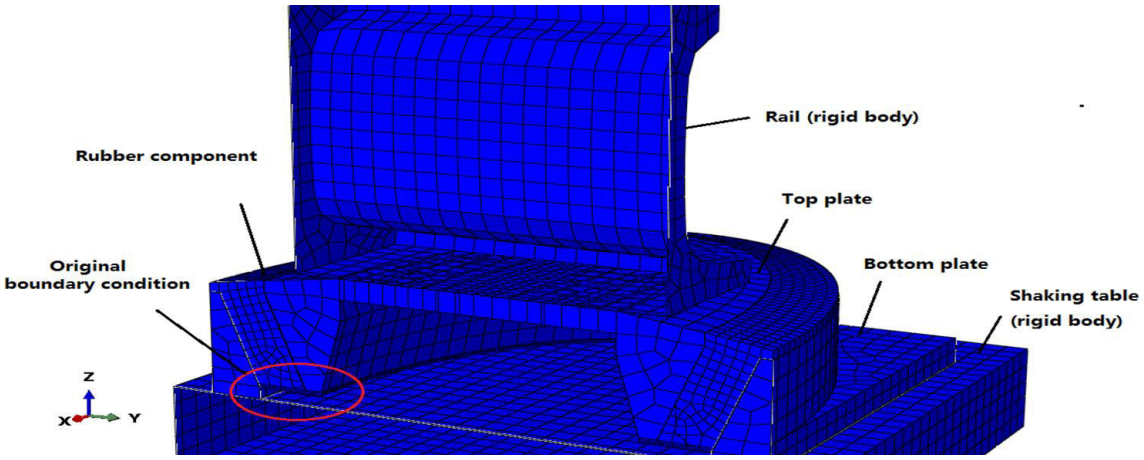

(a) The original boundary condition

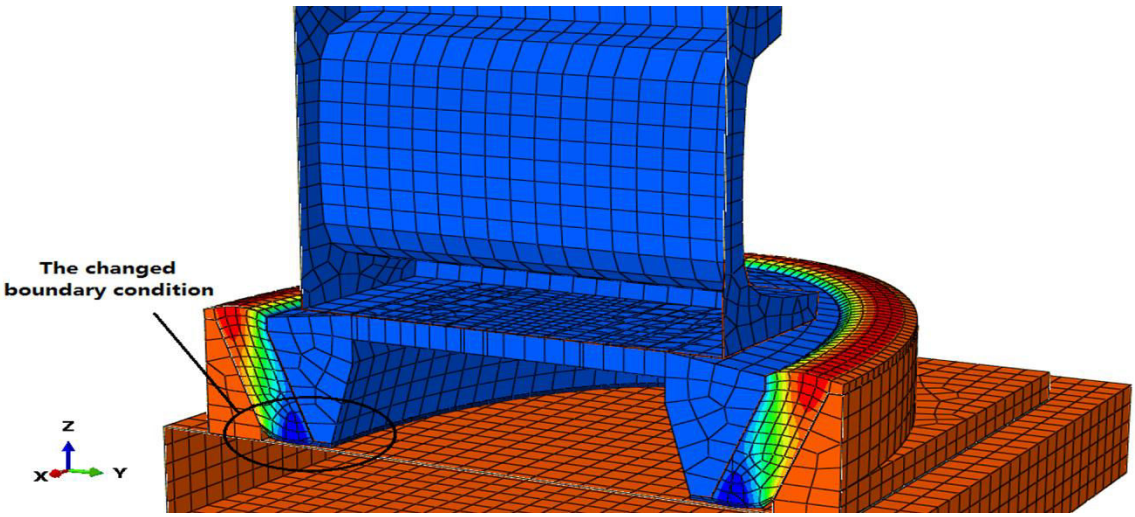

(b) The changed boundary condition

Fig. 5:8 Simulation of the nonlinear contact of the shear type specimen (a half of the model)

In Fig. 5:7 (a) and Fig. 5:8 (a), the original altitude discrepancy can be seen; whereas, in Fig. 5:7 (b) and Fig. 5:8 (b), nonlinear contact between the rubber component and the shaking table is simulated. At this time, the boundary condition of rubber component is changed, giving rise to the nonlinear feature discussed above.

5.2.2.2 Finite mesh element and material definition

After the geometric modelling, assemblies were partitioned to be meshed. For the rubber component, hexahedral-shaped elements are used, see Fig. 5:9. Special attention should be paid to the local areas circled with red lines from the finite element analysing point of view. Since the dimensions of these parts are rather small, discretization for them needs to

be very accurate to avoid computationally unmanageable. For the deformation of the rubber components might be larger than 40%, they are discretized by using 8-node linear brick, reduced integration and hourglass controlled elements (C3D8R). This type of element is confirmed to be convergent and accurate to discretize rubber component. In another hand, the top and the bottom iron frameworks are discretized into elements of 8-node linear brick and incompatible modes (C3D8I) because steel component have much less deformation amount compared to rubber. The section of railway track and the shaking table are defined as rigid body. Due to their geometric characteristics and the contact analysis, discrete rigid (rather than analytical rigid) are selected. We cannot apply mesh control to a rigid surface, as a result the default element type, 4-node and 3-dimension bilinear rigid quadrilateral element (R3D4), are used to discretize the rail and the shaking table.

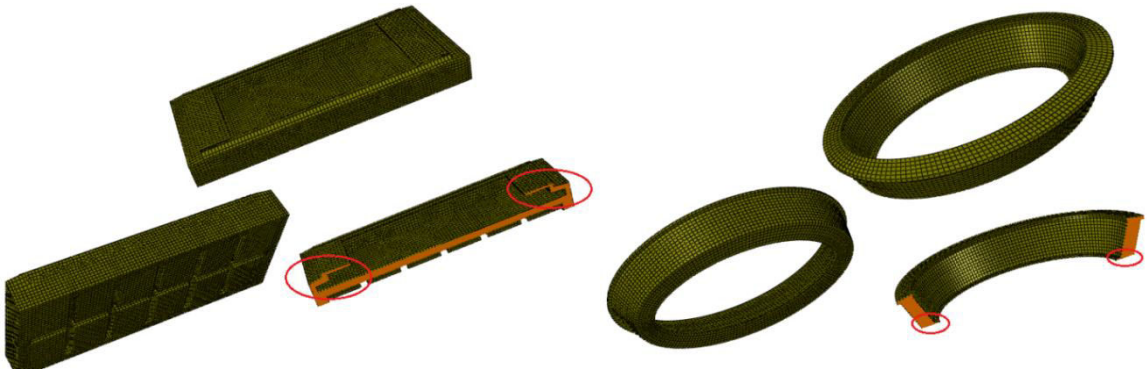

(a) The compressed type specimen (b) The shear type specimen

Fig. 5:9 Rubber components of the fastening specimens

Rubber material shows very complex mechanical behaviour which can be resumed in the following points:

- it shows a mechanical behaviour which is strongly dependent on time or deformation rate;
- it has different hardening behaviour in tension, compression and shear deformation modes;
- the volume of the rubber component is incompressible, etc.

In order to define the rubber material, uniaxial tension in Abaqus, uniaxial compression, planar tension and DMA tests were already carried out and fitted in Chapter 4. Van der Waals model combined with the BB model is used to define the rubber material of

the two fastening specimens. Top plate and bottom plate are defined with steel material with Young's modulus 2.1e5Mpa and Poisson's ratio 0.3.

5.2.2.3 Results and discussion

For the compressed type fastening system, one-quarter of the system is used for calculation as shown in Fig. 5:7; for the shear type specimen half of the model is used, see Fig. 5:8. Displacement is given by the shaking table upward and the responding force is recorded from the reference point of the section of rail. Simulation results are shown in Fig. 5:10 (a) for specimen I and Fig. 5:10 (b) for specimen II. Comparison results show good agreement between the measurement and the simulation results indicating that the calculation process is accurate and the simulation results are acceptable.

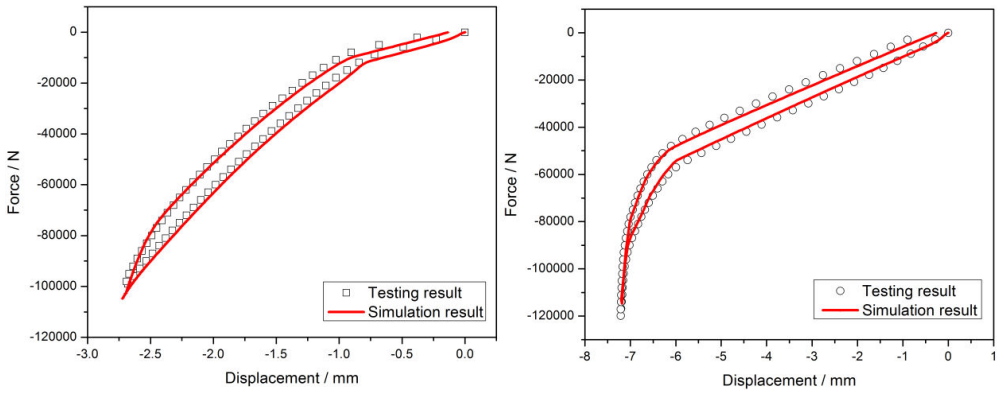

(a) The compressed type specimen (b) The shear type specimen

Fig. 5:10 Comparison of the measured and calculated working curves

By changing the geometries of specimen I in the virtual environment of Abaqus and by diminishing the loading conditions for specimen II, calculated results under the same loading speed whereas excluding the boundary nonlinear features are depicted with blue dotted lines in Fig. 5:11. We can see that the calculated loading curve keeps nearly the same secant stiffness with the originally measured loading curve. It also should be noted that the loading curve of specimen I in comparison with the secant line expressed by dashed lines in both black and blue show nonlinear features in Fig. 5:11 (a); whereas, as for specimen II in Fig. 5:11 (b) the loading curve of both prediction and measurement can almost be regarded as linear. This nonlinear feature and the difference between the two specimens are going to be further studied in the coming sections.

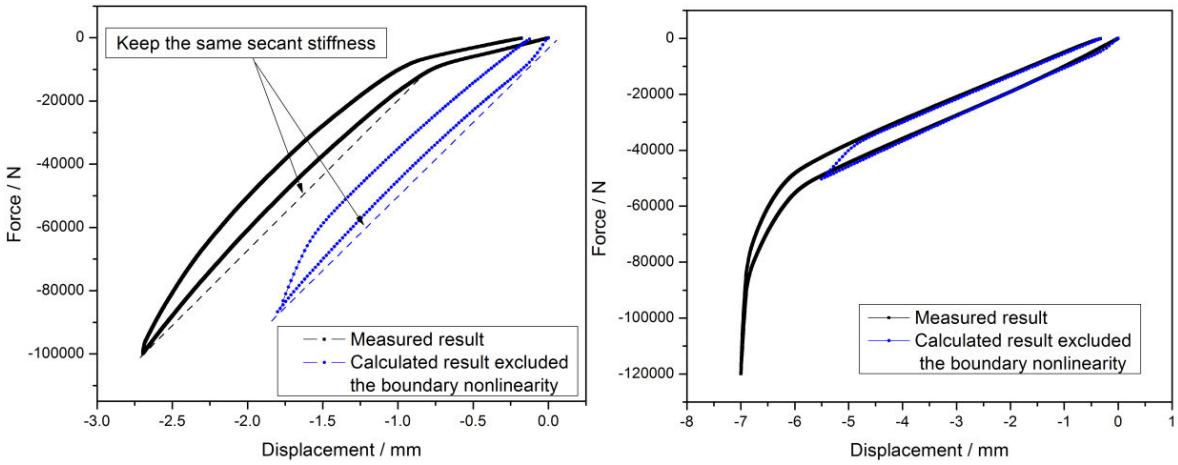

(a) The compressed type specimen (b) The shear type specimen

Fig. 5:11 Calculated results when boundary nonlinearities are excluded

5.3 Geometric nonlinearity

In Fig. 5:12, the quasi-static loading-unloading curve excluded the boundary nonlinearity of specimen I which is depicted in details. As mentioned above, the loading curve obviously has a nonlinear feature and we can use the average displacement between the loading curve and the secant line to describe the nonlinearity. Though, at this time, the nonlinear feature is not as distinguished as the boundary nonlinearity, the secant stiffness

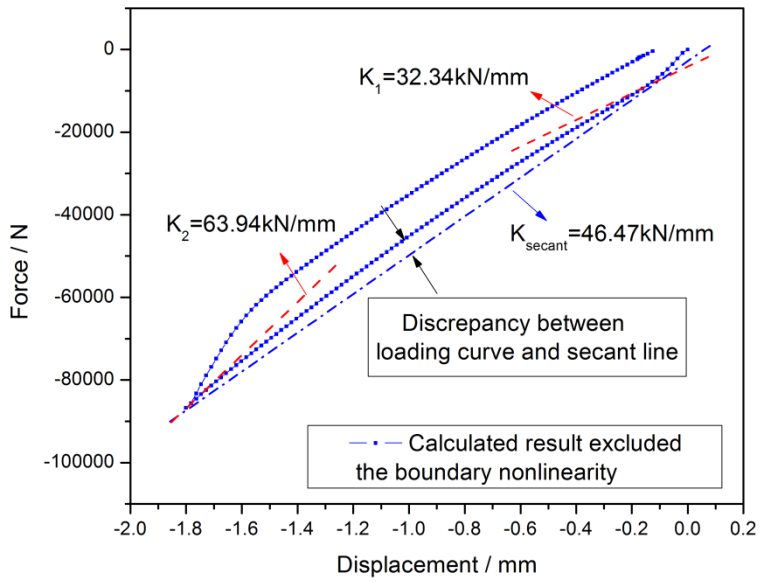

Fig. 5:12 Detailed prediction of the quasi-static working curve of specimen I after eliminating the boundary nonlinearity

value, 46.47kN/mm, is apparently different from the tangent stiffness, 32.34kN/mm at the beginning of the curve and 63.94kN/mm at the end. We can see that this nonlinearity does have an influence on the stiffness value by 30% to 40% and it is believed to be a geometric nonlinearity as rubber component is under compressed deformation mode.

5.3.1 Definition of geometric nonlinearity

Generally speaking, geometric nonlinear features can be induced by the boundary constraint conditions and the largely varied shape after deformation. Sometimes, the constraint condition induced nonlinearity is also ranked into the boundary nonlinearity together with the contact nonlinearity discussed in section 5.2. Since serious boundary constraint may result in irregular and large deformation of rubber component, it is classified into geometric nonlinearity in current research.

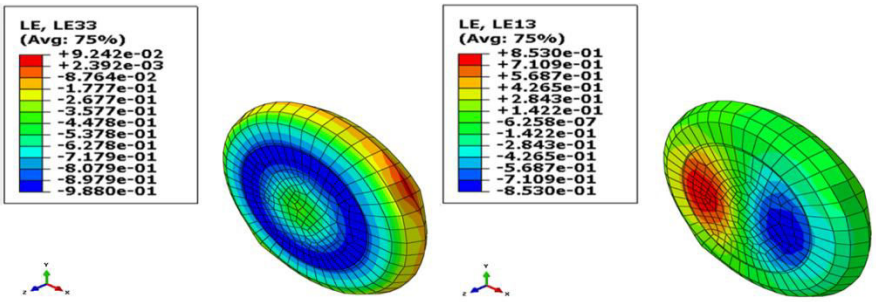

(a) Large frictional coefficient

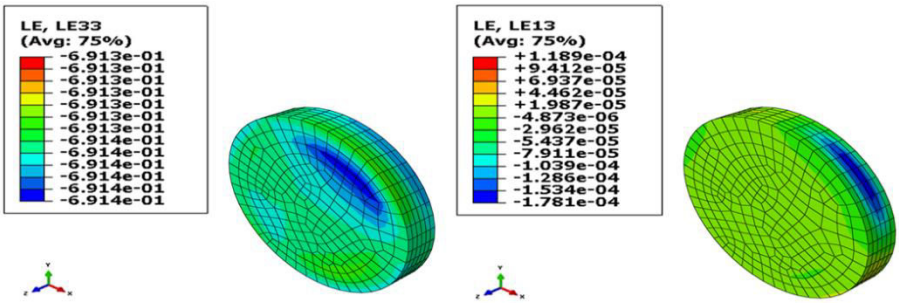

(b) Small frictional coefficient

Fig. 5:13 Influences of boundary constraint on the shear and compression strain

Taking the rubber cylinder used in the uniaxial compression test for instance, from Fig. 5:13 (a) where the frictional coefficient is 0.5, we can find the free surfaces bulging severely and the maximum shear strain (L13=0.85) is almost as large as the compression strain (LE33=0.9). Compared to Fig. 5:13(b), where the frictional coefficient equals 1e-10, the

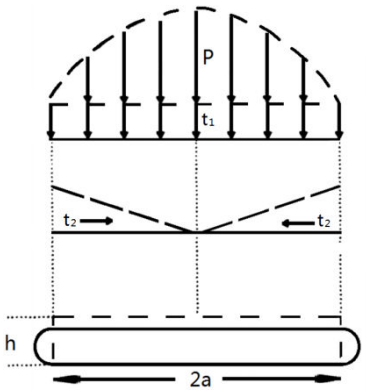

Fig. 5:14 Stress distribution for bonded or fractional rubber block during compression [21]

maximum shear strain (L13=1.8e-4) is so smaller than the compression strain (L33=0.69) that can be omitted. At this situation, the deformation of the rubber cylinder can be considered as simple compression. Referring to the calculation results shown in Fig.4:17, the bigger the frictional coefficient is given the larger the stiffness we get and the more significant nonlinearity would be observed at the large deformed region.

This nonlinearity can be explained by the effect of boundary constraint conditions as follows. The deformation of a rubber block bonded (or with great friction coefficient) between rigid plates is considered to take place in two stages as shown in Fig.5.14: a simple compression requiring a uniform compressive stress t_1 and a distributed shear deformation that restores points in the planes of the frictional surfaces to their original positions corresponding to the shear stress t_2. If the simple compression is ε, it requires a uniform compressive stress $t_1 = E\varepsilon$, where E is the real compressive modulus; the shear stress t_2 acting at the bonded surfaces at a radio distance r from the cylinder axis is given by $t_2 = E(\frac{r}{h})\varepsilon$ increasing linearly with r. This shear stress t_2 is associated with a normal pressure P by $t_2 = (\frac{h}{2})(\frac{\partial P}{\partial r})$. Upon integrating, P is obtained as $P = E\varepsilon\left(\frac{a^2}{h^2}\right)[1 - (\frac{r^2}{a^2})]$. Furthermore, by integrating the normal stresses $(P + t_1)$ acting over the bonded surface, the total compressive force F is obtained as follows:

$$F = \pi a^2 E\varepsilon\left[1 + \left(\frac{a^2}{2h^2}\right)\right] = \pi a^2 \varepsilon E_a \tag{5:1}$$

Equation 5:1 shows that the constraint effect at the bonded faces is to increase the effective compression modulus (or apparent compression modulus) from E to $E_a = E\left[1 + \left(\frac{a^2}{2h^2}\right)\right]$ by a amplification factor $\left[1 + \left(\frac{a^2}{2h^2}\right)\right]$.

In fact, the amplification factor can be defined by a shape factor defined as $S = \frac{A_l}{A_b}$, where A_l and A_b are respectively the loading area and the bulge area of the cylinder component. Integrating it to Equation 5:1 we can obtain

$$F = \pi a^2 E\varepsilon[1 + 2S^2] \tag{5:2a}$$

and

$$E_a = E(1 + 2S^2) \tag{5:2b}$$

where the shape factor of the cylinder specimen $S = a/2h$. For a rubber block with circular cross-section, the relationship between the apparent compressive modulus E_a and the real modulus E as depicted in Equation 5:2b is given by Gent and Lindley [189]. Besides this definition of the shape factor, Williams and Gamonpilas [190] and Timoshenko and Goodier [191] also presented similar expressions to correlate the apparent and real compression modulus of rubber component.

However, from the calculated strain-stress curves at each deformation mode as shown in chapter 4 we can see that, the uniaxial compression curve still shows obvious nonlinear features even though the frictional coefficient is as small as 1e-10. It means that the geometric nonlinearity is not only due to the boundary constraint effect, but also on the large deformation of rubber component.

Normally, when a component has large deformation that is large than 1/20 of its largest dimension, the largely varied shape may give rise to a geometric nonlinearity. Taking the uniaxial compression test for example again, the severely varied cylinder shape when the final diameter $a = 41mm$, loading area $A_l = 1320mm^2$ and the bulging area $A_b = 1545mm^2$ compared with the initial diameter $a = 29mm$, loading area $A_l = 661mm^2$ and the freely bulging area $A_b = 2186mm^2$ is believed to give rise to a geometric nonlinearity. If

we describe the changing shape by shape factor S, it increases to be $S = 1.7$ from $S = 0.6$. When the shape factor furthermore increases, a significant contribution to the observed nonlinearity comes from the volume modulus because E_a is now so large that becoming comparable to the bulk modulus of rubber material, K. For such largely deformed rubber component, contribution of the bulk compression K largely increases the apparent compression modulus in term of the nonlinear displacement-force relationship. However, it's hard to exclude material nonlinearity from the geometric nonlinearity in fact, because high compressive strain which is included in the nonlinear strain range is often in existence in the material accompanied with large deformation of rubber component. The material nonlinearity will be discussed in section 5.4.

5.3.2 Geometric nonlinearity of the compressed type specimen

Generally speaking, geometric nonlinear features can be induced by boundary constraint conditions such as friction effect and the largely varied shape of rubber components. Since strict boundary constraint may result in irregular and uneven deformation of rubber components, it is classified into geometric nonlinearity in the present research. In according with the quasi-static displacement-force curve of the compressed type fastening system as shown in Fig.5:12, frictional coefficient between rubber component and the shaking table is specified as 0.3 during simulation process which means that this boundary constraint may bring about certain nonlinearity. Specifically, when the maximum vertical displacement is reached in Fig. 5:12 the maximum compressed strain and the shear strain on the under-surface of rubber material are nearly the same (about 50%) according to the simulation result. The accompanied shear deformation due to the friction effect may influence the resilient property of the compressed type fastening system; the boundary constraint condition leads to an increasement of the apparent/effective compression modulus with an amplification factor defined by shape factor. This nonlinear feature indicated in Fig. 5:12 therefore can be explained as a geometric nonlinearity. In addition, the more frictional effect is taken into account, the larger stiffness and the stronger nonlinearity can be observed. Fig. 5:15 shows the increased secant stiffness of the compressed type fastening system with the enlarged frictional coefficient, while Fig. 5:16 describes the more obvious nonlinearity along with the increased frictional coefficient measured by the average displacement between the secant line and the loading curve, see Fig. 5:12.

In addition, the varied shape of the rubber component of the compressed type fastening system corresponding to the maximum loading value is shown in Fig. 5:17. The under-surface of the rubber component is still away from self-contact and the shape factor is not largely altered. As a consequence, we can say that the geometric nonlinearity observed from the loading curve in Fig. 5:12 is mainly due to its boundary constraint conditions.

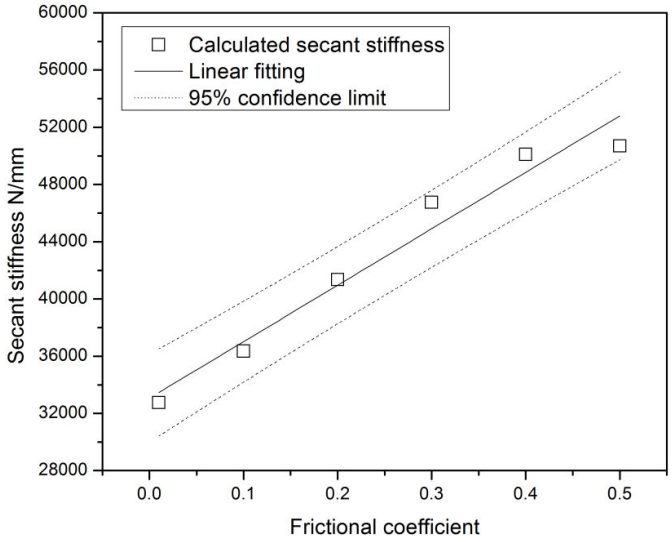

Fig. 5:15 Secant stiffness influenced by frictional coefficient

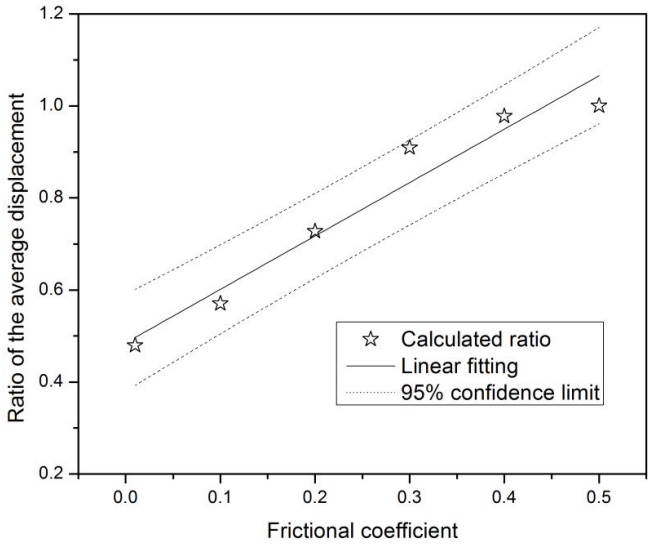

Fig. 5:16 Nonlinear feature of the loading curve influenced by frictional coefficient

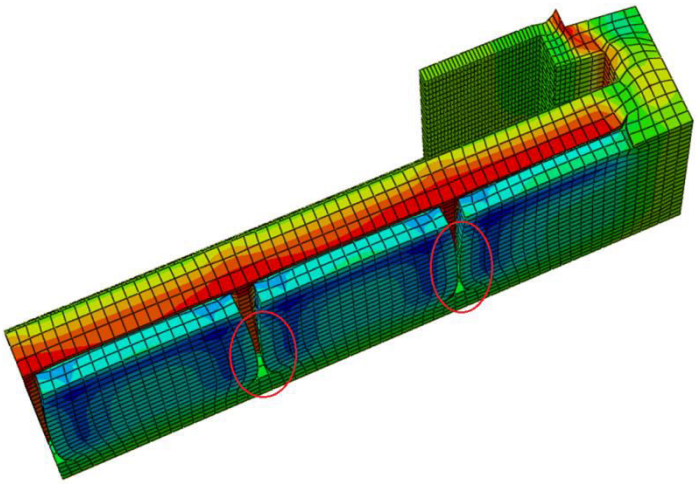

Fig. 5:17 Potential self-contact of the rubber component of the compressed type specimen

5.4 Material nonlinearity

Material nonlinearity is also known as the nonlinear elasticity or hyperelasticity of rubber component as it is under large deformation. The chemical structure of a polymeric chain may be of two types in general: isotactic and atactic [192]. Nature rubber has an isotactic structure so that the side groups lie on the same side of the polymeric chain. The presence of crystallites in nature rubber acts as large junctions or cross links and it has a strain-stiffening effect on the mechanical behaviour of the material. When a piece of natural rubber component is under large deformation, the side groups of chains crystallize because they are able to converge and, therefore, the material stiffens. On the other hand the structure of many synthetic rubber materials is atactic, i.e. the side groups are irregularly placed on each side of the chains. Though an atactic chain never crystallize since the side groups, which have different sizes and chemical properties do not match in space due to the irregularity of their position relative to the chin backbone, severe rise in the strain-stress curves still clearly can be observed in experiments. However, at this situation the stiffening arises from the effect of finite chain extensibility. As large extension of the chains is approached the material stiffens because most of the monomer composing the chain becomes aligned along the direction of stretch, and we have to start stretching the bonds, and changing bound angles, both of which require larger energies used for changing the configurations of the chains.

Hence, mechanical properties of elastomeric materials are usually represented in terms of a strain energy density function as discussed in Chapter 3. In molecular theory,

macroscopic models are obtained from microscopic considerations. Starting from the elastic free energy of a single chain, it's possible to obtain the total elastic free energy of the network composing the mesoscopic structure of the elastomer by a suitable averaging procedure of all the elastic free energies of the individual chains. At first, experimental measurements of strain-stress relationship for rubber materials gave Mooney and Rivlin [193-195] enough evidences, and the linear theory of elasticity, which is used since the 17th century, was an inadequate approach to access the mechanical properties of such material. Soon afterward, nonlinear elastic theory was developed one after another [196-198]. Several well-known hyperelastic constitutive models were reviewed briefly in Chapter 3, eventually Van der Waals model is verified to fit the fundamental experiment results best. In Fig. 5:18, measured and calculated uniaxial tension, uniaxial compression, planar tension tests are shown. The nonlinear feature which can be observed in the uniaxial compression curve was a geometric nonlinearity as discussed in section 5.3. However, according to the relevant references, it's hard to exclude the material nonlinearity especially when the compressive strain is larger than 40%. For uniaxial tension test, hardening phenomenon is still not obvious until the tensile strain approaches 100%; for planar tension test, stiffening effect occurs as the strain reaches 75%.

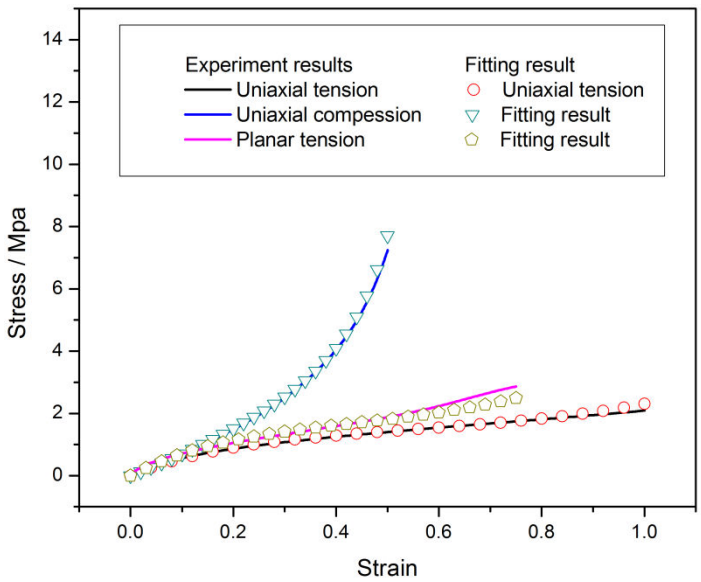

Fig. 5:18 Comparison of the measured and calculated fundamental material experiments by using Van Der Waals models

As the maximum displacement is achieved in the quasi-static experiment of the compressed type fastening system, different deformation modes in the local part of the rubber

component are shown in Fig. 5:19. In Fig. 5:19 (a) we can see that the maximum true compressive strain of about 37% equivalent to nominal strain of about 49% arises in a corner of the bottom surface, while the maximum true tensile strain is about 46% (approximately equals 61% nominal strain). Although a nominal tensile strain of 61% is far away from the material nonlinear range, compressive strain as high as 49% may give rise to the nonlinear feature of the loading curve of the compressed type fastening system. In the meanwhile, from Fig. 5:19 (b) and (c) we can see that true shear strain in XZ and YZ planes on local part of the rubber component subsurface both approach approximate 110%, and the corresponding nominal shear strain is already up to 147%, which will also give rise to a stiffening behaviour of the rubber component. From this point of view, the nonlinear feature shown in Fig. 5:11 (a) and Fig. 5:12 can also be due to material nonlinearity.

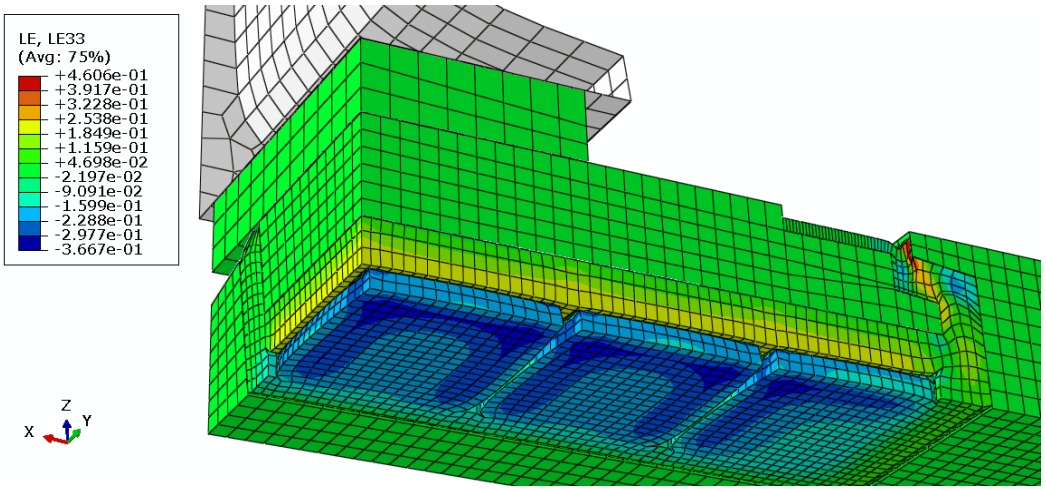

(a) Compressive/tensile strain in Z direction (LE33)

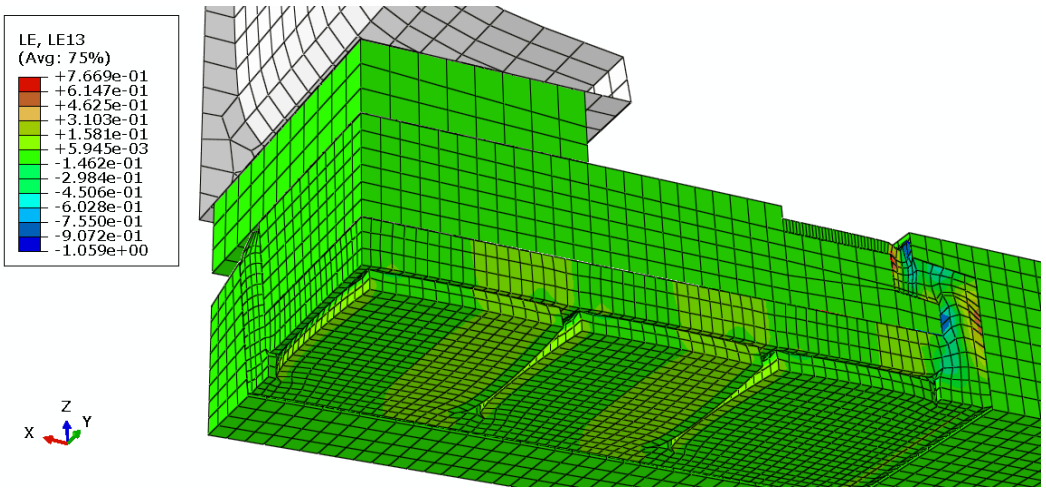

(b) Shear strain in X-Z plane (LE13)

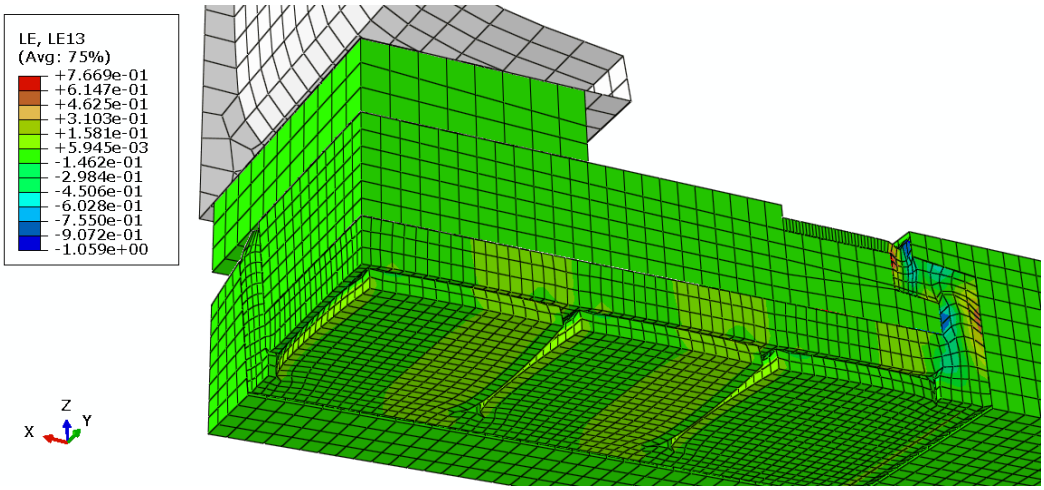

(c) Shear strain in Y-Z plane (LE23)

Fig. 5:19 Maximum strain at the local part of compressed type specimen

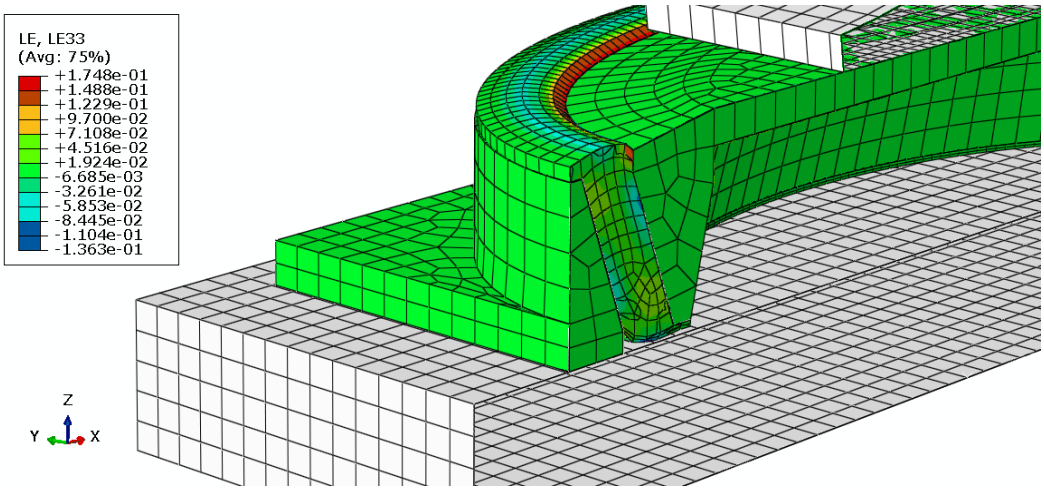

(a) Compressive/tensile strain in Z direction (LE33)

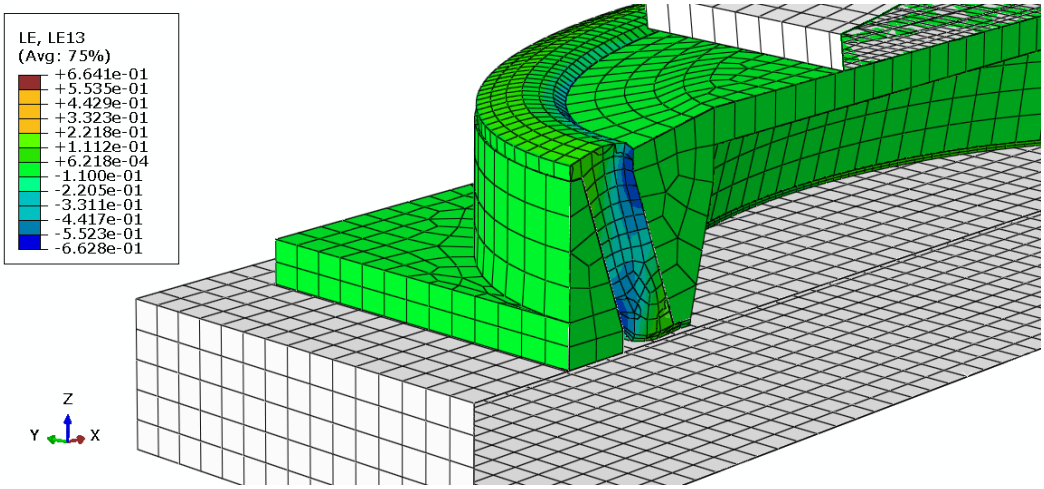

(b) Shear strain in X-Z plane (LE13)

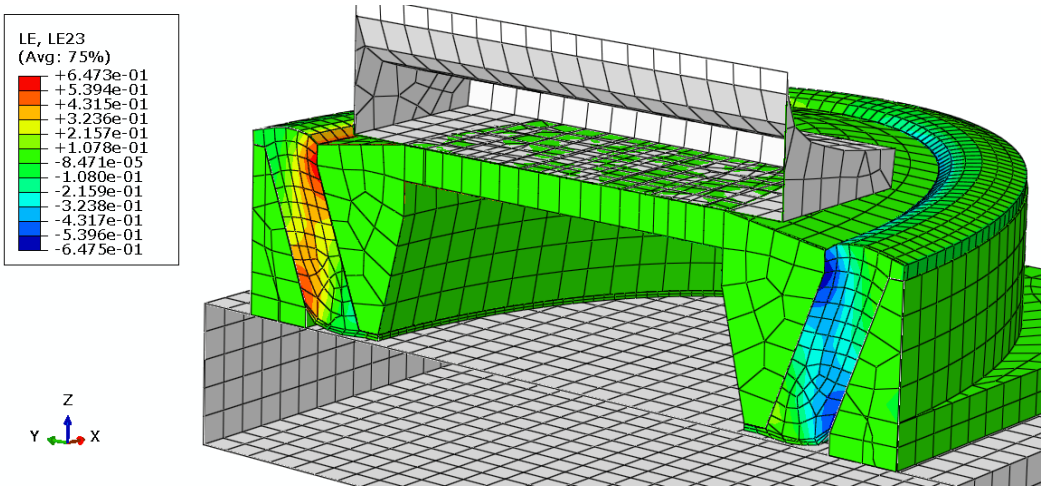

(c) Shear strain in X-Z plane (LE23)

Fig. 5:20 Maximum strain at the local part of shear type specimen

In contrast, from Fig. 5:20 we can see when the maximum displacement is applied to the shear type fastening system, 14% true compressive strain, 17% true tensile strain and 66% true shear strain, corresponding to the nominal strain of 19%, 23% and 88% respectively, both cannot give rise to an obvious nonlinear feature. The shear type fastening system has a better linear elasticity compared to the compressed type.

5.5 Viscoelastic property

5.5.1 Rate-dependent loading-unloading curves

Viscoelastic properties of rubber-like material can be listed briefly as creep/stress relaxation, rate-dependent effective stiffness, phase-lag and hysteresis loop leading to the dissipation of mechanical energy as cyclic loading is applied. As a result of Chapter 4, the evaluated Van de Waal model and Bergstrom-Boyce model and the fitted parameters were verified to be able to accurately fit the quasi-static experimental results of both specimens. The displacement-force relations excluded the boundary nonlinearities were produced in Fig. 5:11, and the geometric nonlinearity combined with material nonlinear properties of specimen I were proved to influence the shape of displacement-force curve as shown in Fig. 5:12, where the loading rate is 0.025 mm/s. In this section, a family of virtual experiments is carried out in order to capture the rate-dependent properties of the two fastening systems [159]. The force responses versus displacement at different loading rate are compared in Fig. 5:21 (a); only the loading curves are refined in Fig. 5:21 (b). From the figure we can see that the

observed force response is very sensitive to the loading speed [199]. For example, at the end of the loading curves, the observed force response when loading speed is 22.5 mm/s is nearly 1.5 times larger than that for the case when the loading speed is 0.0000225 mm/sec.

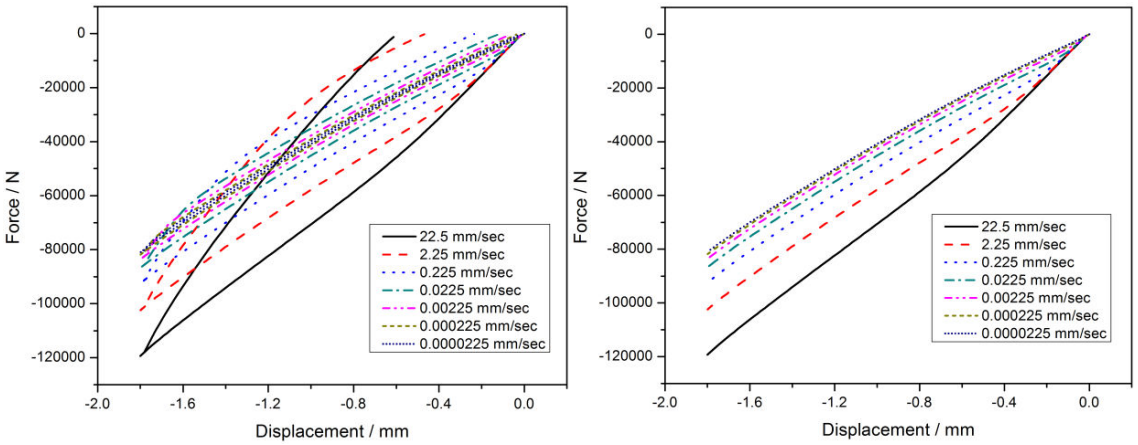

(a) Loading-unloading curves (b) Loading subset of (a)

Fig. 5:21 Quasi-static displacement-force relationships at different loading rate

Specifically, the loading rate dependency depicted in Fig. 5:21 reflects firstly on the varied secant stiffness which is plotted in Fig. 5:22 (a). It can be clearly seen that decreased loading rate gives rise to reduced secant stiffness; especially when the loading rate is relatively small, the stiffness is very sensitive to loading rate. It also tells that as a rail fastening product is measured in order to determine the nominal stiffness value, the loading rate should be slow enough to capture an approximate long-term stiffness. In addition, rate dependency also shows in term of energy loss during the loading-unloading cycle, see Fig. 5:22 (b). The energy dissipation during one loading-unloading cycle equals the area enclosed by the loading and unloading curves as well as Y=0 in Fig. 5:21 (a). Similarly, decreased loading rate leads to reduced energy dissipation especially when the loading rate is relatively slow, at which time the unloading curve nearly follows the same trace as the loading curve.

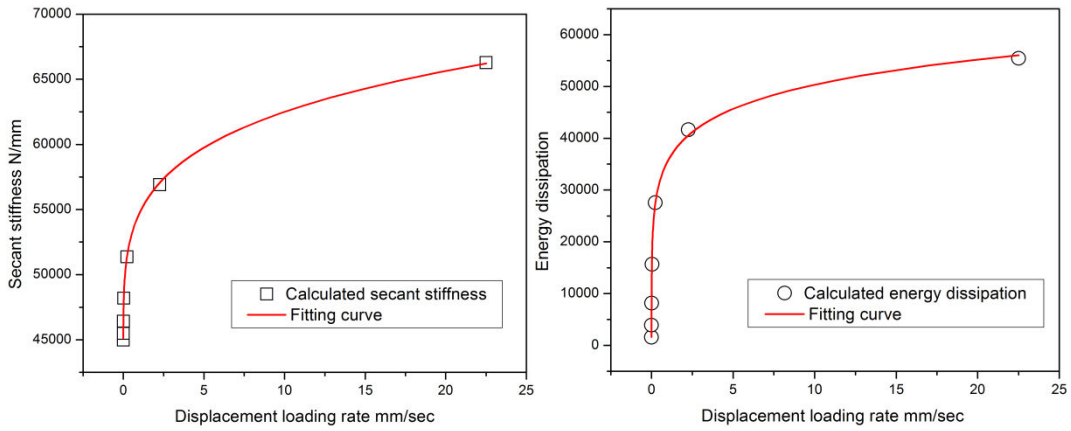

(a) Secant stiffness (b) Energy loss

Fig. 5:22 Loading rate dependent secant stiffness and energy dissipation

5.5.2 Transient effect

The loading rate influenced secant stiffness and energy loss during one loading-unloading cycle was discussed through a family of virtual tests under the Abaqus platform. In addition to this rate-dependent property, viscoelasticity of rubber material also gives rise to a transient effect. In Fig. 5:23 the nonlinear transient stiffness is highlighted with two read circles. These two nonlinearities are followed by the gently changed loading and unloading curves. It is clearly can be seen that this nonlinear transient stiffness is also strongly influenced by the loading rate if we look back to the comparison of the rate-dependent loading curve as shown in Fig. 5:21. When displacement loading rate is as slow as 2.25e-5 mm/sec the nonlinear feature due to the transient effect is even not in existence, whereas as the rate is up to 22.5 mm/sec the nonlinear instantaneous stiffness is very noticeable.

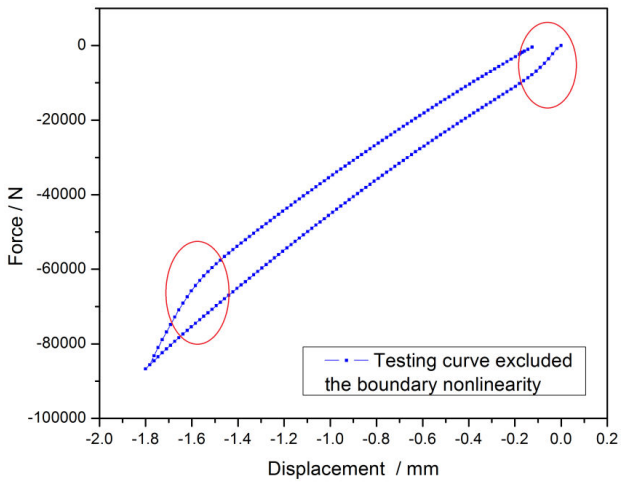

Fig. 5:23 Transient stiffness induced nonlinear feature of the compressed type specimen

According to the viscoelastic properties of rubber material, the nonlinear transient stiffness may partially due to stress relaxation. As a result, a holding step of 2000s is added between the loading and unloading process. Taking the compressed type fastening system for example, the calculated result is compared to that without a holding step as shown in Fig. 5:24 (a), where they are distinguished by green and blue dotted lines respectively, and the holding process is expressed in Fig. 5:24 (b). As the holding time approaches to 2000 second the force relaxation almost approaches to a constant state. As a result, the displacement-force relationship of the original experiment result and the simulated curve with a holding time as shown in Fig. 5:24 (a), though they follows different way approaching to the relatively stable

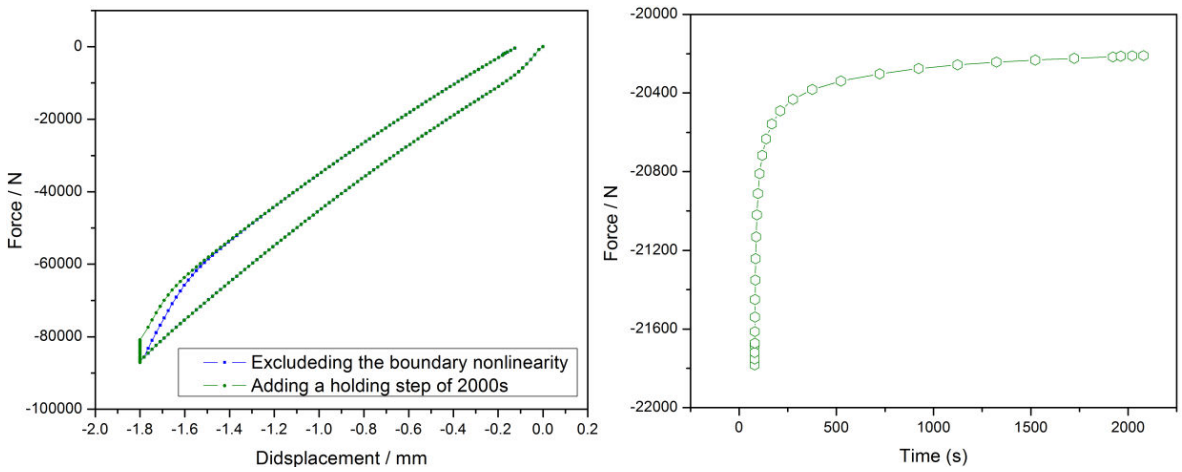

(a) With and without the holding step (b) Time-force relationship during the holding step

Fig. 5:24 Excluding the stress relaxation effect by adding a holding stage of specimen I

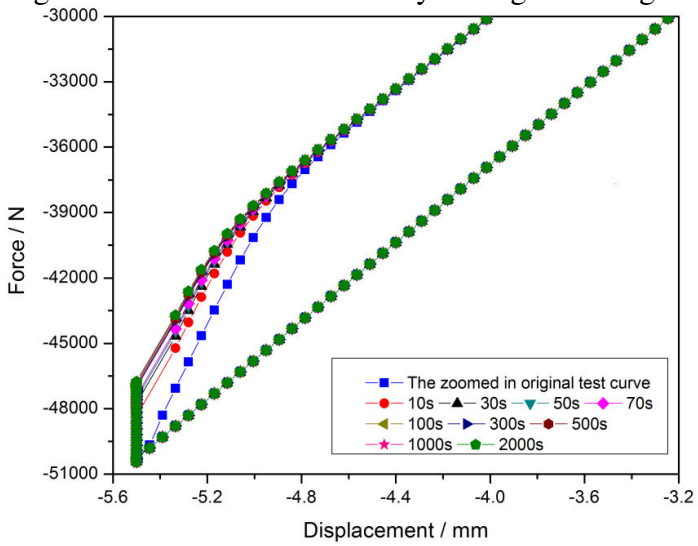

Fig. 5:25 Similar process to exclude the stress relaxation effect performed on specimen II

stiffness value, a noticeable nonlinear feature still exist. Similar analysing process is also performed to the shear type fastening system (specimen II), and the similar results are obtained. A zoomed-in figure of this feature for specimen II is shown in Fig. 5:25, where the calculating results with different holding time are compared to confirm the conclusion that nonlinear transient stiffness still exists after the stress relaxation of the loading process is almost completed.

The transient effect induced nonlinearity is ultimately due to the rubber material viscosity [200]. Fig. 5:26 presents a schematic representation of typical viscoelastic response of a elastomer. When viscoelastic solid is loaded at an infinitely slow speed, the stress-strain curve follows the path O-E'. This behaviour is known as the equilibrium response; on the other hand, if the component is loaded infinitely fast, the response follows the path O-I', and such a response is known as the instantaneous response of transient effect [201]. It should be noted that both equilibrium and instantaneous responses are elastic and they bind the viscosity domain. The area of viscous domain is directly related to the extent of material viscosity. Total stress of a rubber solid corresponding to a certain amount of deformation can be decomposed into equilibrium and viscosity induced overstress parts (instantaneous part) [202-204]. In this decomposition the instantaneous component introduces an intermediate configuration, which is resulted when the stress is unloaded at an infinitely fast rate to an equilibrium state. The larger the strain-rate is, the large the instantaneous response is and, correspondingly, the more noticeable the intermediate configuration is.

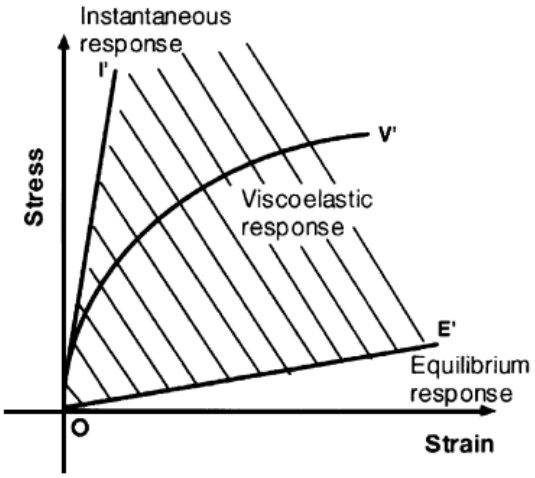

Fig. 5:26 Typical responses of a viscoelastic solid

5.5.3 Hysteresis loop

Except the rate-dependent quasi-static stiffness, the transient effect discussed above, hysteresis loops of the two fastening specimens obtained from the dynamic experiment are also due to the intrinsic viscoelastic property of rubber material. As mentioned above, a phase lag between the input disturbance and its response gives rise to the enclosed loop. The area of the loop equals to the hysteresis loss during one cycle. By using the same model and parameters, simulation results are compared to the measurement as shown in Fig.5:27 (a) for the compressed type fastening system and in Fig. 5:27 (b) for the shear type fastening system. Good agreement between the measurement and the calculation can be observed. Since the frequency dependent and amplitude dependent dynamic stiffness and hysteresis properties were discussed in Chapter 3, only one random testing case is depicted herein. However, it should be emphasized that the obvious difference between the crescent-like hysteresis loop of specimen I and the elliptic hysteresis loop of specimen II also arises from the pre-compression dependency. Since the dynamic displacement-force relationship is superimposed onto a nonlinear segment of the quasi-static loading curve, it makes the equilibrium curve of the hysteresis loop for specimen I change to be nonlinear.

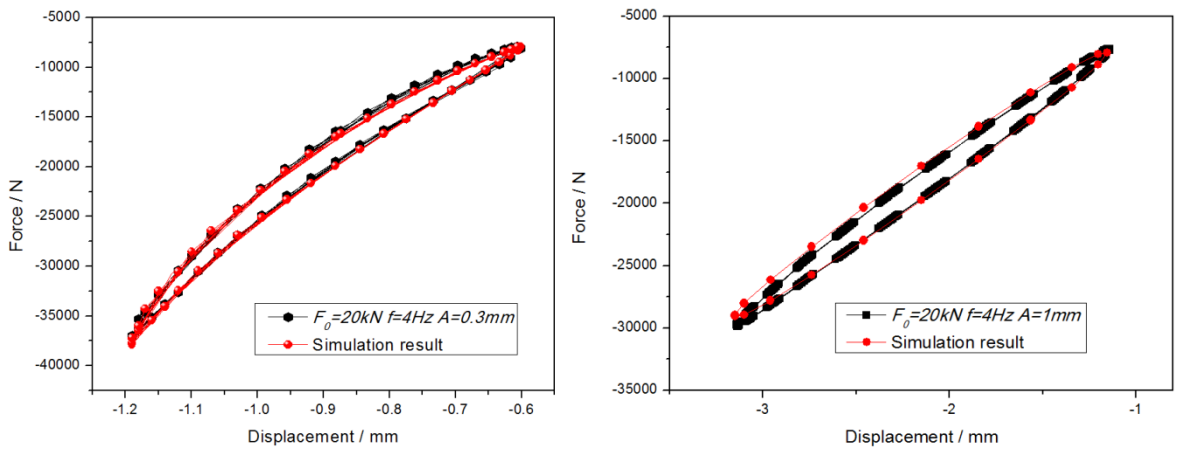

(a) The compressed type specimen (b) The shear type specimen

Fig. 5:27 Calculated hysteresis loops compared with the measurement

5.6 Summary

Nonlinear features due to different reasons, which can be observed from the measured working curves of the two used specimen were studied in this chapter. The most noticeable

nonlinearity is the boundary nonlinearity due to nonlinear contact. This nonlinear feature of each specimen was firstly approved through a set of supplementary experiments. In addition, the quasi-static tests of the two specimens were simulated using Abaqus. Simulating result shows good agreement with measurement indicating the accuracy of the models and the simulation process. Since it is impossible to capture the moment when contacting occurs in a experiment, simulation can reproduce the loading-unloading phase and make it possible to have the contacting moment visible. Besides the boundary nonlinearity, the loading curve of specimen I also exhibits geometric nonlinear properties. Rubber cylinder specimen of uniaxial compression test was used to explain the boundary constraint induced and the largely changing shape caused geometric nonlinearities. In comparison with specimen I, specimen II doesn't show visible geometric nonlinear features. Moreover, from the calculated results we can see that specimen II also does not have a material nonlinearity for its largest strain value of different deformation modes is far away from the nonlinear range. On the opposite, both compressive and shear deformations of the rubber component in the compressed type fastening system is included in the nonlinear material strain range. The material nonlinearity therefore contributes to the nonlinear loading curve of the compressed type specimen. At last, nonlinear property induced by material viscosity was discussed. The quasi-static stiffness and the energy loss during are severely dependent on the loading speed. The nonlinear transient stiffness at the beginning of both loading and unloading phases was studied; in the same while disturbance from stress relaxation was eliminated by adding a holding step of 2000s. Furthermore, the shapes of the hysteresis loops of both fastening specimens were discussed. The shapes were different because of the pre-load dependency. Simulation results were compared to the measured loops, and good agreement between them was obtained.

Nonlinearity analysis on the quasi-static working curves of the two specimens is believed to be helpful in enhancing understanding of their mechanical behaviour and optimizing the geometric properties in details. It will eventually help to guide the product designing and structural optimization, and improve their performance.

Chapter 6 Parameter sensitivity analysing and structural optimization

In this Chapter, parameter sensitivity analysis of the present shear type and the compressed type rail fastening systems are introduced, which are followed by an optimized process from different objectives. Nonlinear properties discussed above are taken good use or avoided during the optimization. Optimization objectives such as isolation efficiency improvement, displacement response control, vertical and lateral stiffness match, free surface rationalization and material cost are put forward. An important term “shear-compression ratio” is firstly proposed in present research in order to meet the expecting vibration isolation capability and the vertical-lateral-stiffness ratio with the lowest optimization cost.

6.1 Introduction

Over the last chapters, quasi-static and dynamic experiments of the two different kinds of fastening systems were performed in Chapter 2. Their pre-load influenced and frequency dependent as well as dynamic amplitude dependent properties were modelled in Chapter 3. In order to accurately define the rubber material used in the two fastening specimens, a family of fundamental material tests was carried out in Chapter 4. Hyperelastic properties and viscoelastic characteristics of rubber material are given by Van der Waals model and BB model respectively. The models and the evaluated parameters are used in Chapter 5 to simulate the quasi-static and dynamic experiments of the two specimens in Abaqus. Nonlinear properties shown in the working curves of each fastening system are studied and explained. So far, we already enhanced understanding of the general mechanical properties of the two present rail fastening systems. In Chapter 6 parameter sensitivity analysis will be conducted for both compressed and the shear type fastening systems. Most of the parameters will be found closely related to the vertical and lateral elastic characteristics. After that, a few geometric optimization objectives will be presented, such as force transmissibility (also known as the force response), dynamic amplification factor (displacement response), damping, fatigue and strength of material, etc. And the corresponding solutions will also be provided on the basis of parameter sensitivity analysing results.

The rubber component of the shear fastening system is an elliptical ring, the detailed geometries of which are shown in Fig. 6:1 (a). The sectional dimension of the rubber component is zoomed in on the top right corner, where the most important dimensions are the inclined angle $\alpha = 110°$, the width $t = 29.36mm$ and the height $h = 52mm$. When the wheel-rail force is transmitted from the above onto the top plate vertically, the rubber elliptical ring undertakes most of the load paralleled to the bonding surface between rubber and the plate components resulting in shear deformation. While a few part of this load is undertaken perpendicular to the bonding surface giving rise to a small quantity of compressive deformation. This shear-compression ratio will be proved very important in determining the vertical and shear stiffness property in the following pages.

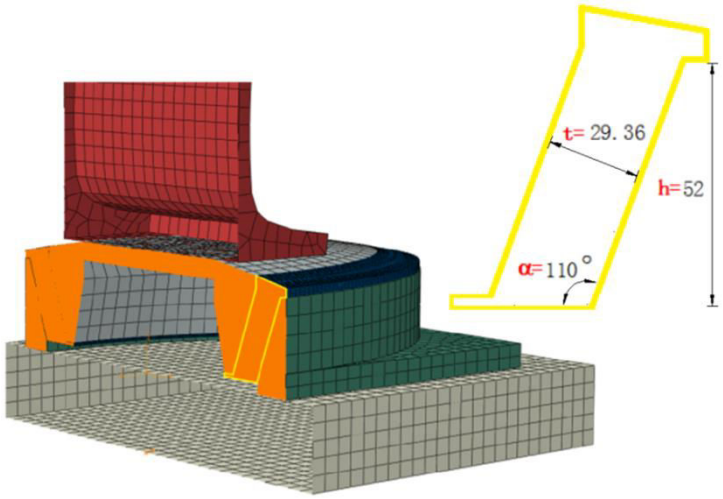

(a) The shear type fastening system

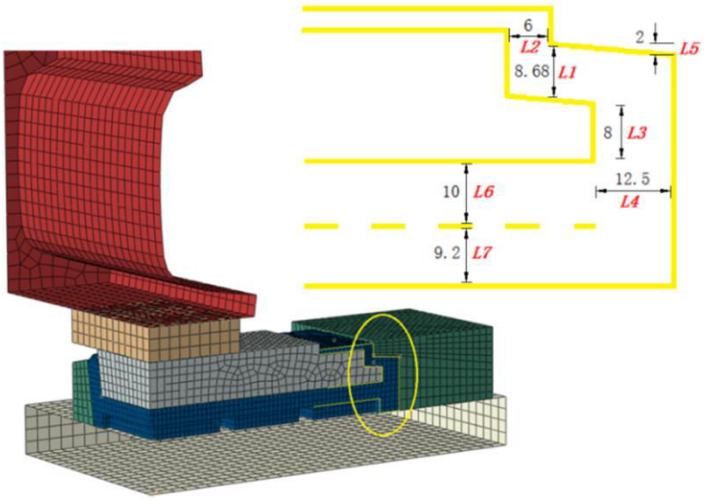

(b) The compressed type fastening system

Fig. 6:1 Geometric parameters of both fastening specimens

The rubber component of the compressed type fastening system is shown in Fig. 6:1 (b) and the important dimensions are also indicated on the top right corner. Since this compressed type specimen has relatively complex geometric properties, code numbers from L1 to L7 are used to represent each geometric parameter. As shown in the figure, the rubber component includes a main compression part and a connecting part relating the rubber component and the top and the bottom plates. The main compression part indicates the rectangle rubber pad on the bottom; the height is the sum of L6 and L7, where L7 is the depth of the grooves. The dimensions of the connecting component includes: width (L4) and height (L3) of the side strake, height (L1) and intersection angle (arc tan (2/L5)) of the non-shear connecting part, as well as the side strake width (L2) on the top. All the original values of these parameters are given in the figure. As the top plate is subjected to the wheel-rail force vertically, the L6-and-L7 part deforms in compression, the L3-and-L4 part, as well as L2 part deform in shear, and the L1-and-L5 part deforms in extension. Since the deformation of the rubber component is mainly compression, this specimen is of the compressed type fastening system.

6.2 The shear type fastening specimen

6.2.1 Parameter sensitivity analysis

6.2.1.1 Inclined angle

In Abaqus, inclined angle (α) of the rubber component in the shear type fastening system is changed. The inclined angle influenced quasi-static hysteresis loops and the loading curves are shown in APPENDIX A1 and the calculated vertical stiffness is depicted in Fig. 6:2, where the larger inclined angel gives rise to significantly enhanced vertical stiffness. The reason can be indicated through a simple stiffness formula $k_v = S_{load} \cdot E_v/t$ and $1/E_v = cos^2(\pi - \alpha)/E_c + sin^2(\pi - \alpha)/E_s$, where E_v is an effective material modulus in the vertical direction, S_{load} is the load bearing area, and E_c, E_s represent the initial compressive modulus and shear modulus of the rubber material.

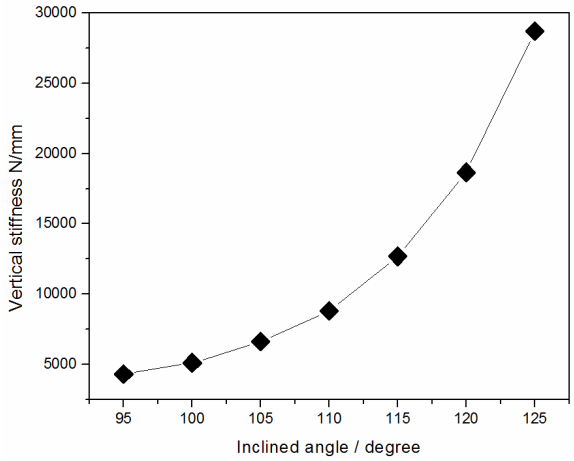

Fig. 6:2 Inclined angle dependent vertical stiffness

Corresponding to the formula, APPENDIX A2 gives the explanations by displaying the inclined angle influenced properties relevant to the vertical stiffness: APPENDIX A2 (a) shows that in order to keep the other parameters constant the loading area (or load bearing area) S_{load} increases with inclined angle; APPENDIX A2 (b) denotes that the effective modulus in the vertical direction E_v increases with the increasing inclined angle. This can be explained by the expression of the apparent vertical modulus $1/E_v = cos^2(\pi - \alpha)/E_c + sin^2(\pi - \alpha)/E_s$. Supposing E_c and E_s are kept constant, increasing the inclined angle will enhance E_v nonlinearly. In fact, this is ultimately due to the changing compression and shear ratio as discussed as follows. APPENDIX A2 (c) indicates that the compression and shear ratio increases linearly with the inclined angle. While the nonlinear relationship between E_v and α is given by $1/E_v = cos^2(\pi - \alpha)/E_c + sin^2(\pi - \alpha)/E_s$, the compression and shear ratio is defined as a linear expression $sin(\pi - \alpha)/cos(\pi - \alpha)$.

After obtaining the vertical stiffness value, natural frequency of the fastening system with different inclined angle are calculated in Abaqus. The first fourth oscillating modes and the frequencies are shown in APPENDIX A3. Since the first vibration mode is mainly in the vertical direction, we only make use of the first order natural frequency as shown in Table 6:1.

Alternatively, if we already have the quasi-static stiffness the natural frequency can also be calculated according to

$$f_n = 15.76\sqrt{K_v/M}, \tag{6:1}$$

Inclined angle (degree)	Natural frequency of the 1st order obtained by using Abaqus (Hz)	Vertical stiffness k_v *(N/mm)*	Natural frequency from the quasi-static vertical stiffness *(N/mm)*	Difference (%)
125	70.41	28705.85	68.36	2.9
120	57.41	18652.08	55.10	4.0
115	47.64	12689.14	45.45	4.6
110	39.06	8809.26	37.87	3.0
105	34.13	6632.60	32.86	3.7
100	30.10	5110.68	28.84	4.2
95	27.30	4302.66	26.47	3.1

Table 6:1 The compared natural frequency from simulation and calculation by using Eq. 6:1

where M is the weight of the railway track. The calculated natural frequency is compared in Table 6:1 in the fourth column. It can be seen that the differences between the simulated natural frequency and that derived from Equation 6:1 for each inclined angle are all below 5%.

After calculating the quasi-static vertical stiffness and natural frequency by using Abaqus, a family of dynamic experiments were simulated. The model with the inclined angle $\alpha = 95$ is used because it has a lowest vertical stiffness and natural frequency. The input cyclic loading is given by $F_{input} = F_0 + Asin(2\pi \cdot f \cdot t)$ where F_0, A, f are respectively the pre-load, the dynamic amplitude and the stimulating frequency; the displacement response can be simulated as $X_{res} = X_0 + Xsin(2\pi \cdot f \cdot t - \phi)$, where X_0 is the pre-compression corresponding to the pre-load, X is the displacement amplitude and ϕ is the phase lag, and the output force can be indicated by $F_{output} = F_0 + A'sin(2\pi \cdot f \cdot t - \phi)$, where A' is the output force amplitude. According to the simulation results, force transmissibility TR eventually can be defined as the ratio of the output force amplitude A' to the input force amplitude A. The simulated TR under different disturbance frequency are plotted in Fig. 6:3 with the black solid circles. On the other hand, force transmissibility can also be calculated by using the basic concept of a single-degree vibration system and the force transmissibility is expressed as

$$TR = \sqrt{\frac{1+(2\xi r)^2}{(1-r^2)+(2\xi r)^2}}. \tag{6:2}$$

where ξ is referred to as damping ratio and normally defined as $\xi = c/2\sqrt{K_v M}$ in a linear viscoelastic system. It correlates with the damping factor in Equation (1:3) following $\eta = 2\xi$. Supposing the damping ratio $\xi = 0.01$, we can find the simulated force transmissibility and the calculated values by using Equation (6:2) in good agreement. It confirms that rail

fastening systems can be explained by a single degree mass-spring system as shown in Fig. 1:5.

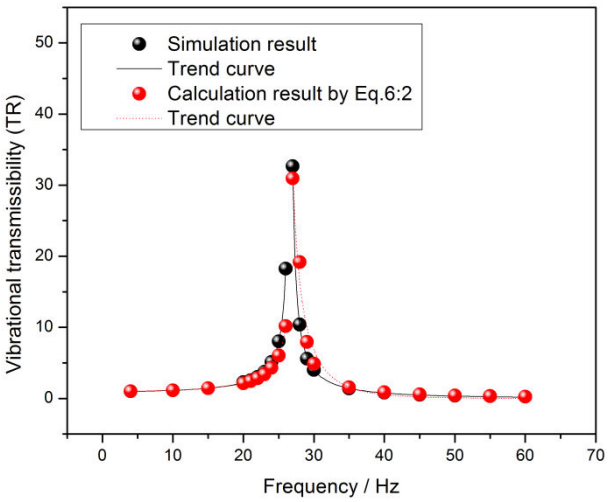

Fig. 6:3 The compared vibration transmissibility between the simulated and the calculated results

As a result, force transmissibility of all the other modified fastening systems including the original model can be calculated directly by using Equation 6:2. They are plotted in Fig. 6:4 (a). It should be noted that the input vibration force is isolated only when the ratio of the disturbance frequency f and the natural frequency f_n satisfies $f/f_n \geq \sqrt{2}$. Above that, the force transmissibility TR is less than 1.0, which indicates the isolated vibration force. If the force transmissibility TR is larger than 1.0, the input force will be amplified. Precisely, (1) a smaller inclined angle gives rise to a wider vibration isolation range. As for the varied model with 95° inclined angle under the disturbance of 40Hz, the force transmissibility is smaller than 1.0; however, for the model with inclined angle 125°, the vibration isolation range begins at 90 Hz; (2) changing the inclined angle can vary the system resonance frequency, it can also decrease the transmitted force amount for a given disturbance frequency and improve the vibration isolation for a given disturbance force; (3) as the disturbance frequency is rather high, inclined angle has fewer influences on the force transmissibility. In addition to the force transmissibility TR, another evaluation indicator of vibration isolation efficiency referred to as vibration reduction in dB reads:

$$W_{dB} = 20log(\tfrac{1}{TR}). \quad (6:3)$$

Since W_{dB} is more often used in rail fastening product report and other formal occasions, the data points in Fig. 6:4 (a) are transformed to be vibration reduction in dB and listed in APPENDIX A4. The smaller force transmissibility and the corresponding larger value of the vibration reduction in dB mean the higher vibration isolation efficiency. Similar conclusions can be drawn from APPENDIX A4 that the smaller inclined angle has the wider vibration isolation range and give a larger vibration reduction value in dB.

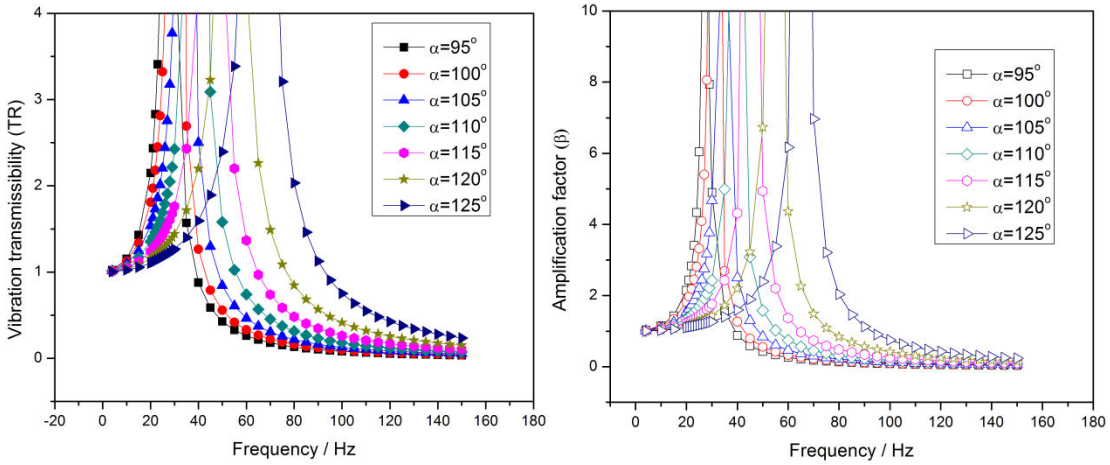

(a) Force transmissibility (b) The dynamic amplification factor

Fig. 6:4 Inclined angle influenced force and displacement response

Besides the force response, i.e. force transmissibility, displacement response is another key factor for the performance of vibration isolation systems. Dynamic displacement response of an isolation system $X_{res} = X_0 + Xsin(2\pi \cdot f \cdot t - \phi)$ under the input cyclic disturbance force $F_{input} = F_0 + Asin(2\pi \cdot f \cdot t)$ is often evaluated by an amplification factor β, defined as the ratio of responding amplitude X to A/K, where K is the static stiffness. Thus A/K can be considered as the static displacement response X_s, and the amplification factor is written as

$$\beta = \frac{X}{X_s} = \sqrt{\frac{1}{(1-r^2)^2+(2\xi r)^2}}. \quad (6:4)$$

The amplification factor β of different modified models throughout the frequency range of [5Hz, 150Hz] can be calculated by using Equation 6:4 and shown in Fig. 6:4 (b). It can be seen that Fig. 6:4 (a) and (b) look similar, which is because the damping ratio of the present rubber material is as small as 0.01, resulting in the similar transmissibility and amplification factor, i.e. $TR \approx \beta \approx \sqrt{1/(1-r^2)^2}$.

In fact, damping property of a rubber material is not only closely related to the relations between the force transmissibility and the dynamic amplification factor, also strongly influences on the amplitude of the force response and displacement response at resonance. From Fig. 6:5 we can see that it is the damping ratio that takes charge of reducing the force transmissibility as well as the dynamic amplification factor at resonance. The most obvious difference between the damping influenced force transmissibility and the amplification factor is in the high frequency range, where the higher damping value decreases β, whereas increases TR instead. This property will be further discussed in section 6.2.2.

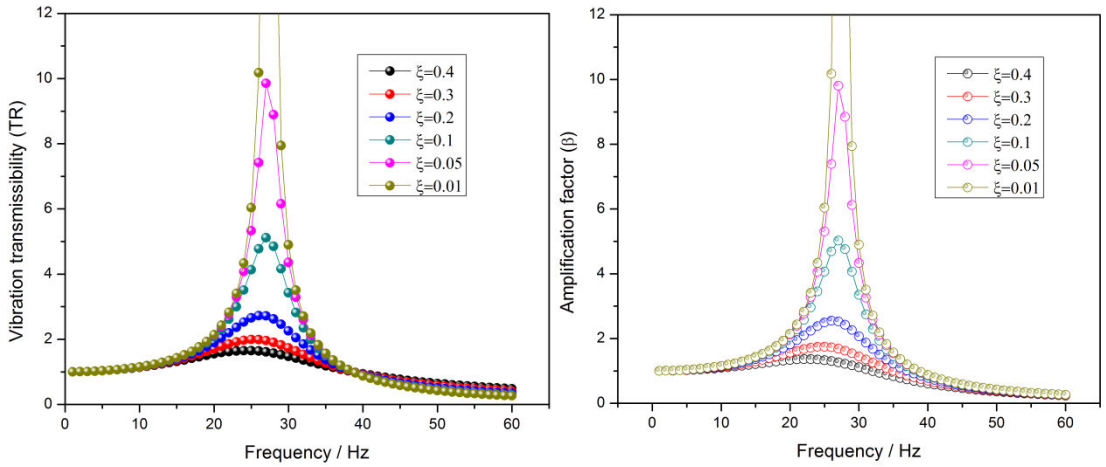

(a) Force transmissibility (b) Amplification factor

Fig. 6:5 Damping ratio dependent resonance response

As discussed above, decreasing inclined angle of the rubber component in the shear type fastening system can decrease the vertical stiffness and correspondingly reduce the system natural frequency. It can help to expand vibration isolation range, improve isolation efficiency at a given disturbance frequency; it also can help the system to avoid resonance happening and decrease the amplification factor for a given disturbance especially at high frequency range. In fact, there is another advantage of reducing the inclined angle: it will not bring about accompanying material cost. As Fig. 6:6 shown, when the inclined angle is decreased from 110° to 95° the vibration isolation for disturbance of 100Hz is increased by approximately 50% while the volume of the rubber component is increased by only 2%. That is to say modifying the inclined angle is an efficient measure for system optimization aiming at improving vibration isolation in the same while considering about material cost.

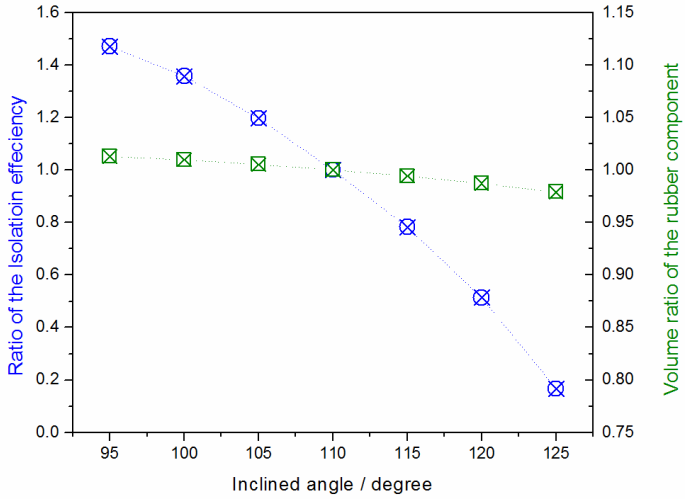

Fig. 6:6 The vibration isolation efficiency versus the volume of the rubber component

Mechanical fatigue is demonstrated in rubber-like materials by a progressive weakening of physical properties as a result of slow crack growth during application of dynamic loads. Correspondingly, a mechanical fatigue limit value comes into use. According to early references, mechanical fatigue failure does not occur on any realistic time scale as long as stress state is below the limit. Until the early 1930s, standard engineering practice for fatigue endurance design was to ensure that no applied stress exceeded the elastic limit of a material. This approach has proved to be inadequate and the overriding importance of local stress concentrations around structural flaws was thus realized. Hence, fracture mechanics approach was evolved. Small-scale crack growth is the slow incremental tearing of rubber, ultimately resulting in fatigue failure. One of the basic premises of fracture mechanics is the presence of natural defects or flaws in any object. Raw rubber material and reinforcing fillers such as carbon black exhibit various degrees of inhomogeneity on a microscopic scale. And all these in-homogeneities have one thing in common: they form highly localized stress concentrations that initiate fatigue failure.

The focus in fracture mechanics of rubber material is actually on fatigue crack propagation scale and speed. Traditionally, fatigue characteristics (and fatigue life) of rubber materials were depicted by a “Wohler” curve, also known as an S-N curve, where S denotes the applied dynamic stress for a stress-controlled test or, alternatively, strain for a strain-controlled test, and N is the number of cycle of input signals (or time) to failure limit. The most important feature of S-N curve is that upon reducing the dynamic stress or strain of input cycle toward a certain low value, fatigue life approaches infinity; on the opposite beyond the

limit value, the larger the input stress/strain amplitude is the earlier fatigue damage occurs. Most engineering elastomers don't dissipate the hysteretic heat generated during cyclic loading in short time. Failure is therefore compounded by the thermal effects especially under large deformation. As a result, local large strain/stress should be another key factor during rail fastening system optimization process.

Fig.6:7 shows the local maximum and minimum principle strain and the maximum shear strain of the rubber component during the deformation process. Clearly, the maximum and the minimum principle strain as well as the maximum shear strain increases with inclined angle. From the figure, the maximum tensile and compressive strain is about 70% and the maximum shear strain of 115% can be read. Such a large strain may result in thermal accumulation, and accelerate crack propagation speed eventually shorten fatigue life. In conclusion, in order to extend fatigue life of the shear type rail fastening system local dimensions should be optimized.

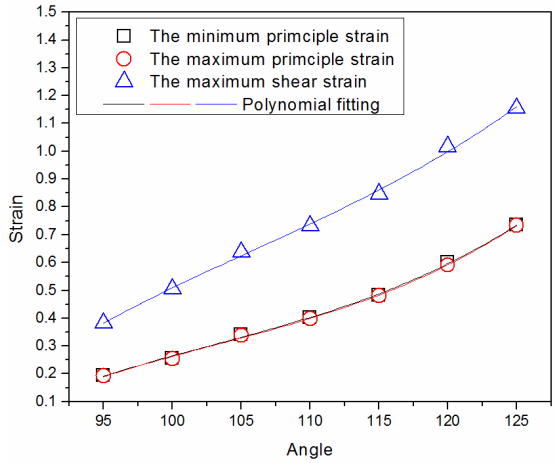

Fig. 6:7 The maximum local strain under the influence of inclined angle

Common technological methods of assessing the strength of rubber are standard tests such as tensile strength or tear measurements. In practice, rubber articles rarely fail due to crack growth in single loadings; instead, such failures are usually given by repeated loading. Though crack growth behaviour relevant to material failure occurs differently (normally more severity) from that relevant to fatigue applications. There are considerable evidences that fracture of rubber material is also initiated from imperfections inadvertently present or introduced in the body of the material or on its surface and the approach adopted for studying strength of rubber material is also fracture mechanics. From these imperfections, cracks may

grow under an applied stress, often slowly at first, until one or more of them reaches sufficient size for gross factor determining its strength. In other words, the crack growths of rubber material constitute the main factor determining its strength property and the maximum local stress is believed to be a direct cause of material damage. The local maximum stress should also be optimized as for rail fastening systems.

Fig. 6:8 depicts the inclined angle dependent local maximum stress during the whole deformation process. The minimum principle stress (black hexagon), the maximum principle stress (red star) and the maximum shear strain (blue rhombus) consistently increase with the inclined angles. When the inclined angle of the rubber component is modified to be 125°, the maximum tensile stress 4Mpa and the maximum shear stress of about 2.2Mpa are far away from the given strength from manufacturer, 12Mpa. Since rubber material has a much larger compressive strength, the maximum compressive stress is acceptable.

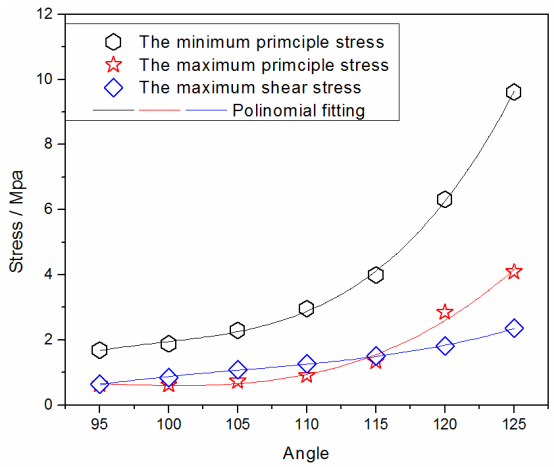

Fig. 6:8 The maximum local stress under the influence of inclined angle

In addition to the vertical properties as discussed above, a set of quasi-static virtual experiments in the lateral direction was also performed by using Abaqus. In Fig. 6:9, the displacement contour is shown as the rubber component is forced to deform laterally. We can clearly find that as the rubber component is loaded towards right both the top and the bottom free surfaces marked with the black circle bulge outside; on the opposite, all the free surfaces marked with a read circle shrink inward.

Fig. 6:9 Displacement contour under lateral load (half of the rubber component)

Similarly, we can read the lateral stiffness value from all the simulated quasi-static loading curves, and compare them to the vertical stiffness for each model with different inclined angles. From Fig. 6:10 we can see that, different from the consistently increasing vertical stiffness along with the inclined angle, there is a minimum lateral stiffness value in exist when the inclined angle is modified to be approximately 105°.

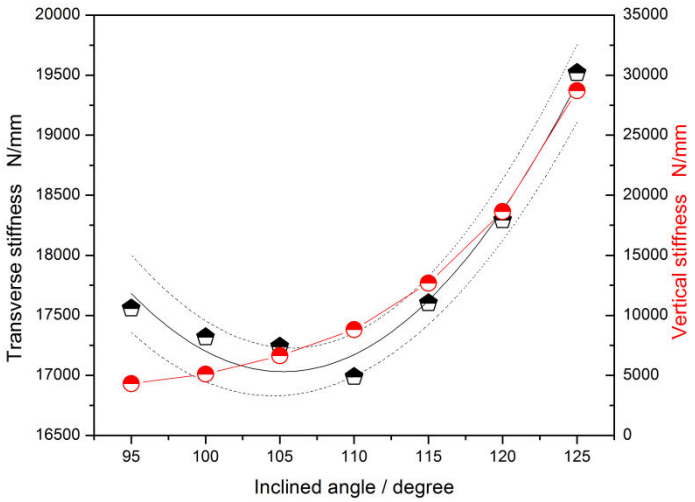

Fig. 6:10 Compared vertical and lateral stiffness

In order to give this variation tendency of the lateral stiffness an explanation, APPENDIX A5 depicts the inclined angle influenced properties relevant to the lateral stiffness. Similarly as the vertical stiffness, the lateral stiffness can be expressed as $k_l = \frac{S_{load} \cdot E_l}{t}$ and $\frac{1}{E_l} = \frac{sin^2(\pi-\alpha)}{E_c} + \frac{cos^2(\pi-\alpha)}{E_s}$. Exactly the same as APPENDIX A2 (a), the loading area increases with the inclined angle; however, totally different from the vertical effective modulus E_v as shown in APPENDIX A2 (b), the effective modulus in the lateral direction E_l decreases with inclined angle as shown in APPENDIX A5 (b). The increased S_{load} and the

decreased E_l let it making sense to have a lateral stiffness decreases firstly and increases next. Finally we have the vertical and lateral stiffness ratio depicted in APPENDIX A5 (c). With inclined angle increasing, the stiffness ratio is below 1.0 at first and gradually the vertical stiffness exceeds the lateral stiffness making the ratio larger than 1.0. We should pay special attention to the fact that it is the compression and shear ratio leads to the reduced E_v as inclined angle decreases, at which time shear deformation gradually dominate in the vertical direction; at the same time (as inclined angle decreases), it is also this compression and shear ratio giving rise to an increased E_l when the compressive deformation is increasingly dominant in lateral direction. We can see that the inclined angle is a very important geometric parameter for the rubber elliptical ring of the shear type fastening system. It determines the compression and shear ratio in the vertical and the lateral directions, consequently controls the vertical and lateral stiffness matching problem. For more information, see section 6.2.2.

6.2.1.2 Width

From Fig. 6:1 (a), the width of the rubber component, t, is another key geometric parameter. The width influenced quasi-static loops, the loading curves and the calculated vertical stiffness are shown in APPENDIX B1. Apparently, vertical secant stiffness decrease with increasing width and the reason can also be concluded from the formula $k_v = S_{load} \cdot E_v/t$ and $1/E_v = cos^2(\pi - \alpha)/E_c + sin^2(\pi - \alpha)/E_s$:

- since the inclined angle α and the loading area S_{load} are kept unchanged, the increased width t leads to the decreased k_v;
- obvious nonlinear variation tendency can be observed from the APPENDIX B1 (c), which conflicts with the influence of t on k_v. In order to explain this nonlinearity, the local maximum shear strain of the rubber component and the local maximum shear stress throughout the loading process are shown in APPENDIX B2. The maximum shear strain increases linearly with the decreased width while the maximum shear stress increases nonlinearly in APPENDIX B2 (a), resulting in the shear modulus E_s, as the apparent shear modulus, nonlinearly influenced by the width as shown in APPENDIX B2 (b). Decreasement of the width results in the increased shape factor S. The shape factor has a strong influence not only on the compressive modulus E_c but also on the shear modulus E_s especially when the combined compressive strain is relatively large. And this effect increases with the increasing

shape factor and the increasing compressive strain. In conclusion, both E_c and E_s are influenced by the varied shape factor, and the increasing compressive deformation. As a result, they give rise to the nonlinear feature of E_v as well as k_v.

After obtaining the width influenced vertical stiffness, we can easily calculate the corresponding system natural frequency, the force response and the displacement response. In terms of the stiffness value, the width influenced properties are similar as those influenced by the inclined angle. For the sake of brevity, they are not shown again herein. However, the differences between them, such as the material costs, the mechanical and the strength properties and the vertical and lateral stiffness ratio will be briefly compared as followed.

Modifying the width of the rubber component aiming at improving the vibration isolation efficiency is different from changing the inclined angle. Decreasing the inclined angle will not bring about the extra material cost as shown in Fig. 6:6. However, in order to improve the vibration isolation efficiency for the disturbance of 100Hz by 25% for example, the volume of the rubber component need to be correspondingly increased by 5% approximately through changing the width, see APPENDIX B3. As a consequence, from the material cost point of view, inclined angle modifying is a more reasonable measure compared with changing the width aiming at improving the vibration isolation efficiency.

For another, in order to avoid thermal accumulation in rubber component and acceleration of fatigue failure, local maximum deformation should be taken special attention during the parameter optimization. In APPENDIX B4, the maximum principle strain can be found reaching 85% and the minimum principle strain is about 45% as the component width is decreased to be 23.56mm. Furthermore, the tensile stress is as high as 11.77Mpa corresponding to maximum tensile strain 85%. Such a large local strain value is not only very easy to accelerate the crack development the corresponding large stress also nearly approaches the breaking strength (12Mpa) of present rubber material. The width of the rubber component, as a result, should have a prescribed minimum value to avoid the very large local strain and stress in exist.

The width influenced vertical stiffness was already discussed above, and the lateral stiffness values obtained from the lateral quasi-static virtual tests are compared in

APPENDIX B5 (a) and the vertical and lateral stiffness ratio is depicted in APPENDIX B5 (b). It can be seen that the lateral stiffness decreases with the increased width similar as the vertical stiffness does. And the vertical and lateral stiffness ratio almost remains unchanged at about 0.5. In brief, modifying the component width is different from changing the inclined angle also in term of the vertical and lateral stiffness ratio.

6.2.1.3 Height

Compared to inclined angle and the component width, height influenced hysteresis loops, loading curves and the vertical stiffness are similarly shown in APPENDIX C1. Clearly can be seen from the figures, the increasing component height gives rise to the enhanced vertical stiffness. With the same vertical stiffness formula $k_v = S_{load} \cdot E_v/t$ and $1/E_v = cos^2(\pi - \alpha)/E_c + sin^2(\pi - \alpha)/E_s$, the expression of the loading area for the elliptical ring can be written as $S_{load} = [2\pi b + 4(a - b)] \cdot h/sin(\pi - \alpha)$, where a is the inner major axis of ellipse, b the minor axis. As a result, when the inclined angle α and the width t are kept constant, vertical stiffness k_v increases linearly with the component height h.

As mentioned above, extra material cost will accompany with the improved vibration isolation capability by modifying the component width, whereas changing the inclined angle has no effect on the component volume. Herein, decreasing the component height may reduce the amount of the rubber material in the mean while improving the vibration isolation efficiency, see APPENDIX C2.

Large local strain values are also inspected as the height is amended. For the maximum component height 64mm, the minimum principle strain is increased from 34% to 45% while the maximum principle strain enlarges from 64% to 84%. APPENDIX C3 shows the corresponding maximum shear stress and the minimum principle stress. Both of them increase with the modified height, but they are far away from the strength limit.

At last, the vertical and lateral stiffness relation dependent on the modified component height is similar as that influenced by component width. In APPENDIX C4 (a), the lateral stiffness increases with the component height linearly as the vertical stiffness does; in APPENDIX C4 (b), the vertical and lateral stiffness ratio also keeps almost unchanged at the initial value 0.5. It can be seen that the decreased component width and the increased

component height don't have much influence on this compression and shear ratio in both vertical and transverse directions.

6.2.2 Structural optimization

6.2.2.1 Vibration isolation requirement

(A) Problem: The original version of the shear type fastening system is subjected to a sinusoidal vibration force $F = F_0 + Asin(2\pi \cdot f \cdot t)$ at 100Hz, i.e. $f = 100\ Hz$, where F_0 is a static preload and A is the dynamic amplitude. Supposing $F_0 = 22.4kN,\ A = 5kN$ and the input disturbance force is only in the vertical direction, the object is to optimize the original geometries of the rubber component that provides 20% more isolation reduction in dB. Note: vibration efficiency of the initial model is 15dB at 100Hz and the damping ratio was determined as $\xi = 0.01$.

To begin the optimization, Equation 6:3 is used to find the proper force transmissibility $TR = 0.126$ that satisfies the improvement of the vibration reduction from 15dB to 18dB for 100Hz. And then according to Equation 6:2 and Equation 6:1, the proper frequency ratio and the system natural frequency can be obtained as $r = 2.99$ and $f_n = 100Hz \cdot r = 33.45Hz$. Finally the objective vertical static stiffness of the rail fastening system is found to be $k_v = 6449\ N/mm$ by using Equation 6:1. Compared with the initial vertical stiffness $8800\ N/mm$, the objective value is decreased by 26.7% to accommodate the requirement.

(a) Supplementary requirement 1: While keeping the vibration reduction of 18 dB for the 100Hz disturbance force, keep the vertical and lateral stiffness ratio unchanged.

According to section 6.2.1.1, inclined angle of the rubber component of in the shear type fastening system should not be modified when the vertical and lateral stiffness ratio is required to be remained. The supplementary requirement demands that the lateral stiffness keeps pace with the vertical stiffness. As analysed in sections 6.2.1.2 and 6.2.1.3, alternative approach as flowed can be adopted:

- increasing the width of the rubber component by about 14% ;

- decreasing the height of the rubber component by about 18%.

Any of them can be used if there is no other additional requirements are presented. However, from the material cost point of view the second measure is more reasonable.

(b) Supplementary requirement 2: While keeping the vibration reduction of 18 dB for the 100Hz disturbance force in the vertical direction, let the lateral stiffness increased by only 2%.

As mentioned above, vertical stiffness should be decreased by 26.7% from 8800 N/mm to meet the vibtation isolation optimization requirement. The second supplementary requirement actually demands to accommodate the vertical and lateral stiffness ratio in term of increasing the lateral stiffness by 2%. From the analysis in section 6.2.1.1, the inclined angle of the rubber elliptical ring should be decreased to 104^o in order to obtain a vertical stiffness of $k_v = 6449\ N/mm$. Accordingly, the lateral stiffness is becoming 1.8% higher, which can be read from Fig. 6:12 and the corresponding lateral stiffness becomes $k_l = 17300\ N/mm$. It can meet the second supplementary requirement.

Though modification requirements presented above is filled, there are still a few deficiencies as for the current shear type fastening system such as:

- as discussed above, the force transmissibility was decreased in order to improve the vibration isolation efficiency from 15dB to 18dB for the given disturbance of 100Hz. In the same while, amplification factor is also reduced from 0.181 to 0.126 at the given 100Hz. However, the decreased amplification factor β at a given vibration frequency does not mean a smaller displacement response amplitude especially near the resonance frequencies; on the contrary, the reduced vertical stiffness enlarges the quasi-static displacement and may also correspondingly increase the dynamic displacement amplitude. In addition, as for a rail fastening system, the real working condition is much more complex than a single cyclic frequency (100Hz). Severe vibrations near the resonance frequency or overlap one of the overtones may happen. At this condition, a decreased vertical stiffness giving rise to the reduced force transmissibility and dynamic amplification factor need to be balanced to the

decreased quasi-static stiffness in order to make the responding displacement amplitude under control.

Specifically, the pre-compression of the original model with the vertical stiffness and the modified model with $k_v = 6449N/mm$ under a static pre-load of 22.4kN are respectively $X_0 = 2.55mm$ and $X_0 = 3.47mm$. The pre-compression is superimposed by the responding dynamic displacement amplitude X as they are subjected to a sinusoidal vibration force $F = 5kN \times sin(2\pi \cdot f \cdot t)$. Considering about the worst case when the disturbance frequency approaches to the resonance frequency, the dynamic displacement amplitude of the original and modified fastening system can be obtained as $X = \beta \frac{A}{k_v} \approx 50 \times 5000\ /8800 = 28.41\ mm$ and $X = \beta \frac{A}{k_v} \approx 50 \times 5000\ /6449 = 38.77\ mm$, respectively when the damping ratio equals 0.01. From the calculating result we can see that, though decreasing the vertical stiffness from 8800N/mm to 6449N/mm can efficiently improve the vibration reduction from 15dB to 18dB for disturbance force of 100Hz and also reduce the dynamic amplification factor at 100Hz from 0.181 to 0.126, it strongly enlarged the pre-compression X_0 and the dynamic displacement amplitude X especially when the disturbance frequency approaches to the system natural frequency. It can be imagined that such high responding displacement amplitude may bring about considerably large compressive strain of $\varepsilon_c = 49\%$ and shear strain of $\varepsilon_s = 135.94\%$, which may very possibly speed up the thermal mechanical fatigue and even fatigue damage. More information can be referred to section 6.2.2.2.

- one of the consequence of the second supplementary requirement is the varied vertical and lateral stiffness ratio, $k_v/k_l = 0.37$. Supposing the vertical displacement x_v is three times larger than the lateral displacement x_l, i.e. $x_v/x_l = 3$, the ratio between the lateral force and the vertical direction thus can be obtained for both initial and the modified system respectively as $F_l/F_v = 17000/8800\ /3 = 0.64$ and $F_l/F_v = 17300/6449\ /3 = 0.89$. This lateral and vertical reactive force ratio is always supposed to be an important indicator of the vehicle traveling safety when the vertical wheel-rail force and the lateral wheel-rail force are integrated, and it is normally referred to as derailment coefficient Q/T. $Q/T = 0.8$ is a standard safety upper limit. Apparently, the modified model with the vertical and lateral stiffness ratio gives rise to a derailment coefficient larger than 0.8. In brief, a reasonable vertical and lateral stiffness ratio k_v/k_t is rather important during the product designing and structural optimization process. For more information, see section 6.2.2.4.

6.2.2.2 Damping properties

(B) Problem: Keep the maximum dynamic displacement amplitude below 4mm throughout 0-100Hz frequency range while maintaining 18dB isolation reduction of 100Hz disturbance force.

The maximum dynamic displacement amplitude arises when resonance happens, i.e. $f \approx f_n = 33.45Hz$, at which time the amplification factor is acceptable to be reduced as $\beta \approx 1/2\xi$. A new damping ratio $\xi = 0.3$ is adopted instead of the initial value $\xi = 0.01$. Correspondingly, a dramatically decreased amplification factor is now obtained as $\beta \approx 1.7$. Fig. 6:11 shows the force transmissibility calculated by using the increased damping ratios. Selecting the appropriate curve with the damping ratio $\xi = 0.3$, it can be used to find the frequency ratio required to provide the force transmissibility equalled to 0.126 at the frequency 100Hz in order to meet the requirement of 18dB vibration reduction. In the figure, the curve for $\xi = 0.3$ intersects with the $TR = 0.126$ line at $r = f/f_n = 5.2$, where $f = 100Hz$ and thus $f_n = 100Hz/5.2 = 19.23Hz$. The vertical stiffness of current rail fastening system is determined as $k_v = 2131.4\ N/mm$. With current vertical stiffness, the maximum dynamic displacement is found to accommodate the damping property optimization requirement as $X = A/2\,\xi k_v = 5000\ /2131.4/\ 0.6 = 3.98mm < 4mm$.

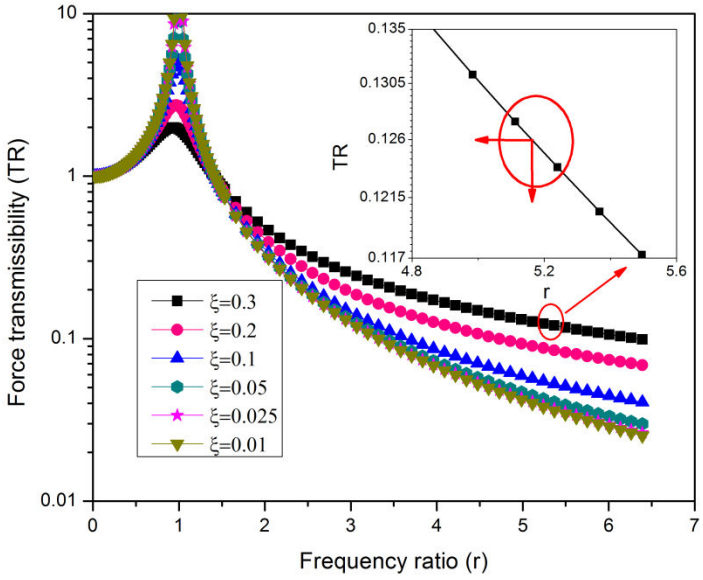

Fig. 6:11 Force transmissibility obtained by using different damping factor

We should pay some attention to that in Fig. 6:11 the increased amount of damping gives rise to the reduced force transmissibility in the isolation range. In other words, in order to achieve the same isolation efficiency of 100Hz disturbance, a lower damping factor $\xi = 0.01$ demands a higher value of vertical stiffness $k_v = 6449\ N/mm$ while a larger damping factor $\xi = 0.3$ corresponds with a smaller vertical stiffness $k_v = 2131.4\ N/mm$. From this point of view, balancing ξ and k_v is another key factor during the optimization process, see section 6.2.2.3.

6.2.2.3 The total responding displacement amplitude

(C) Problem：Keep the total responding displacement below 10mm as the system is subjected to a combined static and dynamic loading $F = F_0 + Asin(2\pi \cdot f \cdot t)$ where $F_0 = 22.4kN$ and $A = 5kN$, in the meanwhile satisfying the requirements in 6.2.2.1 ($W_{dB} = 18dB\ for\ disturbance\ force\ of\ 100Hz$) and 6.2.2.2 (dynamic displacement amplitude at resonance $X < 4mm$).

As discussed above, in order to obtain the minimum dynamic displacement amplitude X_{min} a maximum value of $k_v \cdot 2\xi$ should be determined rather than a maximum stiffness k_v or a maximum damping ratio ξ. By using Equation 6:2 the force transmissibility calculated with different damping ratios are shown in Fig. 6:12. Repeating the same procedure as presented in Fig. 6:11, proper frequency ratio required to provide the force transmissibility of 0.126 for the 100Hz disturbing vibration can be read from the figure. Intersects of all the curves with the *TR=0.126* line are emphasized in the shaded area in Fig. 6:12 (a) and zoomed in in Fig. 6:12 (b). The resulted frequency ratio r, the natural frequencies f_n and the vertical stiffness k_v with different damping ratio ξ are listed in Table 6:2. It is clear to see that r, f_n and k_v all increase with the increasing damping ratio ξ, except $k_v \cdot 2\xi$. There is a peak value of this $k_v \cdot 2\xi$ as the damping ratio values 0.2 and the maximum product is about 1455.5. Finally, the minimum dynamic displacement amplitude are obtained with a damping ratio of 0.2 $\mathrm{X_{min} = A/(k_v \cdot 2\xi) = 5000\ N/1455.5\ N/mm = 3.4m}$. We can see now the damping ratio $\xi = 0.3$ in section 6.2.2.2 is obviously not the most reasonable solution.

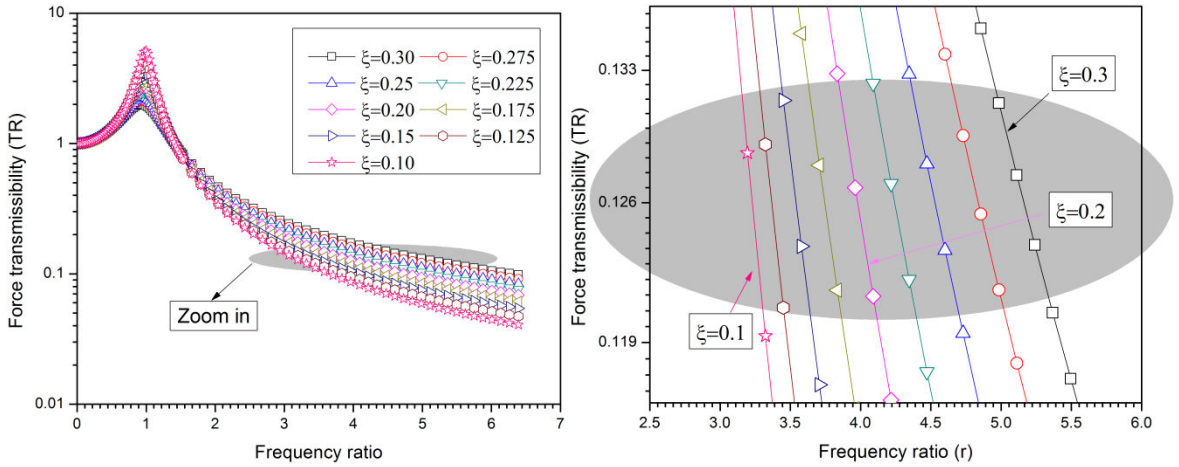

(a) Macroscopic diagram (b) Detailed diagram

Fig. 6:12 Force transmissibility under the influence of damping factor

Damping ratio ξ	**0.10**	**0.125**	**0.15**	**0.175**	**0.20**	**0.225**	**0.25**	**0.275**	**0.3**
Frequency ratio r	3.2	3.4	3.5	3.7	4.0	4.2	4.5	4.8	5.2
Natural frequency f_n (Hz)	31.25	29.41	28.57	26.70	25.13	23.58	22.07	20.83	19.23
Vertical stiffness k_v(N/mm)	5628.8	4986.0	4705.2	4107.5	3638.7	3204.6	2807.5	2501.7	2131.4
$k_v \cdot 2\xi$	1125.8	1246.5	1411.6	1437.6	1455.5	1442.1	1403.8	1375.9	1278.8

Table 6:2 Balancing of the damping ratio and the vertical stiffness

The vertical stiffness $k_v = 3638.7\ N/mm$ can be read from Table 6:2 corresponding to the damping ratio $\xi = 0.2$, and the resulting static displacement as the isolation system is subjected a 22.4kN preload is $X_0 = 6\ mm$. The total displacement is now decreased to meet the requirement $X_{total} = X_0 + X_{min} = 9.4mm < 10mm$. At this moment, the mean compressive strain and the shear strain are approximately 11% and 30% respectively, both of them are acceptable for the real application.

6.2.2.4 Vertical and lateral stiffness matching

As discussed above, a well matched vertical stiffness k_v and the lateral stiffness k_l is necessary to guarantee the train traveling safety. Assuming n is the vertical versus lateral displacement ratio when the fastening system is subjected to the wheel-rail force together in both directions, i.e. $u_v/u_t = n$, accordingly a derailment coefficient Q/T is obtained to estimated whether a given vertical and lateral stiffness ratio is acceptable to meet the safety requirement as below:

$$\frac{Q}{P} = \frac{F_l}{F_v} = \frac{1}{n} \cdot \frac{k_l}{k_v} < 0.8. \tag{6:5}$$

As for the original version of the shear type fastening system, the vertical stiffness k_v, the lateral stiffness k_l and the damping ratio ξ are respectively $k_v = 8800\ N/mm$, $k_l = 17000\ N/mm$ and $\xi = 0.01$; the modified fastening system as the result of 6.2.2.1, 6.2.2.2 and 6.2.2.3 provides a vertical stiffness $k_v = 3638.7\ N/mm$ and a damping ratio is $\xi = 0.2$. Supposing $k_v = 3638.7\ N/mm$ is achieved by amending the width or the height of the rubber component, vertical and lateral stiffness ratio will remain unchanged at about 0.5 and a counterpart lateral stiffness becomes $k_l = 7016.87\mathrm{N/mm}$. Eventually, the result needs to meet $\frac{1}{n} \cdot \frac{k_l}{k_v} < 0.8$ and n should be also determined before the optimization process.

6.2.2.5 Local geometry optimization

After obtaining the objective vertical stiffness k_v and a well matched lateral stiffness k_l, all the other work is to finalize a proper geometric optimization proposal. Besides the geometric sensitivity analysis and the material cost as mentioned above, slenderness ratio t/l of the rubber component and the local maximum tensile, compressive as well as shear strain and the maximum stress are also key factors.

As mentioned above, the vertical stiffness can be determined by

$$k_v = S_{load} \cdot E_v / t, \tag{6:6a}$$

$$1/E_v = cos^2(\pi - \alpha)/E_c + sin^2(\pi - \alpha)/E_s, \tag{6:6b}$$

$$S_{load} = [2\pi b + 4(a - b)] \cdot h/sin(\pi - \alpha) \tag{6:6c}$$

where a is the major axis of ellipse, b the minor axis, α the inclined angle and h the height of the rubber component. The vertical stiffness can thus be directly expressed as

$$k_v = \frac{[2\pi b + 4(a-b)] \cdot h \cdot E}{sin(\pi - \alpha) \cdot t}. \tag{6:7}$$

It keeps consistent with the simulation result. From Equation 6:7 we can see that any of the following measures can be adopted to modify the stiffness value in order to improve the

vibration isolation efficiency: increasing the width t, decreasing the inclined angle α or reducing the height h. However, these three factors are restricted to each other to some extent. For instance, the shear modulus would be greatly influenced by tensile and bending deformation as slenderness ratio t/l is larger than 25%, or it may result in a much smaller apparent shear modulus than the real value. Hence, for the purpose of using the real material modulus, Equation 6:7 can be transformed to satisfy

$$\frac{t \cdot sin(\pi-\alpha)}{h} = \frac{[2\pi b+4(a-b)] \cdot E}{k_v} \leq 0.25, \quad (6:8)$$

where the left side of the equation is the slenderness ratio t/l, and both sides of the equation have to satisfy the inequality. In order to meet Equation 6:8 in the meanwhile decreasing the vertical stiffness to be 3638.7N/mm, three alternative measures could be introduced:

- keep the major and the minor axis of the ellipse a and b fixed, while decreasing the material modulus E to be approximately 0.3Mpa. However, such small modulus for an engineering elastomer is too soft in the real practice;
- on the opposite, keeping the material modulus E unchanged and modifying the elliptical sweeping trace. Assuming that a and b satisfy $a - b = 40\ mm$, the modified major and the minor axis are respectively $a = 101mm$ and $b = 41mm$;
- modifying the material modulus and the sweeping trace simultaneously.

If the second measure is adopted, Equation 6:8 becomes $\frac{t \cdot sin(\pi-\alpha)}{h} = \frac{[2\pi b+4(a-b)] \cdot E}{k_v} = 0.25$. Noting that the original value of $\frac{t \cdot sin(\pi-\alpha)}{h}$ is about 0.38. If the the vertical and lateral stiffness ratio is kept constant: enhancing the height h from 52mm to 78mm or diminishing the width t from 29.36mm to 13.8mm can meet the requirement. If the first method is adopted, the loading area S_{load} is also increased to be $25268.1\ \text{mm}^2$. Furthermore, since the modified vertical stiffness values 3638.7 N/mm, the maximum total displacement and the mean compressive strain as well as the shear strain are respectively $u_v = F_{max}/k_v = (22400\ N + 5000\ N)/3638.7\ N/mm = 7.5mm$, $\varepsilon_c = \frac{u_v sin\theta}{t} = \frac{2.57mm}{29.36\ mm} = 8.7\%$ and $\varepsilon_s = \frac{u_v cos\theta}{t} = \frac{7.05\ mm}{29.36\ mm} = 24\%$. On the other hand, if the second measure is adopted, the loading area S_{load} value $16845.4\ \text{mm}^2$ and the mean compressive and the shear strain are respectively $\varepsilon_c = 18.6\%$ and $\varepsilon_s = 51\%$. Though the resulting mean shear stress by using both methods is acceptable,

the first solution is better than the second from the perspective of minimizing strain and stress of rubber component; while from the material cost point of view, the second method is better than the first.

Sometimes during the geometric parameter optimization, very large local strain and stress may arise. Taking the modified model *t=23.36mm* for example, from the simulation results we can see the maximum compressive strain of about 65% existing in the local part of the rubber component although the mean compressive strain is only 12.4%. That is, the local maximum strain/stress is sometimes more important than working strain/stress during design and optimization process. In section 6.2.2.6 free surface optimization will be illustrated in order to eliminate the unreasonable dimensions in detail and correspondingly diminish local strain and stress.

6.2.2.6 Free surface optimization

Rubber material is characterized as high elasticity, large deformation and incompressibility, as a result improper deformations may arise at some local parts of the rubber component. Throughout the loading process, largely deformed component or loading discontinuity may give rise to wrinkle, crease, folds even self-contact of the rubber component in rail fastening systems. Overriding importance of such improper deformations with local large strain and stress concentrations around structural flaws was realized to speed up the small-scale crack growth. They are all potential menace for the component's mechanical fatigue and damage. The free surface optimization can substantially approve the deforming behaviour of the rubber component. As followed are the compared deformation features of the original model and that with the modified free surface, see Fig. 6:13. Due to the worst dimension optimization result as shown in section 6.2.1.2, the model with $t = 23.36mm$ is taken for example. Fig. 6:13 (a) indicates the original state of model; Fig. 6:13 (b-h) compare the vertical displacement, the maximum compressive strain, tensile strain, shear strain and the maximum compressive stress, tensile stress as well as the shear stress respectively. From Fig. 6:13 (a) and (b) we can see that both the top and the bottom free surfaces are optimized resulting in the decreased vertical displacement (U3): on the top U3 is reduced from 7.763mm to 6.98mm while on the bottom it is decreased from 2.31 to 1.838mm avoiding the contact between the rubber component and the shaking table. From Fig. 6:13 (c-

h), we can see that the maximum compressive strain, tensile strain and the shear strain decrease respectively by 27%, 31.5% and 15.6%; the maximum local compressive stress, tensile stress and the shear stress decrease respectively by 23.5%, 55.3% and 32.6%.

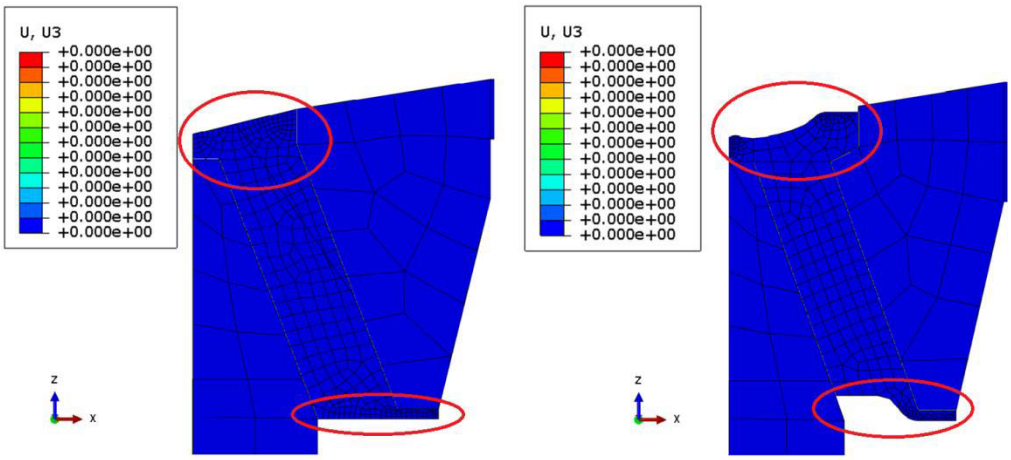

(a)The initial condition

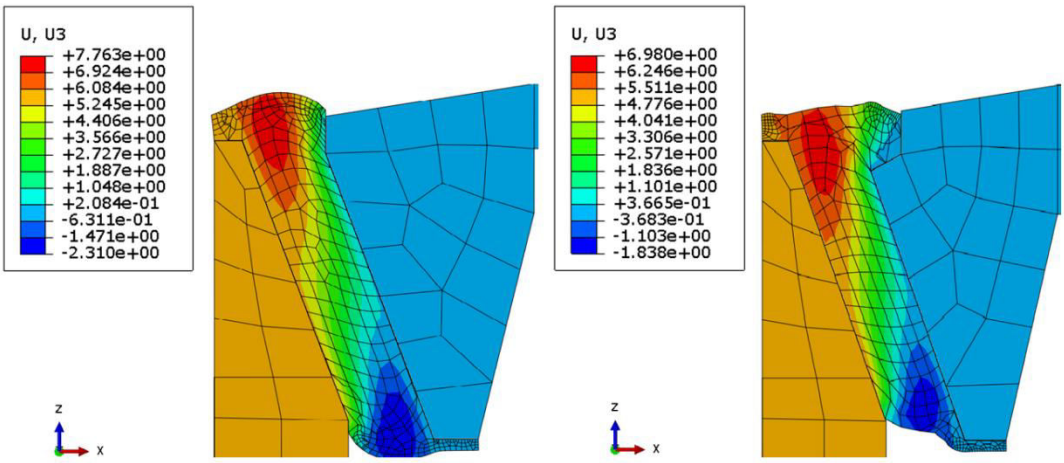

(b) Vertical displacement (U3) at the end of the loading process

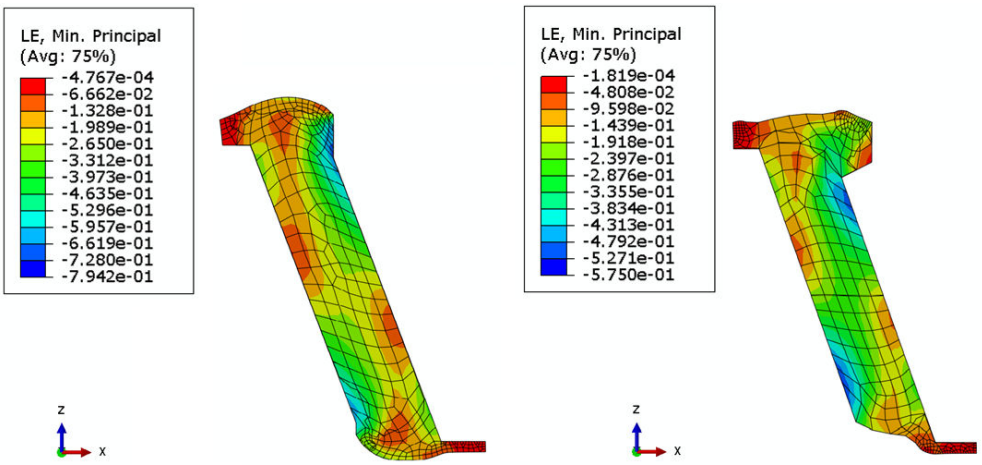

(c) The minimum principle strain (LE, Min. Principal)

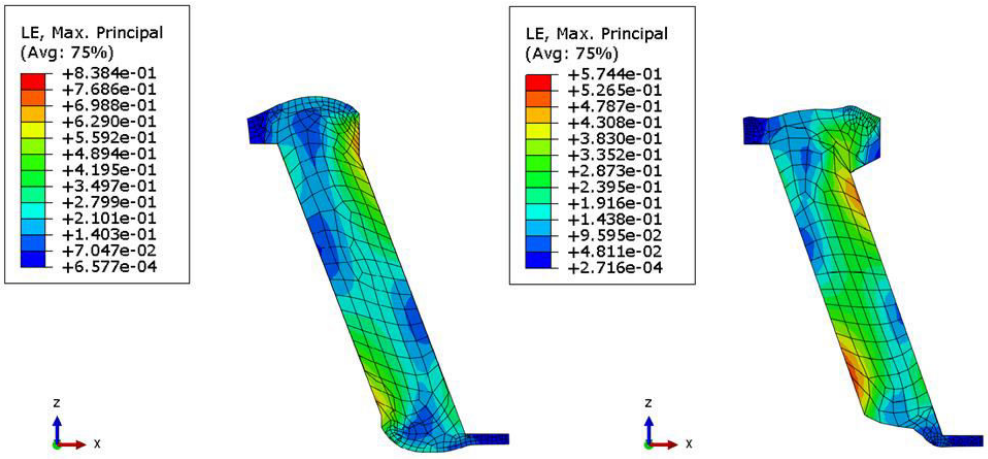

(d) The maximum principle strain (LE, Max. Principal)

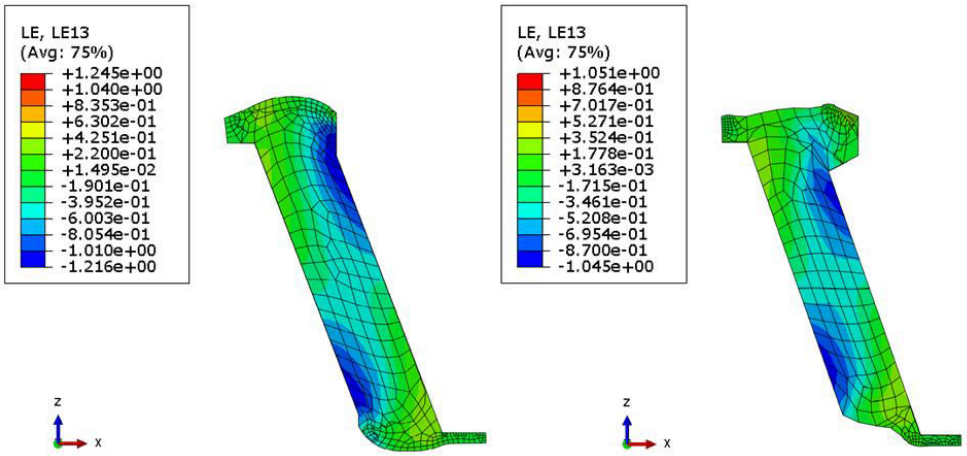

(e) The maximum shear strain (LE13)

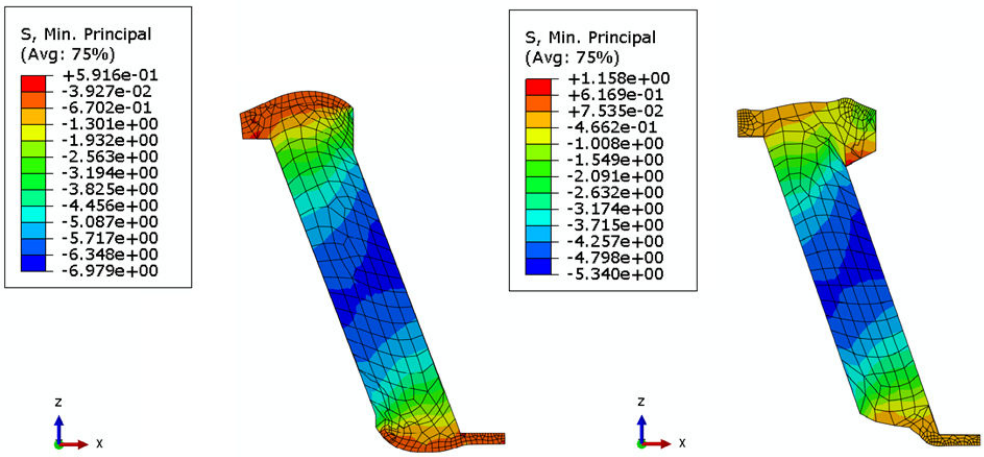

(f) The minimum principle stress (S, Min. Principal)

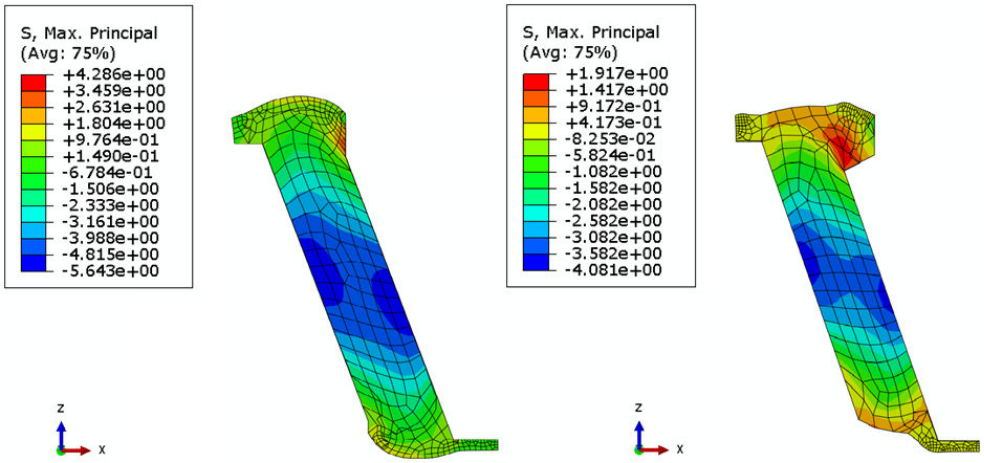

(g) The maximum principle stress (S, Max. Principal)

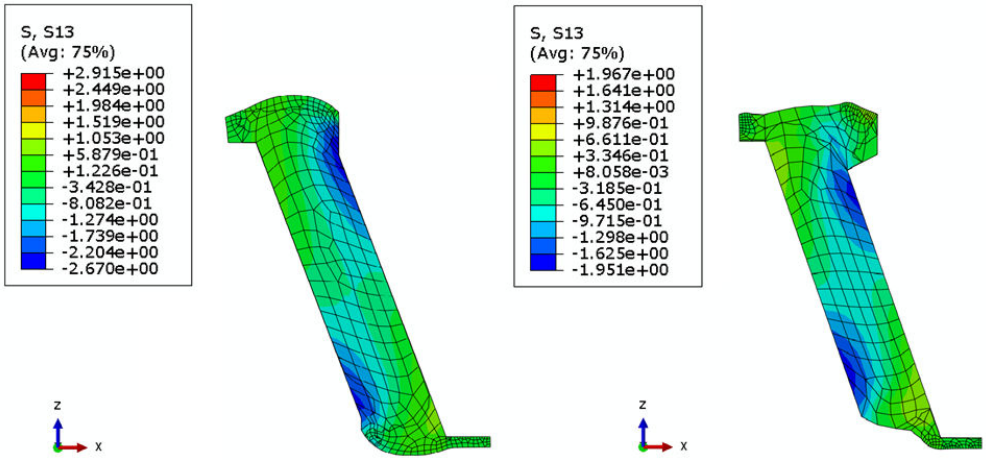

(h) The maximum shear stress (S, S13)

Fig. 6:13 Comparison between the original model and that with the modified free surfaces

6.3 The compressed type fastening system

6.3.1 Parameter sensitivity analysis

Similar as the parameter sensitivity analysing on the shear type fastening system in section 6.2.1, the geometric parameters of the compressed type fastening system is also studied through a family of quasi-static virtual experiment by using Abaqus. Referring to Fig. 6:1 (b), Fig. 6:14 shows the parameter (L1, L3, L4 and L7) influenced vertical stiffness. Correspondingly, APPENDIX D1-D4 depict the parameter influenced displacement-force curves. APPENDIX D5 also describes the parameter (L2, L5 and L6) influenced vertical stiffness. According to the calculation results the increasing, L2, L5 and L6 decrease the

vertical stiffness, however the effects on the vertical stiffness is not as obviously as L1, L3, L4 and L7 do. Generally speaking, the vertical stiffness of the compressed type fastening system k_v can be decomposed into four parts: two shear deformed parts with corresponding stiffness k_{s_top} and k_{s_bottom}, the extensile part with k_e and the main compressive part with k_c. Concisely, the vertical stiffness can be expressed as $k_v = k_{s\_top} + k_{s\_bottom} + k_e + k_c$. The increasing L1 decreases the vertical stiffness because k_e is reduced by L1 in term of $k_e = E_e S_{loading}/L1$. If the subscript e is changed to be s, the influence on the vertical stiffness by L3 and L4 can be explained by $k_s = E_s S_{loading}(L3)/L4$, where the increased L3 or the reduced L4 gives rise to the enlarged k_s and k_v; similarly, if the subscript is changed to be c, the decreased vertical stiffness influenced by the increased L7 can be explained by $k_c = E_c S_{loading}/(L6 + L7)$. It should be noted that the strong effect on the vertical stiffness

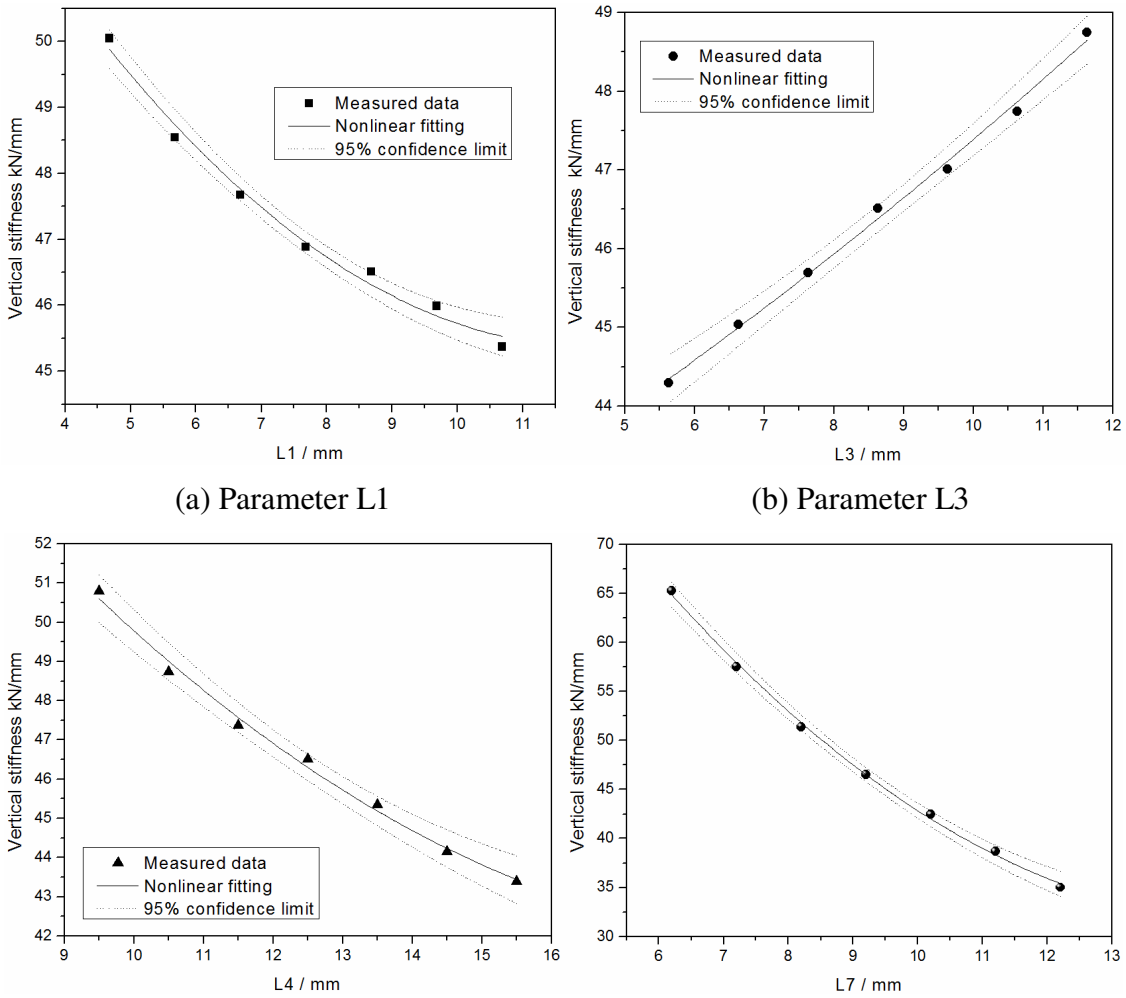

(a) Parameter L1

(b) Parameter L3

(c) Parameter L4

(d) Parameter L7

Fig. 6:14 Parameter influenced vertical stiffness of the compressed type fastening system

by L7 also because the additional L7 may bring more freely bulge surfaces, and a smaller shape factor may decrease the apparent compressive modulus E_c, eventually results in the reduced k_c and k_v.

Since modifying L4 and L7 are the most efficient measures to decrease the vertical stiffness, it is taken for instance to calculate the natural frequency and the vibration reduction in dB. Similar as the shear type fastening system, Equation 6:1 can be used to calculate the system natural frequency and the results compared to the simulated natural frequency in Abaqus is compared in APPENDIX E. Simulation results and the calculated results meet each other rather well. Solving Equation 6:2 and 6:3, APPENDIX F1 and F2 respectively display the calculated force transmissibility and the corresponding vibration reduction values with the modified L7. Since increased L7 results in the decreased vertical stiffness, it decreases the force transmissibility for a given disturbance frequency in the isolation range, and improves the vibration reduction efficiency; it also extends the vibration isolation range. When the damping ratio is increased from 0.01 to 0.2, the dynamic amplification factor calculated by Equation 6:4 are plotted in APPENDIX G. From the figure we can see that it is the damping factor decreasing the dynamic amplification factor, and the models have the similar maximum amplification factors at the resonance frequency with different system natural frequency controlled by L7; but the larger L7 affords the smaller amplification factor for a given frequency in the isolation range such as 150Hz.

As mentioned above, L2 influences on the vertical resilient properties much less than the other geometric parameters. However, it effects on the lateral stiffness strongly as.Fig.6:15 shows. From Fig. 6:15(a) we can see that L2 doesn't have much effect on the vertical stiffness whereas it largely decreases the lateral stiffness as L2 increases. Correspondingly in Fig. 6:15(b) the vertical and lateral stiffness ratio dramatically increases with L2.

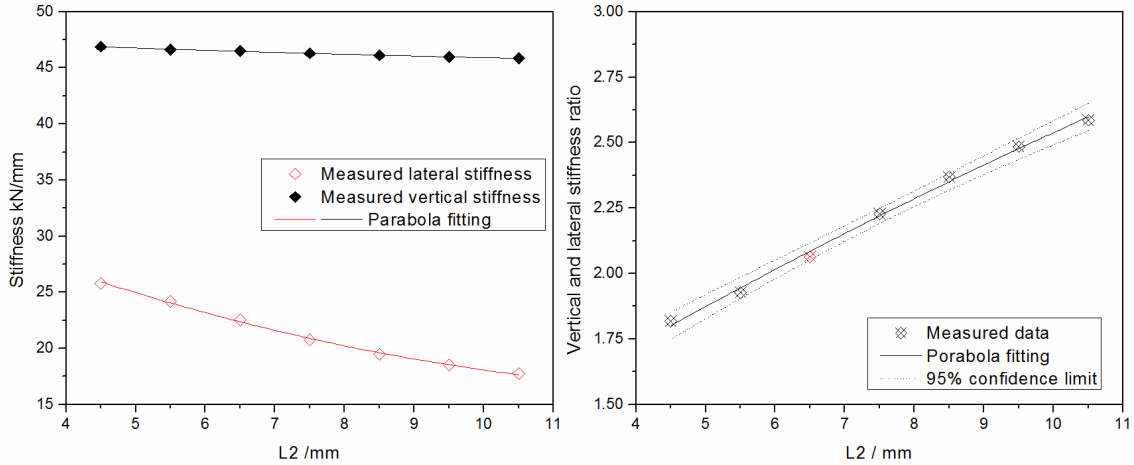

(a) Comparison of vertical and lateral stiffness (b) Vertical and lateral stiffness ratio

Fig. 6:15 L2 influenced vertical and lateral stiffness ratio

Besides L2, L3 also influences on the lateral stiffness more than vertical stiffness, resulting in the modified vertical and lateral stiffness ratio, see APPENDIX H1. Different from L2 and L3, the increasing L7 severely decrease the vertical stiffness whereas it has very little influences on the lateral stiffness; it decreases the vertical-and-lateral stiffness ratio efficiently as APPENDIX H2 depicted. Furthermore, we can see from APPENDIX H3 and H4 that L4 and L1 influence on the resilient properties in both lateral and vertical directions almost the same and the vertical-and-lateral stiffness ratio is nearly kept constant. At last, L5 and L6 also have little influences on the lateral stiffness.

From the fatigue and strength properties perspective, the parameters analysing were also performed. For example, APPENDIX I1 (a) shows that the decreasing L1 enlarges the maximum tensile strain and shear strain severely, while, in comparison, it has little influences on the maximum compressive strain. The corresponding maximum tensile stress should be taken special attention as shown in APPENDIX I1 (a). As L1 is decreased to be about 4.5, the maximum tensile stress almost approaches to the material strength limit. Not only in the vertical direction, when the model is subjected the lateral force as shown in APPENDIX I1 (b) the maximum shear strain is also enlarged to be nearly 100%. Such a large shear strain value also arises when L2 is decreased to be about 4.5 while the model is subjected the vertical force as shown in APPENDIX I2 (a), or when L4 is decreased to be about 9.5 while the model is loaded laterally as shown in APPENDIX I2 (b).

In other hand, we should also pay attention to the influences of L7 on the maximum strain values, see APPENDIX I3. Any other modified geometric parameter brings about a maximum compressive strain in the mean while giving rise to the maximum shear or/and tensile strain; however, the enlarged L7 gives rises to the reduced compressive strain while giving the increasing maximum shear and tensile strain values. It tells us though increasing L7 is the most efficient measure to reduce the vertical stiffness and ultimately improve the vibration isolation efficiency, there is an upper limit due to the concomitantly increasing shear and tensile strain. From this point of view, other methods should be adopted if lower resilient property is demanded.

6.3.2 Structural optimization

In section 6.3.1, all the important geometric parameters were studied in terms of the parameter influenced vertical stiffness, natural frequency, force transmissibility, dynamic amplification factor, vertical and lateral stiffness match, the maximum local strain and stress. Similar optimization problems can be presented in the same way as the shear type fastening system, and the similar solving method can also be obtained on the basis of the parameter sensitivity analysis. As a result, they are not going to be discussed again in this section. However, another optimization object will be proposed instead for the compressed type fastening system.

As mentioned above, the present fastening system deforms mainly in compression. The intrinsic large compressive modulus leads to the general higher stiffness property of compressed type fastening systems in comparison to the shear type specimen. It was also mentioned above that though L7 is a key parameter for the vertical resilience, there is a lower limit value because increasing L7 also brings about the enlarged local strain and stress. As a revelation from the egg-shape fastening system, modifying the compression and shear ratio of the rubber component can help to efficiently reduce the vertical stiffness.

In order to efficiently reduce vertical stiffness, the compressed type fastening specimen is modified to be a combined compressed-and-shear type system as shown in Fig.6:16 (b). Through introducing a reformatory top plate, two columns of rubber component are appended on above the compressive rubber pad. Compared with the cross section of the

original geometries as shown in Fig. 6:16 (a), we can see that when the fastening system is subjected to vertical wheel-rail load the newly introduced parts deform mainly in shear and the original compressive rubber pad still deforms in compression. According to the calculation results, the vertical stiffness is decreased to be 26.31kN/mm from 40kN/mm; besides, the lateral stiffness is also reduced to be 10.58kN/mm.

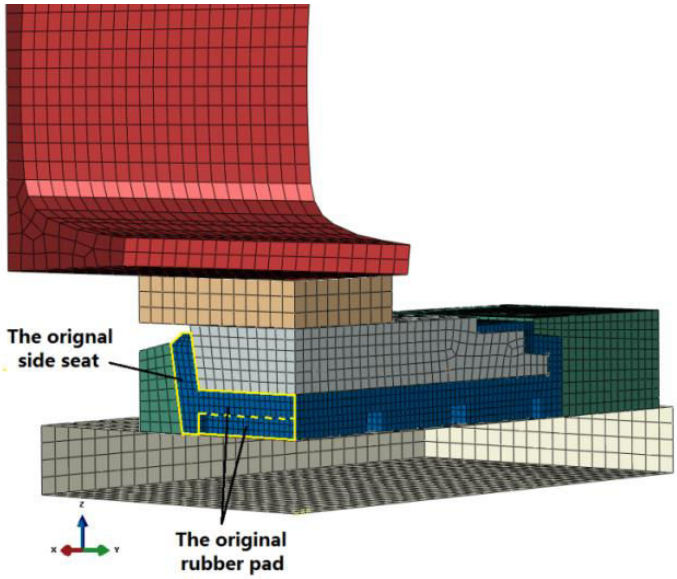

(a) The original model

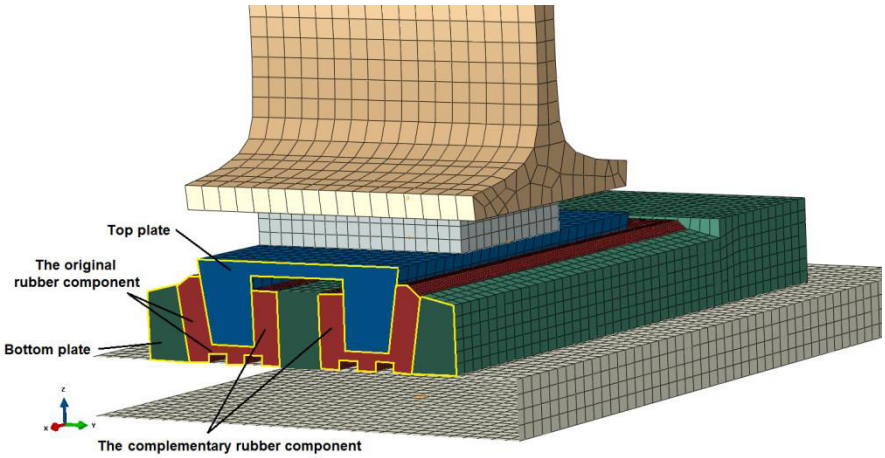

(b) The combined compression-and-shear type

Fig. 6:16 Comparison between the original compressed type fastening system and the combined compression-and-shear type model

If the vertical resilient features or the vertical-and-lateral stiffness ratio needs to be further optimized, the modified top plate can be changed in term of the inclination as shown in Fig. 6:17. The larger the inclination is the higher the compression-and-shear ratio and the

vertical stiffness will be. It can be efficiently used to balance the vertical and lateral stiffness properties.

If necessary, this compressed type fastening system also can be modified to apply as low vertical stiffness as 7.1kN/mm as Fig. 6:18 shows. The compressive pad of the rubber component is removed and all the responding elastic displacement is absorbed by the shear deformation. However, at this moment, the modified rail fastening system actually becomes a shear type highly resilient system. The lateral stiffness of this modified system is reduced to be 8.6kN/mm and the vertical-and-lateral stiffness radio is significantly changed to be less than 1.0.

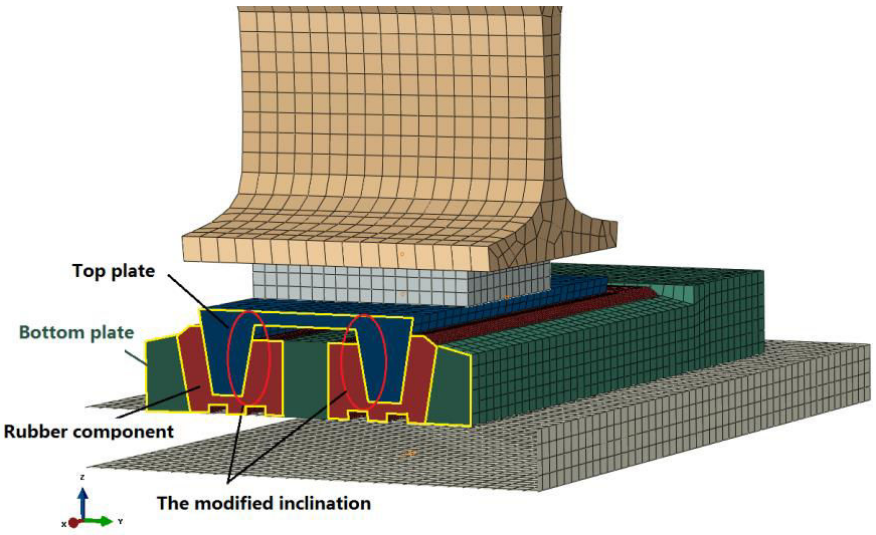

Fig. 6:17 Another combined compression-and-shear type model

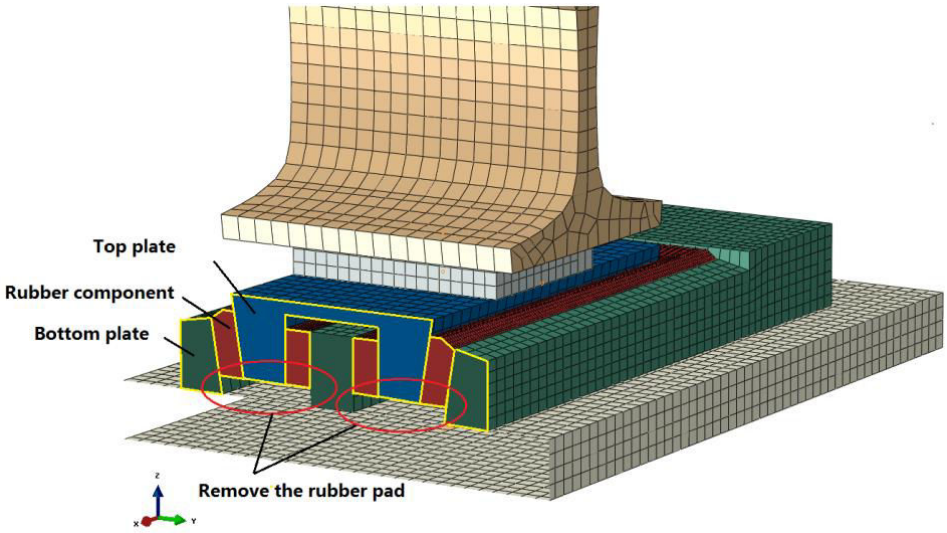

Fig. 6:18 The modified highly resilient fastening system

6.4 Summary

In this Chapter, sensitivity analysing of the geometric parameters of the both fastening systems were performed. As for the shear type specimen, the inclined angle of the elliptical ring, the width and the height of the component largely influence the vertical resilient property. And the inclined angle also strongly effects on the lateral resilience and the vertical-lateral stiffness ratio by adjusting the important compression and shear ratio in both directions. Subsequently, several optimization objects were proposed in terms of improving the vibration isolation efficiency, decreasing the displacement response, reducing the material cost, balancing the vertical and lateral stiffness ratio, diminishing the local maximum strain and stress values and damping property as well as free surface optimization. The corresponding solving process was also presented. As for the compressed type fastening system, similar parameter sensitivity analysing procedure was carried out. Influences on the vertical and the lateral elastic properties by each geometric parameter were explained by plotted figures. Since the similar optimization objects as presented for the shear type fastening system can be solved on the basis of the parameter sensitivity analysis in the same way, they were omitted for brief. However, if the compressed type fastening system is demanded lower stiffness, a combined compression-and-shear type fastening system is introduced by modifying the original model. If a well matched lateral stiffness is also taken into consideration, the proper compression and shear ratio can be again adjusted by changing the inclination of the top plate and the rubber component. Furthermore, if the compression and shear ratio is significantly decreased by removing the compressive part of the original model, a highly elastic fastening system can be obtained. It tells us that compression and shear ratio is a key factor in designing the resilient properties of a rail fastening system in all directions. The parameter sensitivity analysing and structural optimization discussed in the present chapter is believed to be helpful and inspirational to the product designing and optimization of rail fastening systems. The empirical methods can be gradually improved on the basis of theoretical foundation and the enhanced understanding.

GENERAL CONCLUSION

As a consequence of introduction of continuous welded rail (CWR) track and concrete sleepers especially in case of slab track structures, rail fastening systems with great flexibility are increasingly demanded. However, the requirement for the improved performance of high elastic rail fastening systems conflicts with the current development status being dramatically diversified but mainly empirical. Except a few leading companies in the worldwide, nearly most products especially in the developing countries are imported or imitatively and empirically produced. Hundreds of products were newly introduced with only a few simple specifications and nearly no thorough theoretical analysis can be found and well documented; there is even no a generally accepted standard for rail fastening products' designing and selecting. At this situation, the present work aims at enhancing understanding of two typical kinds of rail fastening systems, providing a few reasonable product optimization objects and measures more than empirical methods.

This present research combines the experiments and the numerical analysis to understand and predict the mechanical behaviour of rail fastening systems. Firstly, a set of quasi-static and dynamic experiments of two typical kinds of rail fastening systems were conducted, one of which is a compressed type and the other is the shear type. The quasi-static measurement doesn't aim at determining their static stiffness, but mainly at discovering their nonlinear elastic properties. Through the dynamic experiments, both compressed and shear type specimens exhibit motion amplitude dependent and frequency dependent properties. Preload dependence was also observed by superimposing oscillations to the quasi-static loading curves. It was found that the rail fastening systems show the same basic characteristics concerning stiffness and loss angle as the rubber material does in terms of modulus magnitude and loss factor. The decreased secant dynamic stiffness and increased energy loss during an oscillating cycle, as well as a peak value of the loss angle were observed from the experiment data coinciding with the nonlinear feature of rubber material referred to as Payne effect. Frequency dependency was linearized because the loading frequency range is only below 20Hz. It is so far away from the nonlinear frequency dependent area. Preload influence is supposed to be due to either the finite strain characteristic of rubber material or the geometries and boundary conditions of the specimens.

In order to deepen the understanding of the pre-compression influenced, frequency dependent and amplitude dependent properties of rail fastening systems, the experimental results are simulated by three different numerical models. Numerical models were commonly used to describe the properties of vibration isolation systems, such as the high buildings mounted on top of special rubber pads intending to isolate the building from ground vibrations, nearly all the suspension bridges constructed with vibration controlling component in case of violent torsional vibrations as is suffering from high wind, aircraft wings, vehicle suspension systems, precision machineries, and so on. Though rail fasting systems are typical vibration isolation components and it's increasingly important especially for slab track structures, few numerical models were proposed to analyse the mechanical performance of rail fastening systems so far, don't even say documented materials. The most distinguished difference between rail fastening systems and other vibration isolation systems is that it's consistently subjected to a pre-compressed working condition or sometimes combined with tension and shear; the dynamic force is superimposed onto a pre-load. Different from other systems being free at the normal situations whose main deformation mode is alternating tension and compression, the pre-compression and the superimposed strain may bring about severe nonlinear deformations. Since it is quite difficult to implement a model considering all working conditions of a system, and, if any, a model accounting for too wide range would be not accurate enough, these three models focus on different properties of the two fastening specimens respectively. Though all of them are under special hypotheses and simplification, they can still help to depict and predict the mechanical behaviour from a general point of view.

Besides the numerical models which are believed to enlighten the understanding of the nonlinear mechanical behaviours of rail fastenings systems, FEA process is also promoted dedicating in the detailed features, such as geometric properties. As a result, a family of material fundamental measurements is carried out, followed by the DMA tests. Different hyperelastic and viscolastic models are fitted and compared. Finally, Van der Waals and Bergstrom-Boyce model are selected to define the rubber material during finite element analysis.

By using the evaluated Van der Waals and Bergstrom-Boyce models, the quasi-static and dynamic experiments were simulated by using Abaqus. The simulation can meet the experiment results rather well. And then, nonlinear features due to different reasons are

studied. The most noticeable nonlinearity shown in the quasi-static working curves of the two specimens were found to be the boundary nonlinearity due to nonlinear contact. Since it is impossible to capture the moment when contacting occurs in a real experiment, simulation was used to reappear the loading-unloading phase and make it possible to have the contacting moment visible. Besides the boundary nonlinearity, the loading curve of compressed type fastening system (specimen I) also exhibits geometric nonlinear properties. Rubber cylinder specimen of the uniaxial compression test was used to explain the boundary constraint induced and the largely changing shape caused geometric nonlinearities. In comparison with specimen I, the shear type fastening system (specimen II) doesn't show visible geometric nonlinear features. Moreover, from the calculated results we can see that specimen II also does not show the material nonlinearity for its large strain value. On the opposite, both compressive and shear deformations of the rubber component in specimen I is reaching the nonlinear material strain range. Material nonlinearity therefore contributes to the nonlinear loading curve of specimen I as the measured curve shows. At last, rubber material viscosity is also discussed. The nonlinear transient stiffness at the beginning of both loading and unloading phases was studied; in the mean while disturbance from stress relaxation was eliminated by adding a holding step of 2000s. Furthermore, the hysteresis loops of both fastening specimens are compared and studied. Nonlinearity analysis of the two specimens is believed to be helpful in optimizing the geometric properties in details. Some of them can be taken full use while others should be avoided. It will eventually help to guide the product designing and optimization process in the real practice, and improve their performance.

At last, geometric parameter sensitivity analysing of both the shear type and the compressed type fastening systems was performed. As for the shear type specimen, inclined angle of the elliptical ring, the width and the height of the component efficiently influence on its vertical resilient property. The inclined angle also strongly effects on the lateral resilience and the vertical-lateral stiffness ratio by adjusting the important compression and shear ratio in both directions. Subsequently, several optimization objects are proposed in terms of improving the vibration isolation efficiency, decreasing the displacement response, reducing the material cost, balancing the vertical and lateral stiffness ratio, diminishing the local maximum strain and stress values and damping property as well as free surface optimization; and the corresponding solving process are also presented. As for the compressed type

fastening system, similar parameter sensitivity analysing procedure are carried out. Influences on the vertical and the lateral elastic properties by each geometric parameter are explained by plotted figures. If the compressed fastening system is demanded much lower stiffness, a combined compression-and-shear type fastening system can be introduced to meet the demands. Largely reduced stiffness value was obtained. If a well matched lateral stiffness is also taken into consideration, the proper compression and shear ratio can be again adjusted by changing the inclination of the top plate and the rubber component correspondingly. Furthermore, when the compression and shear ratio is significantly decreased by removing the compressive part of the original model, a highly elastic fastening system can be obtained. The compression and shear ratio was found to be a key factor in designing the resilient properties of rail fastening systems in all directions. In a word, the parameter sensitivity analysing and structural optimization discussed at the end of current research is believed to be helpful and inspirational to the product designing process of rail fastening systems. The imitational and empirical methods can be gradually improved on the basis of theoretical foundation and the enhanced understanding.

Generally speaking, the innovation points of current research can be summarized as:

- quasi-static and dynamic experiments of the two rail fastening systems aiming at exhibiting the pre-load influenced nonlinear features as well as the frequency and dynamic amplitude dependent properties were designed and performed;
- though rail fastening systems are classical vibration isolation systems and it's so important component for providing elastic properties of the whole track structure, numerical models are firstly proposed to describe pre-compression influenced, frequency and dynamic amplitude dependent mechanical behaviour of rail fastening systems;
- novel design approach of rail fastening systems on the basis of nonlinear analysis were raised, including boundary nonlinearity, geometric nonlinearity, material nonlinearity, hysteresis induced nonlinearities. Some of the nonlinear features can be taken full advantage, while some other should be avoided during designing and producing process;
- by using Abaqus, geometric parameter sensitivity analysing benefits understanding their effects on the vertical and lateral resilient properties. In addition, a few optimization

objects and the corresponding problem-solving process lightens the designing and optimization methods, among which the compression-shear ratio is a key factor.

The presented work is believed to deepen the understanding of the static and dynamic mechanical behaviour of both shear and compressed type rail fastening systems and enlighten the designing and optimization measures. Nevertheless, there are possible extensions to current work:

- Future work may focus on extending the single stimulating frequency to multi-frequency even random excitation. However, although single-frequency excitation is the major measurement condition in most published researches on rubber isolation system, rail fastening systems in the real practice are subjected to multi-frequency and random disturbance.
- Another future work can be extending the low stimulating frequency to higher frequency range. In the real practice, rail fastening systems are subjected to the wheel-rail force from zero to more than 2000Hz. Though the low frequency is the main disturbance, higher frequency force may also give rise to serious response. This is a quite hard task for both mechanical modelling and finite element analysing process because it demands a much more versatile mechanical model considering the nonlinear elasticity, severe amplitude dependence and also frequency influence of rather wide range. On the other hand for FEA, another amendatory constitutive model instead of Bergstrom-Boyce model needs to be embedded into the FEA software for the simulation.
- In addition, temperature dependent properties are also very important for rubber components in the real practice. It's fatal to the mechanical fatigue and strength characteristics of rail fastening system which should also be taken full consideration during designing and optimization process. This can be included in the future work.
- Influences of different rubber material prescription on the mechanical properties of both type rail fastening systems should also be taken into consideration.

APPENDIX

APPENDIX A1: INCLINED ANGLE INFLUENCED QUASI-STATIC CURVES

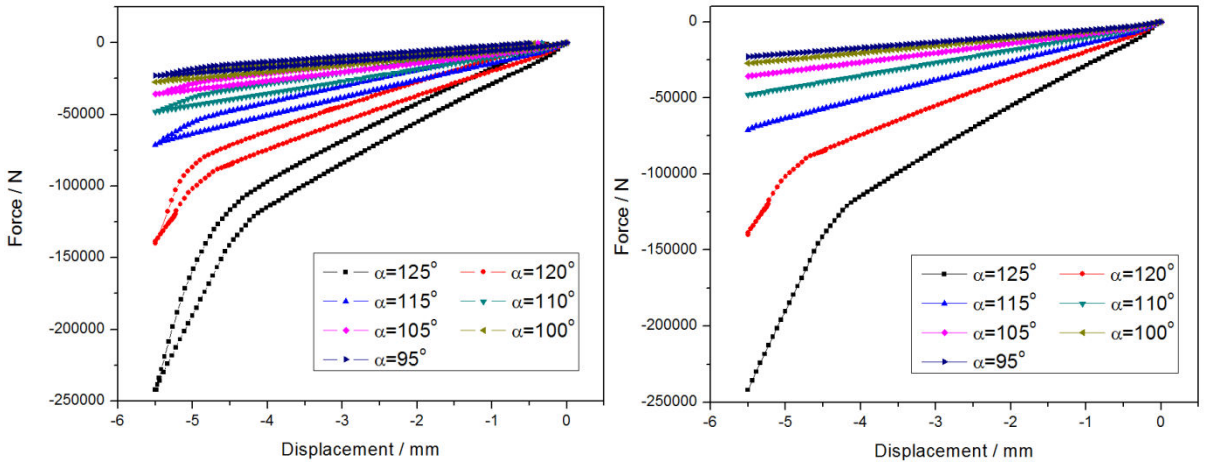

(a) Quasi-static loops (b) Loading curves

APPENDIX A2: INCLINED ANGLE INFLUENCED PROPERTIES RELEVANT TO THE VERTICAL STIFFNESS

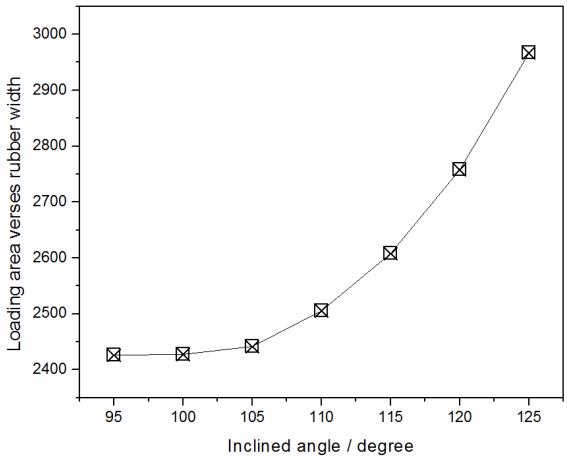

(a) Loading area S_{load} versus width

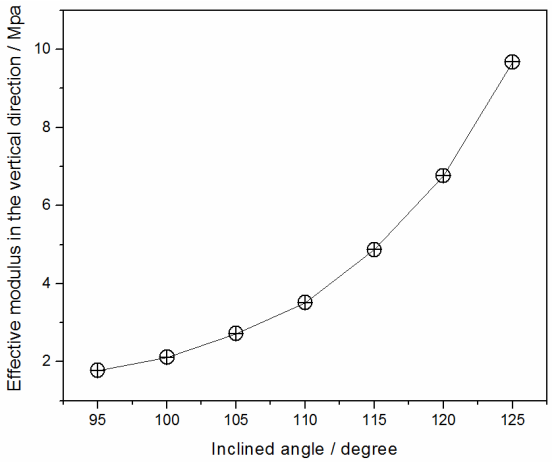

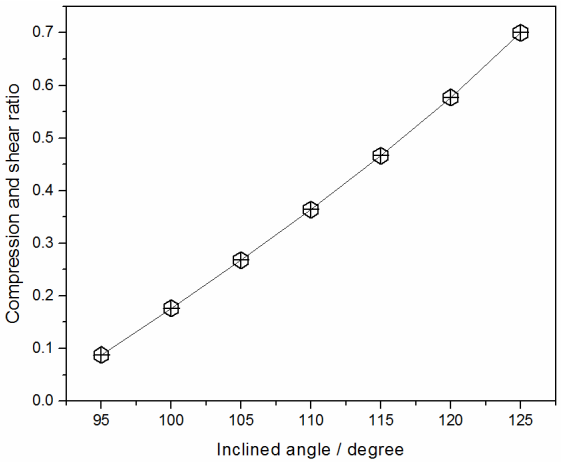

(b) Effective modulus in the vertical direction E_v (c) Compression and shear ratio

APPENDIX A3: NATURAL FREQUENCY OF THE ORIGINAL MODEL SIMULATED BY ABAQUS

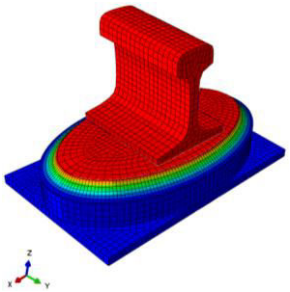

(a) The first vibration mode

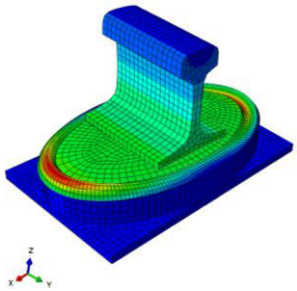

(b) The second vibration mode

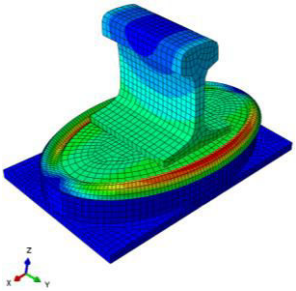

(c) The third vibration mode

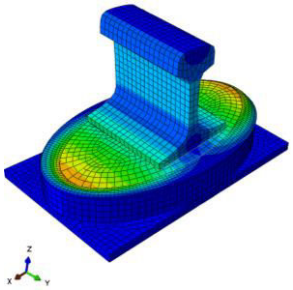

(d) The fourth vibration mode

APPENDIX A4: VIBRATION REDUCTION IN dB

Stimulating frequency \ Inclined angle	125º	120º	115º	110º	105º	100º	95º
40 Hz							1.12
45 Hz						2.04	4.64
50 Hz					1.48	5.09	7.38
55 Hz					4.32	7.54	9.66
60 Hz				2.61	6.63	9.61	11.65
65 Hz			0.25	4.90	8.60	11.42	13.33
70 Hz			2.63	6.84	10.32	13.02	14.87
75 Hz			4.62	8.54	11.85	14.46	16.27
80 Hz		1.45	6.33	10.04	13.23	15.78	17.54
85 Hz		3.30	7.85	11.40	14.50	16.99	18.73
90 Hz		4.91	9.21	12.64	15.66	18.11	19.82
95 Hz	0.85	6.34	10.46	13.78	16.75	19.16	20.85
100 Hz	2.47	7.63	11.60	14.84	17.76	20.14	21.82
105 Hz	3.91	8.81	12.65	15.83	18.71	21.06	22.73
110 Hz	5.19	9.89	13.64	16.76	19.60	21.94	23.59
115 Hz	6.36	10.90	14.56	17.64	20.45	22.77	24.41
120 Hz	7.43	11.83	15.43	18.47	21.26	23.55	25.19
125 Hz	8.43	12.71	16.25	19.26	22.02	24.31	25.93
130 Hz	9.35	13.54	17.03	20.01	22.75	25.02	26.64
135 Hz	10.22	14.33	17.78	20.73	23.45	25.71	27.32
140 Hz	11.04	15.08	18.48	21.41	24.12	26.37	27.98
145 Hz	11.81	15.79	19.16	22.07	24.77	27.01	28.61
150 Hz	12.54	16.47	19.81	22.70	25.39	27.62	29.21

APPENDIX A5: INCLINED ANGLE INFLUENCED PROPERTIES RELEVANT TO THE LATERAL STIFFNESS

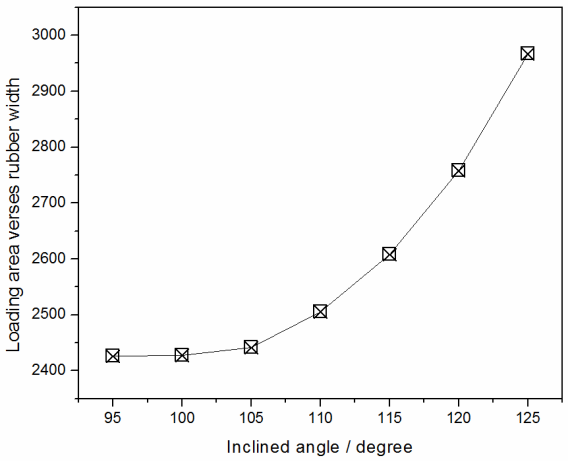

(a) Loading area S_{load} versus width

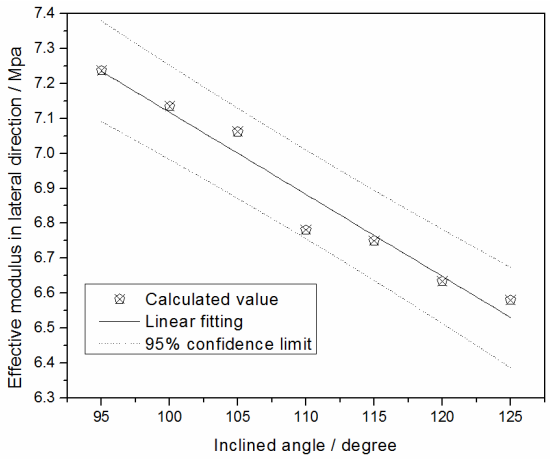

(b) Effective modulus in lateral direction

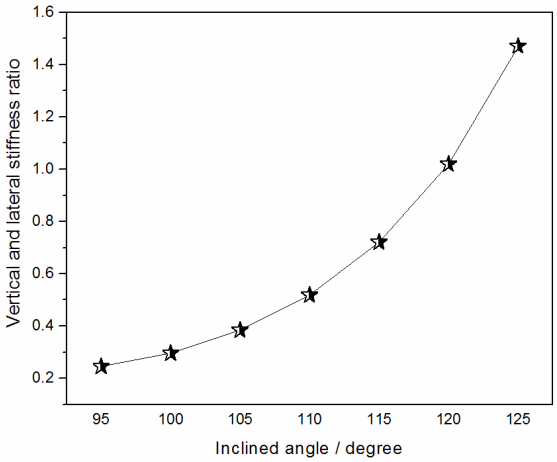

(c) Vertical and transverse stiffness ratio

APPENDIX B1: WIDTH INFLUENCED TESTING CURVES AND THE VERTICAL SITFFNESS

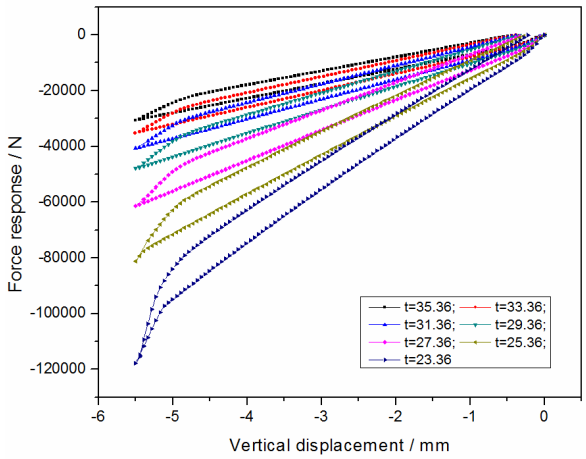

(a) Quasi-static loops

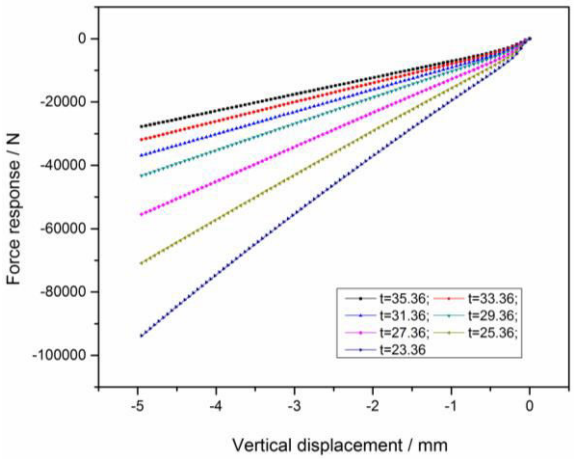

(b) Loading curves

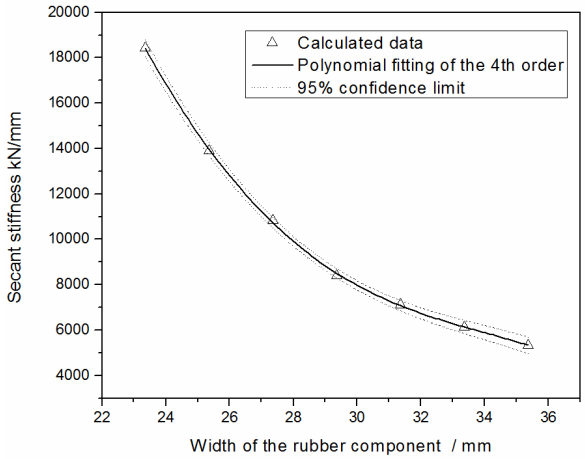

(c) Secant stiffness

APPENDIX B2: THE SHEAR STRAIN-STRESS RELATIONSHIP ON THE INFLUENCE OF RUBBER COMPONENT WIDTH

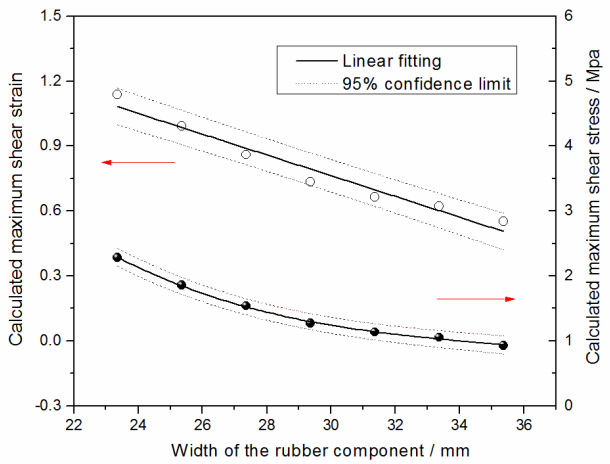

(a) Maximum strain and stress

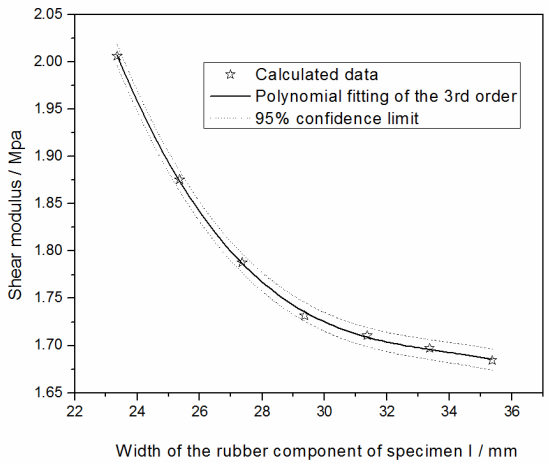

(b) Shear modulus

APPENDIX B3: VIBRATION ISOLATION EFFICIENTY AND VOLUME OF THE RUBBER COMPONENT WHEN CHANGING WIDTH

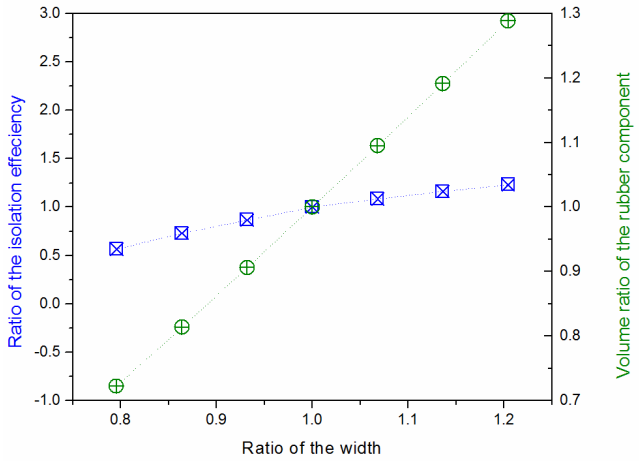

APPENDIX B4: WIDTH DEPENDENT MAXIMUM AND MINIMUM PRINCIPLE STRAIN

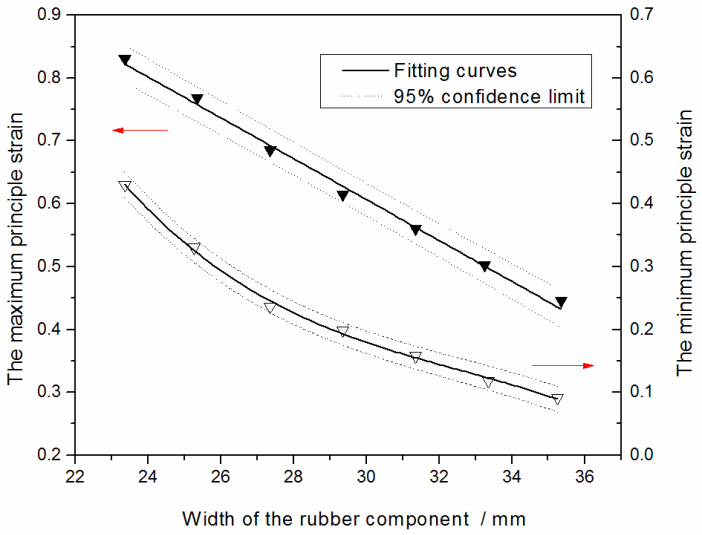

APPENDIX B5: LATERAL STIFFNESS AND THE VERTICAL AND LATERAL STIFFNESS RATIO DEPENDENT ON THE MODIFIED WIDTH

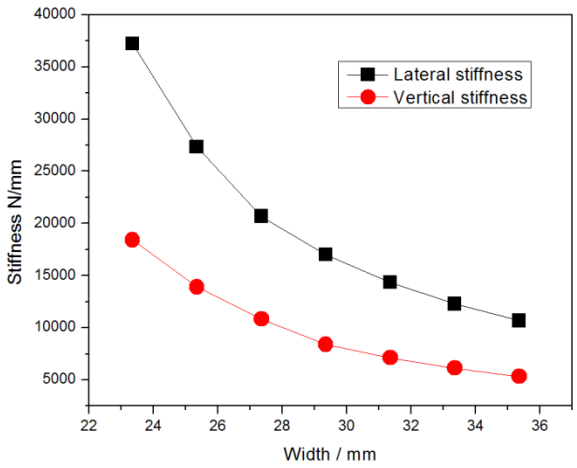

(a) Vertical and transverse stiffness

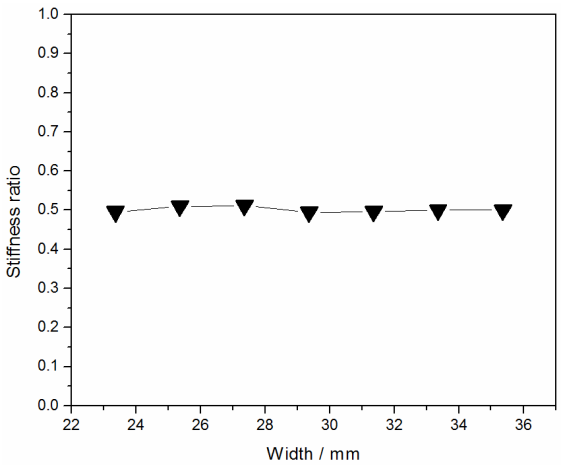

(b) Vertical and lateral stiffness ratio

APPENDIX C1: HEIGHT INFLUENCED VERTICAL STIFFNESS

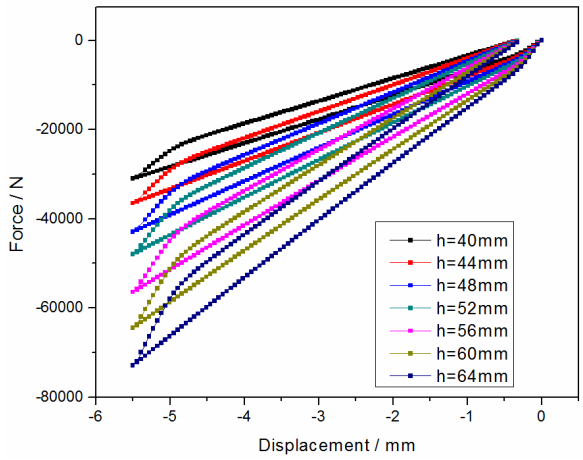

(a) Quasi-static loops

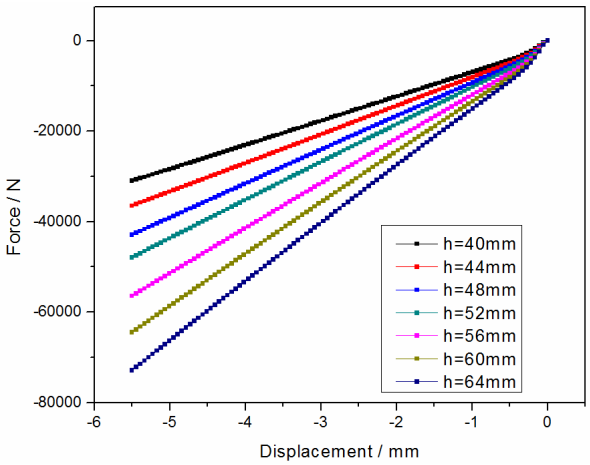

(b) Loading curves

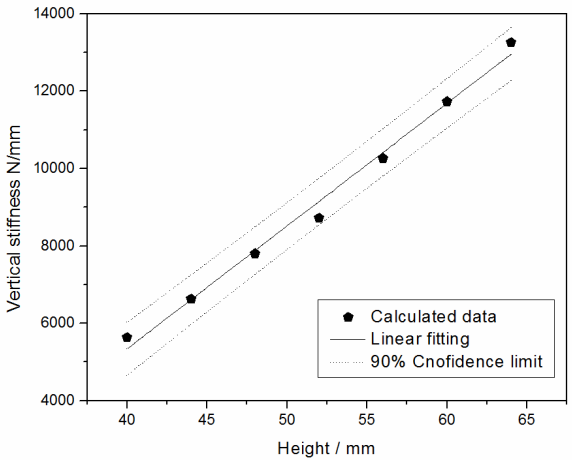

(c) Secant stiffness

APPENDIX C2: VIBRATION ISOLATION EFFICIENTY AND VOLUME OF THE RUBBER COMPONENT WHEN CHANGING HEIGHT

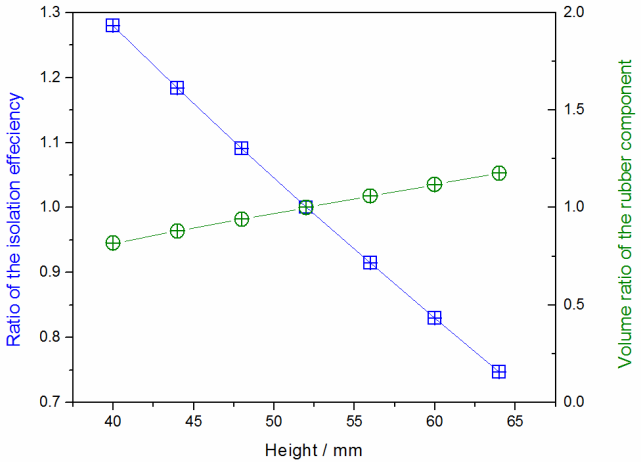

APPENDIX C3: HEIGHT DEPENDENT MAXIMUM AND MINIMUM PRINCIPLE STRAIN

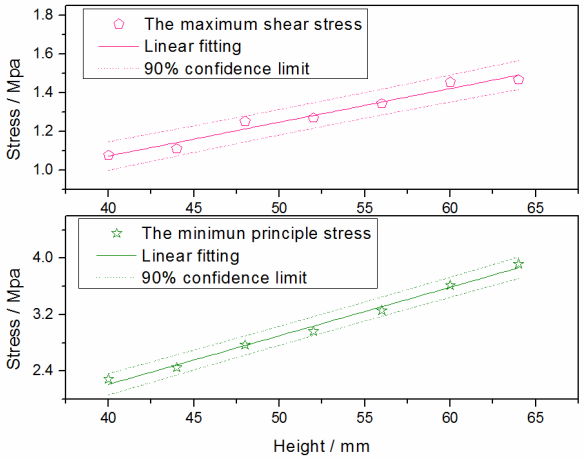

APPENDIX C4: LATERAL STIFFNESS AND THE VERTICAL AND LATERAL STIFFNESS RATIO DEPENDENT ON THE MODIFIED HEIGHT

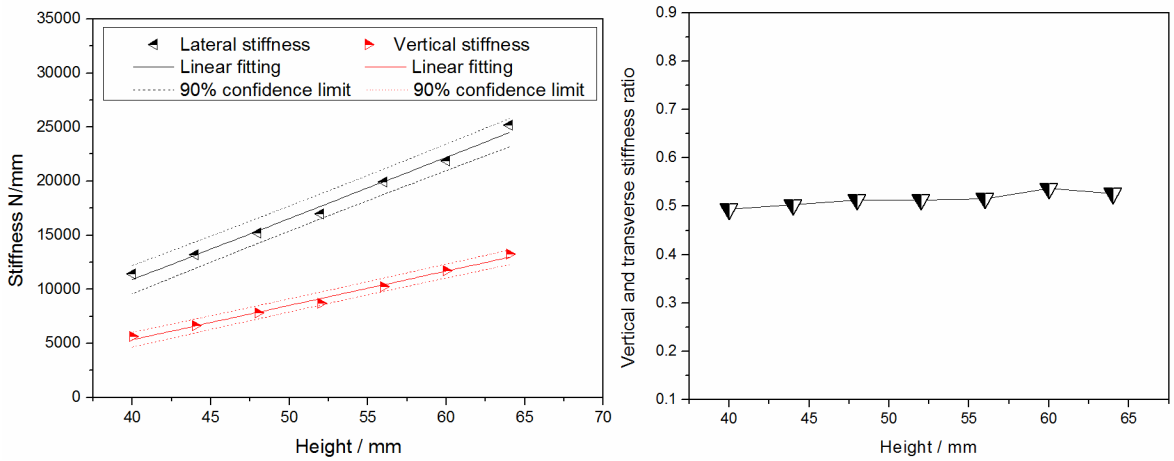

(a) Vertical and lateral stiffness (b) Vertical and lateral stiffness ratio

APPENDIX D1: L1 INFLUENCED VERTICAL QUASI-STATIC LOOPS AND VERTICAL SITFFNESS

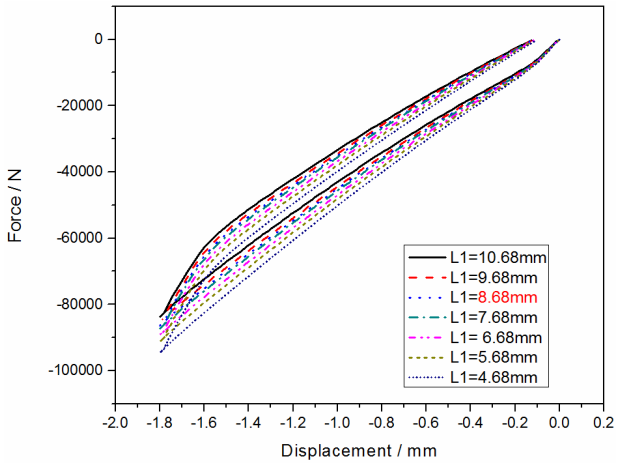

APPENDIX D2: L3 INFLUENCED VERTICAL QUASI-STATIC LOOPS AND VERTICAL SITFFNESS

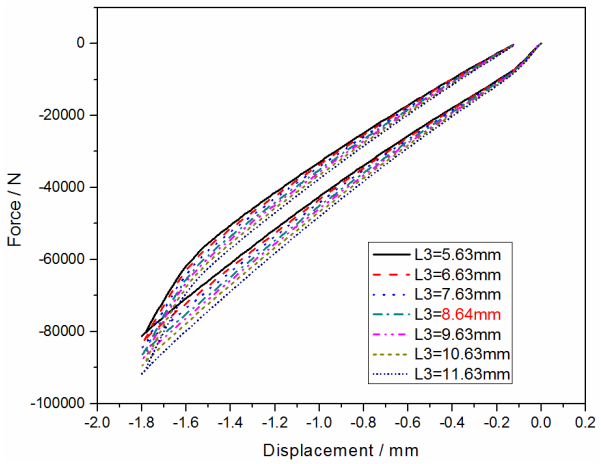

APPENDIX D3: L4 INFLUENCED VERTICAL QUASI-STATIC LOOPS AND VERTICAL SITFFNESS

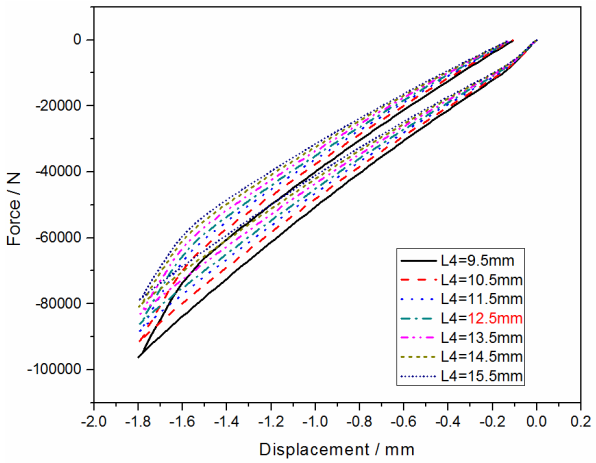

APPENDIX D4: L7 INFLUENCED VERTICAL QUASI-STATIC LOOPS AND VERTICAL SITFFNESS

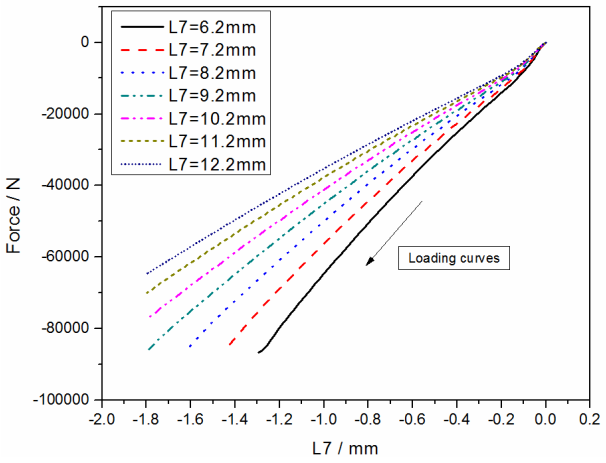

APPENDIX D5: VERTICAL SITFFNESS PROPERTIES INFLUENCED BY L2 L5 AND L6

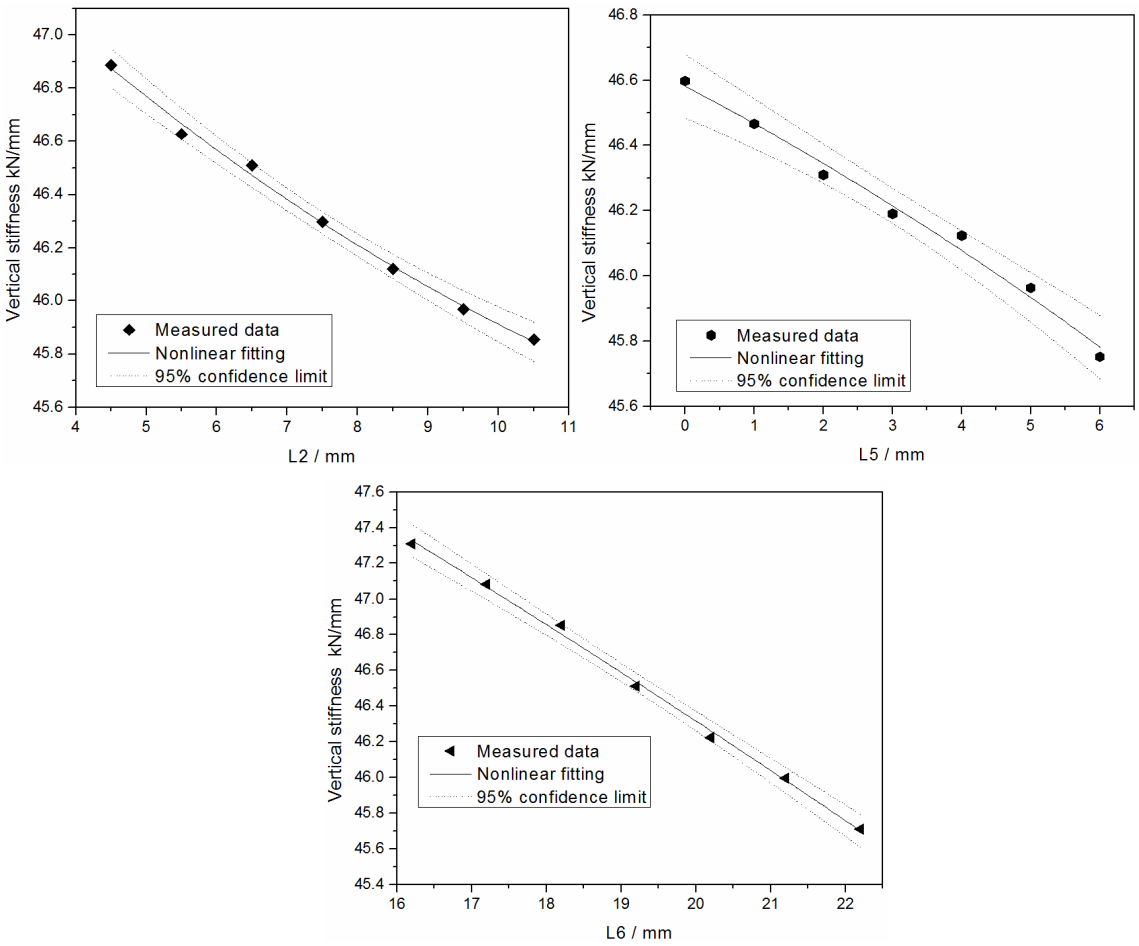

APPENDIX E: COMPARED NATURAL FREQUENCY CALCULATED BY THE MEASURED VERTICAL STIFFNESS AND SIMULATION

L4 (mm)	Vertical stiffness from the virtual static test curve K (kN/mm)	Nature frequency from the virtual static test curve $f_n = \sqrt{k_v/M}$ (Hz)	Nature frequency of the 1st order obtained by using Abaqus (Hz)
9.5	50.80	79.44	76.676
10.5	48.75	77.82	75.066
11.5	47.37	76.71	73.919
12.5	46.51	76.02	73.157
13.5	45.35	75.06	72.426
14.5	44.16	74.07	71.306
15.5	43.39	73.42	70.646

APPENDIX F1: L7 INFLUENCED FORCE TRANSMISSIBILITY AS THE DAMPING RATIO EQUALED 0.01

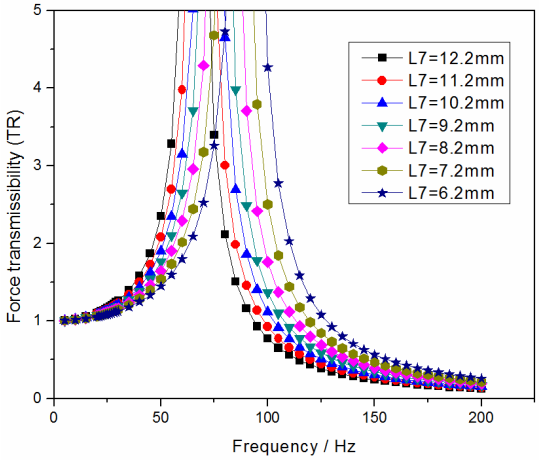

APPENDIX F2: L7 INFLUENCED VIBRATION ISOLATION AS THE DAMPING RATIO EQUALED 0.01

L7 /mm / Stimulating Frequency /Hz	6.2	7.2	8.2	9.2	10.2	11.2	12.2
95							0.63
100						0.67	2.27
105					0.76	2.24	3.72
110				0.77	2.24	3.62	5.01
115			0.60	2.20	3.57	4.87	6.19
120		0.12	1.97	3.47	4.76	6.00	7.27
125		1.48	3.21	4.62	5.86	7.04	8.27
130	0.70	2.69	4.33	5.68	6.86	8.01	9.20
135	1.92	3.80	5.36	6.66	7.80	8.91	10.07
140	3.02	4.82	6.31	7.57	8.68	9.76	10.89
145	4.04	5.76	7.20	8.42	9.50	10.56	11.66
150	4.98	6.63	8.03	9.22	10.28	11.31	12.40

APPENDIX G: L7 INFLUENCED DYNAMIC AMPLIFICATION FACTOR AS THE DAMPING RATIO EQUALED 0.2

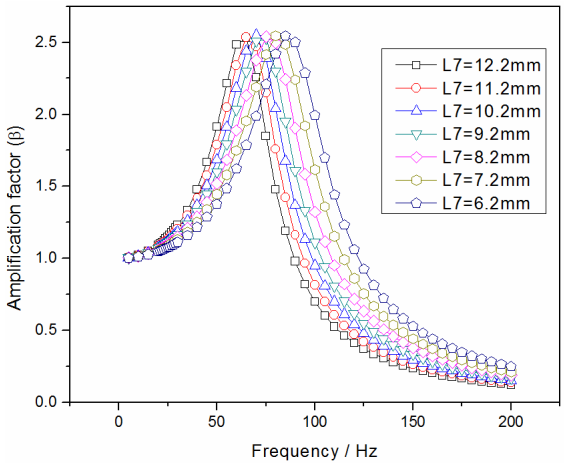

APPENDIX H1:L3 INFLUENCED LATERAL STIFFNESS IN COMPARISON TO THE VERTICAL STIFFNESS

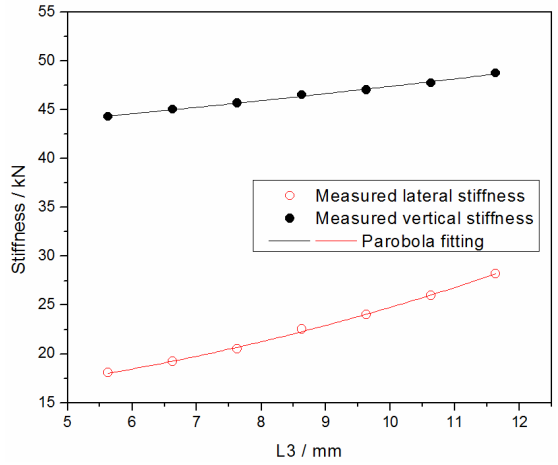

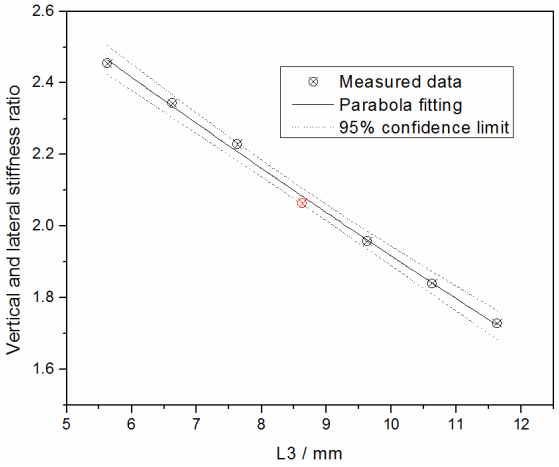

APPENDIX H2: L7 INFLUENCED LATERAL STIFFNESS IN COMPARISON TO THE VERTICAL STIFFNESS

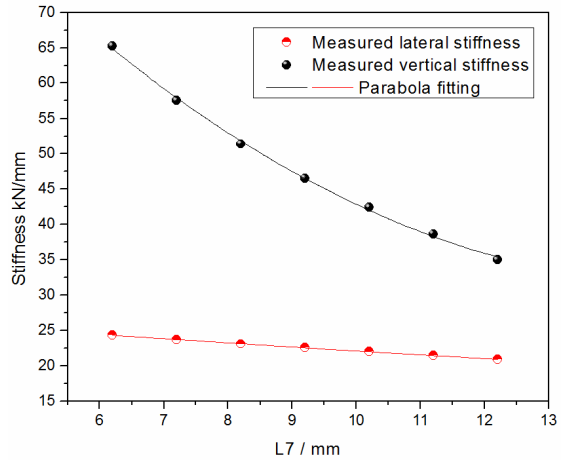

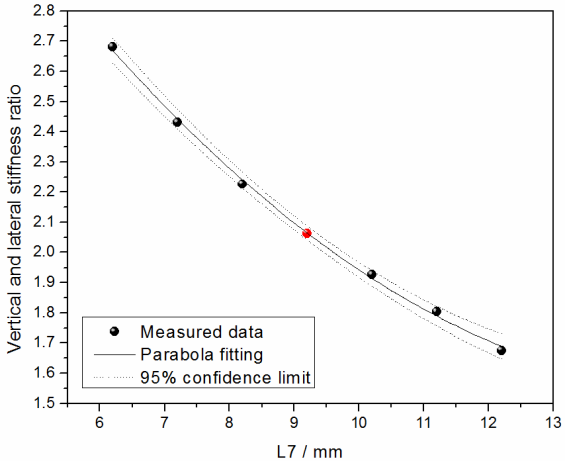

APPENDIX H3:L4 INFLUENCED LATERAL STIFFNESS IN COMPARISON TO THE VERTICAL STIFFNESS

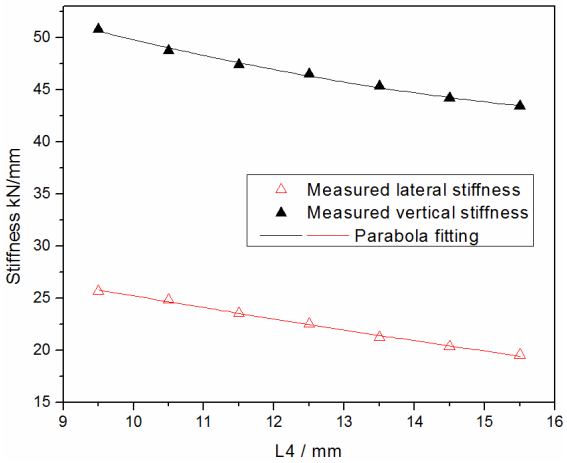

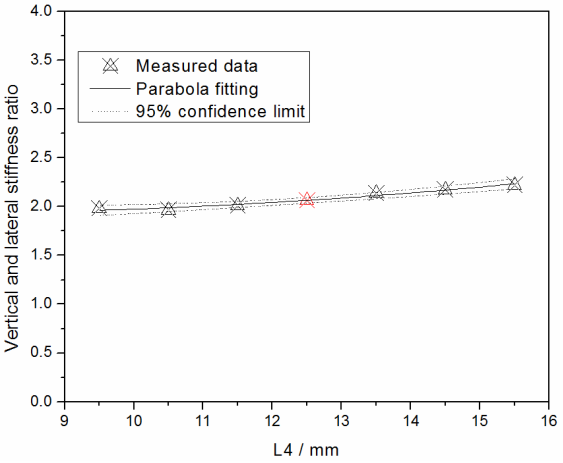

APPENDIX H4: L1 INFLUENCED LATERAL STIFFNESS IN COMPARISON TO THE VERTICAL STIFFNESS

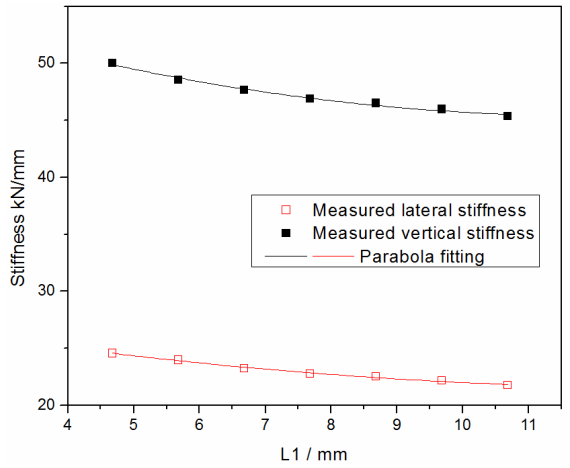

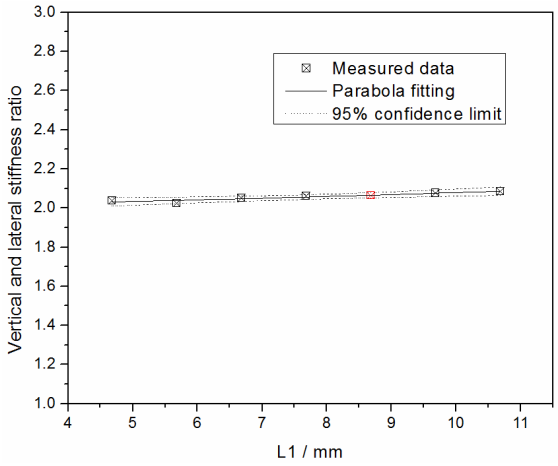

APPENDIX I1: L1 INDUCED MAXIMUM STRAIN AND STRESS

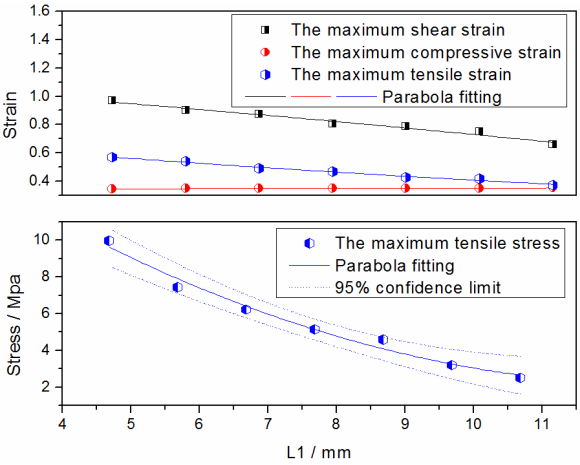

(a) Loaded vertically

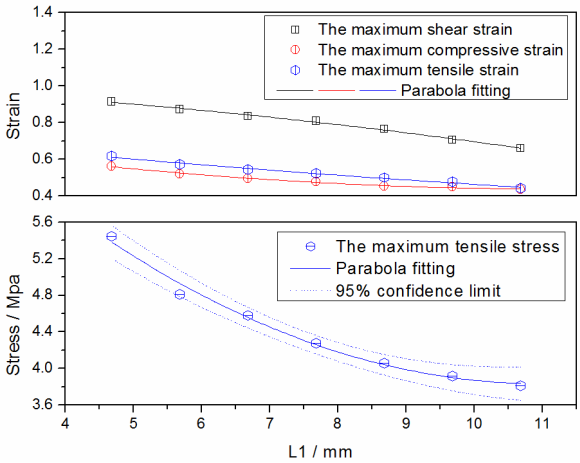

(b) Loaded laterally

APPENDIX I2: GEOMETRIC PARAMETER (L2 AND L4) INDUCED MAXIMUM SHEAR STRAIN

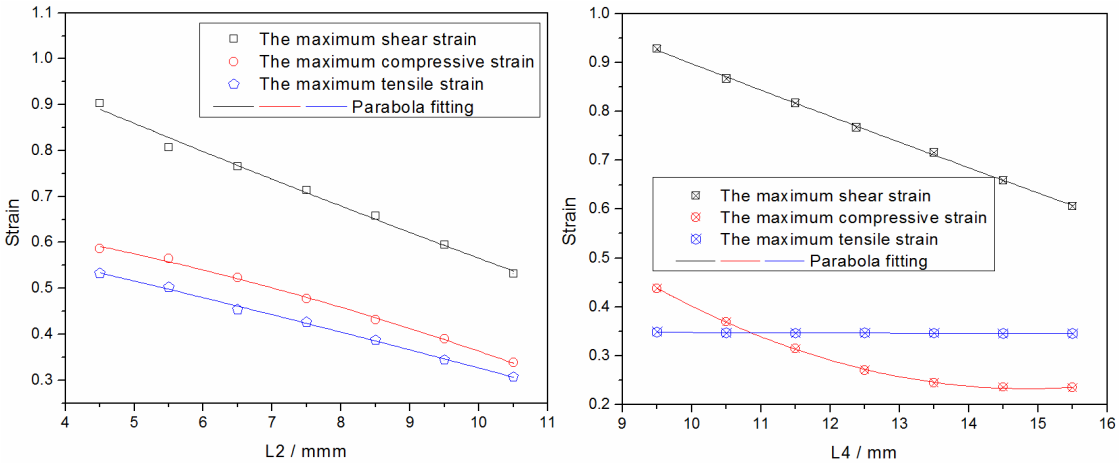

(a) Loaded vertically (b) Loaded laterally

APPENDIX I3: SPECIFICITY OF THE PARAMETER L7

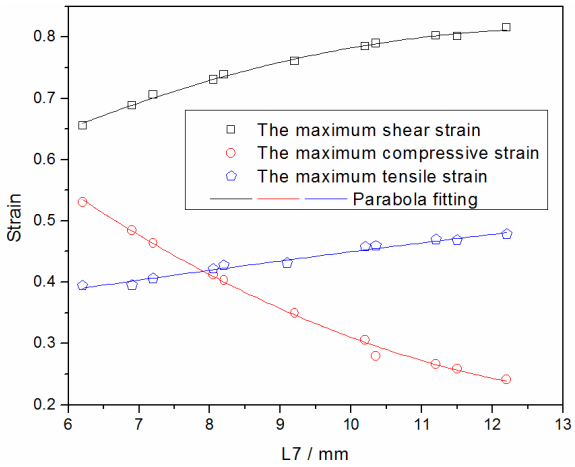

REFERENCES

[1] Coenraad Esveld., Modern Railway Track, Second Edition. 2001.
[2] Becker S and Lier K. H. Bewertung und Varianten-vergleich von Bauarten der Festen Fahrbahn, *Eisenbahn Ingenieur,* 2, 1999.
[3] Darr E. and Fiebig W. Feste Fahrbahn*, Edrtron VDEI*, Tetzlaff Verlag, Germany, 1999.
[4] Oberweiler G.: Die Feste Fahrbahn-Entwicklung und Beurteilung aus der Sicht des Anwenders, *ETR,* 3, 1989.
[5] Bachmann H and Foege T.. Rheda 2000-Erfahrungen aus Einbau und Verarbeitung, *Esenbahn Ingenieur*, 9, 2000.
[6] Hillig J.: Erdbautechnische Anforderungen an eine schotterlose Fahrbahn, *Eisenbahn Ingenieur*, 5, 1994.
[7] Pfleiderer AG: Rheda 2000-Die monolitische Feste Fahrbahn mit Direktafbau auf HGT.
[8] Widmann H.: Feste Fahrbahn Bauan Züblin, *Feste Fahrbahn*. Edition ETR, Hestra Verlag. Germany, 1997.
[9] Eisenmann J.: Oberbauforschung-Oberbautechnik, Stand und Weiterentwicklung, *ETR*, 10, 1985.
[10] Lutz, R., Survey of the work by ORE about Railway Noise, *Third International Workshop on Railway and Tracked Transit System Noise, 1981*.
[11] George Paul Wilson, Rail system noise and vibration control. *Proceedings of ACOUSTICS*, 2004
[12] http://www.delkorrail.com.
[13] http://www.c-km.org.tw.
[14] M Berg, A model for rubber springs in the dynamic analysis of rail vehicles, *Proceedings of the Institution of Mechanical Engineers, Part F: Journal of Rail and Rapid Transit* March 1, 1997 vol. 211 no. 2 95-108
[15] Freakley P. K., Payne A. R. Theory and Practice of Engineering with Rubber, 1978 (*Applied Science Publishers*, London).
[16] Ferry J. D., Viscoelastic Properties of Polymers, 3rd edition, 1980 (*Wiley*, New York).
[17] Battermann W., Köhler R., Elastomere Federung Elastische Lagerungen, 1982 (*Wilhelm Ernst and Sohn*, Berlin).
[18] Göbel E. F., Rubber Springs Design, 1974 (*Newnes-Butterworths*, London).
[19] Lindley P. B., Engineering Design with Natural Rubber, 5th edition, *NR Technical Bulletin,* 1992.
[20] Harris C. M., Shock and Vibration Handbook—Properties of Rubber, 3rd edition, 1988, Ch. 35 (*McGraw-Hill*, London).
[21] Alan N. Gent. Engineering with Rubber-How to Design Rubber Components. 2nd Edition. Hanser Publishers, Munich.
[22] Roderic Lakes., Viscoelastic Materials, Cambridge University Press, 2009
[23] H Dal, M Kaliske, Bergström–Boyce model for nonlinear finite rubber viscoelasticity: theoretical aspects and algorithmic treatment for the FE method, *Computational Mechanics,* November 2009, Volume 44, Issue 6, pp 809-823.
[24] Abaqus Analysis User's Manual, Volume III: Materials, Version 6.12.
[25] M. Sasso, G. Palmieri, G. Chiappini, D. Amodio. Characterization of hyperelastic rubber-like materials by biaxial and uniaxial stretching tests based on optical methods. *Polymer Testing*, 27, 995-1004, 2008.

[26] A Wineman, Nonlinear Viscoelastic Solids—A Review, *Mathematics and Mechanics of Solids* May 2009 vol. 14 no. 3 300-366.
[27] Wineman, A.S. and Rajagopal, K.R., Mechanical Response of Polymers, An Introduction. *Cambridge University Press*, Cambridge, 2000.
[28] H.T. Banks, Shuhua Hu, Zackary R. Kenz, A brief review of elasticity and viscoelasticity, CRSC-TR10-08, NC State University, May, 2010, *Advances in Applied Mathematics and Mechanics* (submitted for publication).
[29] M. Gurtin and E. Sternberg, On the linear theory of viscoelasticity, *Archive for Rational Mechanics and Analysis*, 11 (1965), 291–365.
[30] T.H. Shellhammer, T.R. Rumsey and J.M. Krochta, Viscoelastic properties of edible lipids, *Journal of Food Engineering*, 33 (1997), 305–320.
[31] M. Doi and M. Edwards, the Theory of Polymer Dynamics, *Oxford*, New York, 1986.
[32] C.S. Drapaca, S. Sivaloganathan and G. Tenti, Nonlinear constitutive laws in viscoelasticity, *Mathematics and Mechanics of Solids*, 12 (2007), 475–501.
[33] W.N. Findley, J.S. Lai and K. Onaran, Creep and Relaxation of Nonlinear Viscoelastic Materials, *Dover Publications*, New York, 1989.
[34] Y.C. Fung, Biomechanics: Mechanical Properties of Living Tissue, *Springer-Verlag,* Berlin, 1993.
[35] F.J. Lockett, Nonlinear Viscoelastic Solids, *Academic*, New York, 1972.
[36] K.N. Morman, Jr. Rubber viscoelasticity – a review of current understanding, *Proceedings of the Second Symposium on Analysis and Design of Rubber Parts*, Jan. 14–15, 1985.
[37] R.A. Schapery, Nonlinear viscoelastic solids, *International Journal of Solids and Structures*, 37 (2000), 359–366.
[38] J. Smart and J.G. Williams, A comparison of single integral non-linear viscoelasticity theories, *Journal of the Mechanics and Physics of Solids*, 20 (1972), 313–324.
[39] A.E. Green and R.S. Rivlin, The mechanics of non-linear materials with memory, *Archive for Rational Mechanics and Analysis*, 1 (1957), 1–21.
[40] A.C., Pipkin and T.G. Rogers, A non-linear integral representation for viscoelastic behaviour, *Journal of the Mechanics and Physics of Solids*, 16 (1968), 59–72.
[41] A. Wineman, Nonlinear viscoelastic solids – a review, *Mathematics and Mechanics of Solids*, 14 (2009), 300–366.
[42] R.B. Bird, C.F. Curtiss, R.C. Armstrong and O.Hassager, *Dynamics of Polymeric Liquids, Vol. 2, Kinetic Theory,* Wiley, New York, 1987.
[43] J.G. Oakley, A.J. Giacomin and J.A. Yosick, Molecular origins of nonlinear viscoelasticity: fundamental review, *Mikrochimica Acta*, 130 (1998), 1–28.
[44] M. Liu, MS. Hoo Fatt, A constitutive equation for filled rubber under cyclic loading, *International Journal of Non-Linear Mechanics*, Volume 46, Issue 2, March 2011, Pages 446–456.
[45] H.T. Banks and N. Luke, Modelling of propagating shear waves in biotissue employing an internal variable approach to dissipation, *Communication in Computational Physics*, 3 (2008), 603–640.
[46] H.T. Banks, N.G. Medhin and G.A. Pinter, Nonlinear reptation in molecular based hysteresis models for polymers, *Quarterly Applied Math.*, 62 (2004), 767–779.
[47] J.E. Soussou, F. Moavenzadeh, M.H. Gradowczyk, Application of prony series to linear viscoelasticity, *Trans. Soc. Rheol.*, 14 (1970), pp. 573–584.
[48] P. Haupt, A. Lion, on finite linear viscoelasticity of incompressible isotropic materials *Acta Mech.*, 159 (2002), pp. 87–124.

[49] J.S. Bergström, M.C. Boyce, Constitutive modelling of the large strain time-dependent behaviour of elastomers, *J. Mech. Phys. Solids*, 46 (1998), pp. 931–954.
[50] J.S. Bergström, M.C. Boyce, Constitutive modelling of the time-dependent and cyclic loading of elastomers and application to soft biological tissues, *Mech. Mater.,* 33 (2001), pp. 523–530.
[51] Y. Tomita, K. Azuma, M. Naito, Computational evaluation of strain-rate-dependent deformation behaviour of rubber and carbon-black-filled rubber under monotonic and cyclic straining, *Int. J. Mech. Sci.,* 50 (2008), pp. 856–868.
[52] A. Lion, A constitutive model for carbon black filled rubber: experimental investigations and mathematical representation, *Continuum Mech. Thermodyn.*, 8 (1996), pp. 153–169.
[53] A. Lion, A physically based method to represent the thermo-mechanical behaviour of elastomers, *Acta Mech.,* 123 (1997), pp. 1–25.
[54] S. Reese, S. Govindjee, A theory of finite viscoelasticity and numerical aspects, *Int. J. Solids Struct.*, 35 (1998), pp. 3455–3482
[55] N. Huber, C. Tsakmakis, Finite deformation viscoelasticty laws, *Mech. Mater.*, 32 (2000), pp. 1–18
[56] A.F.M.S. Amin, A. Lion, S. Sekita, Y. Okui, Non-linear dependence of viscosity in modelling the rate-dependent response of natural and high damping rubbers in compression and shear: experimental identification and numerical verification, *Int. J. Plast.,* 22 (2006), pp. 1610–1657
[57] Reese S, Govindjee S (1998) A theory of finite viscoelasticity and numerical aspects. *Int J Solids Struct* 35: 3455–3482
[58] Simo JC, Miehe C (1992) Associative coupled thermoplasticity at finite strains: formulation, numerical analysis and implementation. *ASME J Appl Mech* 98: 41–104
[59] Simo JC (1992) Algorithms for static and dynamic multiplicative plasticity that preserve the classical return mapping schemes of the infinitesimal theory. *Comput Methods Appl Mech Eng* 99: 61–112
[60] Weber G, Anand L (1990) Finite deformation constitutive equations and a time integration procedure for isotropic hyperelastic-viscoplastic solids. *Comput Methods Appl Mech Eng* 79: 173–202
[61] Cuitino A, Ortiz M (1992) a material-independent method for extending stress update algorithms from small-strain plasticity to finite plasticity with multiplicative kinematics. *Eng Comput* 9: 437–451
[62] H.T. Banks, N.G. Medhin and G.A. Pinter, Multiscale considerations in modelling of nonlinear elastomers, Technical Report CRSC-TR03-42, NCSU, October, 2003; *J. Comp. Meth. Engr. Sci. and Mech.,* 8 (2007), 53–62.
[63] H.T. Banks, N.G. Medhin and G.A. Pinter, Modelling of viscoelastic shear: A nonlinear stick-slip formulation, CRSC-TR06-07, February, 2006; *Dynamic Systems and Applications*, 17 (2008), 383–406.
[64] H.T. Banks and G.A. Pinter, Damping: hysteretic damping and models, CRSC-TR99-36, NCSU, December, 1999; *Encyclopedia of Vibration* (S.G. Braun, D. Ewins and S. Rao, eds.), Academic Press, London (2001), 658–664.
[65] P Höfer, A Lion, Modelling of frequency- and amplitude-dependent material properties of filler-reinforced rubber, *Journal of the Mechanics and Physics of Solids,* Volume 57, Issue 3, March 2009, Pages 500–520.
[66] Y.C. Fung, Foundations of Solid Mechanics, *Prentice-Hall*, Englewood Cliffs, NJ, 1965.
[67] Y.C. Fung, A First Course in Continuum Mechanics, *Prentice Hall*, New Jersy, 1994.

[68] H.T. Banks and G.A. Pinter, A probabilistic multiscale approach to hysteresis in shear wave propagation in biotissue, *Multiscale Modelling and Simulation,* 3 (2005), 395–412.
[69] H.T. Banks, G.A. Pinter, L.K. Potter, M.J. Gaitens and L.C. Yanyo, Modelling of quasistatic and dynamic load responses of filled viscoelastic materials, CRSC-TR98-48, NCSU, December, 1998; Chapter 11 *in Mathematical Modelling: Case Studies from Industry* (E. Cumberbatch and A. Fitt, eds.), Cambridge University Press, 2001, 229–252.
[70] H.T. Banks, G.A. Pinter, L.K. Potter, B.C. Munoz and L.C. Yanyo, Estimation and control related issues in smart material structures and fluids, CRSC-TR98-02, NCSU, January, 1998; *Optimization Techniques and Applications* (L. Caccetta, et al., eds.), Curtain Univ. Press, July, 1998, 19–34.
[71] Häggblad B., Finite element techniques for engineering rubber problems, *Int. J. Numer. Methods in Engng* (to be published).
[72] Pipkin A. C., Lectures on Viscoelasticity Theory, 2nd edition, 1986 (Springer, New York).
[73] Nicolin, J. and Dellmann, T. (1985) Über die modellhafte Nachbildung der dynamischen Eigenschaften einer Gummifeder , *ZEV-Glasers Annalen* , Vol. 109 (4), pp. 169 – 175.
[74] Peeken , H. and Lambertz , S. (1994), Nichtlineares Materialmodell zur Beschreibung des Spannungs-Dehnungsverhaltens gefiillter Kautschuk-Vulkanisatc, *Konstruktion*, 46 (1), pp. 9 – 15 .
[75] M. Berg, A Non-Linear Rubber Spring Model for Rail Vehicle Dynamics Analysis, *Vehicle System Dynamics: International Journal of Vehicle Mechanics and Mobility,* Volume 29, Supplement 1, 1998.
[76] M. Sjöberg, On Dynamic Properties of Rubber Isolators, 2002.
[77] Austrell PE. Olsson AK. J¨onsson M. A method to analyse the nonlinear dynamic behaviour of carbon-black-filled rubber components using standard FE codes. in: Besdo D. Schuster RH. Ihlemann J. (eds.), *Constitutive Models for Rubber II.* Swets and Zeitlinger, 205–211, 2001.
[78] Betz E. Spring and dashpot models and their applications in the study of the dynamic properties of rubber. *Mechanical and Chemical Engineering Transactions,* 15–24, May, 1969.
[79] Lodhia BB. Esat II. Vibration simulation of systems incorporating linear viscoelastic mounts using prony series formulation. In: *Proceedings of Engineering Systems Design and Analysis Conference,* ASME 81(9), 171–176, 1996.
[80] Olsson AK. Austrell PE. A fitting procedure for a viscoelastic-elastoplastic material model. in: Besdo D. Schuster RH. Ihlemann J. (eds.), *Constitutive Models for Rubber II. Swets and Zeitlinger,* 205–211, 2001.
[81] Park SW. Analytical modelling of viscoelastic dampers for structural and vibration control. *International Journal of Solids and Structures* 36, 939–970, 2001.
[82] Gaul L. The influence of damping on waves and vibrations. *Mechanical Systems and Signal Processing* 13, 1–30, 1999.
[83] Rossikhin YA. Shitikova MV. Applications of fractional calculus to dynamic problems of linear and nonlinear hereditary mechanics of solids. *Applied Mechanical Review* 50(1), 1997.
[84] Shimizu N. Zhang W. Fractional calculus approach to dynamic problems of viscoelastic materials. *Japaneese Society of Mechanical Engineers C*, 42, No 4, 1999.
[85] Koeller RC. Applications of fractional calculus to the theory of viscoelasticity. *Journal of Applied Mechanics* 51, 299-307, 1984.
[86] Cosson P. Michon JC. Identification by a non-integer order model of the mechanical behaviour of an elastomer. Chaos, *Solitons and Fractals* 7(11), 1807-1824, 1996.

[87] Horr AM. Schmidt LC. A fractional–spectral method for vibration of damped space structures. *Engineering Structures* 18(12), 947–956, 1996.
[88] Bagley RL. Torvik PJ. Fractional Calculus — A different approach to the analysis of viscoelastically damped structures. *American Institute of Aeronautics and Austronatics Journal* 21, 741-748, 1983.
[89] Moreau X. Ramus–Serment C. Oustaloup A. Fractional differentiation in passive vibration control. *Nonlinear Dynamics* 29, 343–362, 2002.
[90] Papoulia KD. Kelly JM. Visco-hyperelastic model for filled rubbers used in vibration isolation. *Journal of Enginnering Materials and Technology* 119(3), 292–297, 1997.
[91] Kari L. Eriksson P. Stenberg B. Dynamic stiffness of natural rubber cylinders in the audible frequency range using wave guides. *Kautschuk Gummi Kunststoffe* 54(3), 106–113, 2001.
[92] Yuan L. Agrawal OP. A numerical scheme for dynamic systems containing fractional derivatives. *Journal of Vibration and Acoustics* 124, 321–324, 2002.
[93] Hwang JS. Hsu TY. A fractional derivative model to include effect of ambient temperature on HDR bearings. *Engineering Structures* 23, 484-490, 2001.
[94] Eldred LB. Baker WP. Palazotto AN. Numerical application of fractional derivative model Constitutive Relations for Viscoelastic Materials. *Computers and Structures* 60(6), 875–882, 1996.
[95] Atanackovic TM. Stankovic B. Dynamics of a viscoelastic rod of fractional derivative type. *Zeitschrift für Angewandte Mathematik und Mechanik* 82(6), 377–386, 2002.
[96] Schmidt A. Gaul L. Finite element formulation of viscoelastic constitutive equations using fractional time derivatives. *Nonlinear Dynamics* 29, 37–55, 2002.
[97] Fenander A. Modal synthesis when modelling damping by use of fractional derivatives. *American Institute of Aeronautics and Astronautics Journal* 34(5), 1051–1058, 1996.
[98] Enelund M. Olsson P. Damping described by fading memory — analysis and application to fractional derivative models. *International Journal of Solids and Structures* 36, 939–970, 1999.
[99] Enelund M. M¨ahler L. Runesson K. Josefson BL. Formulation and integration of the standard linear viscoelastic solid with fractional order rate laws. *International Journal of Solids and Structures* 36, 2417–2442, 1999.
[100] M Sjöberg, L Kari, Nonlinear Isolator Dynamics at Finite Deformations: An Effective Hyperelastic, Fractional Derivative, Generalized Friction Model, *Nonlinear Dynamics* August 2003, Volume 33, Issue 3, pp 323-336.
[101] Harris, J. and Stevenson, A., On the role of nonlinearity in the dynamic behaviour of rubber components, *Rubber Chemistry and Technology* 59(5), 1986, 740–764.
[102] Ravindra, B. and Mallik, A. K., Hard Duffing-type vibration isolator with combined Coulomb and viscous damping, *International Journal of Non-Linear Mechanics* 28, 1993, 427–440.
[103] Ravindra, B. and Mallik, A. K., Performance of non-linear vibration isolators under harmonic excitation, *Journal of Sound and Vibration* 170(3), 1994, 325–337.
[104] Ravindra, B. and Mallik, A. K., Chaotic response of a harmonically excited mass on an isolator with nonlinear stiffness and damping characteristics, *Journal of Sound and Vibration* 182(3), 1995, 345–353.
[105] Natsiavas, S. and Tratskas, P., on vibration isolation of mechanical systems with non-linear foundations, *Journal of Sound and Vibration* 194(2), 1996, 173–185.

[106] Gjika, K., Dufour, R., and Ferraris, G., Transient response of structures on viscoelastic or elastoplastic mounts: Prediction and experiments, *Journal of Sound and Vibration* 198(3), 1996, 361–278.
[107] Shekhar, N. C., Hatwal, H., and Mallik, A. K., Response of non-linear dissipative shock isolators, *Journal of Sound and Vibration* 214(4), 1998, 589–603.
[108] Mallik, A. K., Kher, V., Puri, M., and Hatwal, H., On the modelling of non-linear elastomeric vibration isolators, *Journal of Sound and Vibration* 219(2), 1999, 239–253.
[109] Shekhar, N. C., Hatwal, H., and Mallik, A. K., Performance of non-linear isolators and absorbers to shock excitations, *Journal of Sound and Vibration* 227(2), 1999, 293–307.
[110] Richards, C.M. and Singh, R., Characterization of rubber isolator nonlinearities in the context of single-and multi-degree-of-freedom experimental systems, *Journal of Sound and Vibration* 247(5), 2001, 807–834.
[111] Coveney VA. Johnson DE. Turner DM. A triboelastic model for the cyclic mechanical behaviour of filled vulcanizates. *Rubber Chemistry and Technology* 68, 660–670, 1995.
[112] Coveney VA. Jamil S. Johnson DE. Keavey MA. Williams HT. Rate dependent triboelastic and other models for elastomers and prospects for implementation in finite element analysis. in: Boast D. Coveney VA. (eds.) *Finite Element Analysis of Elastomers,* Professional Engineering Publishing, Wiltshire, 1999.
[113] Gregory MJ. Dynamic properties of rubber in automotive engineering. *Elastomerics* 117(11), 19–24, 1985.
[114] Coveney VA. Jamil S. Johnson DE. Keavey MA. Menger C. Williams HT. Implementation in finite element analysis of a triboelastic law for dynamic behaviour of filled elastomers. in : Boast D. Coveney VA. (eds.) *Finite Element Analysis of Elastomers, Professional Engineering Publishing,* Wiltshire, 1999.
[115] Bruni S. Collina A. Modelling of viscoelastic behaviour of elastomeric components: An application to the simulation of train-track interaction. *Vehicle System Dynamics* 34, 283-301, 2000.
[116] Brackbill CR. Lesieutre GA. Smith EC. Ruhl LE. Characterization and modelling of the low strain amplitude and frequency dependent behaviour of elastomeric damper materials. *Journal of the American Helicopter Society* 45(1), 34–42, 2000.
[117] Mallik AK. Kher V. Puri M. Hatwal H. On the modelling of nonlinear elastomeric vibration isolators. *Journal of Sound and Vibration* 219(2), 239–253, 1999.
[118] Barber AJ. Accurate models for complex vehicle components using empirical methods. *SAE Paper* No 2000-01-1625, 2000.
[119] Berg M. A Three-dimensional airspring model with friction and orifice damping. *Vehicle System Dynamics* 33, 528–539, 1999.
[120] Z Chen, M Shin, B Andrawes, JR Edwards, Parametric study on damage and load demand of prestressed concrete crosstie and fastening systems, *Engineering Failure Analysis,* Volume 46, November 2014, Pages 49–61.
[121] R.D. Frohling, Low frequency dynamic vehicle/track interaction: modelling and simulation, *Vehicle Syst Dynam,* 29 (1998), pp. 30–46
[122] C. González-Nicieza, M.I. Álvarez-Fernández, A. Menéndez-Díaz, A.E. Álvarez-Vigil, F. Ariznavarreta-Fernández, Failure analysis of concrete sleepers in heavy haul railway tracks, *Eng Fail Anal*, 15 (2008), pp. 90–117
[123] F. Rezaie, M.R. Shiri, S.M. Farnam, Experimental and numerical studies of longitudinal crack control for pre-stressed concrete sleepers, *Eng Fail Anal*, 26 (2012), pp. 21–30.
[124] S. Kaewunruen, A.M. Remennikov, Nonlinear transient analysis of a railway concrete sleeper in a track system, *Int J Struct Stab Dyn,* 8 (2008), pp. 505–520

[125] Yu H, Jeong DY. Finite element modelling of railroad concrete crossties – a preliminary study, *ICRE2010 – International Conference on Railway Engineering*, Beijing Jiaotong University, Beijing, China; 2010.
[126] H. Yu, D. Jeong, J. Choros, T. Sussmann, Finite element modelling of prestressed concrete crosstie with ballast and subgrade support, *ASME 2011 international design engineering technical conference & computers and information in engineering conference*, ASME, Washington, DC, USA (2011).
[127] T. Dahlberg, A. Lundqvist, Load impact on railway track due to unsupported sleepers, *Proc Inst Mech Eng, Part F: J Rail Rapid Transit*, 219 (2005), pp. 67–77.
[128] NF EN 13146-9 +A1 December 2011
[129] NF EN 13146-4 June 2003
[130] NF EN 13481-5 February 2003
[131] Tariq S. Giacomin AJ. Gunasekaran S. Nonlinear viscoelasticity of cheese. *Biorheology* 35 (3), 171-191, 1998.
[132] Onogi S. Matsumoto T. Rheological properties of polymer solutions and melts containing suspended particles. *Polymer Engineering Reviews*, 1, 45-87, 1981.
[133] Mullins L. Softening of rubber by deformation. *Rubber Chemistry and Technology* 42, 339-362, 1969.
[134] Mullins L. Mechanical behaviour of polymers – Accomplishments and problems. in: Hepburn C. Reynolds RJW. (eds.), *Criteria for Engineering Design, Applied Science Publishers*, 1-18, 1979.
[135] Sjöberg M. Dynamic behaviour of a rubber component in the low frequency range-Measurements and modelling. In: *Proceedings of the 7th International Conference of Sound and Vibration*, Garmisch-Partenkirchen, (5), 2955-2962, 2000.
[136] Medalia AI. Effects of carbon black on dynamic properties of rubber. *Rubber Chemistry and Technology* 51, 437-523, 1978.
[137] Payne AR. Whittaker RE. Low strain dynamic properties of filled rubbers. *Rubber Chemistry and Technology* 44, 440-478, 1971.
[138] Dean GD. Duncan JC. Johnson AF. Determination of nonlinear dynamic properties of carbon-filled rubbers. *Polymer Testing* 4(2-4), 225-249, 1984.
[139] Jurado FJ. Matero A. Gil-Negrete N. Vinolas J. Kari L. Testing and FE modelling of the dynamic properties of carbon black filled rubber. In: *Proceedings of EAEC 99*, Barcelona, 1999.
[140] Sommer JG. Meyer DA. Factors controlling the dynamic properties of elastomeric products. *SAE Paper* NO 730267, 1973.
[141] WANG MJ. Effect of polymer-filler and filler-filler interactions on dynamic properties of filled vulcanizates. *Rubber Chemistry and Technology* 71(3), 520-589, 1998.
[142] Sjöberg M. Kari L. Testing of nonlinear interaction effects of sinusoidal and noise excitation on rubber isolator stiffness. *Polymer Testing* 22(3), 347-355, 2003.
[143] Wenbo Luo, Xiaoling Hu, Chuhong Wang, Qifu Li. Frequency-and strain-amplitude-dependent dynamic mechanical properties and hysteresis loss of CB-filled vulcanized natural rubber. *International Journal of Mechanical Sciences*. 52, 168-174, 2010.
[144] Y. Liu, Y. Luo, H.P. Yin. Dynamic characteristic analysis of rubber absorber in rail fastening. *Journal of Central South University (Science and Technology)*. 42 (9), 2011.
[145] Y. Luo, Y. Liu, H.P. Yin. Numerical investigation of nonlinear properties of a rubber absorber in rail fastening systems. *International Journal of Mechanical sciences* 69, 107-113, 2013.

[146] F. Dinzart., P. Lipinski.. Improved five-parameter fractional derivative model for elastomers. *Arch. Mech*., 61(6), 459-474, 2009.
[147] R.L. Bagley, P.J. Torvik. Fractional calculus-a different approach to the analysis of viscoelastically damped structures, *American Institute of Aeronautics and Astronautics Journal*, 2, 741-748, 1983.
[148] R. L. Bagley, P.J. Torvik. On the fractional calculus model of viscoelastic behaviour. *Journal of Rheology*, 30, 133-135, 1986.
[149] C. Friedrich. Relaxation and retardation functions of the Maxwell model with fractional derivatives. *Rheologica Acta*, 30(a), 89-93, 1991.
[150] T. F. Nonnenmacher, W.G. Glöckle. A fractional model for mechanical stress relaxation, *Phil. Mag. Lett*., 64(2), 89-93, 1991.
[151] N. Heymans, J.C. Bauwens. Fractal rheological models and fractional differential equations for viscoelastic behaviour, *Rheologica Acta,* 33(3), 210-219, 1994.
[152] H. Schiessel, R. Metzler, A. Blumen, T.F. Nonnenmacher. Generalized viscolastic models: their fractional equations with solutions*, J. Phys. A*, 28(23), 6567-6584, 1995.
[153]. A. Rossikhin, M.V. Shitikova. Applications of fractional calculus to dynamic problems of linear and nonlinear hereditary mechanics of solids. *Appl. Mech. Rev.*, 50, 15-67, 1997.
[154] R. Metzler, T.F. Nonnenmacher. Fractional relaxation processes and fractional rheological models for the description of a class of viscoelastic materials. *Int. J. Plast.*, 19, 941-959, 2003.
[155] Oldham K. B., Spanier J.. The fractional calculus, Academic Press, 1974. New York and London.
[156] Kari L. Extended fractional-order derivative viscoelastic material model for structure-born sound analysis, Trita-FKT 1997:18, Stockholm.
[157] Jörgen S., Bergström. Dynamic finite element modelling of elastomers. In: Proceedings of Abaqus Users' Conference, 2008.
[158] D.J. Charlton, J. Yang. A review of methods to characterize rubber elastic behaviour for use in finite element analysis. AIRBOSS LTD., Perth, Western Australia.
[159] Tod Dalrymple, Jaehwan Choi, Kurt Miller. Elastomer rate-dependence: a testing and material modelling methodology. Fall 172nd Technical Meeting of the Rubber Division of the American Chemical Society, Inc.
[160] Kurt Miller. Testing Elastomers for Hyperelastic Material Models in Finite Element Analysis. Axel Products, Inc.
[161] BS ISO 37:2005. Rubber, Vulcanized or thermoplastic-Determination of tensile stress-strain properties.
[162] Compression or Biaxial Extension? Axel Products, Inc.
[163] J.R. Day, K.A. Miller. Equiiaxial Stretching of Elastomeric Sheets, An Analytical Verification of Experimental Technique. Abaqus 2000 User's Conference Proceedings, Newport, Rhode Island, May 30-June 2, 2000.
[164] ISO 7743. Rubber, Vulcanized or thermoplastic-Determination of compression stress-strain properties. 2004-01-15.
[165] Nonlinear finite element analysis of elastomers. MSC. Software: Whitepaper.
[166] Where do the "pure" and "shear" come from in the pure shear test? www.endurica.com
[167] Sang Jin Lee. Active, Polymer-Based Composite Material Implementing Simple Shear. 2008.
[168] Timoshenko, S.P. Theory of Elasticity. 3rd Ed. McGraw-Hill, New York, NY, 1970.
[169] B C Duncan, A S Maxwell, L E Crocker, R. Hunt. Verification of hyperelastic test methods. *NPL Report No. CMMT (A)*, 226, 1999.

[170] Farbod Nassiri. New Approach in characterizing accessory drive belts for finite element applications.2010.
[171] M. Sasso, G. Palmieri. Characterization of hyperelastic rubber-like materials by biaxial and uniaxial stretching tests based on optical methods. *Polymer Testing*, 27, 955-1004, 2008.
[172] K. Miller. Testing elastomers for ANSYS. Axel Products Inc. The Focus, publication for ANSYS users, ISSUE 12, 2002.
[173] K. Miller. Measuring material properties to build material models in FEA. Axel Products Inc.
[174] M. Wadham Gagnon, P. Hubert, M.P. Paidoussis, C. Semler, D. Lavoie. Hyperelastic modelling of rubber in commercial finite element software (ANSYS), 51ST Sample International Symposium, Long Beach, CA, April 30- May 4, 2006.
[175] ASTM designation D945-06-Standard test methods for rubber properties in compression or shear (Mechanical oscillograph). *Annual book of ASTM standards*, 9(1), 2002.
[176] Standard Test Methods for Vulcanized Rubber and TPE for Use in Finite Element Analysis Modelling. GMN6814.
[177] Justin D.Marshall. Development, Analysis and Testing of a hybrid Passive Control Deice for Seismic Protection of Framed Structures. 2008.
[178] C. Macosko, J. Starita. SPE Journal, 27(38), 1971.
[179] Kevin P. Menard. Dynamic mechanical analysis. A practical Introduction. CRC Press, Boca Raton London, New York, Washington, D.C.
[180] A. Goldman. Prediction of the properties of polymeric and composite materials. ACS, Washington, 1994.
[181] Abaqus Analysis User's Manual, Volume III: Materials, Version 6.12.
[182] http://polymerfem.com/content.php
[183] Ir. J. Van't Zang, Ing. J. Moraal.Static and dynamic tests on rail fastening systems. Delft University of Technology.
[184] P.F. Turnbull, N.C. Perkins, W. W. Schultz. Contact-Induced Nonlinearity on Oscillating Belts and Webs. *Journal of Vibration and Control*, 1, 459-479, 1995.
[185] Nonlinear finite elements/Nonlinearities in solid mechanics. Wikiversity.
[186] Rubber Technology. ZORGE company, Netherlands.
[187] Andreas Hellman. Simulation of complete vehicle dynamics using FE code Abaqus. 2008.
[188] Mauro Olivero, Vincenzo Pulero, Massimo Barbi, Fabriziio Urbinati, Benedetta Peyron and Giancarlo Luciani, Alberto Novarese. Static and dynamic simulations for automotive interiors components using ABAQUS. 2012 SIMULIA Community Conference.
[189] Gent, A. N., Lindley, P.b.. The compression of bonded rubber blocks. *Proceedings of the institution of mechanicalEngineers*, 173 (1), 111-122.
[190] Williams, J.G., Gamonpilas, C.. Using the simple compression test to determine young's modulus, Poisson's ratio and coulomb frictioin coefficient. International Journal of Solids and Structures, 45(16), 4448-4459.
[191] Timoshenko, S.P., Goodier, J.N.. Theory of Elasticity, Mc Graw-Hill College, New York.
[192] Cornelius O. Horgan, Giuseppe Saccomandi. Phenomenological hyperelastic strain-stiffening constitutive models for rubber.
[193] P.A.L.S. Martins, R.M. Natal Jorge, A.J.M. Ferreira. A comparative study of several material models for prediction of hyperelastic properties: application to silicone-rubber and soft tissues. *Strain*, 42, 135-147, 2006.
[194] Mooney, M.. A theory of large elastic deformation. *J. Appl. Phys*., 11, 582-592, 1940

[195] Rivlin, R.S.. Large elastic deformations of isoltropic materials. IV: Further developments of the general theory. Philos. *Trans. R. Soc. Lond*, A241, 379, 1948.
[196] Ogden, R. W.. Nonlinear elastic deformations. Dover Publications Inc., Mineola, NY, USA.
[197] Holzapfel, G. A.. Nonlinear solid mechanics. John Wiley and Sons, New York, 2000.
[198] Lai, W. M., Rubin, D., Krempl, E.. Introduction to continuum mechanics, 3rd end. Butterworth Heinemann.
[199] Jongmin Shim, Dirk Mohr. Rate dependent finite strain constitutive model of polyuria. *International Journal of Plasticity*, 27, 868-886, 2011.
[200] A.F.M.S. Amin, M.S. Alam, Y. Okui. An improved hyperelasticity relation in modelling viscoelasticity response of natural and high damping rubbers in compression: experiments, parameter, identification and numerical verification. Mechanics of Materials, 34, 75-95, 2002.
[201] Huber N., Tsakmakis C.. Finite deformation viscoelasticity laws. *Mech. Mater*, 32, 1-18, 2000.
[202] Lubliner J.. A model for rubber viscoelasticity. *Mech. Res*. Comm, 12, 93-99, 1985.
[203] LeTallac P., Rahier C., Kaiss A.. Three dimensional incompressible viscoelasticity in large strain formulation and numerical approximation. *Comput. Meth. Appl. Mech. Engrg*, 109, 233-258, 1993.
[204] Reese S., Govindjee S.. A theory of finite viscoelasticity and numerical aspects. *Int. J. Solids Structures*, 35, 3455-3482, 1998.